ANNUAL REPORTS ON NMR SPECTROSCOPY

Volume 37

- Dynamic NMR spectroscopy in inorganic and organometallic chemistry
- Solid-state NMR studies of wood and other lignocellulosic materials
- NMR structural studies of iron-sulfur proteins
- NMR studies of wine chemistry and wine bacteria
- Proton phase-sensitive pulsed field gradient double-quantum spectroscopy

ACADEMIC PRESS

ANNUAL REPORTS ON

NMR SPECTROSCOPY

This Page Intentionally Left Blank

ANNUAL REPORTS ON

NMR SPECTROSCOPY

Edited by

G. A. WEBB

Department of Chemistry, University of Surrey, Guildford, Surrey, England

VOLUME 37

ACADEMIC PRESS

San Diego ● London ● Boston
New York ● Sydney ● Tokyo ● Toronto

This book is printed on acid-free paper.

Academic Press Limited
24–28 Oval Road, London NW1 7DX, UK
http://www.hbuk.co.uk./ap/

Academic Press
525 B Street, Suite 1900, San Diego, California 92101-4495, USA
http://www.apnet.com

ISBN 0-12-505337-1

A catalogue record for this book is available from the British Library

Typeset by Keyset Composition, Colchester, Essex
Printed in Great Britain by MPG Books Ltd, Bodmin, Cornwall

99 00 01 02 03 04 MP 9 8 7 6 5 4 3 2 1

List of Contributors

Jean-Marc Böhlen, *Bruker AG, CH 8117 Fällanden, Switzerland*

Claudio Dalvit, *Novartis Pharma AG, CH 4002 Basel, Switzerland*
Present address: Pharmacia & Upjohn, Nerviano (Mi), Italy

A. M. Gil, *Department of Chemistry, University of Aveiro, 3800 Aveiro, Portugal*

Brian J. Goodfellow, *Departamento de Química, Faculdade de Ciências e Tecnologia, Universidade Nova de Lisboa, 2825 Monte de Caparica, Portugal and Departamento de Quimica, Universidade de Aveiro, 3810 Aveiro, Portugal*

Anjos L. Macedo, *Departamento de Química, Faculdade de Ciências e Tecnologia, Universidade Nova de Lisboa, 2825 Monte de Caparica, Portugal*

C. Pascoal Neto, *Department of Chemistry, University of Aveiro, Campus de Santiago, 3800 Aveiro, Portugal*

Keith G. Orrell, *Department of Chemistry, The University, Exeter EX4 4QD, UK*

Ana Ramos, *Instituto de Tecnologia Química e Biológica, Universidade Nova de Lisboa, Apartado 127, 2780 Oeiras, Portugal*

Helena Santos, *Instituto de Tecnologia Química e Biológica, Universidade Nova de Lisboa, Apartado 127, 2780 Oeiras, Portugal*

This Page Intentionally Left Blank

Preface

As in previous volumes of this series, the current one consists of authoritative accounts of the applications of NMR in various areas of molecular science.

Dynamic NMR Spectroscopy in Inorganic and Organometallic Chemistry is admirably covered by K. G. Orrell; A. M. Gil and C. Pascoal Neto provide an interesting account of Solid-state NMR Studies of Wood and other Lignocellulosic Materials; this is followed by a comprehensive report on NMR Structural Studies of Iron–Sulfur Proteins by B. J. Goodfellow and A. L. Macedo; A. Ramos and H. Santos have given a fascinating account of NMR Studies of Wine Chemistry and Wine Bacteria; finally a thorough study of Proton Phase-sensitive Pulsed Field Gradient Double-quantum NMR Spectroscopy is presented by C. Dalvit and J. M. Böhlen.

It has been a great pleasure for me to have the opportunity of working with these reporters and I am very grateful to them for the prompt delivery of their very valuable and interesting contributions. It is also my pleasant duty to extend my thanks to the production staff at Academic Press (London) for their well-established support and cooperation in the production of this series of reports.

University of Surrey
Guildford, Surrey
England

G. A. WEBB
April 1998

This Page Intentionally Left Blank

Contents

NMR Studies of Wine Chemistry and Wine Bacteria
ANA RAMOS and HELENA SANTOS

Proton Phase-sensitive Pulsed Field Gradient Double-quantum Spectroscopy
CLAUDIO DALVIT and JEAN-MARC BÖHLEN

Dynamic NMR Spectroscopy in Inorganic and Organometallic Chemistry

KEITH G. ORRELL

Department of Chemistry, The University of Exeter, UK

This article reviews the main advances in theory, methodology and chemical applications of NMR applied to internal motions in molecules. The literature coverage is for the period 1992–1997. It is far from exhaustive but includes those papers which describe important advances in dynamic NMR theory and experiments, and those applications of well-established theory where emphasis has been given to quantitative accuracy of rate and activation energy data, or where the dynamic processes are particularly novel. Most chemical applications relate to inorganic and organometallic compounds since such species display the widest range of internal rate processes. The review highlights the particular power of combining both one- and two-dimensional NMR methods and covers both solid-state and solution studies.

1. INTRODUCTION

This review represents an update of a previous review of this field that appeared in Volume 27 of this series.[1] The literature coverage is for the period 1992–1997, during which time the uses of NMR for studying time-dependent

ANNUAL REPORTS ON NMR SPECTROSCOPY
VOLUME 37 ISBN 0-12-505337-1

phenomena in molecules have increased greatly. For a review of this timespan the literature chosen for inclusion has had to be tightly selected. Emphasis has been placed on the main advances in theory and methodology of dynamic NMR (DNMR), and to particularly significant chemical applications of the full range of DNMR methods. Most applications are confined to new inorganic and organometallic compounds, since such species display an exceptionally wide range of dynamic processes. The review is far from exhaustive, but it does aim to provide a clear overview of the directions in which DNMR methods are leading and of the diversity of molecular dynamic phenomena that are currently amenable to NMR study.

During the period of this review, a number of books and monographs containing aspects of DNMR have appeared. Of specific mention are the second editions of the books by Friebolin,[2] Günther,[3] and Sanders and Hunter,[4] each of which contains specific chapters on dynamic studies. A multi-authored monograph, *Dynamics of Solutions and Fluid Mixtures*, edited by Delpuech,[5] provides comprehensive coverage of the whole range of time-dependent effects on NMR. This book contains useful chapters on time scales in NMR, with respect to both relaxation phenomena and magnetization transfer induced by nuclear site exchanges. Other chapters relevant to this review include discussions of quadrupolar nuclei as probes of solution dynamics and solvent exchange on metal ions. Finally, the reader is referred to the eight-volume *Encyclopedia of Nuclear Magnetic Resonance*,[6] which contains numerous articles on different aspects of time-dependent phenomena.

2. ONE-DIMENSIONAL METHODS

The accurate study of chemical exchange processes by NMR demands a knowledge of exchange rate constants over as wide a magnitude range as possible. This requires the use of combinations of NMR techniques, since each technique possesses its own optimal time scale. One-dimensional bandshape analysis can be used over slow, intermediate and fast exchange regimes but is most suited to intermediate rates (typically 10–10^3 s^{-1}). Slower exchange rates (typically 0.1–10 s^{-1}) are most accurately measured by magnetization transfer experiments that rely on nuclear spin–lattice relaxation times, T_1 (viz. selective inversion or saturation recovery, Section 2.2) or site exchanges (viz. 2D-EXSY, Section 3.1). Fast dynamic processes (having rates typically $>10^3$ s^{-1}) can be measured from knowledge of spin–spin relaxation times, T_2, or T_1-based molecular correlation times (Section 2.3).

Developments in all these areas will be discussed.

2.1. Developments in bandshape analysis methods

The current theory for calculating dynamic bandshape and magnetization transfer effects has been reviewed by Johnston,[7] and a DNMR spectral simulation program suitable for use on a PC has been developed.[8]

A new approach to the calculation of NMR bandshapes of exchanging systems, based on computations in the time domain, has been developed by Bain.[9,10] The approach involves a re-examination of the nuclear spin transition probability, which may be considered to consist of two terms, one corresponding to the share of the initial magnetization that each spin coherence receives at the start of the experiment, and the other corresponding to how much that coherence contributes to the total detected signal. The final signal intensity is the product of these two terms. For a static spectrum these two terms are complex conjugates, so the product is real and represents the standard transition probability. For an exchanging spectrum the product becomes complex, so the time evolution involves both oscillatory and dispersive terms. The dynamic spectrum is still a sum of individual transitions, but the lineshapes are distorted in phase, intensity, position and linewidth by the dynamic process. The NMR signal is a function of time t as given by

$$\text{NMR signal} = (I_x \,|\, \exp\{(-\mathrm{i}\mathbf{L} - \mathbf{R} - \mathbf{K})t\} \,|\, F_x) \tag{1}$$

where $\mathrm{i}\mathbf{L} + \mathbf{R} + \mathbf{K}$ is the Liouville matrix. If $\mathbf{U}$ is the matrix with the eigenvectors as columns and $\boldsymbol{\Lambda}$ is the diagonal matrix with the eigenvalues on the diagonal, Eq. (1) can be written as Eqs. (2) and (3)

$$\text{NMR signal} = (I_x \,|\, U^{-1}\exp(-\mathrm{i}\boldsymbol{\Lambda}t)U \,|\, F_x) \tag{2}$$

$$= \sum_j (U^{-1}I_x)_j^* \, (UF_x)_j \exp(i\lambda_j t) \tag{3}$$

where λ_j are the individual eigenvalues of $\boldsymbol{\Lambda}$.

This theory has been applied to both uncoupled[9] and coupled[10] two-site exchange. The case of an exchanging AB system is shown (Fig. 1). The approach differs from that of Binsch in that the latter calculates total signal shapes as a function of frequency, whereas this new method presents signals as a sum of absorption and dispersion lines.

Bain[11] has also extended the calculation of dynamic NMR spectra of many-spin systems using a sparse matrix methodology as this is computationally much more efficient than the conventional methodology. The Liouville matrix is a sparse matrix in that it invariably contains many zeros. These can be ignored using the sparse matrix time-dependent Chebyshev method. The computational demands of the new method are predicted to scale as $O(2^{2n})$ as the number of spins n increases, compared to the scale $O(2^{6n})$ of conventional

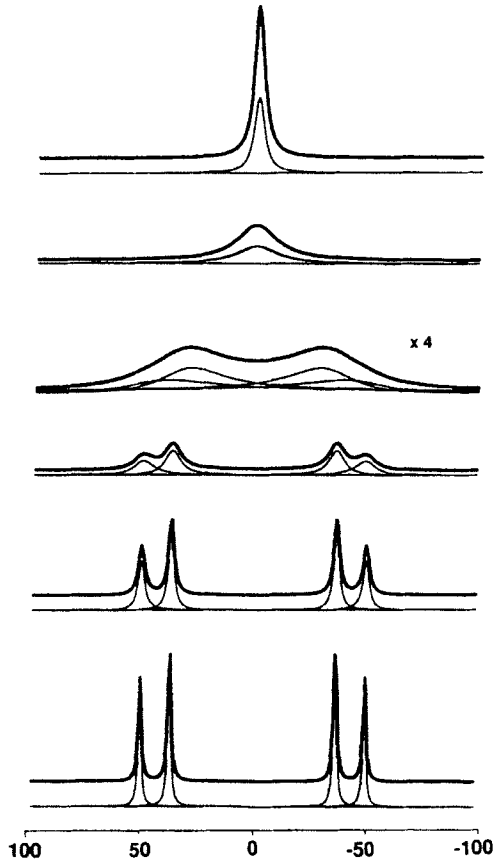

Fig. 1. NMR lineshapes of an AB spin system undergoing mutual exchange. The bold upper line represents the total lineshape and the lighter lines the individual components. The parameters of the spin system are: chemical shift difference 86 Hz, scalar coupling constant 13 Hz, T_2 = 5 s for each site. Exchange rates (k/s^{-1}) are 0.1, 5, 25, 125, 625 and 3125. (Reproduced with permission from *Canad. J. Chem.*, 1996, **74**, 819.)

methodology. The method is based on splitting the propagator into Liouville, relaxation and exchange components using Chebyshev expansion of the total exponential function. The author has illustrated the method by simulating the dynamic ^{1}H spectra of trimethylsilylcyclopenta[*l*]phenanthrene. In this compound the Me_3Si- group migrates from H(1) to H(3) of the 5-membered ring causing mutual exchange of the eight coupled ^{1}H spins of the phenanthrene ring. Such a simulation could not have been tackled by conventional methodology.

Goldman[12] has developed a new formalism for the analysis of NMR spectra in the presence of exchange that works equally well for all types of exchange-

driven modulations produced either by intramolecular rearrangements or by intermolecular exchange. The method uses the sudden-jump approximation and describes directly the FID signals without analysing their derivative. The method is seen as particularly powerful for cases of intermolecular exchange, the effect of which is to modulate indirect interactions (including single- and multi-partner exchanges).

Seliger[13] has applied second-order perturbation theory to the calculation of resonance frequencies and lineshapes of nuclei subject to a random two-site exchange. The time-dependent perturbation averages out in two steps. A resonance line that is a doublet at very long correlation times (τ_c) of the random exchange changes into a singlet when τ_c^{-1} exceeds the splitting of the doublet. The second-order shift of the resonance lines, caused by the off-diagonal matrix elements of the perturbation, vanishes when τ_c^{-1} exceeds the resonance frequencies of the main Hamiltonian. The theory is applicable to solid-state NMR and NQR and is illustrated by $I = 3/2$ nuclei (e.g. ^{39}K) undergoing random two-site exchange.

Two-site exchange where the population imbalance is very high can cause analytical problems since the weak signals can become broadened beyond the detection limit. Such hidden exchange partners can provide negative effects in $^1H\{^1H\}$ NOE difference spectra and lead to erroneous structural conclusions. Szántay and Demeter[14] have examined this problem in some detail. Their conclusions are that hidden exchange signals occur only if the population of the minor signal does not exceed ~10% and the rate constant (major → minor component) is within the approximate range 2–25 s^{-1}. In very biased exchange systems, the minor signal can be unresponsive to selective saturation, which accentuates the possibility of spectral misinterpretations in NOE difference spectra. The minor resonance is more efficiently saturated by irradiating its major partner, and this provides a means of measuring the population of the minor component. Diagrams are given for the assessment of population ratios using peak-height ratios determined from saturation-transfer difference experiments.

Szymanski[15] has developed a computer program to simulate one-dimensional dynamic multiple quantum (MQ) spectra of spin-$\frac{1}{2}$ nuclei. The program is based on the master complex lineshape equation, (4),

$$Y_\tau(\omega) = \langle V_\tau|[-i(\mathbf{L} + \Delta\omega\mathbf{F}_2^D - \omega\mathbf{E}) + \mathbf{X} + \mathbf{R}^{eff}]^{-1}|W_\tau\rangle \qquad (4)$$

This describes the complete set of MQ spectra, ranging from quantum order $-N$ to $+N$ where $N/2$ is equal to the maximum z-component of the total spin. Calculation of dynamic MQ spectra of individual quantum orders involves diagonalization of the pertinent blocks of the supermatrix $-i\mathbf{L} + \mathbf{X} + \mathbf{R}^{eff}$ analogous to the Binsch method for single-quantum spectra. The program has been used to predict the MQ spectra of hypothetical homonuclear molecules of D_{4h} symmetry undergoing mutual exchange,[15] heteronuclear molecules

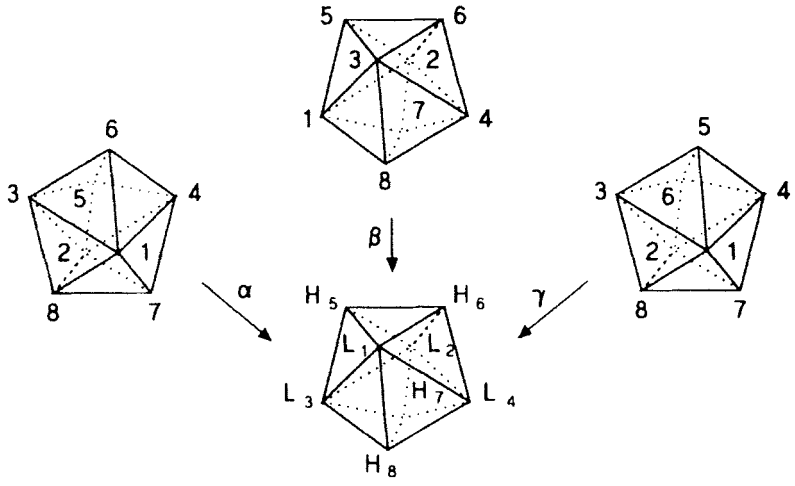

I

Scheme 1

which exchange between D_{4h} and C_{2v} symmetries,[15] and the real tetrahydride complexes of molybdenum and tungsten, H_4ML_4 (M = Mo, W).[16] Magnetic equivalence is not conserved in the course of these exchanges and it is shown that the coupling constants between magnetically equivalent nuclei can slightly affect the calculated lineshapes of their MQ spectra. The lineshapes are much more sensitive than those in conventional DNMR spectra. For example, H_4ML_4 molecules[16] can undergo three possible rearrangement mechanisms, α, β and γ (Scheme 1). These give rise to almost identical theoretical ^{31}P conventional (one-quantum) DNMR lineshapes, but their two-quantum ^{31}P spectra are significantly different (Fig. 2). As the exchange rate increases, the overall intensity of the MQ spectra falls to zero and does not recover in the motional narrowing limit. Each of the mechanisms α–γ averages the three different J_{HP} couplings. Mechanisms α and γ do not affect J_{HH} and J_{PP}, while mechanism β averages out J_{PP}. Mechanisms α and γ differ only in minute detail yet their MQ spectra are distinctly different!

2.2. Developments in magnetization transfer methods

Such methods apply to rate processes that are too slow on the chemical shift time scale to produce significant dynamic line broadening but are comparable to rates of spin–lattice relaxation. For complicated multisite exchanges, two-dimensional methods (e.g. 2D-EXSY, Section 3.1) are of unsurpassed power, but for simpler 2- or 3-site exchanges one-dimensional methods such as selective inversion or 1D-EXSY methods may be more appropriate.

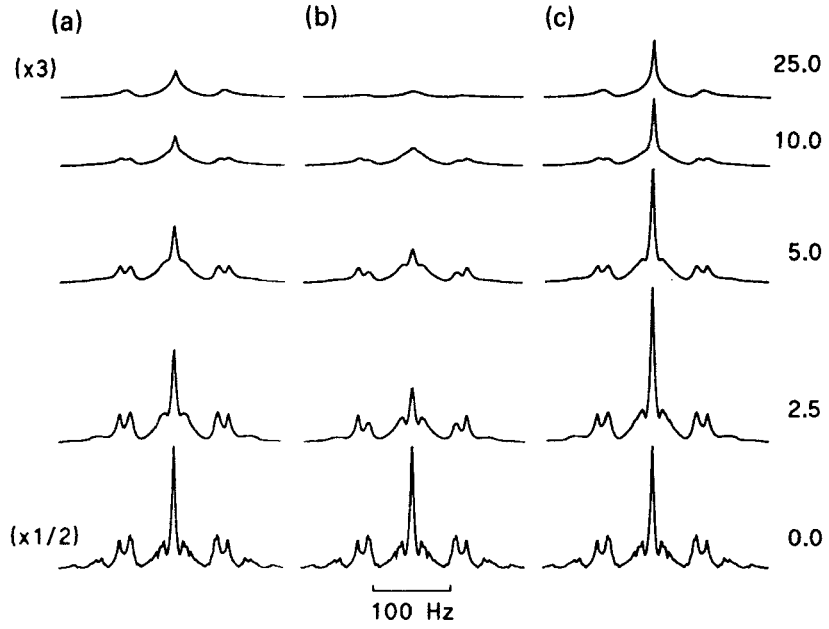

Fig. 2. Theoretical ^{31}P TPPI spectra in the 2-quantum domain calculated for the rearrangement mechanisms α (a), β (b), and γ (c). First-order rate constants (k/s^{-1}) for one-step elementary reactions are shown. Coupling constants used in the calculations are $J_{12} = 3$ Hz, $J_{13} = 35$ Hz, $J_{15} = 46$ Hz, $J_{17} = -2$ Hz, $J_{18} = 34$ Hz, $J_{56} = -6$ Hz and $J_{57} = -3$ Hz. Labels refer to structure **I** in Scheme 1. (Reproduced with permission from *J. Magn. Reson.*, 1995, **A115**, 254–256.)

Bain[17] has considered the factors that need to be considered for optimizing the study of slow exchange by spin relaxation measurements. For a system of n sites, spin relaxation occurs according to

$$\frac{\partial}{\partial t}\begin{bmatrix} M_1(\infty) - M_1(t) \\ \vdots \\ M_n(\infty) - M_n(t) \end{bmatrix} = -\mathbf{A}\begin{bmatrix} M_1(\infty) - M_1(t) \\ \vdots \\ M_n(\infty) - M_n(t) \end{bmatrix} \tag{5}$$

where $M_i(t)$ is the magnetization of site i at time t, $M_i(\infty)$ is the equilibrium magnetization at the same site, and **A** is the matrix

$$\begin{bmatrix} R_1 & -k_{21} & -k_{31} \ldots & -k_{n1} \\ -k_{12} & R_2 & -k_{32} \ldots & -k_{n2} \\ \vdots & \vdots & \vdots & \vdots \\ -k_{1n} & -k_{2n} & -k_{3n} \ldots & R_n \end{bmatrix}$$

and $R_i = T_{1i}^{-1} + \Sigma_{l \neq j} k_{il}$, T_{1i} being the spin–lattice relaxation time of site i and k_{ij} the exchange rate from site i to j. This formulation neglects off-diagonal cross-relaxation terms, which are usually negligible for small molecules. The relaxation of any given site will depend on the initial states of all the other sites and on all the rates, since all sites are coupled together by the relaxation matrix. The choice of the initial, nonequilibrium states of nuclei caused by selective or nonselective inversion of nuclei is crucial to the accuracy of measurement of exchange rates. For a 2-site exchange the problem is simple. An experiment in which both sites are inverted gives mainly the two diagonal elements of the matrix, and selective inversions of each site separately can provide a complete determination of the parameters. If there are 3 sites, inversion of site 1 provides good information of the $1 \rightleftharpoons 2$ and $1 \rightleftharpoons 3$ rates, but little data on the $2 \rightleftharpoons 3$ process. Bain has shown that the choice of which selective excitation to use is best made by the partial derivative criterion since partial derivatives reveal how sensitive a data point is to a given parameter. He considers a 6-site system (associated with CO scrambling in $Ru_2(CO)_6(\mu_2\text{-}PPh_2)(\mu_2\text{-}\eta^2\text{-}CCBu^t)$) and calculates the partial derivatives of each line intensity as a function of transmitter offset and the delay time between the two $\pi/2$ pulses. By plotting contour maps, transmitter-offsets and pulse delays can be chosen so that for each rate there is at least one site to which it is sensitive and good-quality data will be available on all the rate processes. Bain *et al.*[18] have also used selective inversion to study the 2-site exchange associated with the [1,5]-suprafacial shifts in the isomers of bis(indenyl)dimethylsilane.

Carbonyl rotation in $[Ru_2(CO)_6(\mu_2\text{-}PPh_2)(\mu_2\text{-}\eta^1\text{:}\eta^2\text{-}C{\equiv}C\text{-}Pr^i)]$ is a more challenging DNMR problem.[19] In the temperature range studied, there are three distinct carbonyl environments, each CO group showing coupling to ^{31}P. Each of the six ^{13}C carbonyl signals has a relaxation rate T_1^{-1}, and magnetization values $M(\infty)$ and $M(0)$. The CO scrambling is defined by three pairwise exchange rates. Crucial to this study are the error estimates of the parameters involved, and methods for data fitting and error analysis are given. The conclusions are that the CO scrambling is a concerted process with an energy barrier, $\Delta H^{\ddagger}$, of 46 kJ mol^{-1}.

Perrin and Engler[20] have also considered the accuracy of rate data extracted from multiple 1D-EXSY experiments. The 1D-EXSY pulse sequence is 90°–t_1–90°–t_m–90°–t_2–(observe) where t_1 and t_m are evolution and mixing times, respectively. A method for specifying the optimal choice of t_1 values is given. The data were analysed by an improved weighted linear-least-squares fitting procedure, and yielded highly accurate rate constants with realistic error estimates. The method was applied to *E*/*Z* methyl exchange in *N*,*N*-dimethyl propionamide, to $H_E/H_Z/H_{solvent}$ exchange in acrylamide, and to methoxy exchange between stereoisomeric 4,6-dimethyl-2-methoxy-1,3-dioxanes and methanol. The latter system was the subject of a more detailed study[21] in which the acid-catalysed mechanism was shown to involve a cationic intermediate.

The effects of a saturating field on a 2-site exchanging system have been

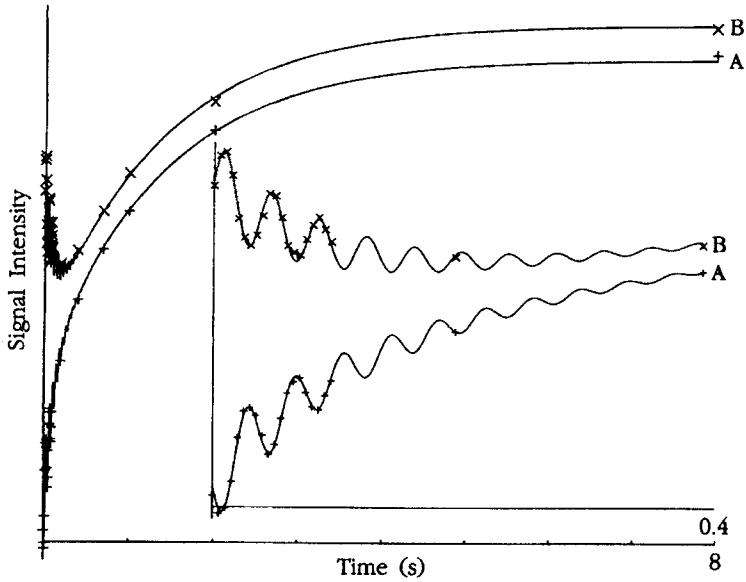

Fig. 3. Comparison of observed (+, A ; ×, B) and calculated (curve) 200 MHz signal intensities of the CH_2 resonances of 2,7-dihydro-1,4,5-thiadiazepine in nitrobenzene/dimethylformamide solution at 70°C following selective inversion of the A (high-frequency) lines in the spectrum. The calculated curves represent a least-squares fit of the data with $k = 5.5 \pm 0.6\ s^{-1}$ and $R_1 = 0.72\ s^{-1}$. The inset shows the oscillatory time dependence at short times on an expanded scale. Magnetic parameters: $\nu_A - \nu_B = 23$ Hz and $J_{AB} = 12.8$ Hz. (Reproduced from *J. Magn. Reson.*, 1995, **A115**, 145–154.)

studied by Baguet and Roby,[22] who showed that a fast inversion–recovery sequence reliably measures longitudinal relaxation rates if the chemical exchange is slow. They concluded that the relaxation delay can be reduced to zero if the acquisition time is long enough to ensure the complete disappearance of any transverse magnetization. The conclusions have been tested on the exchanging protons of *N*,*N*-dimethylacetamide arising from restricted rotation about the amide bond. The same authors have examined the off-resonance irradiation ('spill-over') effect occurring in steady-state saturation transfer experiments on 2-site exchanging systems.[23] The theory is developed in terms of a saturation-transfer ratio parameter expressed as a function of the saturating RF field magnitude. It is shown that the RF field applied off-resonance during acquisition of the reference spectrum does not correct the experimental saturation-transfer ratio for the 'spill-over' effect; instead the ratio increases with the magnitude of this RF field.

The theory and application of multisite magnetization transfer in strongly coupled spin systems have been reported by McClung.[24] DANTE selective-

inversion creates zero quantum coherences (ZQCs) and the interaction of these with the longitudinal magnetizations during the exchange/relaxation period leads to observable oscillations in the signal amplitudes as the system relaxes to thermal equilibrium. The case of the AB system associated with the CH_2 groups of 2,7-dihydro-1,4,5-thiadiazepine is illustrated (Fig. 3). The signal intensities were fitted according to the theory developed in the paper and gave a value for the rate constant that was in good agreement with bandshape analysis. The decrease in signal B when the time τ is ≤ 0.2 s is due to exchange of magnetization with the inverted site A, whose signal intensity increases rapidly during this time period. At longer times the signals of both sites vary more slowly as they relax back to their equilibrium values. The signals A and B oscillate at the ZQC frequency ($\nu_A - \nu_B = 23$ Hz) but these oscillations are damped out at longer times. These oscillatory effects are less important for ABX systems and are unlikely to feature strongly in larger, strongly coupled systems.

The above work involved inverting complete multiplets of each magnetic site. Bain and Fletcher[25] have chosen to invert only one or at most a small number of lines of any multiplet in their approach to the problem, which is particularly suited to crowded spectra with overlapping lines. This approach does lead to some technical complications in the analysis of data, but the authors have convincingly demonstrated their method by applying it to the 3-spin aromatic system of $[ReBr(CO)_3L]$ (L = diethyl-2,6-pyridine dicarboxylate) and to the 4-spin aromatic system of 4-nitroso-*N*,*N*-dimethylaniline. Exchange in the 3-spin system is due to a metallotropic shift and in the 4-spin system to restricted rotation of the $-N=O$ group. In both cases, rate constants agree well with those calculated by standard bandshape analysis.

Krishnan and Rance[26] have analysed the effects of chemical exchange among homonuclear spins in heteronuclear coherence-transfer experiments. They consider the specific cases of the heteronuclear single-quantum coherence (HSQC) experiment and the heteronuclear cross-polarization technique applied to [^{15}N]acetamide. The cross-polarization experiment is shown to have significant theoretical and experimental sensitivity advantages over the free-precession-type sequences such as HSQC in the presence of chemical exchange processes. In the I_1I_2S spin system ($I_1 = I_2 = {}^1H$, $S = {}^{15}N$) of [^{15}N]acetamide, where the two I spins are mutually exchanging, the cross-polarization step between I and S spins is completely insensitive to the exchange process whereas the pulsed free-precession method can be severely undermined by irreversible losses of magnetization due to exchange occurring during the free precession periods.

Applications of magnetization transfer techniques to exchanging organometallic systems include ^{13}C studies of inter-metal carbonyl exchange in $[\eta^5\text{-}C_5H_5)_2Mo_2(CO)_6]$ and $[(\eta^5\text{-}\ C_5H_5)_2MoW(CO)_6]$ by Mann[27] and isomeric interconversion of the vinyl complex $[(\mu\text{-}H)Os_3(CO)_9(PPh_3)(\mu\text{-}CH{=}CH_2)]$.[28] ^{19}F and ^{1}H magnetization transfer techniques (plus bandshape analyses)

have been used to understand the dynamic behaviour of the complexes $[M(C_6F_5)X(OPPy_nPh_{3-n})]$ (M = Pd, Pt; X = C_6F_5, halide; Py = pyridyl; n = 1–3).[29] The dynamic processes involve rotation about the M-aryl bond and Py associative exchange. Rotation of the C_6F_5 groups is particularly slow when X is halide and was detectable only by magnetization transfer experiments.

^{1}H Magnetization transfer studies (including both saturation and inversion methods) have been applied to the vinyl complex $[Fp_2(CH{=}CH_2)]^+BF_4^-$, where Fp = $Fe(CO)_2(\eta^5\text{-}C_5H_5)$, and where the μ-vinyl ligand exhibits slow

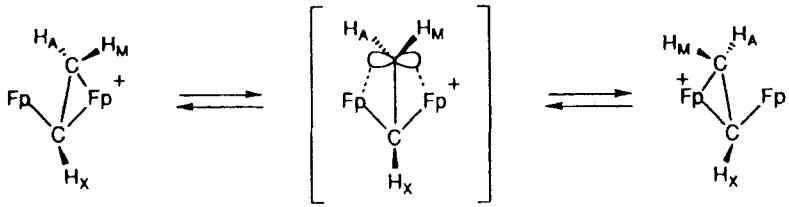

Scheme 2

oscillation between the two Fp centres (Scheme 2).[30] At room temperature the rate constant for the process was 0.045–0.049 s^{-1} which corresponds to a free energy of activation $\Delta G^{\ddagger}$ of 80.8 kJ mol^{-1}. Proton saturation transfer experiments have enabled the rate of axial ligand rotation in 6-coordinate low-spin Fe^{III} tetraphenylporphyrinates[31] to be measured. The four distinct pyrrole protons were used to monitor the rotation. Analytical expressions were derived for the steady-state signal intensities in this case of cyclic 4-site exchange. Reliable rate constants for the ligand rotation were derived, and activation enthalpies and entropies compared to molecular mechanics-based values. ^{17}O Magnetization transfer studies have been used to investigate oxygen and vanadium exchanges in linear tri- and tetravanadate anions in aqueous solution.[32] Results suggest the exchanges occur via a short-lived, probably cyclic intermediate species.

2.3. Developments in relaxation time-based methods

2.3.1. T_2-based methods

The techniques discussed here correspond to rates in the fast exchange limit of dynamic broadening where chemical shifts and scalar couplings of individual nuclei have been averaged out. This traditional method of averaging has been questioned by Weitekamp *et al.*[33] because it neglects spin-dependent energies. They presented an alternative method, based on a full equilibrium statistical mechanics treatment, which is in agreement with the standard method for

degenerate equilibria but not for nondegenerate equilibria. However, Anet and Freedberg[34] have argued that this method is not applicable to resonant methods such as NMR, as it ignores coherences. Spin energies do not influence averaged NMR parameters because these arise from coherent superposition states and the energies, in a magnetic field, of spins that are directly involved in the coherences are zero. Thus, the traditional averaging of NMR parameters remains valid!

Evaluation of exchange rates that are fast on the NMR chemical shift time scale are dependent on accurate linewidth measurements. These can be based on measurements of T_2 values, which do not contain contributions from magnetic field inhomogeneities, or on $T_{1\rho}$ values, the latter being equal to T_2 values in mobile liquids, but not in solids (see later). Bain[35] has developed an offset-saturation experiment that provides accurate values of T_2 and simultaneous measurement of T_1 values for nuclei. It consists of irradiating the spectral line of interest with an RF power γB_2 at an offset from resonance $(\omega - \omega_0)$ for a period long enough for the z-magnetization to reach a steady state. A delay time τ, which is some fraction of the estimated T_1 value of the nucleus, is inserted prior to a 90° pulse which is then applied to measure the partially saturated z-magnetization. A plot of z-magnetization intensity as a function of resonance offset from the offset-saturation experiment exhibits a dip at the resonance frequency ω_0. It follows from the Bloch equations that the width of the curve at half-maximum height is equal to $(\gamma B_2)\,(T_1/T_2)^{1/2}$. Importantly, T_2 is obtained independent of magnetic field inhomogeneities, providing γB_2 is sufficiently large, as it should be under normal saturating conditions. The equation for this dip is

$$M_z = M(\infty)\left(1 - \frac{(\gamma B_2)^2 T_1/T_2}{(\omega - \omega_0)^2 + (\gamma B_2)^2 T_1/T_2} e^{-\tau/T_1}\right) \tag{6}$$

For a set of offsets and corresponding intensities, a nonlinear least-squares fit can be made to Eq. (6) using $M(\infty)$, $e^{-\tau/T_1}$ and $(\gamma B_2)^2(T_1/T_2)$ as parameters. Knowing the calibrated value for the irradiating field γB_2, absolute values of T_1 and T_2 may be obtained simultaneously.

This offset-saturation method has been applied to *N*-acetylpyrrole,[36] and the results are shown in Fig. 4. Nonlinear least squares fitting of this graph led to a T_2 value of 0.97 s for the 2- and 5-position ring protons of this compound. These protons undergo rapid exchange as a result of the *N*-acetyl rotation. In the fast exchange regime, the rate constant is given by

$$k = \pi \Delta\nu^2 T_2^{\text{exch}}/2 \tag{7}$$

where $\Delta\nu$ is the chemical shift difference between the 2- and 5-position ring protons in the absence of exchange (= 114.6 Hz in this case), and T_2^{exch} is the

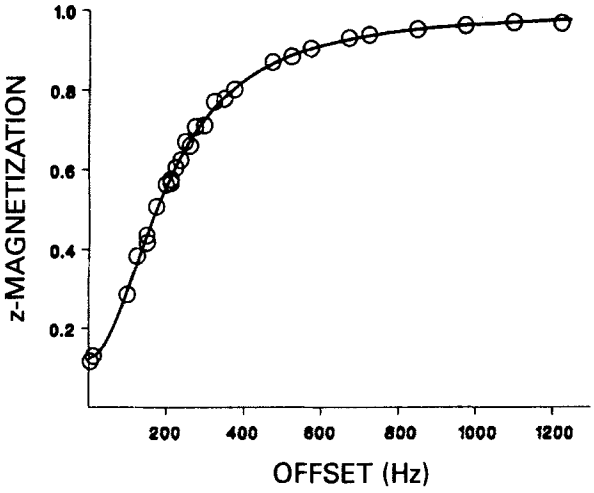

Fig. 4. Results of an offset-saturation experiment on *N*-acetylpyrrole at 335 K. The circles represent the steady-state z-magnetization after irradiation, as a function of irradiation frequency-offset from resonance. The z-magnetizations are reported relative to the equilibrium value obtained from the fitting procedure. The irradiation time was 80 s and the strength of the RF field, γB_2, was 102 Hz. The solid (best-fit) line gives a value of T_2 of 0.97 s. (Reproduced with permission from *J. Phys. Chem.*, 1994, **98**, 7458.)

exchange contribution to the measured T_2 value. It is assumed that $T_1 = T_2$ in the absence of exchange and so the T_1 values of each site are equal, i.e. T_1(2-H) = T_1(5-H). T_2^{exch} can therefore be calculated from the relationship

$$\frac{1}{T_2^{\text{exch}}} = \frac{1}{T_2} - \frac{1}{T_1} \tag{8}$$

where T_1 and T_2 are the relaxation times measured directly by the offset-saturation method. The method was applied to spectra recorded in the temperature range 297–347 K. The resulting rate data were then combined with data obtained in the range 232–291 K by bandshape analysis and in the range 210–219 K by selective inversion. This led to accurate estimates of activation enthalpy $\Delta H^{\ddagger}$ (53 ± 0.6 kJ mol^{-1}) and activation entropy $\Delta S^{\ddagger}$ (5 ± 3 J K^{-1} mol^{-1}).

A similar study has been carried out on the *cis–trans* isomerization in 2-furanaldehyde where the aldehyde rotation represents a 2-site exchange system with unequal populations. The authors[37] again demonstrate the power of combining their offset-saturation method with bandshape and selective inversion methods to enable rates to be measured over several orders of magnitude.

2.3.2. $T_1/T_{1\rho}$-based methods

Whereas magnetization transfer techniques rely on spin–lattice relaxation rates for their efficacy in measuring exchange rates that are slow on the NMR chemical shift time scale, the temperature dependences of T_1 values of nuclei can be used to measure fast motional processes. This technique has been applied particularly successfully to dynamically active groups in solids, such as rotating methyl groups, fluxional hydride ligands, and cyclopentadienyl rotations. Measurements of ^{13}C and ^{1}H T_1 values over as wide a temperature range as possible can provide accurate assessment of rotational correlation times, which then lead to rates and energy barriers for the dynamic process being studied. Aime and his group have been particularly associated with this method. Recent studies of theirs have included estimates of cyclopentadienyl ring rotation in metal carbonyl complexes $Cp_2W_2(CO)_6$ and $Cp_2Ru_2(CO)_4$,[38] and in $[Fe_2(\eta^5\text{-}Cp)_2(\mu\text{-}CO)(CO)_2\{\mu\text{-}CR(CN)\}]$ (R = H, CN).[39] In the former study, the activation energies for Cp rotation were 15.5(W) and 10.2(Ru) kJ mol^{-1} respectively. In the latter study the separate intramolecular and intermolecular contributions to the total reorientational barriers were evaluated. Rotations of permethylated Cp* rings have been measured[40] in a range of compounds, such as $Cp_2{*}Fe$, $Cp{*}Rh(CO)_2$, $Cp{*}Cr_2(CO)_4$, $Cp{*}Fe_2(\mu_2\text{-}CO)_2(CO)_2$ and $Cp_2{*}Rh_2(\mu_2\text{-}Cl)_2Cl_2$, using variable-temperature ^{1}H T_1 measurements, together with potential energy barrier calculations within a pairwise atom–atom approach. In all cases, in addition to Cp* ring rotation about its C_5 axis, methyl rotations about their C_3 axes were found. Energy barriers for Cp* and Me rotations were in the ranges 10–24 kJ mol^{-1} and 6.5–10.5 kJ mol^{-1}, respectively. Intra- and intermolecular contributions to the total reorientational barriers varied considerably between complexes. In the dinuclear Cr and Fe complexes a synchronous motion of the Me groups during Cp* ring reorientation appeared to be the lowest-energy pathway. Cyclopentadienyl rotation has also been studied in a series of chalcogen ether complexes $[CpFe(CO)_2(EMe_2)]^+$ (E = S, Se, Te).[41] ^{13}C T_1 values showed the Cp ring reorientation rates were in the order S < Se < Te. Phenyl ring rotations featured in a ^{13}C T_1 study of a family of bis(carbyne) cluster complexes of types such as **[1]** and **[2]**.[42] The relaxation time measurements enabled rotational diffusion coefficients about the different axes of the molecule to be calculated. The motions were highly anisotropic. Rapid internal rotation of the phenyl groups contributes to this anisotropy. Phenyl rings adjacent to an alkyne group rotate at a similar rate to that of benzene, whereas phenyls bound to $(CpCo)_3$ through a μ_3-carbyne ligand rotate more slowly.

Methyl group rotation in the complexes $[MeM(CO)_5]$, (M = Mn, Re) was studied by ^{1}H spin–lattice relaxation time measurements,[43] whereas ^{27}Al and ^{13}C T_1 measurements were used for similar studies in aminoalanes, viz. $[Me_2AlNMe_2]_2$, etc.[44] Here the relaxation of the ^{27}Al nucleus was assumed to be due solely to quadrupolar interaction modulated by molecular orientation,

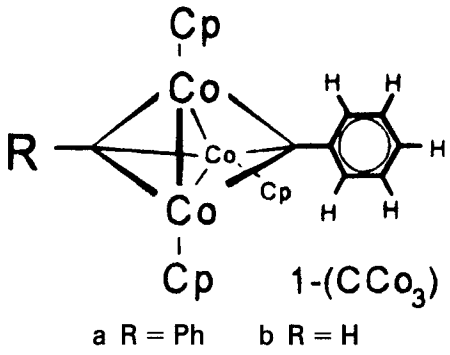

[1]

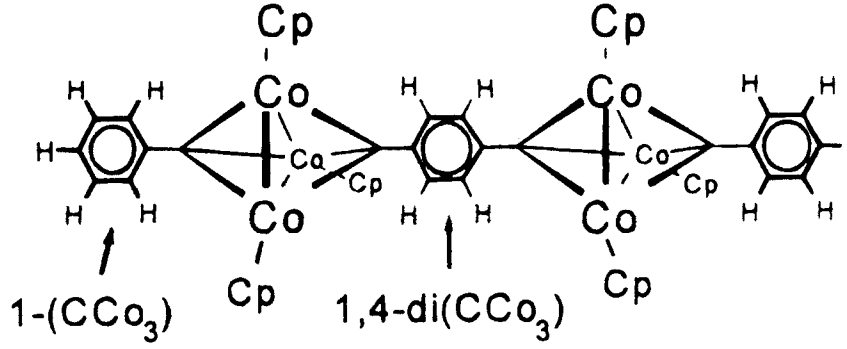

[2]

whereas dipole–dipole relaxation involving only directly bound protons was assumed to dominate the ^{13}C methyl relaxation. Aime *et al.*[45] have used both spin–lattice and spin–spin relaxation time data of carbonyl groups, combined with high-resolution solid-state ^{13}C MAS spectra, to evaluate carbonyl exchange in $Ru_3(CO)_{12}$. T_1 data were dominated by the CSA mechanism since a graph of T_1^{-1} against B_0^2 (B_0 being the applied magnetic field) was linear. T_2 data are normally determined by CSA, SC and exchange contributions. T_2^{CSA} values were determined from T_1^{CSA} values. In the present case T_2^{SC} values were shown to be negligible, whereas the exchange contribution to T_2, T_2^{ex}, was obtained by subtracting the $1/T_2^{CSA}$ term from the observed relaxation rate $1/T_2$. The relaxation rate due to exchange $1/T_2^{ex}$ corresponds to modulation of the axial–equatorial CO chemical shift separation by the exchange lifetime τ_M according to the equation

$$\frac{1}{T_2^{ex}} = \sum_i p_i \delta_i^2 \tau_M \left[1 - \frac{2\tau_M}{t_{cp}} \tanh \frac{t_{cp}}{2\tau_M} \right] \tag{9}$$

where p_i is the fractional population of the ith site, δ_i is the chemical shift difference from the centre of gravity of the exchanging signals, and t_{cp} is the time between the 180° pulses in the CPMG sequence. For the conditions used in this work, the term in square brackets was approximated to unity. Results led to rate data, the temperature dependence of which gave an activation energy of 20.5 kJ mol^{-1}, which agreed well with a ^{13}C bandshape analysis study. The same research group has investigated the solid-state dynamics of $H_4Ru_4(CO)_{12}$ by a variety of NMR techniques (namely, temperature dependences of ^{1}H T_1 values and static linewidths, and ^{13}C CP/MAS spectra).[46] In this case they found that the motion involved hydride, and not carbonyl, ligands. Two possible mechanisms were proposed, one involving the H_4Ru_4 moiety moving as a whole, the other involving the hydrides moving over the surface of the metallic core.

Hydrogen dynamics have also been investigated by spin–lattice relaxation time data in cluster compounds of type $Th_6H_xB_{15}$ (x = 5, 7).[47] Two different modes of motion were identified. At temperatures >250 K, T_1 values were dominated by a thermally activated intercluster jump process, whereas below this temperature, and down to 80 K, a local intracluster mode occurs.

A method has been developed for the direct determination of NMR rotational correlation times from T_1 and T_2 data.[48] It has been applied to dipolar relaxation between ^{1}H nuclei and ^{1}H, ^{13}C, ^{31}P and ^{113}Cd nuclei in viscous solutions from knowledge of the ratios of relaxation times T_1/T_2 (or relaxation rates R_2/R_1) over a range of field strengths. Cobalt-59 spin–lattice and spin–spin relaxation times have been applied to evaluate molecular motion in the mixed metal cluster $HFeCo_3(CO)_9[P(OMe)_3]_3$ both in the solid state and in solution.[49]

2.4. Selected applications to liquids and solutions

2.4.1. Pyramidal and configurational inversions

Pyramidal inversion of nitrogen atoms has been very extensively studied by DNMR. More recent work has concentrated on pyramidal inversion of metal-coordinated chalcogen atoms. Coordination to transition metals greatly accelerates the rates of pyramidal inversion of S, Se and Te atoms and brings these rates within the detectable time scale of NMR experiments. Two studies of pyramidal inversion have been concerned with dichalcogen ether complexes of metallocenes, e.g. $[Cp_2M(MeSCH_2CH_2SMe)]PF_6$, (M = Mo, W), $[Cp_2Mo(SCH_2CH_2SMe)]PF_6$, $[Cp_2M(SCH_2CH_2S)]$, (M = Mo, W), where S inversion was studied,[50] and $[PtCl_2(undecenylseleno)_2Cp_2Fe]$ where Se inversion and Cp bridge reversal were studied.[51] In the former case, total ^{1}H bandshape analysis yielded Arrhenius activation energies in the range 30–55 kJ mol^{-1} that were attributed to local inversion of S atoms rather than

inversion of the complete S—C—C—S chain. In the case of copper(I) arenethiolates, S inversion ($\Delta G^{\ddagger} = 48\,\text{kJ mol}^{-1}$) was accompanied by Cu—N bond dissociation/association, a boat-to-boat flip of the Cu_3S_2C units and an intermolecular exchange process.[52] ^{31}P NMR has been used to probe the dynamics of the P_7^{3-} ion when coordinated to Cr and W.[53] In the complexes $[(en)(CO)_3W(\eta^1, \eta^4\text{-}P_7)M(CO)_3]^{3-}$ where M = Cr or W, phosphorus inversion was rapid on the NMR time scale at all accessible temperatures, whereas in $[\eta^4\text{-}(C_6H_{11})_3SnP_7W(CO)_3]^{2-}$ it became slow at −50°C with the energy barrier ($\Delta G^{\ddagger}$) being $54.4\,\text{kJ mol}^{-1}$. Such a magnitude is very low for ^{31}P, and π-bonding, steric and substituent electronegativity effects were suggested as an explanation.

Pyramidal inversions normally proceed by a vertex mechanism via a trigonal planar transition state. However, an edge-inversion mechanism involving a T-shaped transition state has also been postulated. A recent study of inversion at trivalent bismuth in some organobismuth compounds (see Scheme 3) in different solvents (viz. pyridine and 2,6-lutidine) strongly favoured the edge-inversion mechanism.[54] Energy barriers were in the range 61.0–$86.2\,\text{kJ mol}^{-1}$.

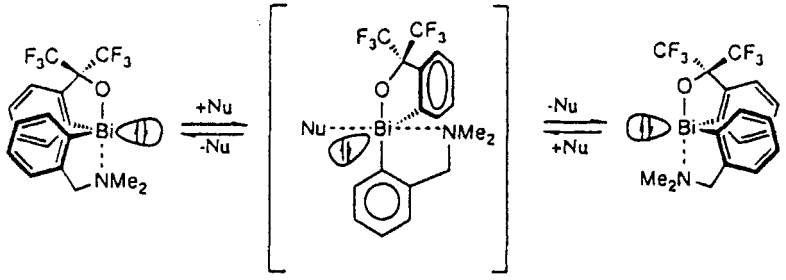

Scheme 3

NMR techniques have been much used to follow rates of configurational inversion of metal centres. Intramolecular inversion of tetrahedral zinc(II) complexes have been studied by dynamic ^1H, ^{13}C and ^{15}N measurements,[55] which suggested that two competitive mechanisms were in operation, one being a twist through a square planar complex and the other a bond-breaking process. Time-dependent NMR studies were used to follow the isomerization of the *cis*- and *trans*- palladium(II) complexes, $[Pd(C_6F_5)_2(tht)_2)]$ (tht = tetrahydrothiophene).[56] The rate data suggest a dissociative loss of tht and the interconversion of two geometrically distinct 3-coordinate intermediates. A detailed NMR study, involving spin saturation transfer, spin inversion transfer and 2D-exchange spectroscopy, has been applied to the 1,1-binaphthyl complex [**3**].[57] The intramolecular process (C_2 symmetry) does not alter the *cis*/*trans* relationship between the 1,1′-biisoquinoline and 2,2′-

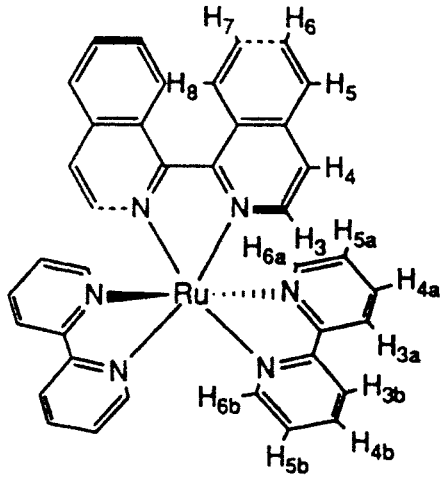

[3]

bipyridine ligands, and the conclusion of the NMR experiments was that the mechanism involved a planar η^2-1,1′-biisoquinoline intermediate. A DNMR study[58] of pentamethylcyclopentadienyl ruthenium alkoxo complexes revealed, in addition to dimer–monomer dissociation, inversion of the pentanedionato ligand at Ru. Activation parameters for both inversion and ligand exchange processes were reported. Dimer–monomer equilibria also existed in some O → Si coordinated compounds, which additionally underwent inversion of configuration at silicon. The $\Delta G^{\ddagger}$ values for the process were attributed primarily to dissociative and/or associative mechanisms rather than the regular Berry pseudorotation mechanism.[59] Detailed DNMR studies have been made on a series of dinuclear M(III) (M = Fe or Ga) catecholate complexes such as $K_6Ga_2L_3$, where L is a bisbidentate catecholate ligand.[60] Total bandshape analysis (DNMR3) provided activation energy data that suggested an independent trigonal twisting of each metal centre via a *meso* intermediate, but not involving any *cis–trans* isomerization.

2.4.2. *Restricted rotations*

Consideration will be given first to restricted rotations of N-heterocyclic rings with respect to other parts of the ligands. Rotations of pyrazol-1-yl rings relative to attached 2,2′-bipyridyl moieties occur in octahedral rhenium(I) complexes of type *fac*-$[ReX(CO)_3L]$.[61] These rotations could be 'frozen' on the ^1H chemical shift time scale at ~173 K, rotation barriers being in the range 39–51 kJ mol^{-1} according to the substitution on the pyrazol-1-yl ring. In some porphyrinato osmium(II) ylide complexes the barrier to rotation around the C–NMe_2 axis of the (dimethylamino)pyridine ylide fragment was measured

to be 54.4 ± 2.1 kJ mol^{-1} at 240 ± 2 K. In this work[62] ^{1}H spin saturation transfer experiments were used to study the reversible addition of 4-methylpyridine to the carbene complex (TPP)Os:CH(SiMe$_3$). In the bis-indenyl complex of niobium, [NbH(η-C$_9$H$_7$)$_2$(pyr)] pyridine rotation about the Nb—N bond occurs ($\Delta G^{\ddagger} = 52 \pm 1$ kJ mol^{-1}).[63] A related styrene complex is fluxional owing to hydride exchange, and this was studied by one- and two-dimensional techniques.

There have been a number of reports of restricted rotation about bonds attached to phosphorus. For example, [Fe(CO)$_4$L] complexes where L = P(*o*-tolyl)$_3$, etc.,[64] and [M(CO)$_5$L] complexes where M = Cr, Mo or W and L = P (*o*-tolyl)$_3$[65] exhibited restricted P—C rotation which has been followed by ^{1}H/^{13}C/^{31}P studies. In [Fe(CO)$_4$P(*o*-tolyl)$_3$] the phosphine conformational process is accompanied by an intramolecular carbonyl exchange.[64] Restricted rotation about a P—Ir bond has been reported in the pyrazole (pz) complex [(η^5-C$_5$Me$_5$)Ir(pz)$_2$PPh$_3$][66] and about a P—Ga bond in [(Me$_3$C)$_2$GaPMes*(SiPh$_3$)] (Mes* = 2,4,6-(Me$_3$C)$_3$C$_6$H$_2$).[67] The approximate $\Delta G^{\ddagger}$ value of 53.1 kJ mol^{-1} about the Ga—P bond represents the first experimental measurement of a rotational barrier in a bond between heavier main group 3 and 5 elements.

Hindered rotation about the M—Si bond in mono- and bis-silyl complexes of Mo and W has been reported.[68] Trimethylenemethane (TMM) rotation is considerably restricted in η^4-TMM [Fe(CO)$_2$L] complexes[69] where L = Bu^{t}NC, AsPh$_3$ and *t*-phosphines, energy barriers ($\Delta H^{\ddagger}$) being in the range 59–67 kJ mol^{-1}. A detailed dynamic NMR study of the restricted rotations of thiophenes (Th) and selenophenes (Seln) in [Cr(CO)$_3$(η^5-Th)] and [Cr(CO)$_3$(η^5-Seln)] was carried out by ^{13}C NMR bandshape analysis.[70] Energy barriers were rather greater for Seln than for Th, and alkyl substitution of these heterocyclic rings increased the barriers. Rates of rotation of 2,6-dimethoxyphenyl groups in tris((2,6-dimethoxyphenyl)methyl)tin trihalides were examined by variable-temperature and spin-saturation transfer methods.[71] Since this aryl ring rotation requires concomitant Sn—O bond breaking, the calculated activation energies (in the range 59–83 kJ mol^{-1}) provide a measure of the relative strengths of the Sn ligation by the ether oxygens. Variable-temperature and 2D-EXSY spectra were used to identify the rotational barriers associated with rotations about Re—(C—C) axes in alkene complexes of the chiral rhenium Lewis acid [(η^5-Cp)Re(NO)(PPh$_3$)]$^+$, and the preferred isomerization pathway was identified.[72] Restricted rotations about the Te—C bonds in dihalodiaryltelluranes have also been reported.[73]

Finally, the power of the ^{15}N NMR has been demonstrated in a study of end-to-end rotation of dinitrogen in rhenium-bound complexes of type [CpRe(CO)L(^{15}N^{14}N)] where L = CO, and [Cp*Re(CO)L(^{15}N^{14}N)] where L = CO, PMe$_3$ or P(OMe)$_3$.[74] Variable-temperature and time-dependent ^{15}N experiments were used to measure the kinetics of the linkage isomerization. Energy barriers were quite high ($\Delta G^{\ddagger} = 93$–95 kJ mol^{-1}), it being concluded

that the preferred mechanism involves end-to-end rotation via a side-on-bonded (η^2) configuration.

Fraenkel and co-workers have reported a series of studies of restricted rotation in allylic or benzylic lithium compounds. Carbon-13 bandshape analysis was applied to (1,1,3,3-tetramethylallyl)lithium coordinated to TMEDA (i.e. *N,N,N′,N′*-tetramethylethylenediamine) as a contact ion pair.[75] The barrier to allyl rotation was $\Delta H^{\ddagger} = 58.6$ kJ mol^{-1}, whereas the TMEDA displayed two dynamic processes, one a reorientation of coordinated Li^+ within the ion pair and the other exchange of TMEDA between its free and complexed states. A similar DNMR study was performed on [1-silylallyl]lithium with a pendant ligand [bis(2-methoxyethyl)amino]methyl.[76] An equilibrium exists between *endo-* and *exo*-silyl species in which lithium is tridentately coordinated. ^{1}H and ^{13}C bandshape analyses established the energy barriers ($\Delta H^{\ddagger}$) for rotation around the SiC_1-C_2 allyl bond and rotation of coordinated Li^+ around the $Si-C_1$ (allyl) bond. These data are summarized in Scheme 4. A more recent DNMR study[77] carried out on some allylic lithium compounds provided dynamics of intermolecular C—Li bond exchange, inversion at the Li-bound carbon and 1,3-Li sigmatropic shifts. The dynamics of benzylic lithium compounds was the subject of another study. These included ion reorientation rotation around the ring-benzyl bond and bi-molecular C—Li exchange.[78]

Alkene/alkyne rotation has been examined by a number of groups. In

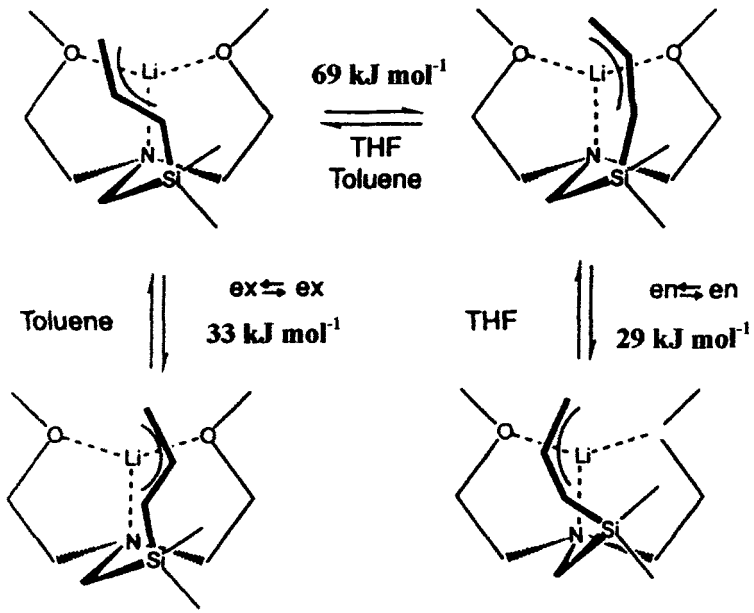

Scheme 4

octahedral *trans*-bis(alkene) complexes of molybdenum, the NMR study (^{1}H, 185–313 K) led to the conclusion that the mechanism involved a conrotatory motion of the two coordinated alkenes.[79] A similar conclusion was reached in the case of corresponding bis-alkyne complexes.[80] Energy barriers ($\Delta G^{\ddagger}$) to alkene rotation in [(η^2-alkene)W(CO)$_5$] complexes are in the range 38–49 kJ mol^{-1} and reflect the energy difference between the orthogonal and parallel arrangements of the two C=C units.[81] A detailed 1D and 2D-EXSY study of new chiral palladium(0) and -(II) complexes of (aminoferrocenyl)phosphine ligands revealed, in addition to alkene rotation, Pd—N bond rupture and selective η^3–η^1–η^3–allyl isomerization.[82] Rotation of tetrafluoroethene ligands was unexpectedly facile ($\Delta G^{\ddagger}$ = 53–81 kJ mol^{-1}) in a variety of d^6 ruthenium complexes [**4**], and required low-temperature ^{19}F

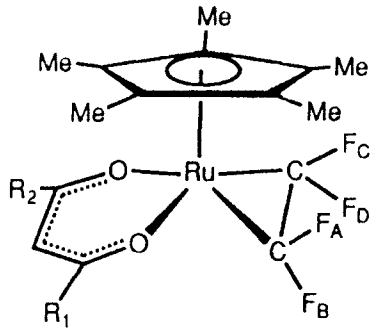

(a) $R_1 = R_2 = CH_3$ ($F_A \equiv F_C$; $F_B \equiv F_D$)
(b) $R_1 = CH_3$; $R_2 = CF_3$
(c) $R_1 = R_2 = Pr^i$ ($F_A \equiv F_C$; $F_B \equiv F_D$)

[4]

studies.[83] The barriers to rotation of arene rings in [(arene)Fe(CO)(SiCl$_3$)$_2$] complexes were even lower ($\Delta G^{\ddagger}$ (298 K) = 40.2–45.2 kJ mol^{-1}) and were attributed to a gearing of the R and SiCl$_3$ groups with the rotation.[84] The 1,3,5-$C_6H_3Me_3$ and C_6Me_6 derivatives did not reveal any restriction to arene ring rotation even at −120°C, suggesting that the methyl groups considerably destabilize the ground states of these complexes. A ^{13}C and ^{31}P study of some chiral (pentaphenylcyclopentadienyl) iron complexes[85] has revealed two fluxional processes. When the rotation of the chiral tripod becomes slow on the NMR time scale, the five-fold degeneracy of the cyclopentadienyl ring carbons is removed. Rotation of the peripheral phenyl rings and rotation of the phosphine ligand can lead to a mixture of diastereoisomers. An estimation of the energy barriers for the two processes ($\Delta G^{\ddagger}$ = 36.4 ± 1.3 and 49.0 ± 1.3 kJ mol^{-1}, respectively) showed that the processes are not correlated.

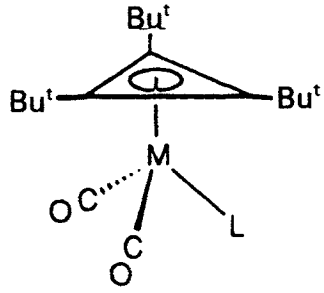

(a) M = Co; L = PMe_3
(b) M = Rh; L = PMe_3
(c) M = Ir; L = PMe_3
(d) M = Ir; L = PPh_3
(e) M = Ir; L = $P(OMe)_3$
(f) M = Ir; L = Bu^{t}NC

[5]

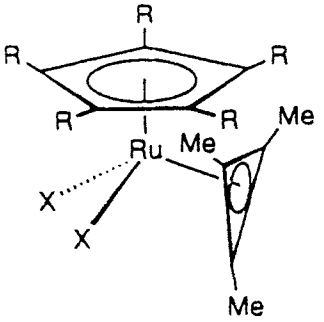

R = H; X = Cl
R = H; X = Br
R = H; X = I
R = Me; X = Cl
R = Me; X = Br
R = Me; X = I

[6]

There have been a number of DNMR studies on the rotational characteristics of the η^3-triphenylcyclopropenyl ligand.[86–88] Rotations of this ligand about metal–C_3 axes have previously been reported to be either extremely fast or extremely slow on the NMR time scale. In cobalt, rhodium and iridium complexes of type **[5]**, $\Delta G^{\ddagger}$ data for the cyclopropenyl rotation were in the range 57–77 kJ mol^{-1} with values increasing down the order Co < Rh < Ir.[86] In the related ruthenium complexes **[6]**, rotational energy barriers were in the region of 60 kJ mol^{-1} and essentially independent of halide or cyclopentadienyl ligand.[87] In the three complexes $[M(\eta^3\text{-}C_3Ph_3)L]PF_6$, (M = Ni, Pd or Pt; L = 1,1,1-tris(diphenylphosphinomethyl)ethane), the rotational energy barriers, determined by $^{13}C\{^1H\}$ bandshape analysis, increased in the order Ni < Pd < Pt.[88]

2.4.3. Metallotropic shifts

This section includes metallotropic shifts that may or may not involve linkage isomerism between ground-state metal coordination complexes. Shifts that do give rise to such isomerism will be considered firstly.

^1H and ^{13}C NMR studies have been applied to the $\eta^1 \rightleftharpoons \eta^3$ equilibrium of [α-(dimethylamino)benzyl]lithium.[89] The η^1 species is formed at low tempera-

ture, this being confirmed by MNDO calculations and ^{6}Li–^{1}H HOESY (heteronuclear Overhauser effect spectroscopy) experiments. The equilibrium is controlled by solvation/complexation, low Lewis basicity of the solvent or bidentate ligands favouring the η^3 species. $[Ru(NH_3)_5(acetone)]^{3+/2+}$ complexes display $\eta^1 \rightleftharpoons \eta^2$ linkage isomerism and this was investigated by spectroscopic (including NMR) and electrochemical methods.[90] The molecule 4*H*-cyclopenta [*def*]phenanthrene (cppH) is theoretically capable of binding to metals in an η^6, η^5, η^4, η^3, η^2 or η^1 fashion. In fact it forms the complexes $[(\eta^6\text{-cppH})Cr(CO)_3]$ and $[(\eta^5\text{-cppH})Mn(CO)_3]PF_6$. However, the complex (**A**, Scheme 5) undergoes an $\eta^6 \rightarrow \eta^5$ haptotropic shift on heating. This can be monitored by NMR and proceeds via species (**B**, Scheme 5) to the η^5-complex (**C**, Scheme 5).[91] The ligand 1,8-naphthyridine (naph) can bind to metals in η^1 or η^2 modes. In *fac*-$[Mn(\eta^1\text{-naph})(\eta^2\text{-naph})(CO)_3]ClO_4$, both binding modes occur, but these are only detected individually at low temperatures.[92] At higher temperatures there is an $\eta^1 \rightleftharpoons \eta^2$ exchange of binding modes with an approximate activation energy of 44 kJ mol^{-1}.

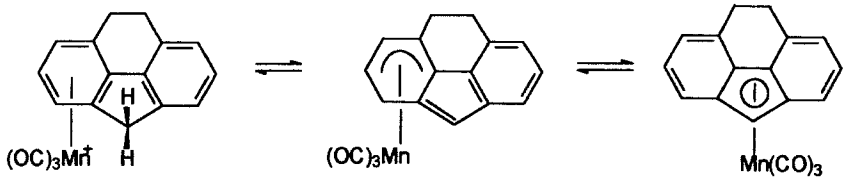

A **B** **C**

Scheme 5

Metallotropic shifts without linkage isomerism occur widely in organometallic systems. They often lead to exchange between chemically degenerate species, but this is no limitation for their study by NMR. 'Ring whizzing' via a series of [1,3] shifts was suggested on the basis of $^{31}P\{^{1}H\}$ spectra of the N-bonded *exo* and *endo* isomers of $[PtCl_2(PEt_3)(Me_2NC_2N_4S_2)]$.[93] Similar studies on Pt and Pd complexes of 1,5-diphosphadithiatetrazocines ($1,5\text{-}Ph_4P_2N_4S_2$) revealed another [1,3]-shift process.[94] ^{31}P and ^{77}Se studies were performed[95] on Pt and Pd complexes of the selenium analogues of the previous ligands, namely $1,5\text{-}Ph_4P_2N_4Se_2$. A [1,3]-shift process occurs in $[Pt(PPh_3)\ (1,5\text{-}Ph_4P_2N_4Se_2)]_2$, whereas in the η^1-Se-bonded *trans*-$[PtCl(PEt_3)_2Ph_4P_2N_4Se_2Ph)]$ complex variable-temperature ^{31}P spectra revealed a 2-site exchange process involving the two PEt_3 ligands. Precise bandshape analysis and 2D-EXSY studies of the exchange between the *E*- and *Z*- isomers of 2,4-pentadienyldipropylborane yielded activation data for the metallotropic rearrangements of each isomer and for $E \rightleftharpoons Z$ interconversion. The data suggested that [1,3] rather than [1,5] shifts occur.[96]

2,2′:6′,2″-Terpyridine (terpy) is a strong N-donor ligand towards metals and

normally uses all three of its nitrogens in terdentate coordination. When it acts as a bidentate ligand its consequent complexes are fluxional, exhibiting double [1,4]-metallotropic shifts as the metal coordination switches between adjacent pairs of nitrogen donors. This process has been followed by DNMR for cases of Ru^{II}, Mo^0 and W^0 complexes[97] and for Pd^{II}/Pt^{II} complexes.[98] Relative rates and energies of this fluxional process vary widely according to the metal moiety, the order being Mo^0, $W^0 < Pd^{II} < Ru^{II} < Pt^{II}$, with $\Delta G^{\ddagger}$ values in the range 48–94 kJ mol^{-1}. The complexes *cis*-$[M(C_6F_5)_2(terpy)]$ (M = Pd^{II} or Pt^{II}) were studied by both ^1H and ^{19}F spectra. Variable-temperature ^1H spectra exhibit exchange broadening of five pairs of signals. The process is described as a 'tick-tock' twist mechanism and proceeds via an associative 5-coordinate transition state structure. The process also interconverts the pairs of C_6F_5 ring environments so these rings can also be used as monitors of the exchange rates via their ^{19}F spectra. At low temperatures these complexes also exhibit restricted rotation of the C_6F_5 rings and of the pendant pyridyl ring.[98]

Analogous double [1,4] shifts occur in bidentate complexes of 2,6-diacetylpyridine (DAP), viz. *fac*-$[ReX(CO)_3(DAP)]$, where the fluxion involves switching between N and O ligand donors.[99] This process is also thought to be an associative twist mechanism as it produces exchange between the pairs of equatorial carbonyl environments as evidenced by variable-temperature ^{13}C spectra. Rhenium complexes of bispyrazolylpyridine ligands are similarly fluxional and their rates and energies have been measured by DNMR.[100] When the ligand is unsymmetrical, the switching exchanges chemically distinct complexes with different solution populations (Scheme 6). A fluxion involving switching between N and S ligand donors occurs in the complexes $[M(CO)_4L]$ (L = 2,6-bis(methylthiomethyl)pyridine; M = Mo or W).[101] Bandshape analysis quantified the rates of this fluxion together with those of pyramidal inversion of the coordinated S atom and of the combined processes.

2.4.4. Ring conformational changes

Metal complexes of polyaza macrocycles have been widely studied in past decades. Recent DNMR conformational studies of such complexes include ruthenium(II) tetraaza-porphyrinogen complexes,[102] and lanthanide complexes (La^{III}, Eu^{III}) of tetraazacyclododecane derivatives.[103] In the Ru^{II} complexes two dynamic processes were quantified, an interconversion of the double saddle-shaped macrocyclic ring and hindered rotation of the axial ligands.[102] In the lanthanide complexes, macrocyclic ring rigidity is lost at ambient temperatures and, by 50°C, is fast on the ^1H chemical shift time scale.[103]

^1H spectra were used to identify two types of dynamic processes occurring in the polypyrazolyl borate complex $[H_2B(pz)_2]_2Pb$.[104] The axial and equatorial pyrazolyl rings in the pseudo-trigonal-bipyramidal structure were shown to

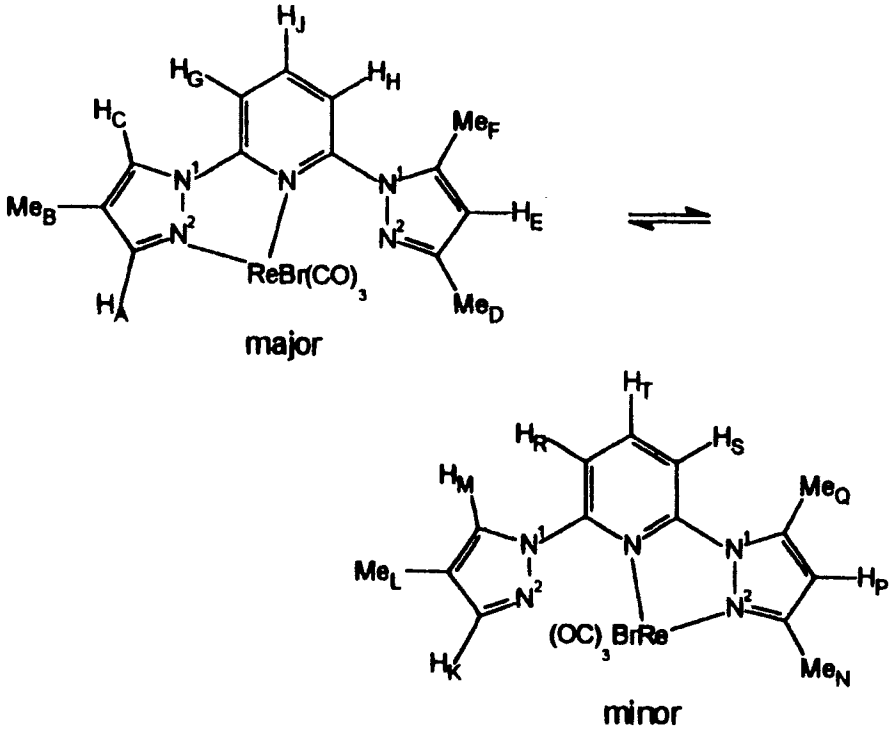

Scheme 6

equilibrate with a very low energy barrier, but also a boat–boat flip of the PbN_4B rings of the bidentate ligand equilibrates all four rings on each ligand. This work is also notable for its ^{207}Pb studies. Chair-to-chair interconversion of fused cyclohexane rings associated with zirconium complexes such as [Zr(*cis*-dsd)$_2$] (*cis*-dsdH = *N*,*N*-disalicylidene-*cis*-1,2-diaminocyclohexane) has been measured.[105] The coalescence temperature was ~226 K and the energy barrier, $\Delta G^{\ddagger}$ (298 K), was 46.5 ± 0.9 kJ mol^{-1}. The silylhydrazine [**7**] also consists of two fused 6-membered rings. Variable-temperature ^{1}H, ^{13}C, ^{15}N and ^{29}Si NMR studies have yielded a $\Delta G^{\ddagger}$ value of 52 ± 3 kJ mol^{-1} for the ring inversion.[106] Germaoxaphosphorinenes also consist of heterocyclic

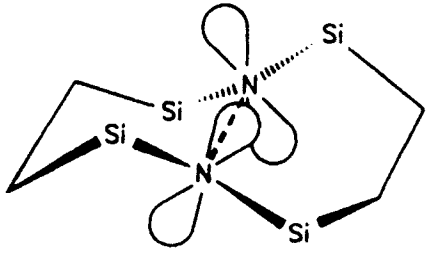

[**7**]

6-membered rings. In this case the inversion process involves exchange between sofa forms with large folding along the Ge—C axis. Phosphorus inversion also occurs.[107]

Six-membered cyclohexadienyl rings have been used to monitor the relative rotations of metal tripods.[108] Complexes were of type [8] where M = manganese or rhenium. The DNMR analysis was detailed as the spectra were sensitive to more than one rate constant. The case of $[(PhC_6H_6)Mn(dppe)NO]PF_6$ is illustrated by the variable temperature spectra

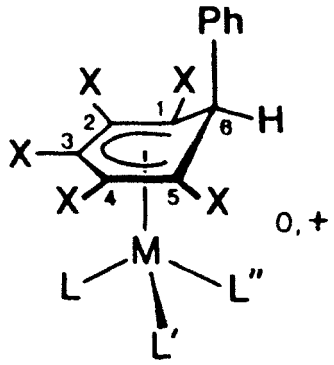

[8]

in Fig. 5. Here the rate constants k_1 and k_2 refer to Scheme 7. The conclusions of this work were that there was exclusive preference for the C_1-symmetric enantiomeric conformers that have the unique unidentate ligand eclipsing carbons C2 or C4 of the cyclohexadienyl ring. Barriers to conformational exchange ($\Delta G^{\ddagger}$) were in the range 38.5–47.7 kJ mol^{-1}.

Metal phosphine complexes have been the subject of a number of recent DNMR studies. The stereodynamics of sterically crowded metal phosphine complexes such as *trans*-$[(Bu^t)_2P(Pr^i)]_2MCl_2$ (M = Pt^{II} or Pd^{II}) were studied by 1D-bandshape and 2D-EXSY experiments, mainly as $^{31}P\{^1H\}$ and $^{13}C\{^1H\}$ spectra.[109] Four diastereomeric equilibrium conformations for the *iso*-propyl and *tert*-butyl groups were identified and this allowed elucidation of the preferred conformational interconversion pathways. The bandshapes of these $^{31}P\{^1H\}$ and $^{13}C\{^1H\}$ signals were ambitiously fitted using up to 8 rate constants for certain temperatures. $^{31}P\{^1H\}$ studies were also carried out on some carbonyl phosphine and phosphite complexes. The stereodynamics were fast at room temperature but at low temperatures (~185 K) two unequal intensity signals were assigned to two stereoisomers which differed in the orientation of the aryldiazenido ligand.[110] Full activation parameters for the isomerization process of this ligand are reported.

Some octahedral metal(II) complexes containing ether-phosphine ligands,

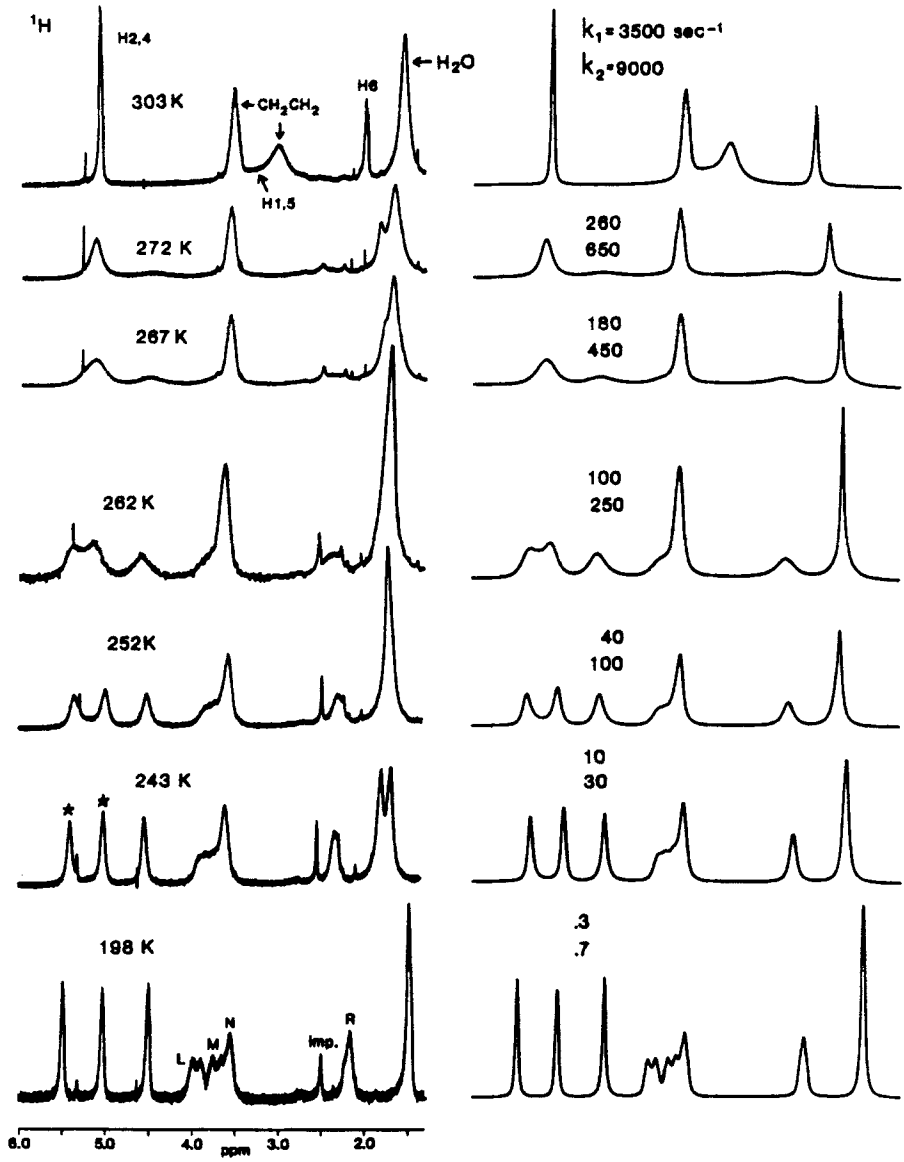

Fig. 5. 400 MHz ^{1}H spectra of the cyclohexadienyl 1,2,4,5,6 and PCH_2CH_2P protons of $[(PhC_6H_6)Mn(dppe)NO]PF_6$ in $CDCl_3$ (left) compared with computer-simulated spectra (right). (Reproduced with permission from *Organometallics*, 1992, **11**, 2841.)

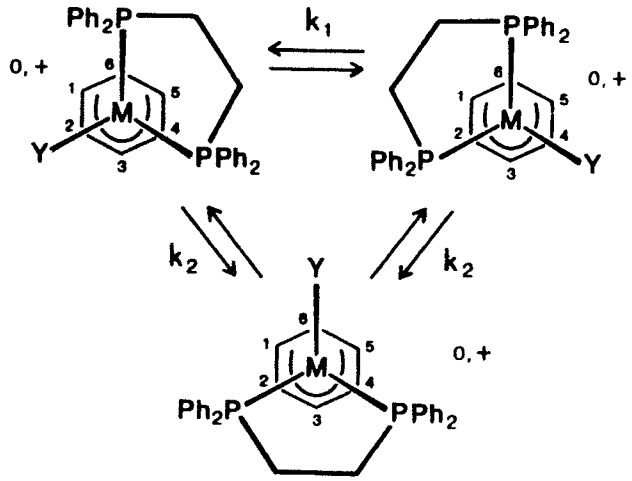

Scheme 7

viz. $[X_2M(P^{\frown}O)_2]$ ($P^{\frown}O = \eta^2$(O,P)-chelated ether-phosphine; M = Pd^{II}, Ru^{II}) exhibit various types of fluxionality that have been quantitatively assessed by variable-temperature $^{31}P\{^1H\}$ studies and iterative bandshape analysis.[111,112] Two studies have been reported on the dynamics of allylpalladium[113] and niobium[114] complexes of poly(pyrazol-1-yl)methane ligands. The 6-membered metallacycle ring undergoes boat-to-boat inversion and this has been carefully followed by ^1H studies. π-Allylpalladium complexes with ligands such as 2-(1H-pyrazol-1-yl)pyridine have been shown to undergo a dynamic process that suggests selective Pd—N cleavage leading to opening up of the 5-membered chelate ring.[115]

Finally in this section, there is a report of an 8-membered ring conformational study. 1,5-Dithiacyclooctane (1,5-DTCO) forms the complex $[W(CO)_4$(1,5-DTCO)] where the ligand acts as a bidentate chelate, and undergoes facile boat-chair $\rightleftharpoons$ chair-boat interconversion (Scheme 8).[116] The changes in its ^1H spectra on cooling to 156 K were complex due to the 12 different hydrogen environments of each ring, but bandshape analysis was accomplished on the exchanging H_A and H_E signals.

2.4.5. Miscellaneous fluxions

As it is not possible within the scope of this review to attempt any comprehensive coverage of the full range of fluxional processes in organometallic and inorganic compounds, it was decided instead to highlight certain topics of special current chemical or NMR interest, and where NMR has been particularly crucial in identifying the dynamics.

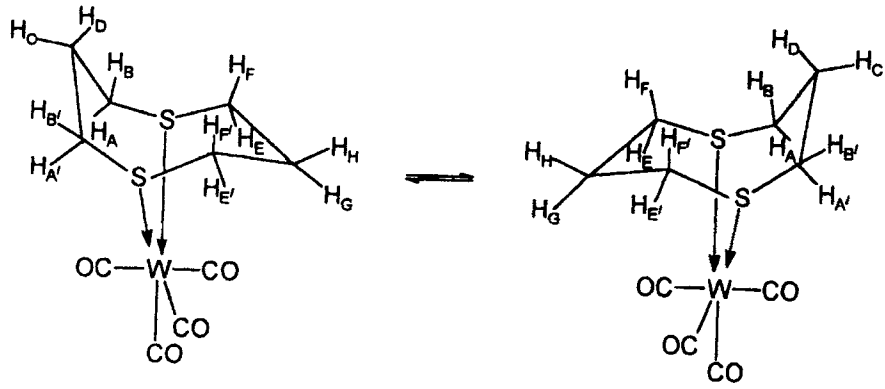

Scheme 8

(i) Dihydrogen complexes and hydride fluxionality. Transition metal hydrides display novel fundamental NMR features in addition to their intramolecular dynamics. Large scalar spin–spin couplings between hydride protons occur at low temperatures (viz. ~180 K), but on increasing the temperature there is a rapid, nearly exponential growth of the coupling constant. Simultaneously, the resonance lines broaden, coalesce and sharpen again into a simpler spectral pattern with no exchange-coupling discernible. Szymanski[117] has provided a theoretical rationalization of these observations. His approach uses the Wangness–Bloch–Redfield (WBR) theory for describing the interactions of the relevant spatial degrees of freedom of the hydride protons with a quantum mechanical thermal bath. When the vibrational modes are eliminated from this model (as they relax too rapidly to be observed on the NMR time scale) the WBR theory becomes equivalent to the Alexander–Binsch theory of exchanging nuclei where the scalar coupling term has been replaced by (or augmented with) the quantum exchange term. Calculations were performed on a two-proton system assuming a one-dimensional model of the relevant spatial motions. The assumed motion included correlated rotation of the proton pair where the interproton distance varied with the rotational angle. A set of calculated spectra is shown in Fig. 6. Lineshapes are a function of the thermal coupling constants Γ and Γ'.

The theory of hydride dynamics as applied to pairs of deuteron nuclei in solid-state transition metal complexes has been developed by Buntkowsky, Limbach *et al.*[118] Like Szymanski's, their method is based on the Alexander–Binsch density matrix formalism. It accounts for the coherent and incoherent exchange of two deuterons, the former causing a splitting of the spectral lines, and the latter leading to broadening and later to a narrowing of lines due to a relaxation of coherences between states of different symmetry with respect to particle permutation. The differences between the coherent and incoherent exchanges were shown to be most pronounced when the coherent exchange

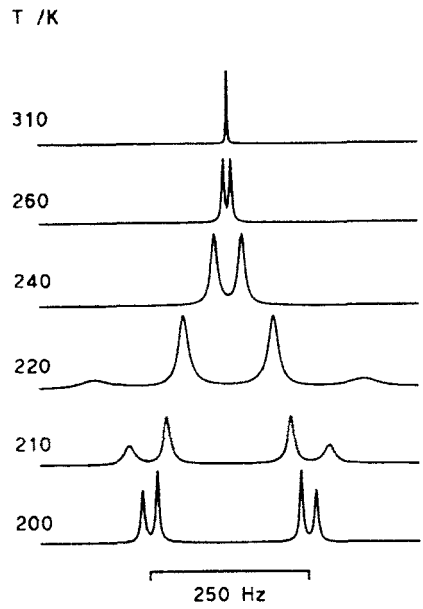

Fig. 6. Theoretically predicted pattern of thermal effects in NMR spectra of a 2-proton coupled system. Temperature dependences of $2J_{av}$ and $K/4\pi$ were calculated assuming thermal coupling constants $\Gamma = 2.5 \times 10^{11}\ s^{-1}$ and $\Gamma' = 0.25 \times 10^{11}\ s^{-1}$. Frequency difference between binding sites was 250 Hz and $(\pi T_2^*)^{-1}$ was 1.2 Hz. (Reproduced with permission from *J. Chem. Phys.*, 1996, **104**, 8216.)

frequencies were of the same order as the quadrupole coupling constant. The theory was applied to single-crystal and non-oriented powder samples.

Hydride fluxionality in transition metal complexes has recently been reviewed by Gusev and Berke.[119] They acknowledge the enormous reliance placed on NMR data in classifying hydride motions. They distinguish between principal and secondary topological changes of coordinated ligands, and further subdivide the principal changes into replacement (R) and migratory (M) types. In the complexes $[Ir(H)_2X(PBu^t_2Ph)_2]$ (X = Cl, Br or I) the exchange rate increases substantially for the lighter halides, indicating that it is probably migration of the X ligand that determines the kinetics.[120] However, for the complexes $[OsH_2X_2L_2]$ (X = Cl, Br or I; L = P^iPr_3) the spectroscopic features favour a simultaneous migration of the two X ligands by an M mechanism.[121] The relative energetics of hydride versus alkyl migration were examined in complexes of type $[(\eta^5\text{-}C_5R'_5)Rh(L)(C_2H_4)R^+]BF_4^-$ using both ^1H and ^{13}C studies.[122] Temperature-dependent ^2H spectra, in addition to ^1H spectra, were used to study the facile H/D exchange and the formation of dihydrogen derivatives of rhenium hydride complexes in acid solutions.[123] A similar study was performed on the pseudo-

octahedral complexes $[Re(CO)H_2L_2(NO)]$ (L = phosphorus donor). From the kinetic data, based on 1D and 2D-EXSY NMR experiments and MO calculations, an intramolecular dihydride/dihydrogen exchange mechanism was proposed.[124] NMR was used to study the equilibrium between the classical structure $[ReH_2(CO)_2(PMe_2Ph)_3]^+$ and its nonclassical dihydrogen tautomer $[Re(\eta^2\text{-}H_2)(CO)_2(PMe_2Ph)_3]^+$. Variable-temperature ^1H studies provided the thermodynamic parameters for the conversion process.[125]

Turning now to metal trihydride complexes, ^1H and selective $^1H\{^{31}P\}$ NMR experiments have followed the fluxionality of the nonclassical species $[(PP_3)OsH(\eta^2\text{-}H_2)]BPh_4$ where PP_3 is the tetraphosphine $P(CH_2CH_2PPh_2)_3$.[126] In contrast, the hydrido dihydrogen complex $[(dppm)_2HRu(H_2)]^+(OR)^-$ is in dynamic equilibrium with the dihydride species *trans*-$[RuH_2(dppm)_2]$, in the presence of phenol or hexafluoroisopropyl alcohol.[127] This intermolecular proton transfer equilibrium was measured by ^1H NMR in the temperature range 223–293 K. Some bimetallic trihydrides $[Cp_2TaH_2(\mu\text{-}H)M(CO)_5]$ (M = Cr, Mo, W) have been prepared.[128] They undergo a rearrangement that was followed by variable-temperature ^1H T_1 measurements and saturation-transfer experiments. Pairwise exchanges between terminal and bridging hydride ligands occur that require an out-of-plane twist of two adjacent H atoms and their binding to both metal centres in a transition state. Three different types of hydride exchange processes were predicted to occur by *ab initio* MO calculations, two of which were confirmed experimentally by ^1H NMR spectra in the osmium trihydride complexes $[OsH_3(BH_4)(PR_3)_2]$.[129] ^1H spectra were recorded in the range 153–360 K. The third exchange process was assumed to have a high barrier energy and to be observable only at temperatures >360 K. The complex $[PtH_3(PBu^t_3)_2]^+$ was prepared as its triflate salt. The species is in free equilibrium with free H_2 and $[PtH(PBu^t_3)_2]^+$. It represents the first dihydrogen complex of d^8 electron configuration. Rates of the H_2 exchange process were assessed by the iterative DNMR5 program.[130] A very detailed DNMR study of exchange couplings and hydrogen dynamics in RuH_3 adducts with coinage-metal cations (viz. Cu^+, Ag^+ or Au^+) has been reported.[131] Variable-temperature studies down to 130 K were carried out. At low temperatures these species exhibit couplings that arise from quantum mechanical dihydrogen exchange corresponding to a coherent tunnelling process. These increase strongly with increasing temperature, but eventually cease to be observable because they become much larger than the associated chemical shift differences and/or because of the onset of a classical dihydrogen exchange process. Such couplings have been referred to earlier in the work of Szymanski.[117] At higher temperatures, the classical exchanges between the hydride protons were measured by total bandshape analysis. The results indicated (i) the absence of kinetic hydrogen/deuterium isotope effects, (ii) only small effects of the presence of Lewis-acid cations on the classical exchange dynamics, but (iii) important effects of these cations on the quantum mechanical exchange couplings, with these couplings increasing with

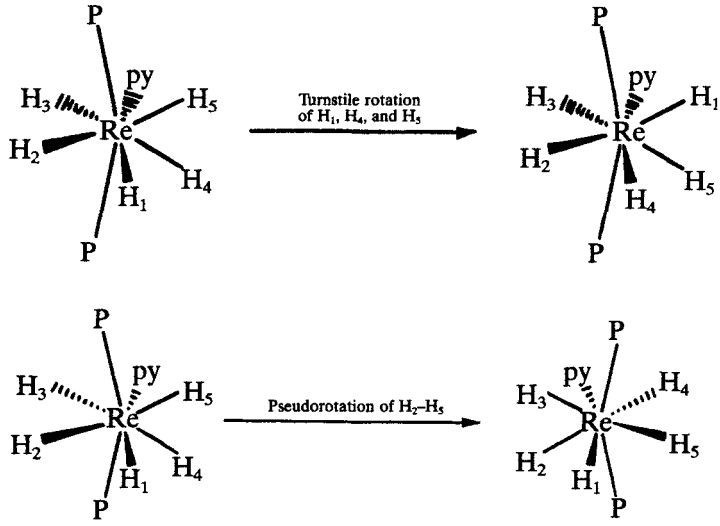

Scheme 9

increasing electronegativity of the coinage metal by favouring dihydrogen configurations.

There have been two reports on the solution dynamics of polyhydride complexes.[132-133] Variable-temperature $^{31}P\{^1H\}$ spectra were used to monitor the reversible loss of hydrogen from iridium nonclassical complexes $[IrClH_2(PR_3)(H_2)]$ (R = Pr^i, Cy, Bu^t).[132] In the complexes $[ReH_5(PPh_3)_2(L)]$ (L = pyridine or substituted pyridines) two ^1H coalescence events were detected. These were attributed to turnstile rotation and pseudorotation mechanisms (Scheme 9). $^1H\{^{31}P\}$ ROESY spectra at low temperatures were used for assignment purposes.[133]

(ii) Organolithium compounds. Lithium-7 is an invaluable nuclide for following the solution dynamics of organolithium compounds, and some recent studies are reported here.

Two examples of the coordination of Li^+ towards macrocyclic nitrogen donors are the dibenzotetraaza[14]annulene derivatives[134] and the complexes of 1,4,7,10-tetrakis(2-methoxyethyl)-1,4,7,10-tetraazacyclododecane.[135] The first case involved a ^7Li dynamic study of the exchange of Li^+ between two different environments,[134] whereas the second study was concerned with intramolecular enantiomerization, intermolecular metal ion exchange and intermolecular ligand exchange.[135]

^1H and ^7Li spectra were used to probe the solution dynamics of the dimeric diethyl ether adduct $[\{Li[N(SiMe_3)CH_2CH_2NSiMe_3]Li{\cdot}OEt_2\}_2]$ and the unsolvated trimer $[\{Li[N(SiMe_3)CH_2CH_2NSiMe_3]Li\}_3]$.[136] The dimer undergoes a rapid exchange between unsolvated and diethylether-solvated dimers (Scheme 10), whereas the trimer exists in a temperature-dependent equilibrium of

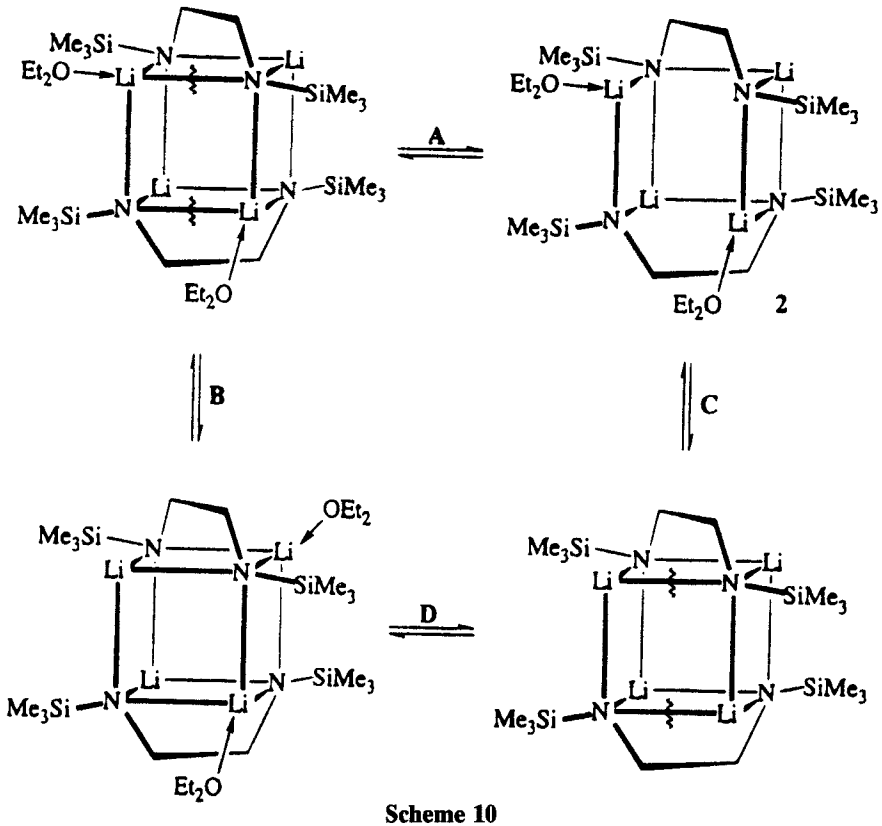

Scheme 10

dimeric and trimeric species, of which the trimer is fluxional and exchanges inequivalent ligands by an intramolecular distortion of the Li_6N_6 cage structure. A combined ^7Li, ^{31}P study has been carried out on a series of chelated organolithium reagents where individual diastereomeric ether solvates were detected under slow exchange in dimethyl ether solution.[137]

(iii) Metallocenes. Manganocenes have special magnetic properties that are reflected in their NMR spectra. The deuterated compounds $[(C_5D_5)_2Mn]$, $[(C_5H_4CD_3)_2Mn]$ and $[(C_5D_4CH_3)_2Mn]$ have been studied by temperature- and concentration-dependent ^2H NMR.[138] This allowed detection of the low-spin isomer ($^2E_{2g}$) of $[(C_5D_5)_2Mn]$ for the first time, the investigation of the spin cross-over ($^2E_{2g} \rightleftharpoons {}^6A_{1g}$) and the formation of the antiferromagnetic dimers that contain η^3,η^2-bridging and η^5-terminal cyclopentadienyl rings. The bridging rings are involved in a rapid dynamic process so that the η^3 and η^2 fragments are indistinguishable down to 160 K. This study illustrates the advantages of ^2H over ^1H studies for such paramagnetic species. Linewidths are reduced by a factor of ~40 and the ^2H shift range is ~200 ppm. ^1H spectra

were used in the study of stereochemical nonrigidity of the $MeB(C_6F_5)_3^-$ salts of a series of ring-substituted Zr- and Hf-containing metallocenium ions such as $(RCp)_2ZrCH_3^+$. Two exchange processes with their $\Delta G^{\ddagger}$ data were reported.[139] In another study the complexes $[M(1,3\text{-}Bu^t_2\text{-}\eta^5\text{-}C_5H_3)(\eta^5\text{-}C_5H_5)(CH_3)]^+$ (M = Zr, Hf) were shown to undergo an exchange whereby the chiral character of the complexes was lost at higher temperatures.[140] Bandshapes of the Bu^t signals were fitted iteratively using the DNMR5 program. The same program was used in a study of the inversion of the butadiene ligand in some s-*cis*-η^4-butadiene metallocene compounds,[141] and in the fluxionality of complexes **[9]** where the two phosphine arms of the 5-coordinate species undergo exchange via an associative pseudo-six-coordinate structure. This detailed study involved ^1H, $^{31}P\{^1H\}$ and $^{13}C\{^1H\}$ spectra.[142]

(iv) Metal clusters. The range of DNMR studies here is very great, but many

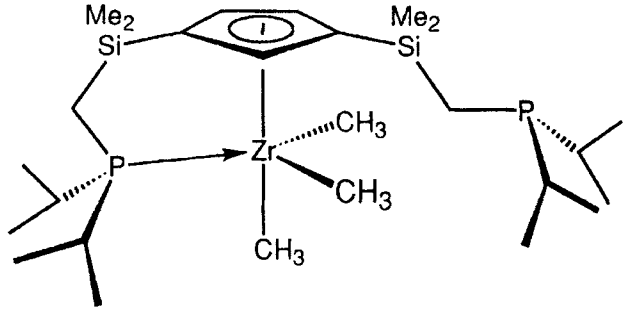

[9]

are qualitative in nature. The ones chosen for inclusion represent more quantitative work. One such study[143] concerns the dimolybdenum complex $[(2\text{-propynylbornyl})Cp_2Mo_2(CO)_4]^+$. This undergoes complex fluxionality (Scheme 11) involving antarafacial migrations (1a⇌1c, 1b⇌1d, Scheme 11) and suprafacial migrations (1a⇌1b, 1c⇌1d, Scheme 11). The processes were monitored by the ^1H signals of the alkynyl-methyl region and by the ^1H and ^{13}C signals of the cyclopentadienyl ring. Total bandshape analysis of the ^{13}C Cp signals led to an energy for the antarafacial migration of 54.8 ± 1.7 kJ mol^{-1} and for the suprafacial migration of 75 kJ mol^{-1}. The diruthenium complex $[Cp_2{*}Ru_2(\mu\text{-}CH_2)(SiMe_3)(\mu\text{-}Cl)]$ undergoes two dynamic processes that were followed by variable-temperature ^1H and ^{13}C spectra.[144,145] The lower-temperature process ($\Delta H^{\ddagger} = 37.7 \pm 0.8$ kJ mol^{-1}) involves hopping of the silyl ligand between the two Ru centres, whereas the higher-temperature process ($\Delta H^{\ddagger} = 50.2 \pm 1.3$ kJ mol^{-1}) involves the reversible re-formation of the C—Si bond between the silyl and methylene ligands.

The cluster $[Cp_3{*}Co_3(\mu_2\text{-}CO)(\mu_3\text{-}CO)(\mu\text{-}H)_2]$ consists of an equilateral

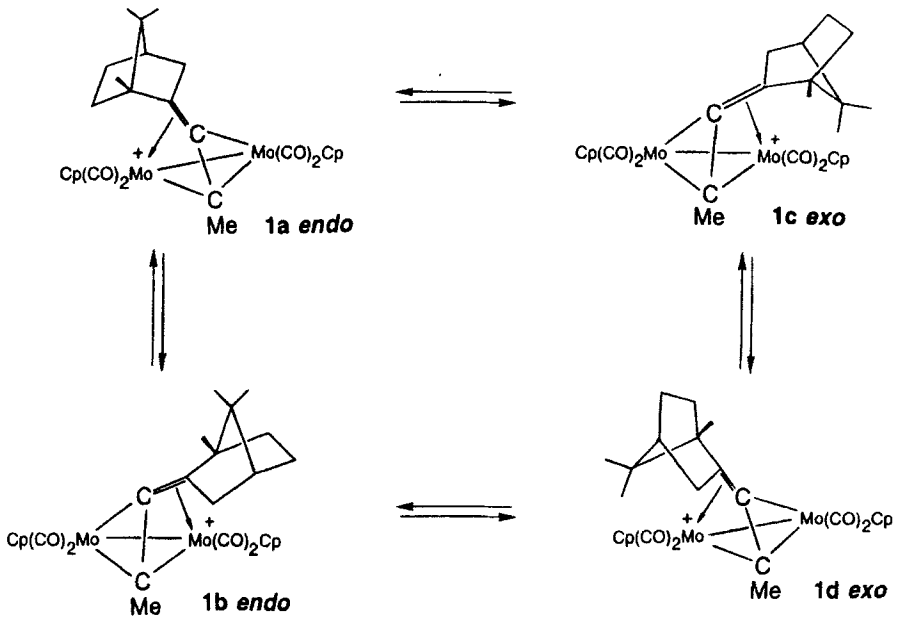

Scheme 11

triangle of Co atoms capped on each face by a μ-CO ligand. ^{13}C bandshape analysis of the CO signals allowed the barrier to interconversion of the μ_2- and μ_3-CO ligands to be measured.[146] Allowance was made for the quadrupolar broadening of ^{57}Co in this analysis. The fluxionality of the related formimidoyl cluster $[Cp_3{*}Co_3(\mu_2\text{-}H)(\mu_3\text{-}\eta^2\text{-}CH{=}NCMe_3)]$ was also investigated. This consisted of complete rotation of the formimidoyl ligand parallel to the tricobalt plane (Scheme 12). The trinuclear cluster anions $[ReM(CO)_9\{(\mu\text{-}H)ReH(CO)_4\}]^-$ (M = Re, Mn) were shown by ^1H and ^{13}C studies to exhibit a dynamic process which exchanges the two hydrides and the carbonyls *trans* to them (E_a = 67 kJ mol^{-1}).[147] It might also be described as a windshield-wiper motion of the $H_2Re(CO)_4$ fragment around the two *trans* diaxial carbonyls. The tetranuclear Re cluster $[Re_4(\mu\text{-}H)_4(CO)_{13}]^{2-}$ exhibits two fluxional processes involving hydride exchange.[148] ^1H studies identified one process, frozen only below 153 K, which equalizes the three hydrides bridging the edges of the basal triangle, and a second process, frozen below 188 K, which exchanges all the hydrides. Energy barriers ($\Delta H^{\ddagger}$) were 29.0 ± 1.3 kJ mol^{-1} (intrabasal

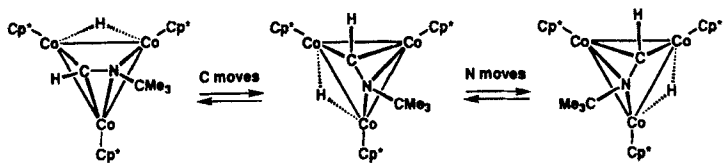

Scheme 12

exchange) and 40.7 ± 0.6 kJ mol^{-1} (total scrambling). The same research group has also investigated the dynamics of the rhenium–platinum dinuclear adduct $[(CO)_4Re(\mu\text{-}H)(\mu\text{-}CO)Pt(PPh_3)_2]$, by ^{13}C, ^{31}P and ^{1}H variable-temperature spectra. Two mutual exchange processes were identified.[149] The tetranuclear Ru clusters $[Ru_4(\mu\text{-}H)_4(CO)_{12-x}L_x]$ (x = 1–4, L = $P(OEt)_3$, PPh_3; x = 1, 2, L = $AsPh_3$) undergo numerous types of hydride scrambling that were the basis of a multinuclear (^{1}H, $^{13}C\{^{1}H\}$, $^{31}P\{^{1}H\}$) variable-temperature study.[150]

Finally, reference should be made to a DNMR study of hexanuclear clusters with fluxional SO_2 and NO ligands, viz. $[Ru_6C(CO)_{14}(SO_2)(\mu\text{-}\eta^3\text{-}C_3H_5)]^-$ and $[Ru_6C(CO)_{14}(NO)(\mu\text{-}\eta^3\text{-}C_3H_5]$. The protons of the π-allyl ligand were used to probe the dynamic behaviour. Energy barriers ($\Delta H^{\ddagger}$) were 30.5 kJ mol^{-1} (SO_2 complex) and 38.5 kJ mol^{-1} (NO complex).[151]

2.5. Developments in solid-state methods and applications

A general formalism has been presented by Heaton[152] of a direct time-domain propagation method for lineshapes of rotating samples. The method is applicable to both fast and slow spinning regimes and its utility has been demonstrated for two-site jump motions and for diffusive reorientation. The method involves a direct matrix propagation of the complex transverse magnetization. Matrix elements are determined by the spin Hamiltonians at each site visited by the spins, and by the conditional probability function that describes the motion of the spins between these sites. Chemical exchange, diffusion and sample rotation can all be appropriately accounted for. The method has been applied to deuterons undergoing 180° flips and to ^{31}P lineshapes of phospholipids undergoing lateral diffusion across curved membrane surfaces.

A new 1D exchange experiment in the slow-motion regime of spinning solids has been proposed[153] for chemically equivalent nuclei exhibiting quadrupole coupling or chemical shielding anisotropy. It consists of the usual three-pulse sequence for 2D-EXSY experiments but with the evolution time fixed at one-half of the spinning period, i.e. $t_1 = T_R/2$, and a mixing time equal to an integral multiple of the spinning period, i.e. $t_m = GT_R$. The magnetic polarizations associated with the various spinning sidebands are directed in alternate directions at the start of the mixing time. Dynamic processes during t_m redistribute the polarizations, resulting in modified sideband patterns during the detection time, t_2. The method has been given the acronym ODESSA for one-dimensional exchange spectroscopy by sideband alternation. It has been demonstrated for ^{13}C and ^{2}H in solid dimethyl sulfone, where the spin exchange occurs between the chemically equivalent methyl groups. The ^{2}H ODESSA spectra of dimethyl sulfone, together with the computer-simulated spectra for a rate constant, k, of 65.2 s^{-1}, are shown in Fig. 7. A time-reverse ODESSA experiment has also been proposed[154] for samples with several groups of equivalent nuclei undergoing internal exchange such as pure

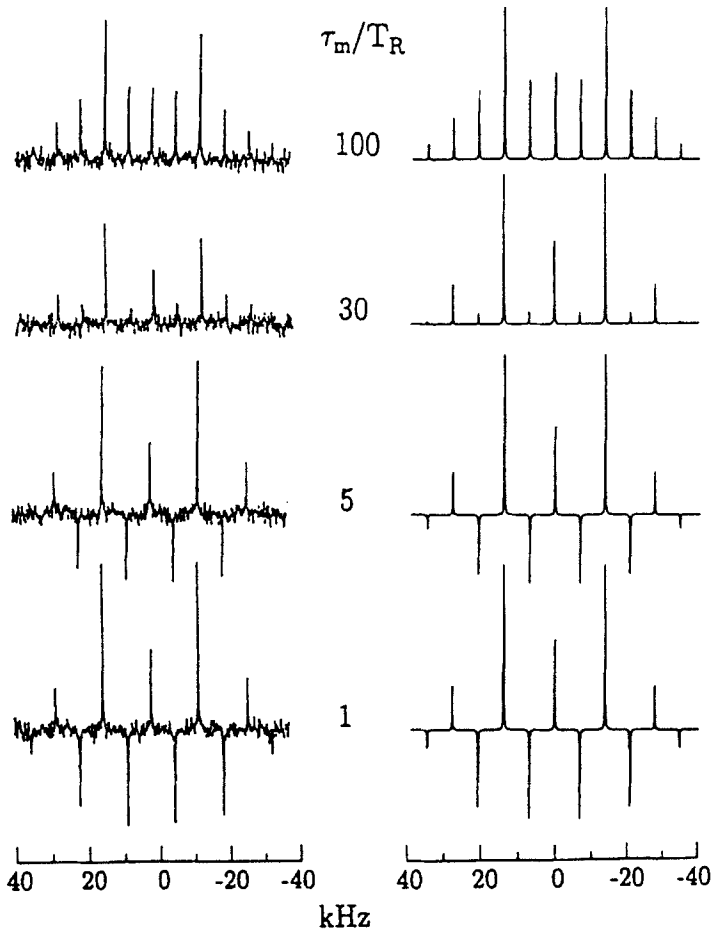

Fig. 7. (Left) Experimental ^2H ODESSA spectra of an unenriched sample of dimethyl sulfone recorded without phase alternation at room temperature with $\nu_R = 7.0$ kHz, and the indicated mixing times. Each spectrum was obtained with 670 000 scans, 0.1 s recycle time and without proton decoupling. (Right) Simulated spectra for $k = 65.2\ s^{-1}$, $T_1 = 6.0$ ms, $T_2^{-1} = 500\ s^{-1}$. (Reproduced with permission from *J. Magn. Reson.*, 1996, **A123**, 7–15.)

reorientation as opposed to mutual exchange. This experiment differs from the earlier ODESSA experiment in that the mixing time is now set to an odd number of half-rotation periods, i.e. $t_m = (2G\text{-}1)T_R/2$, and the acquisition starts at t_2 ($= T_R/2$) after the detection pulse. This method has been applied to the ^{13}C spectra of dimethyl sulfone, enriched tropolone and 1,4-diphenoxybenzene. Tropolone was also the subject of a single-crystal NMR study of hydrogen disorder of the hydroxyl groups.[155]

The theory of dynamic MAS spectra of solids exhibiting both reorientation

and chemical exchange has been reformulated using an expansion method, and applied to the particularly challenging case of solid bullvalene.[156]

A number of studies of ligand rotations in organometallic complexes have been reported. Although olefin rotations occur commonly in solution, reports of such rotations in the solid state are rare. However, a recent ^{13}C, ^{1}H and ^{2}H study has shown that ethene rotation does occur in solid $[Rh(acac)(C_2H_4)_2]$,[157] with an activation energy ($\Delta G^{\ddagger}$) of 56.5 kJ mol^{-1}. This value was based on lineshape analysis of the ^{2}H powder spectra and variable temperature studies of proton $T_{1\rho}$ values in the range 253–353 K. There have been a number of reports of arene rotations in organometallic compounds.[158–160] The dynamics of the benzene moiety in $[(\eta^6\text{-}C_6D_6)Cr(CO)_3]$ have been measured by ^{2}H bandshape analysis and ^{2}H T_1 values.[158] The temperature dependence of the quadrupole echo ^{2}H NMR bandshape and the temperature dependence of the ^{2}H T_1 values were interpreted in terms of a $2\pi/6$ nearest-neighbour-jump model of the benzene moiety about an axis perpendicular to the molecular plane. The data gave an activation energy of 17.7 kJ mol^{-1}. The power of ^{2}H NMR for studying molecular motions in the solid state was also demonstrated in a number of bis(η-arene)molybdenum complexes,[159] where the ring rotation rates were a sensitive function of the nature of the arene. In $[Mo(\eta\text{-}C_6D_6)_2]$ the spectra were invariant in the temperature range 160–360 K, indicative of rapid ring rotation, whereas in the case of $[Mo\{\eta\text{-}C_6D_3(CD_3)_3\text{-}1,3,5\}_2]$ the ligands were static up to 360 K, according to its quadrupole echo ^{2}H spectra. This conclusion is compatible with that reached in the case of $[Cr(\eta^6\text{-}C_6HMe_5)(CO)_3]$ where ^{13}C CP-MAS studies showed that the aromatic ring was not rotating but there was rapid carbonyl exchange ($E_a = 30.6 \pm 1.5$ kJ mol^{-1}).[160] In a related study[161] of a wider range of substituted arene complexes, the rate of carbonyl exchange was shown to depend on the extent of methyl substitution of the arene ring, being more facile in complexes with less symmetric rings.

Rotations of expanded η^5-cyclodienylium rings such as cyclohexadienyl (η^5-C_6H_7) and cycloheptadienyl (η^5-C_7H_9) in the solid state have very rarely been reported. However, there has been a $^{1}H/^{13}C$ variable-temperature study on $[(C_6H_7)Fe(CO)_3]BF_4$ and $[(C_7H_9)Fe(CO)_3]BF_4$. Both complexes exhibit a phase transition above which there is rapid reorientation of the rings and fast exchange of the carbonyl groups.[162] The C_6H_7 rotation barrier was estimated from ^{1}H T_1 measurements to be 17.5 kJ mol^{-1}. This work was augmented by ^{57}Fe Mössbauer studies, differential scanning calorimetry and x-ray crystallography.

A ^{13}C CP-MAS and static quadrupole echo ^{2}H study of $[W(\eta^5\text{-}Cp^*Me_4)][PF_6]$ provided quantitative data for the hopping of the axial methyl of the WMe4 moiety between its three hydrogen sites.[163] The barrier of 26.8 ± 1.7 kJ mol^{-1} is unusually large for sterically hindered CH_3 group motions. The hopping rate of the equatorial methyl groups was determined by ^{2}H T_1 inversion recovery measurements to be 10.9 ± 0.4 kJ mol^{-1}.

The propeller-like reorientations of Me_3Sn groups in a variety of trimethyltin compounds have been studied by ^{13}C and ^{119}Sn CP-MAS spectra.[164–166] In $[Me_3Sn\{\mu\text{-}MeSO_2)_2N\}MeSn(\mu\text{-}OH)]$, $2\pi/3$ propeller-like jumps occur at the two nonequivalent Me_3Sn sites with different energy barriers ($E_a = 101$ and $125\,kJ\,mol^{-1}$).[164] In solid $[(Me_3Sn)_2CO_3]$, which is polymeric with bidentate $Me_3Sn{-}O{-}CO_2$ units connecting trigonal-bipyramidal Me_3SnO_2 units, the $2\pi/3$ jump processes of the trigonal-bipyramidal and tetrahedral Me_3Sn sites were again very different ($E_a = 22.1 \pm 2.4$ and $E_a \approx 50\,kJ\,mol^{-1}$, respectively).[165] A comparative study of the isostructural pair of compounds $[Me_3Sn(O_2CMe)]$ and $[Me_3Pb(O_2CMe)]$ led to very similar activation energies for the Me_3M jump process ($E_a = 68.5 \pm 6.1$ and $62.1 \pm 6.9\,kJ\,mol^{-1}$, respectively).[166] This work also included some ^{13}C 2D-EXSY studies.

There have been a number of reports of solid-state dynamics involving R_3Si groups.[167–169] Tetrakis(trimethylsilyl)methane, $C(SiMe_3)_4$, exists in an anisotropic phase in which, according to ^{13}C and ^{29}Si NMR spectra, one $SiMe_3$ group becomes distinguishable from the other three and the molecules undergo two different types of dynamic process. One involves exchange between the unique $SiMe_3$ group and an $SiMe_3$ group within the equivalent set, and the other involves hindered rotation of each $SiMe_3$ group about the relevant C(central)—Si bond. Energy barriers for these processes are reported.[167] Detailed ^{13}C and ^{29}Si CP-MAS studies have been conducted on the compounds Si_2R_6(R = Bu^t, $SiMe_3$). It was found that the ^{13}C spectral lineshapes could be theoretically simulated only by assuming unequal rates of Bu^t reorientation, i.e. a model where two Bu^t groups are reorienting at a slower rate than the third Bu^t in the $SiBu^t_3$ moiety. The two best models of assignment and unequal rates of Bu^t reorientation are shown (Fig. 8).[168] The same research group has examined the molecular dynamics of solid $(Me_3Si)_3C{-}C{\equiv}C{-}C(SiMe_3)_3$.[169] One- and two-dimensional ^{13}C and ^{29}Si studies showed there to be two different reorientational modes in the temperature range 150–240 K, reorientation about the $C{-}C{\equiv}C{-}C$ axis and internal reorientation of the Me_3Si groups.

3. TWO-DIMENSIONAL METHODS

3.1. Developments in the 2D-EXSY method

The 2D-EXSY method was described in some detail in the previous review of this series[1] and in one of the chapters of the *Encyclopedia of Nuclear Magnetic Resonance*.[170] It has now become well established as the NMR method of preference for most multi-site exchange processes, or for processes with exceptionally high energy barriers. In the past few years, certain refinements and extensions of the method have been reported. For example, Mao[171] has

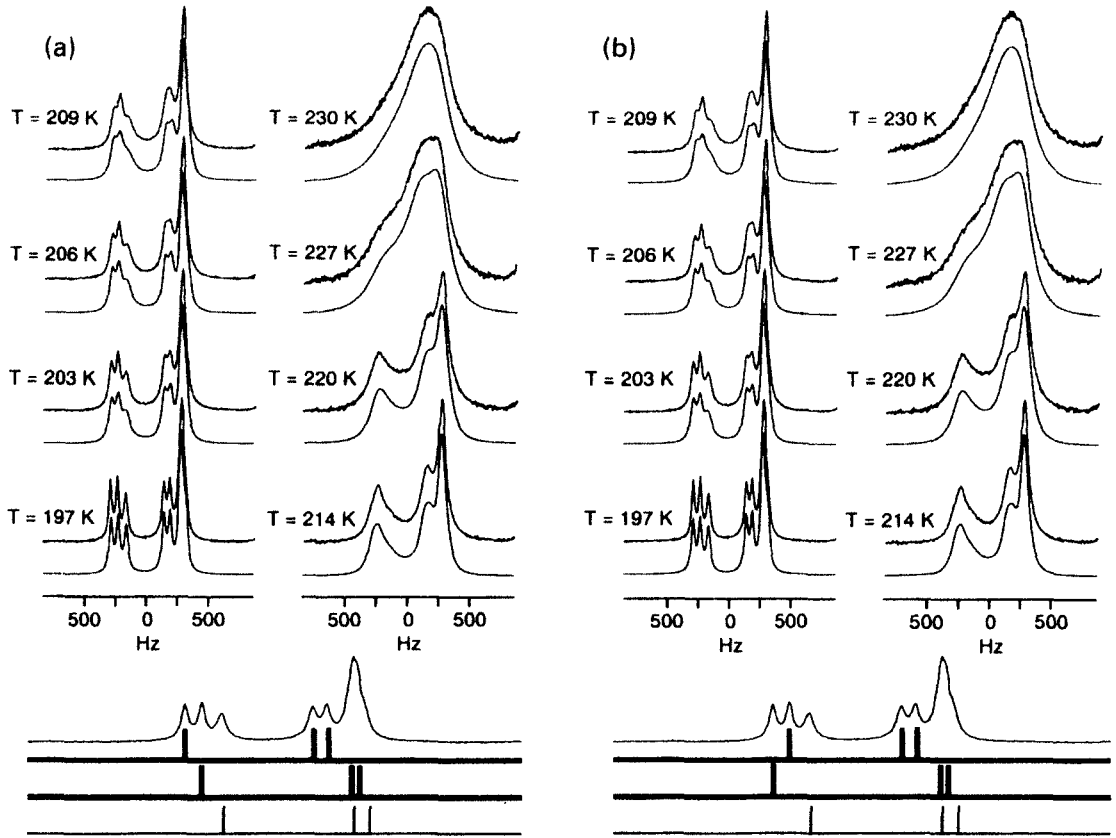

Fig. 8. The two best models of assignment and unequal exchange rates for internal Bu^t reorientation in Si_2Bu^t2. Assignments are indicated at the bottom by bar codes and narrow widths of the bars indicate faster exchange (twice as fast as the other two Bu^t groups) for the respective Bu^t group. Only the methyl signals are shown. (Reproduced with permission from *Organometallics*, 1997, **16**, 2971.)

examined the mathematical properties of the amplitude matrix **A** where $\mathbf{A} = \exp(\mathbf{L}t_m)$, **L** being the kinetic matrix, and t_m the mixing time. It has been shown that the eigenvalues of **A** are always real, positive and never exceed unity. This allows the use of methods for directly diagonalizing **A**, expanding ln **A**, and thus evaluating first-order rate constants. Two-spin and three-spin systems are discussed in this paper.

Quantitative accuracy of 2D-EXSY experiments is very dependent on choosing optimal values of t_m for exchanging species. A procedure has been proposed for achieving this, and it has been tested on a 4-site exchange system.[172] The method involves plotting the cross-peak intensity as a function of mixing time, and drawing a tangent to the curve at the origin (0, 0). The optimal value of t_m is chosen such that the relative difference between the tangent and the curve is less than or equal to a prescribed value, d, typically of the order 0.03 (3%). In the 2D 'accordion' experiment the mixing time t_m is incremented synchronously with the evolution time t_1 according to $t_m = \kappa t_1$. This method has now been generalized for multi-site exchange.[173] It requires iterative computer lineshape analysis of cross-sections taken along the ω_1 axis of the 2D accordion spectrum. In matrix notation this is written as

$$\mathbf{I}(\omega_1) = \mathbf{H} \cdot \mathbf{X} \cdot \mathbf{N}(\omega_1) \cdot \mathbf{P} \tag{10}$$

where $\mathbf{I}(\omega_1)$ is the column vector composed of intensities of n cross-sections corresponding to a given ω_1 value. **H** is a diagonal matrix reflecting the dependence of intensities on ω_2 with elements h_{kk} calculated for Lorentzian lineshapes in the ω_2 domain, where

$$h_{kk} = \frac{R_{2k}^*}{R_{2k}^{*2} + (\omega_{2k} - \omega_k)^2} \tag{11}$$

and where ω_{2k} is the frequency in the ω_2 domain at which the kth cross-section is taken, and **P** is the column vector of relative populations p_j. The method was tested on a 3-site exchange problem, and the authors conclude that the rate constants calculated by this method are considerably greater than those based on conventional 2D-EXSY. Further consideration of the accuracy of data resulting from 2D-EXSY(NOESY) experiments has been given by Macura,[174] who has presented a full matrix analysis of error propagation. He derives an explicit expression for the error propagator that is a function of eigenvectors and eigenvalues of the dynamic matrix **L** and experimental signal volume errors. Every magnetization exchange rate constant has its own optimal mixing time at which its error is minimal. The broader the magnitude range of rate constants the more important is the error analysis. It is particularly important for systems with both cross-relaxation and chemical exchange. In 2D-EXSY spectra the experimenter has the choice of measuring 2D signal intensities by either row or volume integration, and if there is some overlapping of signals

the choice is difficult. Gesmar and Led[175] have proposed a least-squares estimation of 2D signal intensities from two 1D intensities based on a single row and column integration. The result is independent of artefacts associated with Fourier transformation, and is unaffected by phase distortions and poor base-plane definition. Optimal results can be obtained even when signal overlap is substantial.

There have been a number of important developments in magnetization exchange network editing, i.e. designing experiments to measure selected chemical exchange rates from the full set of magnetization transfers. Zolnai *et al.*[176] have presented the mathematical principles behind magnetization exchange network editing (MENE) starting from equilibrium or nonequilibrium conditions. The latter case leads to much greater errors in the derived rate constants. The basic principles of network editing concern the mixing period of the 2D experiments, during which the magnetization can be perturbed by continuous-wave irradiation, by composite pulse sequence decoupling or by inverting pulses. MENE is achieved by setting to zero the time-average of the magnetization that is to be edited as seen from the reference frame of the rest of the system. The authors' conclusions, based on full error-propagation analysis, are that exchange rate constants derived from MENE experiments are more accurate than those from unedited exchange experiments. Also, complete decomposition of the exchange network can be achieved only with short inversion intervals. The theory was illustrated by the spectral analysis of a small protein labelled uniformly with ^{15}N and ^{13}C.

Boulat and Rance[177] have proposed an adaptation of the synchronous nutation experiment to monitor chemical exchange. The essence of the approach is to force the exchanging spins to nutate synchronously after having excited one of them along a transverse axis. As the double RF radiation proceeds, a transfer of magnetization due to the underlying exchange process occurs between the excited spin and its exchange partner, which is reflected in the intensity of the resonance of the latter spin at the end of the experiment. The exchange process must be slow on the NMR chemical shift time scale and was tested on the slow rotational isomerization of bovine pancreatic trypsin inhibitor protein. The method has also been demonstrated on the 3-site exchange of keto–enol tautomerism of ethyl acetoacetate, and on the 2-site exchange of OH protons between 2-hydroxyacetophenone and salicylaldehyde in a 1:1 molar mixture.[178]

An essentially equivalent experiment has been proposed by Bodenhausen *et al.*[179] It has been named QUIET- NOESY since it is based on the suppression of spin diffusion by quenching undesirable indirect external trouble in nuclear Overhauser effect spectroscopy! It has been described by reference to a chemical system in which source nuclei in site A are converted to a target site X. However, magnetization transfer for direct $A \rightarrow X$ conversion might be contaminated by that due to 2-step processes such as $A \rightarrow K \rightarrow X$. The QUIET-NOESY experiment relies on removing effects of indirect $A \rightarrow K \rightarrow X$

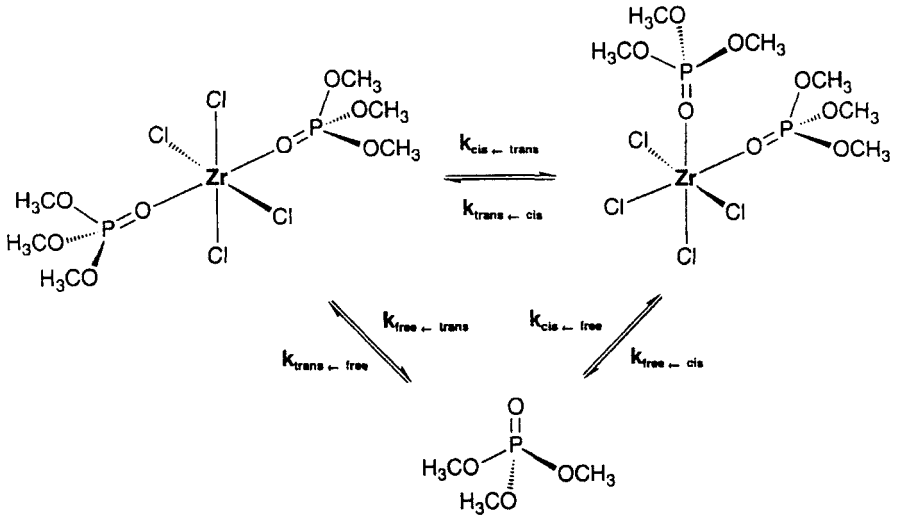

Scheme 13

transfers by selective inversion of longitudinal magnetization in the middle of the mixing time, t_m. The system chosen to illustrate this exchange problem was a mixture of *cis*- and *trans*-$ZrCl_4L_2$ complexes with excess free ligand L (L = $(CH_3O)_3PO$) (Scheme 13). The $^{31}P\{^1H\}$ spectrum consists of three singlets due to ^{31}P nuclei of the *trans*, *cis* and free ligands. The intensities of the EXSY cross-peaks may be measured in a selective 1D manner. The result for conventional EXSY and QUIET-EXSY experiments are shown (Fig. 9). The A (*trans*) → K (free) transfer changes sign during the second half of the mixing period so that net transfer is very small. Thus the time dependences of the signals reflect essentially only A (*trans*) → X (*cis*) interconversion, the exchange with free ligand (K) being effectively 'decoupled' by selective inversion. By swapping the roles of the sites K and X using selective inversion of the *cis* signal, the exchange between *trans* and free sites should be obtained since the *cis* site is now effectively decoupled. The traces (Fig. 9) do show some slight *trans* → *cis* conversion because of second-order effects. These experiments enabled the rate constants k (free → *cis*) and k (*cis* → *trans*) to be measured. Values were 0.018 s^{-1} and 3.32 s^{-1}, respectively, and were accurately determined despite the almost two-hundredfold difference in their magnitudes.

Although the 2D-EXSY experiment will detect slow exchange between species with different resonance frequencies, a new experiment has been devised to detect exchange between species with different transverse relaxation times. The experiment has been given the acronym ARTDECO (altered relaxation times detect exchange correlation) and is based on 2D-inverse Laplace transform (ILT) NMR.[180] The pulse sequences used are given in

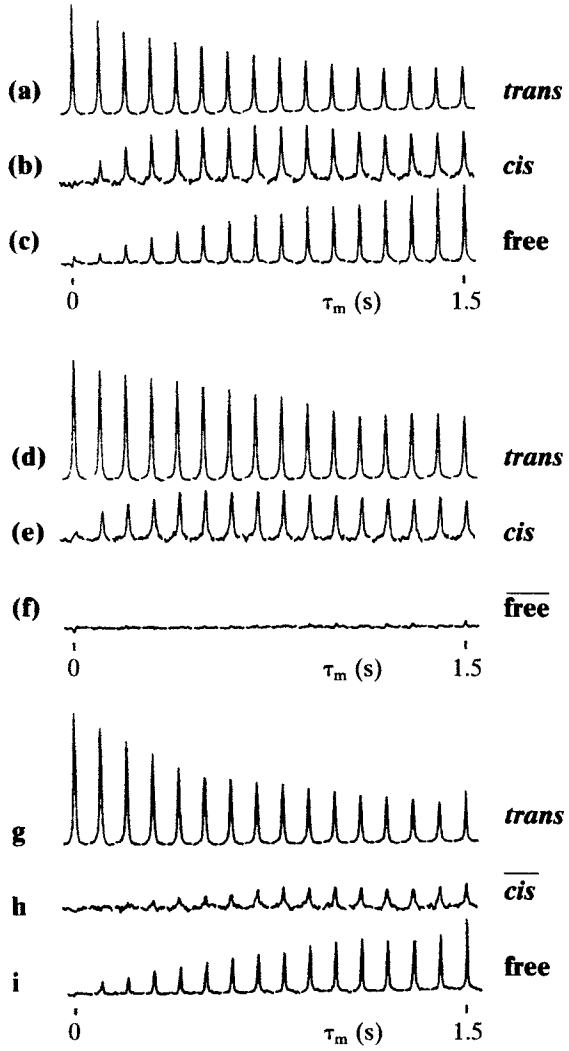

Fig. 9. Time dependence of the ^{31}P resonances of the mixture in Scheme 13: (a)–(c) difference spectra obtained by initially inverting the *trans* resonance (site A); (d)–(f) QUIET-EXSY experiments obtained by applying an additional selective inversion pulse to the free resonance (site K, inversion indicated by overbar) in the middle of the t_m interval; (g)–(i) analogous QUIET-EXSY experiments, but swapping the roles of sites K and X by using a selective inversion of the *cis* resonance (now site K) in the middle of the t_m interval. (Reproduced with permission from *Chem. Eur. J.*, 1996, **2**, 45–49.)

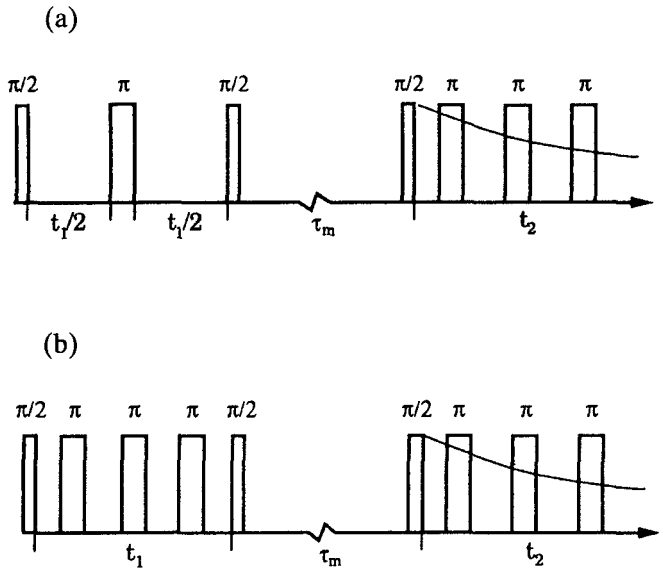

Fig. 10. (a) Simple ARTDECO sequence, which uses a single refocusing pulse during the evolution period (t_1). The latter is split symmetrically about the π pulse and incremented from slice to slice in the 2D data matrix. (b) Symmetrical ARTDECO sequence, which uses similar Carr–Purcell echo trains in the t_1 and t_2 periods to avoid shifting of the diagonal peaks due to asymmetrical scaling of the exchange contribution to T_2 by the echo train during t_2. The evolution period is incremented by a $t_1/2-\pi-t_1/2$ interval. (Reproduced with permission from *J. Am. Chem. Soc.*, 1993, **115**, 7761.)

Fig. 10. Signals that have evolved with a transverse relaxation rate $R_{2I} = (T_{2I})^{-1}$ during the t_1 period and have not undergone exchange will give rise to a detected signal

$$I(t_1,t_2) = I_0 \exp(-R_{2I}t_1) \exp(-R_{2I}t_2) \tag{12}$$

which, upon inverse Laplace transformation, gives a peak at (R_{2I}, R_{2I}) on the diagonal of the 2D relaxation spectrum. Species that have undergone exchange such that the relaxation rate during t_2 is R_{2S} ($\neq R_{2I}$) will give an off-diagonal peak at (R_{2I}, R_{2S}). Thus, the overall spectrum has the same appearance of diagonal and cross-peaks as in 2D-EXSY. It is suggested that the method may be particularly useful for measurement of exchange and diffusion of water *in vivo* and for detecting slow exchange in glassy polymers. In this paper it was tested on concentrated solutions of urea in water.

There are many chemical systems, particularly biomolecular systems, in which both chemical exchange and cross-relaxation effects occur simultaneously. Although one effect may dominate over the other, it is still important for quantitative studies to know how the cross-peak intensities are

affected by both processes. Krishna[181] has examined the effect of slow conformational exchange on a two-spin-$\frac{1}{2}$ system. Intensity variations of the different signals in the spectrum (viz. diagonal, exchange, direct NOESY and exchange-mediated NOESY signals) have been computed as a function of the mixing time. The NOESY spectrum as a function of mixing time shows significant dependence on the absolute magnitudes of the exchange rates and on how these rates compare with dipolar cross-relaxation rates. The theoretical formalism used is readily applicable to the case of conformational exchange that is fast on the chemical shift time scale. Another study[182] showed that when chemical exchange rates were 6–7 times faster than the cross-relaxation rate, the NOE cross-peaks became unobservedly weak. This conclusion was based on a study of a platinum–selenium ligand complex undergoing Se pyramidal inversion.

The most widely employed method for separating chemical exchange and cross-relaxation effects is phase-sensitive NOESY/EXSY. This is based on the fact that chemical exchange-mediated cross-peaks have the same phase as diagonal signals, while cross-relaxation cross-peaks, for small molecules that fulfil the extreme-narrowing condition ($\omega\tau_c \ll 1.12$), are of opposite phase to diagonals. For larger molecules, e.g. many bio-oligomers, proteins and even large metal coordination compounds, cross-relaxation cross-peaks may be of the same sign as the diagonal signals and thus their intensities may be derived from both chemical exchange and NOE effects. In such cases the ROESY experiment is preferred since now cross-relaxation cross-peaks will be of opposite sign to chemical exchange cross-peaks irrespective of molecular size and correlation time.

The technique of off-resonance ROESY has been proposed for the study of dynamic processes.[183] Its theory has been developed and its advantages over more standard methods have been described. These include the suppression of HOHAHA transfers and the possibilities of studying dipolar relaxation or chemical exchange as separate phenomena. Conventional ROESY and EXSY methods have been compared by Shukla,[184] for a 2-site exchange system. Calculated build-up curves suggest a contribution of ROE on chemical exchange magnetization transfer. When the exchange rate approximates to the transverse cross-relaxation rate, and reorientation in solution is slower than that defined by the extreme narrowing (CAMELSPIN) limit ($\omega\tau_c \approx 1.12$), the theory suggests that observation of exchange and NOE cross-peaks may be compromised. This paper also examined the technique of off-resonance ROESY and concluded that under certain circumstances spin-locking may compromise either exchange rate or internuclear distance measurements.

Diffusion-ordered 2D NMR (DOSY) can be constructed from pulsed field gradient data sets. The effects of chemical exchange in DOSY have now been investigated. The main conclusion drawn was that exchange rates may be measured under certain circumstances but high spectral signal/noise ratios and sophisticated data-inversion techniques are required.[185] The experimental and

theoretical application of 2D-EXSY to rotational diffusion of colloidal particles has been presented.[186] The technique relies on the orientation dependence of NMR frequencies in the solid state. This study relied on the ^{13}C CSA parameter and was applied to a colloidal suspension of spherical poly(methyl methacrylate) particles containing 20% ^{13}C enrichment at the carbonyl site. Two different correlation times were computed, suggesting two different particle sizes, this being confirmed by scanning electron microscopy.

The technique of variable-angle correlation spectroscopy (VACSY) has been shown to provide kinetic and geometric information on molecular dynamics over a wide range of exchange rates.[187] The 2D technique separates the broad anisotropic chemical shift lineshapes of nuclei in a sample according to the isotropic shift of each site. It can therefore be used to characterize molecular reorientations by monitoring the changes these processes introduce in the resolved powder patterns as a function of temperature. This paper used the ^{13}C CSA parameter as the basis of the study and applied the method to the 2-site exchange in dimethyl sulfone and multi-site exchange in tyrosine ethyl ester. A 3D version of this technique (3D-VACSY) both with[188] and without[189] rotor hopping has been introduced and applied to the analysis of motions in isotactic polypropylene. The rotor hopping technique is experimentally demanding and it was shown not to be an essential requirement for obtaining the anisotropic–isotropic shift correlations. A series of 2D-EXSY spectra were recorded with the sample spinning at different rotation axis angles. Using the scaling of the anisotropic frequency at different angles, it is possible to map the time-domain data onto a 3D matrix so that Fourier transformation yields the required correlations.

Finally in this section on developments in multi-dimensional techniques in solid-state NMR, mention should be made of an extensive review of 2D- and 3D-^{2}H exchange techniques.[190] A 5-pulse sequence, with special phase cycling, is proposed for 2D-^{2}H spectra, and 6- and 8-pulse sequences, with phase cycling, are described for 3D-^{2}H spectra. Dimethyl sulfone was again chosen as the test compound.

3.2. Chemical applications of 2D-EXSY

3.2.1. ^{1}H studies

(i) Metallotropic shifts. Metallotropic shifts are very widespread in transition metal complexes and there have been numerous studies of such shifts involving N-heteroaromatic ligands. Ligands such as benzo[*c*]cinnoline (bzc) and pyridazine (pydz) possess adjacent N-heteroatoms that can form transition metal $M(CO)_5$ complexes that are fluxional as a result of the metal coordination switching between the two N donors. Because of the limited thermal stability of many of these complexes, 2D-EXSY experiments were better suited

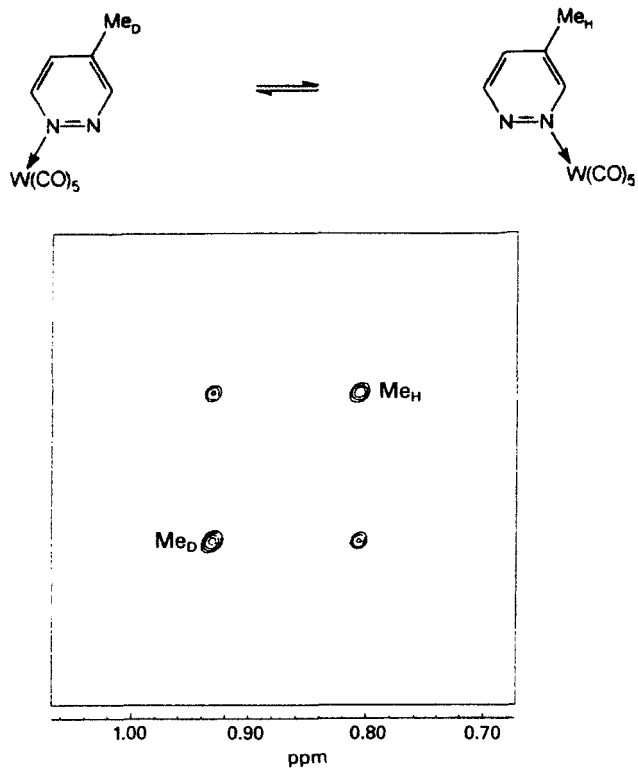

Fig. 11. ^{1}H 2D-EXSY spectrum of [W(CO)$_5$(4-Mepydz)] in C_6D_6 at 30°C (methyl region only). Mixing time was 1.5 s. (Reproduced with permission from *J. Organomet. Chem.*, 1994, **464**, 163–170.)

than 1D bandshape analysis experiments for measuring fluxional dynamics. One series of complexes studied was [W(CO)$_5$L] (L = bzc, pydz, 3-Mepydz or 4-Mepydz).[191] The 1,2-W—N fluxion was followed by 2D-EXSY spectra. The methyl ^{1}H EXSY spectrum of [W(CO)$_5$(4-Mepydz)] is particularly simple (Fig. 11), as it represents a 2-site exchange between the two different coordination complexes (relative populations 55/45%). Pyridazine ligands (L) form stable bis(monodentate) complexes with Pt^{IV} and Re^I, viz. *fac*-[PtXMe$_3$L$_2$] and *fac*-[ReX(CO)$_3$L$_2$] where X = halogen in both series. When L = 4-Mepydz[192] or 3-Mepydz,[193] 4 linkage isomers of the complexes are possible (Scheme 14), with the (1,2) and (2,1) isomers being an enantiomeric pair. ^{1}H 2D-EXSY spectra of the methyl signals again provided rate data on the 1,2-metallotropic shifts. ^{195}Pt 2D-EXSY spectra were also obtained for the complexes [PtXMe$_3$(4-Mepydz)$_2$]. Energy barriers ($\Delta G^{\ddagger}$, 298 K) were in the range 69–78 kJ mol^{-1} for the Pt^{IV} complexes and 84–90 kJ mol^{-1} for the Re^I complexes. Similar studies were also made on the ionic complexes *fac*-[PtMe$_3$(L-L)(pydz)][BF$_4$][194] and *fac*-[Re(CO)$_3$(L-L)(pydz)][BF$_4$],[195] and the

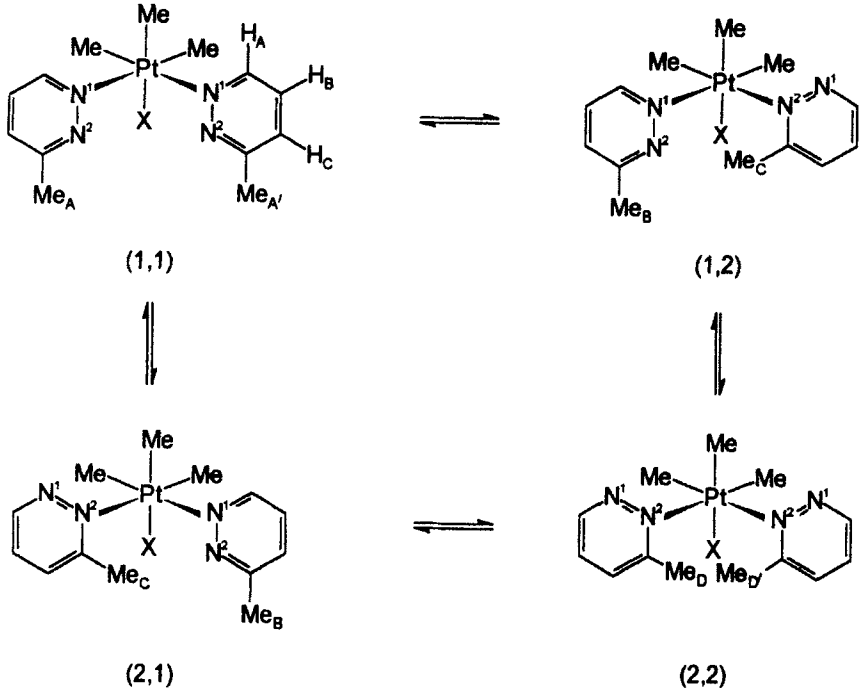

Scheme 14

dependence of the fluxional activation energies on the nature of the chelate ligand (L-L) were reported.

Metal complexes with ligands based on 2,6-disubstituted pyridines [**10**] have been widely investigated. $ReX(CO)_3$ complexes of [**10**], (L = pyridyl, L′ = pyrazol-1-yl) consist of pairs of chemically distinct complexes involving bipyridyl and pyridyl/pyrazol-1-yl N-coordination. The bipyridyl-coordinated complexes predominate (>80%) in solution. These exchange with the pyridyl/pyrazol-1-yl coordination species by a double 1,4-metallotropic shift that was followed by ^1H 1D bandshape analysis and 2D-EXSY spectra.[196] The mechanism of this 1,4-N,N-metallotropic shift has been the subject of some controversy. However, it would appear that the NMR evidence strongly supports an associative mechanism. This conclusion was based on some $^1H/^{19}F$ studies of Pd^{II} and Pt^{II} complexes of an unsymmetrical substituted

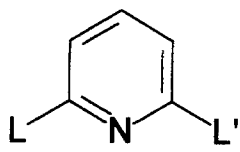

[10]

terpyridine ligand (viz. 4-chlorophenyl-[**10**] where L = 4-methylpyridyl, L′ = pyridyl).[197,198] ^{19}F 2D-EXSY spectra of the complexes $[M(C_6F_5)_2L]$ ($M = Pd^{II}$, Pt^{II}; L = the above unsymmetrical terpyridine) showed there to be pairwise exchange between the fluorines of the C_6F_5 groups, namely A⇌C and B⇌D only (Scheme 15). Any type of dissociative mechanism would lead to exchange of all four C_6F_5 rings. There has been a series of detailed DNMR studies of transition metal complexes of 2,6-bis[(1-phenylimino)ethyl]pyridine (BIP). This ligand is represented by structure [**10**] with L = L′ = −C(Me)=N−Ph. It forms square-planar complexes of type $[M(C_6F_5)_2(BIP)]$ ($M = Pd^{II}$, Pt^{II}),[199] and octahedral complexes of types $[ReX(CO)_3(BIP)]$ (X = Cl, Br or I)[200] and $[PtXMe_3(BIP)]$ (X = Cl, Br or I).[201] These complexes exhibit a variety of internal dynamic processes in solution, namely, 1,4-metallotropic shifts, *E*, *Z*-isomerizations of the pendant imine bond and restricted C−C bond rotations of the pendant portion of the BIP ligand. The case of the Re(I) complexes is illustrated in Scheme 16, where the seven nonzero rate constants refer to 1,4-metallotropic shifts (k_{34}), imine isomerizations (k_{13}, k_{23}, k_{45} and k_{46}) and restricted C−C bond rotations (k_{12} and k_{56}). The system represents a 6-site exchange problem that was solved by the D2DNMR program[1] on the methyl region of the spectrum. The different internal motions were shown to occur at comparable rates, but were able to be individually measured over a range of temperatures by appropriate adjustment of mixing times. Energies were in the range 79–88 kJ mol^{-1}.

The ligand [**11**], where the central ring is either 1,3,5-triazine (Z = N) or pyrimidine (Z = CH), can form a wide range of transition metal complexes. When Z = N and L = pyrazol-1-yl or substituted pyrazol-1-yls, both 1:1 and 2:1 metal:ligand species can be isolated, but only the 1:1 species are fluxional.[202] These undergo 1,4-metallotropic shifts between chemically equivalent structures. When Z = CH and L = substituted pyrazol-1-yls, the fluxional shifts cause exchange between chemically distinct complexes with radically different solution populations,[203] the major solution species involving coordination with the 2-pyrazolyl ring nitrogen rather than the 4- or 6-pyrazolyl ring nitrogens. 1:1 Metal:ligand complexes of ligand [**11**] [Z = N, L = pyridyl (TPT), or

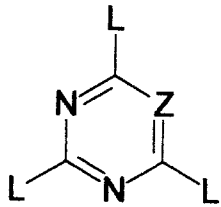

Z = N or CH

[**11**]

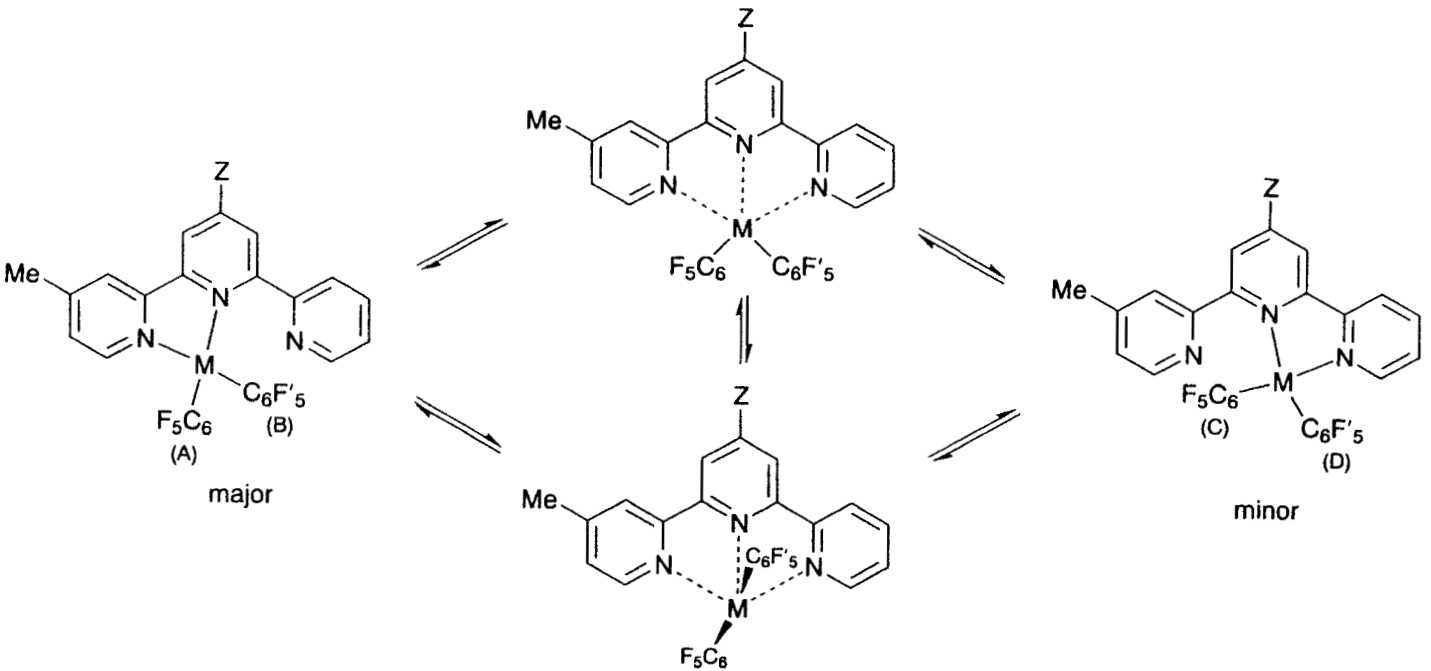
Z
Me
N
N
N
M
C6F'5
F5C6
(A)
(B)
major
Z
Me
N
N
N
M
F5C6
C6F'5
Z
Me
N
N
C6F'5
N
M
F5C6
Z
Me
N
N
N
M
F5C6
(C)
C6F'5
(D)
minor

Scheme 15

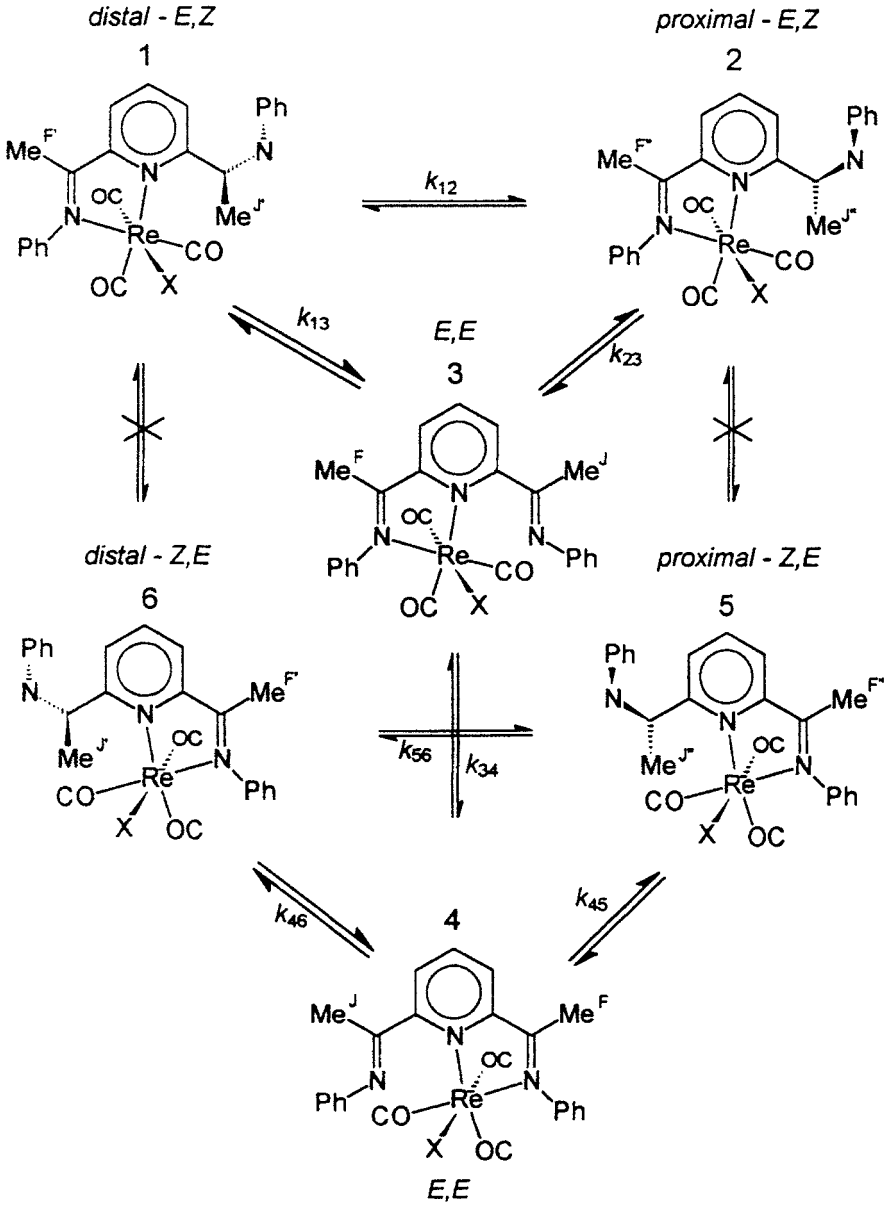

Scheme 16

Z = CH, L = pyridyl (TPP)] undergo some remarkable fluxionality, which was revealed by variable-temperature ^{1}H 2D-EXSY spectra.[204,205] The ^{1}H 2D-EXSY spectrum of [Pt($C_6F_4CF_3$)$_2$(TPT)] at 393 K (Fig. 12) clearly shows cross-peaks associated with the exchanges ABCD ⇌ EFGH arising from the expected 1,4-metallotropic shift, the ^{1}H labelling being in accordance with

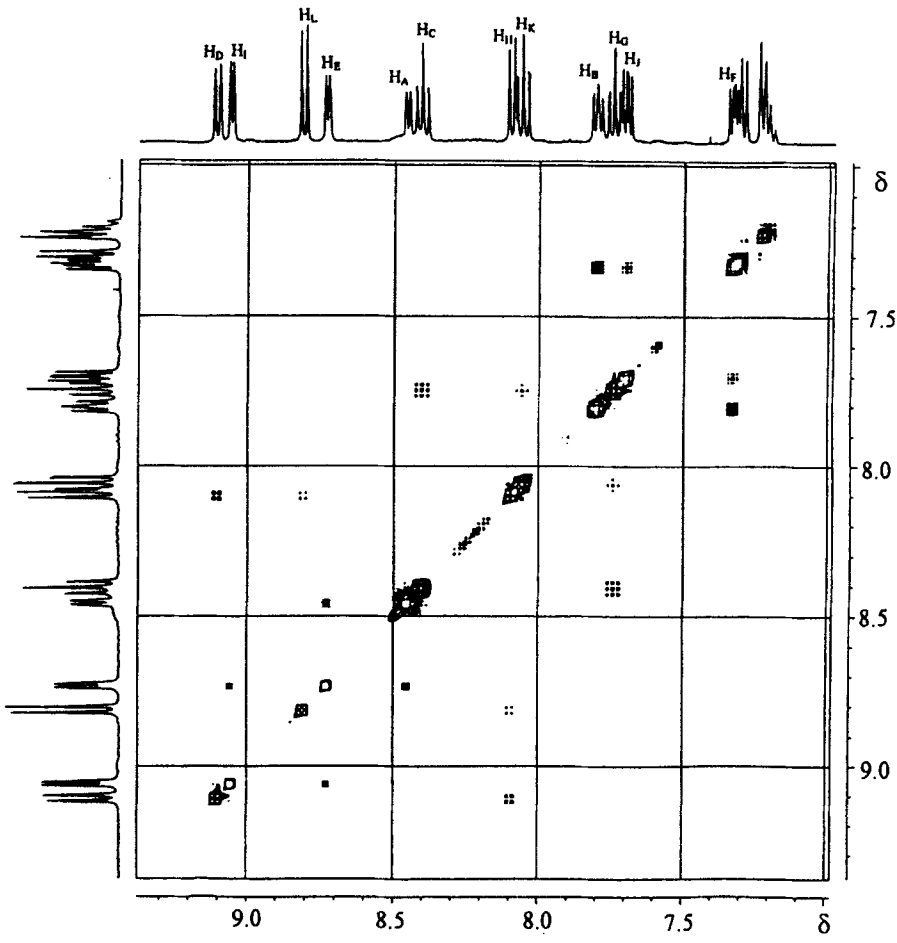

Fig. 12. ^{1}H 2D-EXSY spectrum of $[Pt(C_6F_4CF_3)_2(TPT)]$ in $CDCl_2{\cdot}CDCl_2$ at 393 K with mixing time 0.8 s. The cross-peaks result from 1,4-metallotropic shifts H_A–$H_D \rightleftharpoons H_E$–$H_H$ and rotational hurdlings H_E–$H_H \rightleftharpoons H_I$–$H_L$. The unlabelled signals at δ 7.2–7.3 are due to an impurity. (Reproduced with permission from *Inorg. Chim. Acta*, 1997, **264**, 257–268.)

Scheme 17. However, a second set of cross-peaks associated with the exchanges EFGH $\rightleftharpoons$ IJKL is also clearly visible. This set involves exchanges between corresponding hydrogens of the two uncoordinated pyridyl rings and is clearly due to a second mode of fluxion. It can be rationalized in terms of movement of the metal moiety from one side of the pyridyl-triazine C—C bond of the chelate ring to the other. This effective 'hurdling' of this C—C bond can occur by cleavage of the triazine N–metal bond followed by 180° rotation of the metal-bound pyridyl about the C—C bond followed by recombination of the

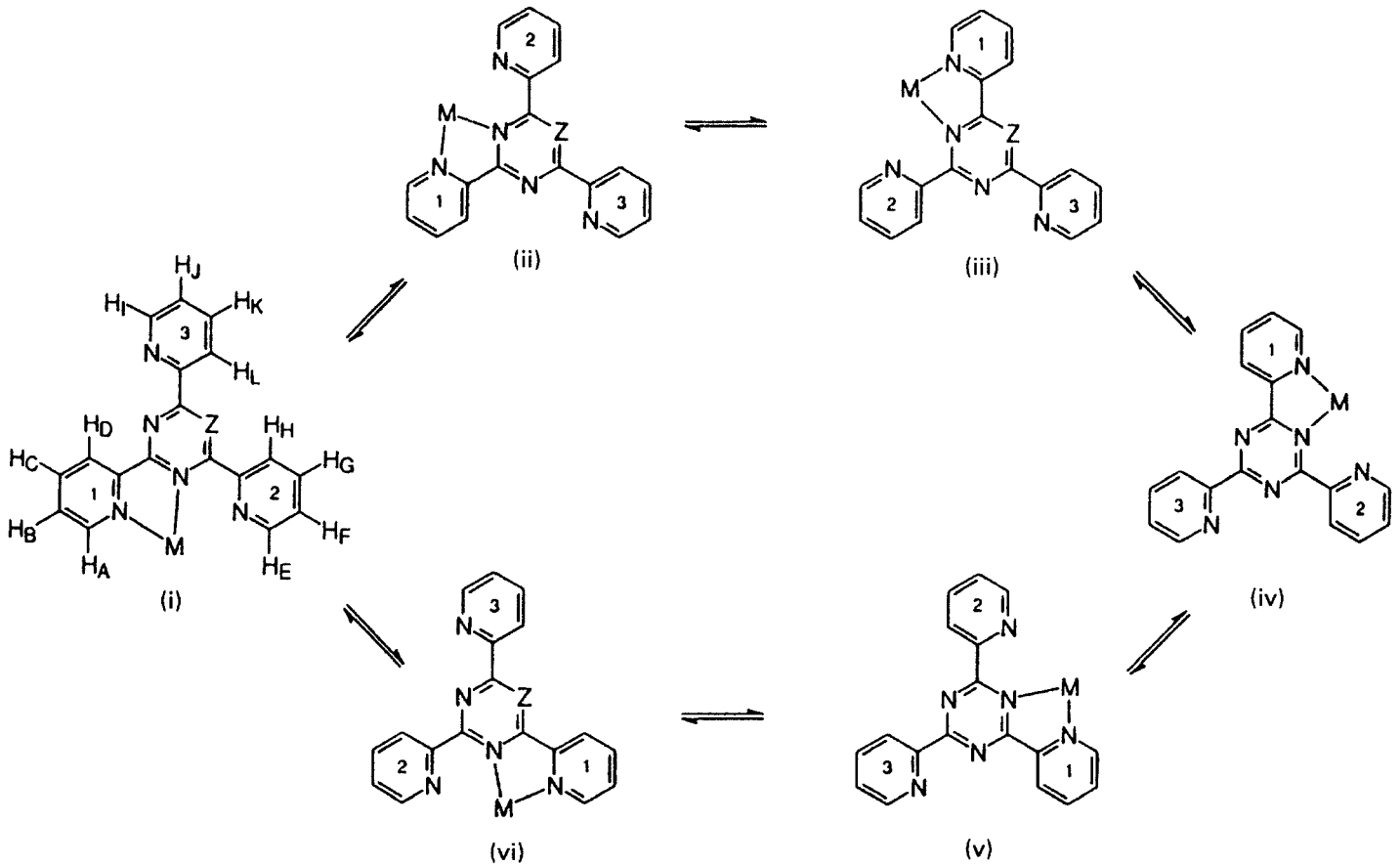

Scheme 17

metal to the new triazine nitrogen. A combination of the 1,4-metallotropic shift and metal hurdling processes enables the metal moiety to move completely round the outside of the triazine ring, passing through structures (i)–(vi) (Scheme 17). Activation energies ($\Delta G^{\ddagger}$ 298 K) of both processes were deduced from the 2D-EXSY data.

(ii) Isomerizations, internal rotations and conformational changes. This section includes a wide variety of such processes.

A novel fluxion involving coordinated solvent ligands has been reported. The complex *fac*-[$PtMe_3L(H_2O)$] (L = 1-phenylpropane-1,2-dione 2-oximate) dissolves in polar solvents to form species of general formula *fac*-[$PtMe_3L(solv)$] (solv = Me_2SO, MeOH, Me_2CO), which undergo a 'windscreen wiper' fluxion that exchanges two of the three Pt-methyl environments. ^1H 2D-EXSY spectra were recorded to measure rates of this fluxion for different bound solvents.[206]

There have been reports of two 2D-EXSY studies of metal complexes of macrocyclic ligands. One study[207] concerned the solution dynamics of lanthanide complexes of the 18-membered macrocyclic polyaminocarboxylate DTPA-dien. The large paramagnetic shifts of these Ln^{III} complexes enabled informative 2D-EXSY spectra to be obtained. The other study[208] related to low-spin Fe^{III} and Co^{III} tetraphenylporphyrinates (TMPs) that exhibited slow rates of axial ligand rotations. The motion represented 4-site exchange with a single magnitude of rate constant at any temperature. The ^1H study was notable for its attention to detail on questions such as the most accurate method for measuring signal intensities by experimental peak volumes, NOE contributions to cross-peak intensities, and optimization of mixing times. The ^1H spectra of the Fe^{III} species exhibited wide ranges of chemical shifts arising from the paramagnetism. Exceptionally wide ranges of ^1H shifts ($\Delta\delta \sim 240$) occur in the 2D-EXSY spectra of YbDOTA (DOTA = the macrocyclic chelate 1,4,7,10-tetraazacyclododecane-*N*,*N'*,*N''*,*N'''*-tetraacetic acid),[209] and of DOTA-like La, Gd, Ho and Yb complexes containing a *p*-nitrophenyl substituent.[210] In the YbDOTA study[209] both inter- and intramolecular exchanges occurred between two isomeric forms of the complex. These were interpreted respectively as due to a reorientation of the acetate substituents and to a complete inversion of the chelate conformation. In the other study[210] the 2D-EXSY spectrum of the DOTA-like Yb complex identified inversion of the ethylenic groups of the macrocycle rather than motion of the acetate arms as occurs in the parent DOTA complex. This study also included relaxometric studies, i.e. NMRD (nuclear magnetic relaxation dispersion) profiles, on the GdDOTA-like complex.

Phase-sensitive ^1H 2D-EXSY experiments have been applied to some new Ti^{IV} complexes with tripodal amido ligands such as $H_3CC(CH_2NR)_3$ where R is Me, Me_3Si or Me_2Bu^tSi.[211] The study was qualitative but it did carefully distinguish between NOE cross-peaks (of opposite phase to the diagonal

peaks) and exchange (EXSY) cross-peaks (of the same phase as the diagonal peaks). In practice a third type of cross-peak may also be identified. This is an exchange-NOE cross-peak, which results from direct NOE interactions followed by magnetization transfer as a result of chemical exchange. Such exchange-NOE cross-peaks may contain important dynamic information. This has been demonstrated[212] in the case of planar N-donor heterocyclic metal-coordinated ligands, where exchange-NOE signals define the extent of ligand rotation about the metal—N bond, the direction of ligand rotation and which halves of the C_2 symmetrical ligands interchange during dynamic processes. The complexes studied were $[Re_2O_3Cl_4L_4]$ (L = 1,5,6-trimethylbenzimidazole or 3,5-lutidine). Each Re atom is part of a nearly linear O=Re—O—Re=O grouping and has a terminal L and a stacked L. The fluxional inversion of the two chiral dimers involves near-180° rotations about the Re—O—Re bonds and near-90° rotations about all four Re—L bonds. The exchange-NOE data of the 3,5-lutidine complex helped to establish the direction of L rotation. This is an interesting study, but it is surprising that the authors did not use phase-sensitive NOESY/EXSY experiments or at least comment on the possible advantages of this type of experiment over the non-phase-sensitive type they adopted.

Phase-sensitive 2D-EXSY was used to study the fluxionality of the carbenium ion complex **[12]**,[213] where the mechanism involved interconversion and rotation steps for which rate constants were calculated. In the mixed metal clusters **[13]**,[214] the ligand 1,1′-bis(diphenylphosphino)ferrocene undergoes dynamic behaviour involving inversion at the phosphorus atoms and twisting of the cyclopentadienyl rings. This behaviour was accurately mapped by ^1H 2D-EXSY spectra of the Cp hydrogens (Fig. 13), and it enabled accurate activation energy data, based on 1D bandshape analysis, to be obtained.

There have been a number of dynamic NMR studies of π-allyl complexes of transition metals, particularly by Pregosin *et al.* who have exploited the power of 2D-EXSY and/or 2D-ROESY experiments for measuring internal

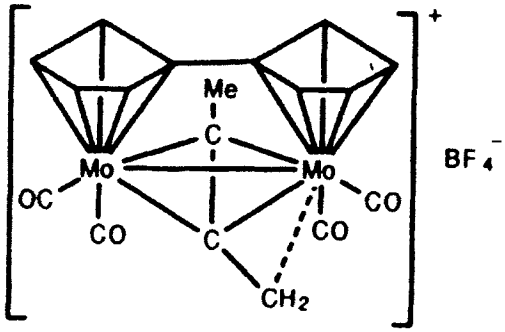

[12]

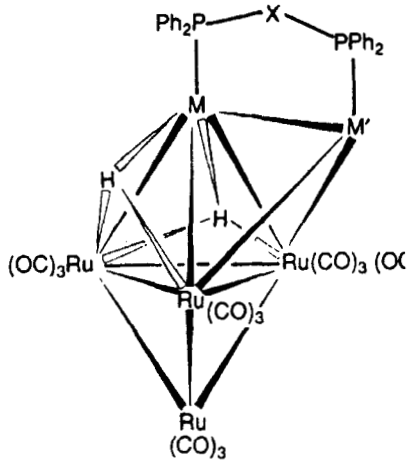

M	M'	X
Cu	Cu	$Fe(\eta^5\text{-}C_5H_4)_2$
Ag	Ag	$Fe(\eta^5\text{-}C_5H_4)_2$
Cu	Au	$Fe(\eta^5\text{-}C_5H_4)_2$
Cu	Au	$(CH_2)_2$

[13]

dynamics such as π-allyl rotations, restricted σ-bond rotations, pyramidal inversions and other isomerization processes. Studies of (π-allyl)palladium (bpm) complexes (bpm = 2,2′-bipyrimidyl) showed that the apparent π-allyl rotation is due to a Pd—N bond cleavage followed by an internal rotation of the two pyrimidyl rings past each other.[215] Studies on chiral allyl ferrocenyldiphosphine complexes of Pd^{II} revealed an exchange process in cationic complexes of type $[Pd(\eta^3\text{-}C_3H_5)L]$ (L = various 1,2-ferrocenyldiphosphines) involving a selective η^3–η^1–η^3 isomerization.[216] A related study[217] examined analogous complexes of chiral ferrocene-based phosphinopyrazole ligands. The ^1H and ^{31}P 2D-EXSY studies identified allyl rotation and chelate-ring conformational processes. Some new Pd^{II} complexes with chiral P,S bidentate ligands have been prepared.[218,219] Some of these[218] exist as pairs of rotational isomers that interconvert by a mechanism that causes selective exchange, i.e. selective η^3–η^1 ring opening. Another chiral complex $[Pd(\eta^3\text{–}Ph_2CCHCHPh)\{(-)\text{-sparteine}\}][PF_6]$ exhibits restricted rotation about the *ipso*-C—allyl—C—bonds as revealed by variable-temperature 1D, 2D-EXSY and NOE measurements.[220] Several Rh^I, Ir^{III} and Pt^{II} complexes of chiral P,S-bidentate ligands have been synthesized and subjected to detailed 2D investigation.[221] Chelate ring reversal and pyramidal S inversion processes were detected. Rates were not quantified but mechanisms were discussed. ^1H 2D-ROESY spectra in addition to ^1H bandshape analyses were obtained on

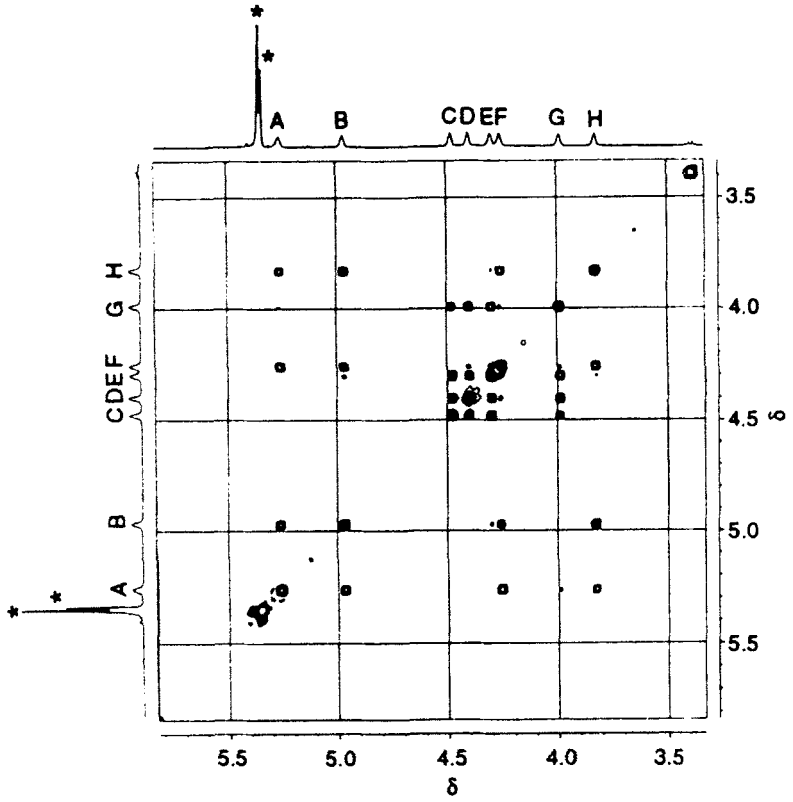

Fig. 13. ^{1}H 2D-EXSY spectrum (Cp hydrogens only) of $[Cu_2Ru_4(\mu_3\text{-}H)_2(\mu\text{-dppf})(CO)_{12}]$ in CD_2Cl_2 at −70°C. Signals marked with an asterisk are due to solvent. (Reproduced with permission from *J. Chem. Soc. Dalton Trans.*, 1996, 643–652.)

some π-allylpalladium(II) complexes with 2-(iminomethyl)pyridine ligands.[222] These undergo isomeric interconversion as in Scheme 18. The phase-sensitive ROESY spectrum shows no exchange cross-peaks between *syn* and *anti* protons of isomers I and II, but does show exchange cross-peaks associated with *syn–syn* and *anti–anti* exchanges. 2D-ROESY experiments were also used to study the dynamics of some chiral palladium(0) complexes with P,S and P,P bidentate ligands that exhibit olefin dissociation or rotation, and hindered rotation about the aryl P—C bonds.[223] Ruthenium(II) complexes have also been synthesized with one of the above P,P bidentate ligands.[224] 2D-EXSY spectra suggest that the double bond of the complex dissociates and exchange occurs. A study of some tungsten π-allyl complexes $[Tp'(CO)_2W(\eta^3\text{-CHRCHRCHR'})]$ {Tp' = hydridotris(3,5-dimethyl-1-pyrazolyl)borate} identified another η^3–η^1–η^3 mechanism in which rotation about the W—C bond in the η^1 form occurs.[225]

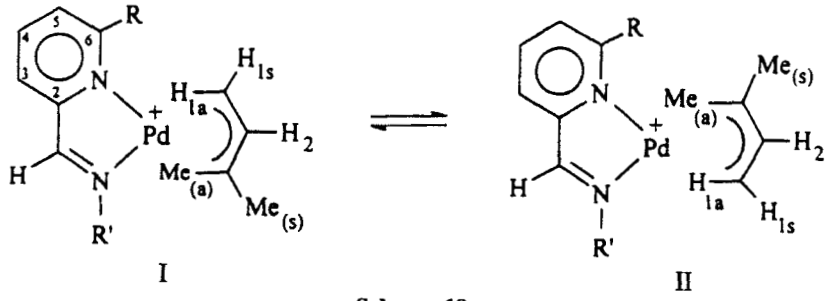

I II

Scheme 18

A detailed one- and two-dimensional ^1H study has been performed on the binuclear niobium complex **[14]**.[226] NOE- and chemical exchange cross-peaks in the EXSY spectra were distinguished by their different phases. The fluxional process was identified as involving interchange of the two methyl groups under the bridging *ansa* system.

The stereodynamics of tris(1-indenyl)methylsilane have been revealed by a detailed ^1H, ^{13}C and ^{29}Si study including ^1H 2D-EXSY spectra.[227] This compound exists in solution as a mixture of *RRR*, *RRS*, *RSS* and *SSS* isomers that may be interconverted by two [1,5]-suprafacial sigmatropic shifts (Scheme

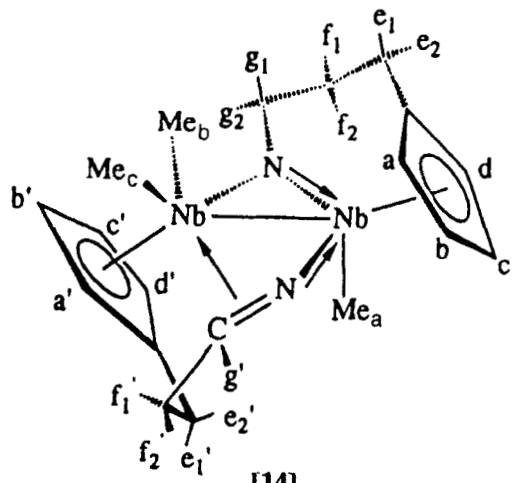

[14]

19). The molecular dynamics of the compound have been deduced by a combination of 1D-selective inversion experiments and 2D-EXSY data. It was found that the exchange pathways between indenyl sites could be conveniently mapped onto a hypercube.

(iii) Intermolecular exchanges. A multinuclear (^1H, ^{19}F and ^{31}P) study has shown that the tris(pentafluorophenyl)borane–phosphine adduct undergoes

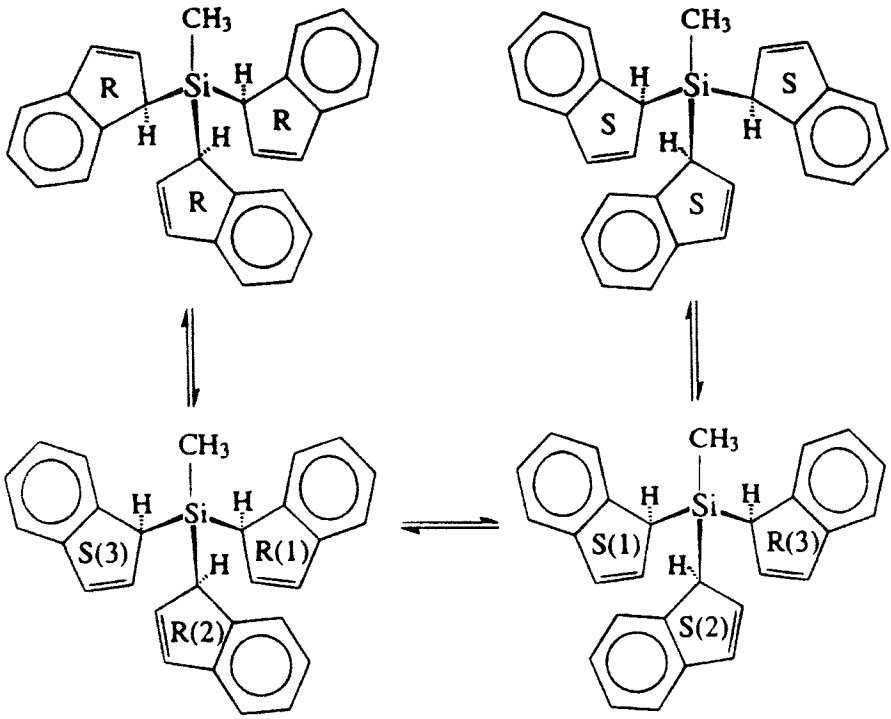

Scheme 19

intermolecular phosphine transfer in toluene solution.[228] Selective ^{31}P inversion experiments provided a rate constant of $3.60 \pm 0.15\ s^{-1}$ for the phosphine exchange at 254 K, and the temperature dependence of this parameter gave a value of $126\ kJ\ mol^{-1}$ for the activation energy of the dissociation step. ^{1}H 2D-NOESY/EXSY spectra were analysed qualitatively. The absence of certain cross-peaks at short mixing times was ascribed to very little ^{31}P spin–lattice relaxation during the mixing time. Quantitative analysis of the 2D-EXSY spectra was not possible because of the size of the spin exchange problem.

Proton exchange between ^{15}N-enriched ammonium ion and ammonia in H_2O/D_2O was investigated by ^{1}H 2D-EXSY.[229] In this system the ammonium ion exists as $^{15}NH_4^+$, $^{15}NH_3D^+$, $^{15}NH_2D_2^+$, $^{15}NHD_3^+$ and $^{15}ND_4^+$, four species of which were distinguishable by $^{1}H\{D\}$ spectra. Exchange was observed between all four H-containing species. The NH region of the spectrum consisted of an 8-line pattern due to $^{15}N-H$ coupling ($J = -73.6$ Hz). Analysis of peak intensities led to an 8×8 kinetic + relaxation matrix and all site-to-site exchange rate constants were evaluated. Averaging 44 of these gave a value of $(1.6 \pm 0.2) \times 10^8\ dm^3\ mol^{-1}\ s^{-1}$ for the second-order rate constant per proton for the NH_3-catalysed exchange. These results also provided an estimate of the H/D primary kinetic isotope effect for direct N-to-N proton transfer.

The use of *para*-hydrogen to enhance proton NMR signals has been known for some years. It has now been shown that *para*-H_2-induced polarization can be used to study ligand exchange processes.[230] The complexes $[IrH_2Cl(CO)(PPh_3)_2]$ and $[IrH_2Cl)PPh_3)_3]$ undergo ligand exchange via a 16-electron complex $[IrH_2Cl(PPh_3)_2]$. The technique is based on the antiphase magnetization of the hydride resonances (with respect to J_{AB}), which is optimized when the hard pulse flip angle is $\pi/4$. EXSY cross-peaks were solely due to magnetization transfer from *para*-H_2-enhanced signals but included both positive chemical exchange and negative NOE contributions.

A novel use of 2D-EXSY was made in the study of the structure and dynamics of the reaction intermediate $[Cp^*Rh(\mu\text{-}OH)(H_2O)]_2^{2+}$ as a function of pH.[231] Reaction rates were measured by spin polarization transfer experiments.

3.2.2. *^{6}Li studies*

Organolithium chemistry has been greatly aided by the suitable spin properties of ^{6}Li nuclei. Two recent studies involving ^{1}H,^{6}Li-HOESY, and ^{6}Li,-^{6}Li-COSY and ^{6}Li,^{6}Li-EXSY illustrate this point. One study[232] concerned the complex between *n*-butyllithium and a dilithiated chiral amine. The complex was shown to contain four lithium atoms in an asymmetric environment. An intra-aggregate exchange occurs but no intermolecular exchange of lithium atoms. The other study[233] concerned a lithium cyclopentadienide, which was shown to exist as a rapid *exo*-monomer/*endo*-monomer equilibrium at room temperature. At −110°C a quinternary mixture in THF was detected in the ^{6}Li,- ^{6}Li-EXSY spectrum. The two major species were identified and their structures were supported by MNDO calculations.

3.2.3. *^{13}C studies*

The papers selected in this section relate to metal carbonyl clusters, where 1D and 2D ^{13}C techniques are essential in elucidating rates and mechanisms of carbonyl fluxionality.

This topic has recently been reviewed by Farrugia,[234] who stresses the care needed in relating 2D-EXSY data to CO exchange mechanisms, and highlights the cases of $[Fe_2(CO)_4Cp_2]$ and $[M_3(CO)_{12}]$ (M = Fe, Ru or Os). In the former case a proper quantitative analysis of the 2D-EXSY data shows that the rate constants for direct bridging–terminal CO exchange are negligible, the presence of cross-peaks for this process at long mixing times being purely a consequence of second-order effects of the magnetization transfer. The metal clusters of the iron triad $[M_3(CO)_{12}]$ (M = Fe, Ru or Os) have been the subject of intense study over many years and extensive solution and solid-state NMR data have been acquired. The solution NMR data are interpreted in terms of a ligand polyhedral model by Johnson and in terms of a concerted bridge-

opening–bridge-closing mechanism by Mann. Currently there seems to be no reconciliation in their differing views. Farrugia has also contributed to this topic by obtaining ^{13}C EXSY spectra of $[Fe_3(Co)_{12}]$, $[Fe_2M(CO)_{12}]$ (M = Ru or Os), and $[FeRu_2(CO)_{12}]$. The general conclusion is that the metal triangle disorders arise from dynamic phenomena. In the case of $[Fe_2Os(CO)_{12}]$ ^{13}C-EXSY and CP-MAS spectra showed that carbonyl exchange is rapid above 306 K, and involves two independent processes, one being an 'in-plane' rotation of the Fe_2Os triangle in 60° steps within a relatively rigid icosahedral CO manifold, and the other a localized axial–equatorial exchange in the $Os(CO)_4$ group.[235] At least two fluxional mechanisms also occur in the ruthenium cluster $[Ru_3(CO)_7(\mu\text{-}CO)_2$ (1,1,1-η^3-1,5,9-trithiacyclododecane)]. The lowest-temperature mechanism can be explained in terms of a series of bridge–terminal CO exchanges.[236] In the triangular rhenium cluster anion $[Re_3(\mu\text{-}H)_3(\mu\text{-}\eta^2\text{-}NC_5H_4)(CO)_{10}]^-$, the carbonyls were shown to undergo synchronous axial–axial and equatorial–equatorial exchange on the apical metal. Rate constants were calculated and the data were shown to be consistent with rigid rotation of the whole apical $[H_2Re(CO)_4]$ moiety around an axis passing through the midpoint of the basal bimetallic fragment.[237]

In the triruthenium imidoyl clusters $[Ru_3(CO)_9(\mu_3\text{-}\eta^2\text{—}RC{=}NR')(\mu\text{-}H)]$ a number of fluxional processes occur, in which that of lowest energy is the 'windshield wiper' motion over the face of the cluster (Scheme 20) in contrast to the analogous osmium compounds where tripodal rotation of the carbonyl groups on the unbridged metal atom is the lowest-energy process.[238]

There have been two reports of ^{13}C 2D-EXSY studies of tetranuclear iridium clusters, namely $[Ir_4(CO)_{11}H]^-$ and $[Ir_4(CO)_8(\mu_2\text{-}CO)_3X]^-$(X = Br, I, SCN, NO_2) and $[Ir_4(CO)_8(\mu_2\text{-}CO)_3L]$ (L= various phosphines). In the hydrido cluster,[239] quantitative evaluation of the two CO exchange pathways was achieved. In the other clusters, two successive CO scrambling processes were identified, a merry-go-round process of six basal carbonyls and a carbonyl bridging process to alternative faces of the Ir_4 tetrahedron.[240]

Finally, in a series of Ru_{10}-based anionic clusters involving triphenylphosphine ligands, a detailed ^{13}C EXSY study identified rapid tripodal rotation, CO exchange between basal-edge, tetrahedral, apex and basal sites, and hydride site exchanges, but the work was only qualitative in nature.[241]

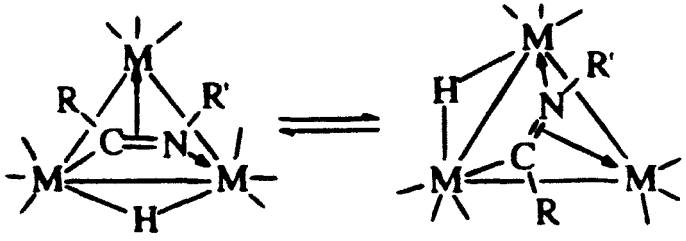

Scheme 20

3.2.4. ^{19}F studies

The stereodynamics of octahedral metal tris-chelate complexes were an early challenge to DNMR bandshape analysis and many publications ensued during the period 1960–75. Mechanistic arguments were based on subtly different changes in 1D spectral bandshapes with temperature, and it was usually assumed that rates of *cis–trans* isomerization and Δ–Λ racemization were equal. A more recent ^{19}F 2D-EXSY study of the complexes $[M(tta)_3]$ ($M = Al^{III}$, Ga^{III}; tta = 2-thenoyltrifluoroacetone) has shown conclusively that the rates of both processes are indeed equal and therefore there is a common transition state. Activation energies ($\Delta G^{\ddagger}$(298 K) were 89.8 ± 0.3 (Al^{III}) and 75.4 ± 0.2 kJ mol^{-1} (Ga^{III}).[242] The complexes $[PdR_2(SPPy_2Ph)]$ ($R = C_6F_5$, py = 2-pyridyl) exist in solution in slow equilibrium between N,N and N,S-bonded isomers.[243] A phase-sensitive ^{19}F EXSY study reveals this slow equilibrium exchange together with intramolecular processes that suggest a turnstile mechanism in a square-pyramidal intermediate rather than the more usual Berry pseudorotation in a trigonal-bipyramidal intermediate. Hexafluorobenzene was an ideal spectator ligand to measure rates of [1,2]-shifts (or ring whizzing) that occur in complexes $[Re(\eta^5\text{-}C_5H_4R)(CO)_2(\eta^2\text{-}C_6F_6)]$ (R = H or Me) (Scheme 21).[244] Intense ^{19}F cross-peaks were seen linking F_a and F_m sites, and F_m and F_x sites, and much weaker cross-peaks between F_a and F_x sites. Analysis of these spectra provided reliable rate constant and activation energy data for the [1,2]-shift process.

Three ^{19}F EXSY studies have been reported on the dynamics of uranyl^{2+} complexes.[245–247] One study[245] was concerned with fluoride exchange in aqueous solution and involved 1D bandshape, ^{19}F magnetization transfer and ^{19}F EXSY experiments. A second study examined the dynamics of carbonate and uranyl exchange in the complexes $[UO_2(CO_2)_3]^{4-}$ and $[(UO_2)_3(CO_3)_6]^{6-}$ using ^{13}C and ^{17}O line broadening, selective magnetization transfer and 2D-EXSY experiments.[246] The third study was concerned with ligand exchange and intramolecular exchange in complexes of type $[UO_2LF_n(H_2O)_{3-n}]$ (n = 1–3, L = picolinate (pic), oxalate, carbonate or acetate).[247] One- and two-dimensional ^{19}F magnetization transfer experiments were performed and first-order rate constants for inter- and intramolecular exchanges evaluated. The proposed intramolecular exchange pathways are shown in Scheme 22.

3.2.5. ^{31}P studies

Phosphorus-31 EXSY experiments, among other types, have been used to investigate the solution and solid-state dynamics in chiral phosphine complexes of mercury(II)[248] and of palladium(II).[249] The former study involved the complexes $[Hg_3X_4L_2]$ (X = Cl, Br or I; L = 1,1′-bis(diphenylphosphino)ferrocenyl ligand containing a chirotopic side-chain). Low-temperature ^{31}P studies, combined with ^{31}P EXSY spectra, suggested the

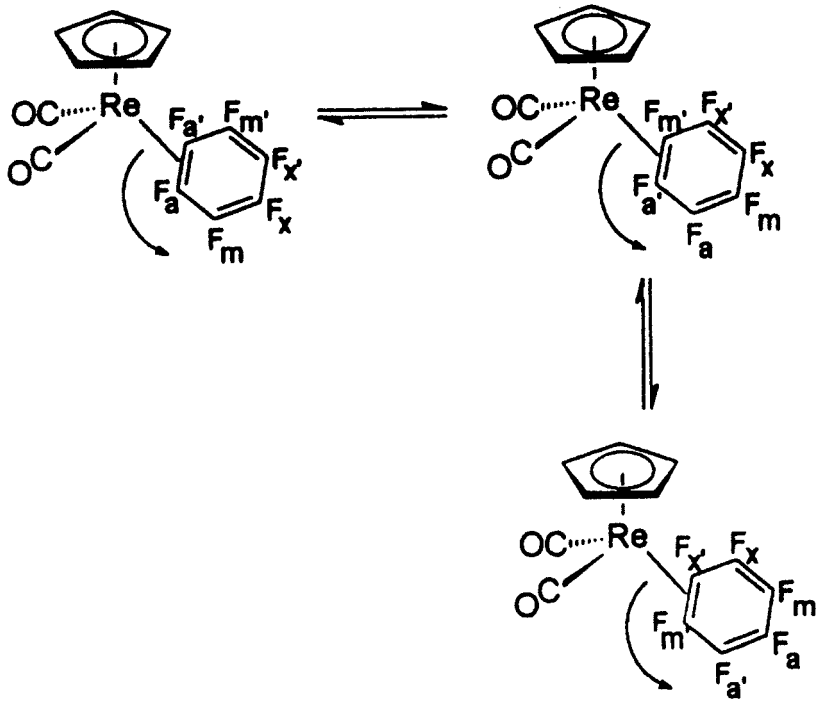

Scheme 21

existence of species with one and two Hg atoms. These were detected in solution by ^{31}P, ^{199}Hg and ^{1}H-^{199}Hg 2D-HETCOR spectra. Solid-state ^{31}P studies (1D and 2D spectra) were also performed. The other study[249] concerned palladium(II) complexes of chiral ligands based on β-D-thioglucose tetraacetate. Some of these complexes existed as two or four diastereoisomers in solution and detailed ^{31}P and ^{1}H EXSY spectra were used to characterize several of the equilibria. Dinuclear palladium(I)–μ-phosphido secondary phosphine complexes such as $[Pd_2(\mu\text{-}PBu^t_2)(PCy_2H)_3(CO)]^+$ equilibrate in solution to a mixture of monocarbonyl derivatives arising from bridging phosphido/terminal phosphine interchange. These were characterized by multinuclear 1-D and 2-D NMR including ^{31}P-EXSY spectra.[250]

There have been two studies of dynamics in metal complexes of biologically important ligands. One study[251] involved ^{31}P EXSY for measuring rotational energy barriers about Pt^{II}–N^7 purine bonds in *cis*-$[Pt(NH_3)_2L_2]$ (L = 1-methyladenosine, adenosine 5′-mono-, -di-, or tri-phosphate or guanosine 5′-monophosphate). The two head-to-tail diastereomers represented a two-site exchange problem. Activation energies for all the 6-aminopurine complexes were in the range 46–95 kJ mol^{-1}. The other study[252] involved the structure and solution dynamics of $Al^{III}(ATP)_2$ and $Al^{III}(ATP)$ at physiological pH by multinuclear (^{31}P, ^{13}C, ^{1}H and ^{27}Al) NMR. The exchange rate between

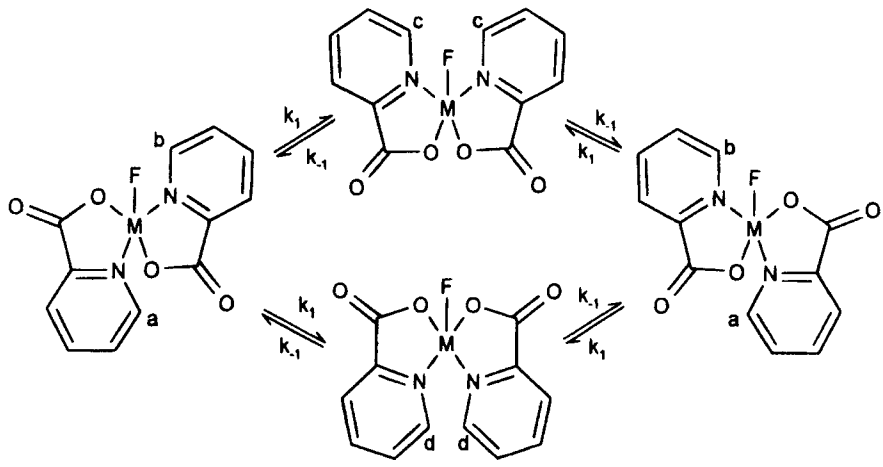

Scheme 22

free and Al^{III}-bound ATP in $Al^{III}(ATP)_2$ was measured by ^{31}P EXSY and found to be $3.4\,s^{-1}$ at 295 K, suggesting a dissociative mechanism. The ^{31}P signals of the complexed species exhibited considerable broadening for which the authors offered a number of explanations, namely, scalar relaxation of the second kind due to coupling of ^{27}Al with ^{31}P, CSA contribution to the ^{31}P relaxation or chemical exchange between two or more of the species in the moderately fast exchange limit.

3.2.6. Miscellaneous nuclide studies

A ^{77}Se 2D-EXSY study[253] enabled the exchange rates in mixtures of S_2Cl_2 and Se_2Br_2 which contain disulfur, diselenium, and selenium–sulfur dihalides to be measured. The 2D-EXSY data imply that magnetization transfer takes place predominantly by an exchange process in which only selenium–halogen bonds are broken. Transfers by means of a bimolecular halogen-bridged intermediate or by an ionic process are consistent with the pattern of cross-peaks observed. First-order rate constants for any cross-peak were measured using the initial-rate approximation rather than the more usual direct matrix transformation method.

Willem *et al.* have reported a series of halogen exchange studies in allyltin and vinyltin compounds.[254–256] They have employed both initial-rate and matrix transformation methods to measure rate constants. One study[254] was concerned with compounds of general formula $RSnCl_2Br$ that underwent halogen exchange to give equilibrium mixtures of $RSnCl_3$, $RSnCl_2Br$, $RSnClBr_2$ and $RSnBr_3$. Another study[255] investigated halogen exchange between $RPhSnCl_2$, RPhSnBrCl and $RPhSnBr_2$ by $^{119}Sn\{^1H\}$ 2D-EXSY, see

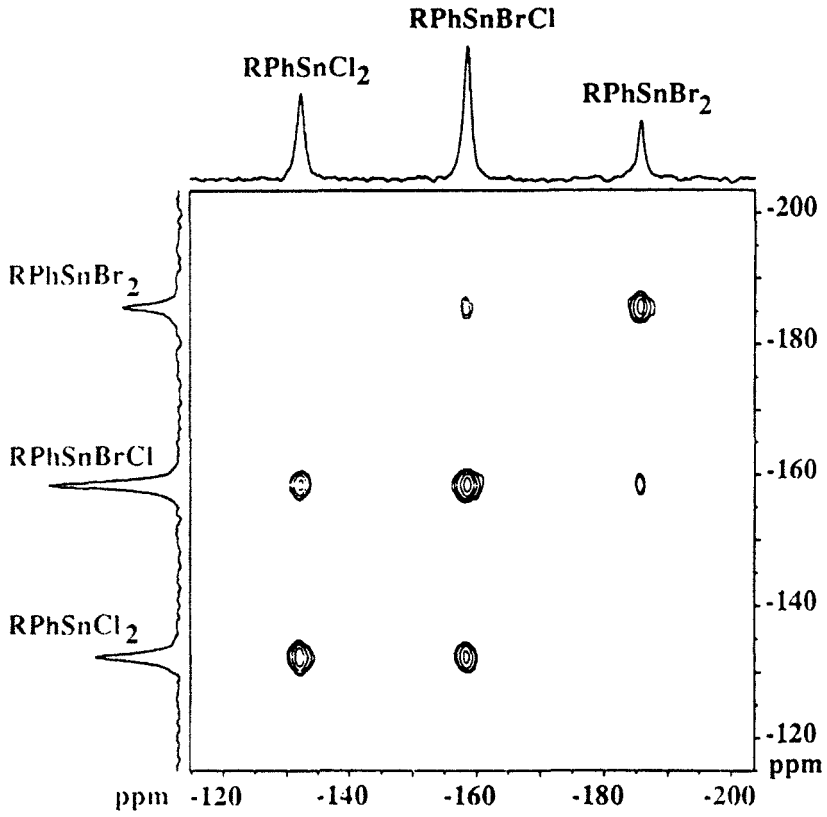

Fig. 14. $^{119}Sn\{^1H\}$ 2D-EXSY spectrum showing halogen exchange in a mixture of $RPhSnCl_2$, RPhSnBrCl and $RPhSnBr_2$. (Reproduced with permission from *J. Organomet. Chem.*, 1995, **485**, 263–265.)

Fig. 14. Rate data for this 3-site exchange problem were based on normalized cross-peak volumes with or without symmetrization. Pseudo-first-order rate constants for the exchanges

$$RPhSnCl_2 \underset{k_{-1}}{\overset{k_1}{\rightleftharpoons}} RPhSnBrCl \underset{k_{-2}}{\overset{k_2}{\rightleftharpoons}} RPhSnBr_2$$

$$RPhSnCl_2 \underset{k_{-3}}{\overset{k_3}{\rightleftharpoons}} RPhSnBr_2$$

were evaluated. It was found that $k_1 \approx 4k_2$. The rate constant k_3 is associated with a double halogen exchange and magnitudes were not statistically different from zero. The general conclusion therefore was that only a single halogen exchange mechanism occurs. A similar study has been carried out on two monoallyltin compounds.[256]

Thallium-205 EXSY spectra have been used to study rates of cyanide exchange in aqueous solutions of $[Tl(^{13}CN)_3]$, $[Tl(^{13}CN)_4]^-$ and $H^{13}CN$.[257] When allowance was made for ^{205}Tl–^{13}C and ^{13}C–^{1}H scalar couplings, the system represented one of 6 exchanging sites for ^{13}C NMR and 9 exchanging sites for ^{205}Tl NMR. Both ^{13}C and ^{205}Tl EXSY experiments were carried out. Rate constants for different exchange pathways were evaluated, but the data from ^{205}Tl EXSY spectra suffered from larger errors compared to the ^{13}C-based EXSY data.

ACKNOWLEDGEMENTS

I thank Dr Vladimir Šik for stimulating discussions and Professor Alex Bain for the receipt of a manuscript prior to publication.

REFERENCES

1. K. G. Orrell and V. Šik, *Annu. Rep. NMR Spectrosc.*, 1993, **27**, 103.
2. H. Friebolin, *Basic One- and Two-Dimensional NMR Spectroscopy*, 2nd edn, VCH, Weinheim, 1993.
3. H. Günther, *NMR Spectroscopy*, 2nd edn, Wiley, Chichester, 1995.
4. J. K. M. Sanders and B. K. Hunter, *Modern NMR Spectroscopy, A Guide for Chemists*, 2nd edn, Oxford University Press, Oxford, 1993.
5. J.-J. Delpeuch (ed.), *Dynamics of Solutions and Fluid Mixtures by NMR*, Wiley, Chichester, 1995.
6. D. M. Grant and R. K. Harris (eds), *Encyclopedia of Nuclear Magnetic Resonance*, Vols 1–8, Wiley, Chichester, 1996.
7. E. R. Johnston, *Concepts Magn. Reson.*, 1995, **7**, 219.
8. J. Rohonczy, *Kem. Kozl.*, 1992, **74**, 161.
9. A. D. Bain and G. J. Duns, *J. Magn. Reson. A*, 1995, **112**, 258.
10. A. D. Bain and G. J. Duns, *Canad. J. Chem.*, 1996, **74**, 819.
11. R. S. Dumont, S. Jain and A. D. Bain, *J. Chem. Phys.*, 1997, **106**, 5928.
12. M. Goldman, *Mol. Phys.*, 1995, **86**, 301.
13. J. Seliger, *J. Magn. Reson. A*, 1993, **103**, 175.
14. C. Szántay and A. Demeter, *J. Magn. Reson. A*, 1995, **115**, 94.
15. S. Szymanski, *J. Magn. Reson. A*, 1994, **108**, 151.
16. S. Szymanski, *J. Magn. Reson. A*, 1995, **115**, 254.
17. A. D. Bain and J. A. Cramer, *J. Magn. Reson. A*, 1993, **103**, 217.
18. S. S. Rigby, L. Girard, A. D. Bain and M. J. McGlinchey, *Organometallics*, 1995, **14**, 3798.
19. A. D. Bain and J. A. Cramer, *J. Magn. Reson. A*, 1996, **118**, 21.
20. C. L. Perrin and R. E. Engler, *J. Magn. Reson. A*, 1996, **123**, 188.
21. C. L. Perrin and R. E. Engler, *J. Am. Chem. Soc.*, 1997, **119**, 585.
22. E. Baguet and C. Roby, *J. Magn. Reson. A*, 1994, **108**, 189.
23. E. Baguet and C. Roby, *J. Magn. Reson.*, 1997, **128**, 149.
24. R. E. D. McClung and G. H. M. Aarts, *J. Magn. Reson. A*, 1995, **115**, 145.
25. A. D. Bain and D. A. Fletcher, *Mol. Phys.*, in press.
26. V. V. Krishnan and M. Rance, *J. Magn. Reson. A*, 1995, **116**, 97.
27. X. Chen and B. E. Mann, *Organometallics*, 1996, **15**, 3703.

28. M. Koike, D. H. Hamilton, S. R. Wilson and J. R. Shapley, *Organometallics*, 1996, **15**, 4930.
29. J. A. Casares, P. Espinet, J. M. Martinez-Ilarduya and Y.-S. Liu, *Organometallics*, 1997, **16**, 770.
30. D. L. Tarazano, T. W. Bodnar and A. R. Cutler, *J. Organomet. Chem.*, 1993, **448**, 139.
31. K. I. Momot and F. A. Walker, *J. Phys. Chem. A*, 1997, **101**, 2787.
32. I. Andersson, L. Pettersson, J. J. Hastings and O. W. Howarth, *J. Chem. Soc., Dalton Trans.*, 1996, 3357.
33. D. H. Jones, N. D. Kurur and D. P. Weitekamp, *Bull. Magn. Reson.*, 1992, **14**, 214.
34. F. A. L. Anet, *Chem. Phys. Lett.* 1993, **208**, 187.
35. A. D. Bain and G. J. Duns, *J. Magn. Reson. A*, 1994, **109**, 56.
36. A. D. Bain, G. J. Duns, S. Ternieden, J. Ma and N. H. Werstiuk, *J. Phys. Chem.*, 1994, **98**, 7458.
37. A. D. Bain, G. J. Duns, F. Rathgeb and J. Vanderkloet, *J. Phys. Chem.*, 1995, **99**, 17338.
38. S. Aime, L. Cordero, R. Gobetto and G. Szalontai, *Spectrochim. Acta A*, 1993, **49**, 1307.
39. S. Aime, L. Cordero, R. Gobetto, S. Bordoni, L. Busetto, V. Zanotti, V. G. Albano, D. Braga and F. Grepioni, *J. Chem. Soc., Dalton Trans.*, 1992, 2961.
40. S. Aime, D. Braga, L. Cordero, R. Gobetto, F. Grepioni, S. Righi and S. Sostero, *Inorg. Chem.*, 1992, **31**, 3054.
41. A. P. M. Kentgens, H. Karrenbeld, E. De Boer and H. Schumann, *J. Organomet. Chem.*, 1992, **429**, 99.
42. F. H. Försterling, C. E. Barnes and W. D. King, *Inorg. Chem.*, 1997, **36**, 3532.
43. D. Lafleur, Y. Huang, D. F. R. Gilson and I. S. Butler, *J. Solid State Chem.*, 1994, **108**, 99.
44. C. L. Watkins, L. K. Krannich and S. J. Schauer, *Inorg. Chem.*, 1995, **34**, 6228.
45. S. Aime, W. Dastrù, R. Gobetto, J. Krause and L. Milone, *Organometallics*, 1995, **14**, 4435.
46. S. Aime, R. Gobetto, A. Orlandi, C. J. Groombridge, G. E. Hawkes, M. D. Mantle and K. D. Sales, *Organometallics*, 1994, **13**, 2375.
47. T. P. Braun, M. Mehring and A. Simon, *J. Am. Chem. Soc.*, 1996, **118**, 7203.
48. W. R. Carper and C. E. Keller, *J. Phys. Chem. A*, 1997, **101**, 3246.
49. P. Kempgens, J. Hirschinger, K. Elbayed, J. Raya, P. Granger and J. Rosé, *J. Phys. Chem.*, 1996, **100**, 2045.
50. J. R. Ascenso, M. de D. Carvalho, A. R. Dias, C. C. Romao, M. J. Calhorda and L. F. Veiros, *J. Organomet. Chem.*, 1994, **470**, 147.
51. X.-A. Mao, J.-Z. Yao, B.-S. Tian and Y.-Y. Chen, *Magn. Reson. Chem.*, 1996, **34**, 109.
52. D. M. Knotter, D. M. Grove, W. J. J. Smeets, A. L. Spek and G. Van Koten, *J. Am. Chem. Soc.*, 1992, **114**, 3400.
53. S. Charles, J. A. Danis, J. C. Fettinger and B. W. Eichhorn, *Inorg. Chem.*, 1997, **36**, 3772.
54. Y. Yamamoto, X. Chen and K. Akiba, *J. Am. Chem. Soc.*, 1992, **114**, 7906.
55. V. I. Minkin, M. S. Korobov, L. E. Nivororozhkin, O. E. Kompan, R. Ya. Olekhnovich, G. S. Borodkin and Y. T. Struchkov, *Mendeleev Commun.*, 1993, 2.
56. D. Minniti, *Inorg. Chem.*, 1994, **33**, 2631.
57. M. T. Ashby, G. N. Govindan and A. K. Grafton, *J. Am. Chem. Soc.*, 1994, **116**, 4801.
58. U. Koelle, C. Rietmann and G. Raabe, *Organometallics*, 1997, **16**, 3273.
59. V. V. Negrebetsky, A. G. Shipov, E. P. Kramarova, V. V. Negrebetsky and Y. I. Baukov, *J. Organomet. Chem.*, 1997, **530**, 1.
60. M. Meyer, B. Kersting, R. E. Powers and K. N. Raymond, *Inorg. Chem.*, 1997, **36**, 5179.
61. A. Gelling, K. G. Orrell, A. G. Osborne, V. Šik, M. B. Hursthouse and S. J. Coles, *J. Chem. Soc., Dalton Trans.*, 1996, 203.
62. J.-P. Djukic, V. G. Young and L. K. Woo, *Organometallics*, 1994, **13**, 3995.
63. M. L. H. Green and A. K. Hughes, *J. Chem. Soc., Dalton Trans.*, 1992, 527.
64. J. A. S. Howell, M. G. Palin, P. McArdle, D. Cunningham, Z. Goldschmidt, H. E. Gottlieb and D. Hezroni-Langerman, *Inorg. Chem.*, 1993, **32**, 3493.
65. J. A. S. Howell, P. C. Yates, M. G. Palin, P. McArdle, D. Cunningham, Z. Goldschmidt, H. E. Gottlieb and D. Hezroni-Langerman, *J. Chem. Soc., Dalton Trans.*, 1993, 2775.

66. L. A. Oro, M. P. Lamata, M. L. Jimeno, J. Elguero, A. Belguise and P. Lux, *Inorg. Chem.*, 1994, **33**, 2196.
67. M. A. Petrie, K. Ruhlandt-Senge and P. P. Power, *Inorg. Chem.*, 1992, **31**, 4038.
68. T. S. Koloski, D. C. Pestana, P. J. Carroll and D. H. Berry, *Organometallics*, 1994, **13**, 489.
69. L. Girard and M. C. Baird, *J. Organomet. Chem.*, 1993, **444**, 143.
70. M. J. Sanger and R. J. Angelici, *Organometallics*, 1994, **13**, 1821.
71. S. Dostal, S. J. Stoudt, P. Fanwick, W. F. Sereatan, B. Kahr and J. E. Jackson, *Organometallics*, 1993, **12**, 2284.
72. J. Pu, T. S. Peng, C. L. Mayne, A. M. Arif and J. A. Gladysz, *Organometallics*, 1993, **12**, 2686.
73. Y. Takaguchi, H. Fujihara and N. Furukawa, *J. Organomet. Chem.*, 1995, **498**, 49.
74. A. Cusanelli and D. Sutton, *Organometallics*, 1996, **15**, 1457.
75. J. Cabral and G. Fraenkel, *J. Am. Chem. Soc.*, 1992, **114**, 9067.
76. G. Fraenkel and J. A. Cabral, *J. Am. Chem. Soc.*, 1993, **115**, 1551.
77. G. Fraenkel and F. Qiu, *J. Am. Chem. Soc.*, 1997, **119**, 3571.
78. G. Fraenkel and K. V. Martin, *J. Am. Chem. Soc.*, 1995, **117**, 10336.
79. C. H. Lai and C. H. Cheng, *Organometallics*, 1993, **12**, 3561.
80. C. H. Lai, C. H. Cheng and S. L. Wang, *J. Organomet. Chem.*, 1993, **458**, 147.
81. M. Jaroszewski, T. Szymanska-Buzar, M. Wilgocki and J. J. Ziółkowski, *J. Organomet. Chem.*, 1996, **509**, 19.
82. R. Fernandez-Galán, F. A. Jalón, B. R. Manzano, J. Rodríguez-de la Fuente, M. Vrahami, B. Jedlicka, W. Weissensteiner and G. Jogl, *Organometallics*, 1997, **16**, 3758.
83. O. J. Curnow, R. P. Hughes, E. N. Mairs and A. L. Rheingold, *Organometallics*, 1993, **12**, 3102.
84. V. M. Hansen, R. J. Batchelor, F. W. B. Einstein, J. L. Male, R. K. Pomeroy and M. J. Zaworotko, *Organometallics*, 1997, **16**, 4875.
85. L. Li, A. Decken, B. G. Sayer, M. J. McGlinchey, P. Bregaint, J. Y. Thepot, L. Toupet, J. R. Hamon and C. Lapinte, *Organometallics*, 1994, **13**, 682.
86. R. P. Hughes, D. S. Tucker and A. L. Rheingold, *Organometallics*, 1993, **12**, 3069.
87. R. Ditchfield, R. P. Hughes, D. S. Tucker, E. P. Bierwagen, J. Robbins, D. J. Robinson and J. A. Zakutansky, *Organometallics*, 1993, **12**, 2258.
88. C. A. Ghilardi, P. Innocenti, S. Midollini, A. Orlandini and A. Vacca, *J. Chem. Soc., Dalton Trans.*, 1995, 1109.
89. H. Ahlbrecht, J. Harbach, T. Hauck and H. O. Kalinowski, *Chem. Ber.*, 1992, **125**, 1753.
90. D. W. Powell and P. A. Lay, *Inorg. Chem.*, 1992, **31**, 3542.
91. A. Decken, J. F. Britten and M. J. McGlinchey, *J. Am. Chem. Soc.*, 1993, **115**, 7275.
92. M.-J. Bermejo, J.-I. Ruiz, X. Solans and J. Vinaixa, *J. Organomet. Chem.*, 1993, **463**, 143.
93. T. Chivers and R. W. Hilts, *Inorg. Chem.*, 1992, **31**, 5272.
94. T. Chivers, M. Edwards, A. Meetsma, J. C. Van de Grampel and A. Van der Lee, *Inorg. Chem.*, 1992, **31**, 2156.
95. T. Chivers, D. D. Doxee and R. W. Hilts, *Inorg. Chem.*, 1993, **32**, 3244.
96. M. E. Gurskii, I. D. Gridnev, A. V. Geiderikh, A. V. Ignatenko, Yu. N. Bubnov, V. I. Mstislavskii and Yu. A. Ustynyuk, *Organometallics*, 1992, **11**, 4056.
97. E. W. Abel, K. G. Orrell, A. G. Osborne, H. M. Pain and V. Šik, *J. Chem. Soc., Dalton Trans.*, 1994, 111.
98. E. W. Abel, K. G. Orrell, A. G. Osborne, H. M. Pain, V. Šik, M. B. Hursthouse and K. M. A. Malik, *J. Chem. Soc., Dalton Trans.*, 1994, 3441.
99. K. G. Orrell, A. G. Osborne, V. Šik and M. Webba da Silva, *Polyhedron*, 1995, **14**, 2797.
100. M. A. M. Garcia, A. Gelling, D. R. Noble, K. G. Orrell, A. G. Osborne and V. Šik, *Polyhedron*, 1996, **15**, 371.
101. E. W. Abel, E. S. Blackwall, M. L. Creber, P. J. Heard and K. G. Orrell, *J. Organomet. Chem.*, 1995, **490**, 83.

102. M. Gal, M. A. Lobo-Recio, C. Marzin, S. Seghrouchni and G. Tarrago, *Inorg. Chem.*, 1994, **33**, 4054.
103. J. R. Morrow and K. O. A. Chin, *Inorg. Chem.*, 1994, **32**, 3357.
104. D. L. Reger, M. F. Huff, A. L. Rheingold and B. S. Haggerty, *J. Am. Chem. Soc.*, 1992, **114**, 579.
105. M. L. Illingsworth, B. P. Cleary, A. J. Jensen, L. J. Schwartz and A. L. Rheingold, *Inorg. Chim. Acta*, 1993, **207**, 147.
106. N. W. Mitzel, P. Bissinger, J. Riede, K. H. Dreihaeupl and H. Schmidbaur, *Organometallics*, 1993, **12**, 413.
107. H. Ranaivonjatovo, J. Escudie, C. Couret, J. P. Declercq, A. Dubourg and J. Satge, *Organometallics*, 1993, **12**, 1674.
108. R. D. Pike, T. J. Alavosus, W. H. Hallows, N. S. Lennhoff, W. J. Ryan, D. A. Sweigart, C. H. Bushweller, C. M. DiMeglio and J. H. Brown, *Organometallics*, 1992, **11**, 2841.
109. C. M. DiMeglio, K. J. Ahmed, L. A. Luck, E. E. Weltin, A. L. Rheingold and C. H. Bushweller, *J. Phys. Chem.*, 1992, **96**, 8765.
110. A. Cusanelli, R. J. Batchelor, F. W. B. Einstein and D. Sutton, *Organometallics*, 1994, **13**, 5096.
111. E. Lindner, J. Dettinger, H. A. Mayer, H. Kuehbauch, R. Fawzi and M. Steimann, *Chem. Ber.*, 1993, **126**, 1317.
112. E. Lindner, M. Geprägs, K. Gierling, R. Fawzi and M. Steimann, *Inorg. Chem.*, 1995, **34**, 6106.
113. F. A. Jalón, B. R. Manzano, A. Otero and M. C. Rodríguez-Perez, *J. Organomet. Chem.*, 1995, **494**, 179.
114. J. Fernandez-Baeza, F. A. Jalón, A. Otero and M. E. Rodrigo-Blanco, *J. Chem. Soc., Dalton Trans.*, 1995, 1015.
115. J. Elguero, A. Fruchier, A. de la Hoz, F. A. Jalón, B. R. Manzano, A. Otero and F. G. de la Torre, *Chem. Ber.*, 1996, **129**, 589.
116. E. W. Abel, K. G. Orrell, M. C. Poole, V. Šik, M. B. Hursthouse and M. A. Mazid, *Polyhedron*, 1995, **14**, 585.
117. S. Szymanski, *J. Chem. Phys.*, 1996, **104**, 8216.
118. G. Buntkowsky, H.-H. Limbach, F. Wehrmann, I. Sack, H.-M. Vieth and R. H. Morris, *J. Phys. Chem. A*, 1997, **101**, 4679.
119. D. G. Gusev and H. Berke, *Chem. Ber.*, 1996, **129**, 1143.
120. B. E. Hauger, D. Gusev and K. G. Caulton, *J. Am. Chem. Soc.*, 1994, **116**, 208.
121. D. G. Gusev, R. Kuhlman, J. R. Rambo, H. Berke, O. Eisenstein and K. G. Caulton, *J. Am. Chem. Soc.*, 1995, **117**, 281.
122. M. Brookhart, E. Hauptman and D. M. Lincoln, *J. Am. Chem. Soc.*, 1992, **114**, 10394.
123. S. Feracin, T. Burgi, V. I. Bakhmutov, I. Eremenko, E. V. Vorontsov, A. B. Vimenits and H. Berke, *Organometallics*, 1994, **13**, 4194.
124. V. Bakhmutov, T. Buergi, P. Burger, U. Ruppli and H. Berke, *Organometallics*, 1994, **13**, 4203.
125. X. L. Luo, D. Michos and R. H. Crabtree, *Organometallics*, 1992, **11**, 237.
126. C. Bianchini, K. Linn, D. Masi, M. Peruzzini, A. Polo, A. Vacca and F. Zanobini, *Inorg. Chem.*, 1993, **32**, 2366.
127. J. A. Ayllón, C. Gervaux, S. Sabo-Etienne and B. Chaudret, *Organometallics*, 1997, **16**, 2000.
128. V. I. Bakhmutov, E. V. Vorontsov, G. Boni and C. Moise, *Inorg. Chem.*, 1997, **36**, 4055.
129. I. Demarchy, M. A. Esteruelas, Y. Jean, A. Lledós, F. Maseras, L. A. Oro, C. Valero and F. Volatron, *J. Am. Chem. Soc.*, 1996, **118**, 8388.
130. D. G. Gusev, J. U. Notheis, J. R. Rambo, B. E. Hauger, O. Eisenstein and K. G. Caulton, *J. Am. Chem. Soc.*, 1994, **116**, 7409.
131. B. Manzano, F. Jalón, J. Matthes, S. Sabo-Etienne, B. Chaudret, S. Ulrich and H.-H. Limbach, *J. Chem. Soc., Dalton Trans.*, 1997, 3153.

132. M. Mediati, G. N. Tachibana and C. M. Jensen, *Inorg. Chem.*, 1992, **31**, 1827.
133. J. C. Lee, Jr, W. Yao, R. H. Crabtree and H. Rüegger, *Inorg. Chem.*, 1996, **35**, 695.
134. H. Schumann, *Polyhedron*, 1996, **15**, 2327.
135. A. K. W. Stephens, R. S. Dhillou, S. E. Madbak, S. L. Whitbread and S. F. Lincoln, *Inorg. Chem.*, 1996, **35**, 2019.
136. M. G. Gardiner and C. L. Raston, *Inorg. Chem.*, 1996, **35**, 4162.
137. H. J. Reich and K. J. Kulicke, *J. Am. Chem. Soc.*, 1996, **118**, 273.
138. F. H. Koehler and B. Schlesinger, *Inorg. Chem.*, 1992, **31**, 2853.
139. A. R. Siedle and R. A. Newmark, *J. Organomet. Chem.*, 1995, **497**, 119.
140. J. I. Amor, T. Cuenca, M. Galakhov, P. Gómez-Sal, A. Manzanero and P. Royo, *J. Organomet. Chem.*, 1997, **535**, 155.
141. T. Bürgi, H. Berke, D. Wingbermühle, C. Psiorz, R. Noe, T. Fox, M. Knickmeier, M. Berlekamp, R. Fröhlich and G. Erker, *J. Organomet. Chem.*, 1995, **497**, 149.
142. M. D. Fryzuk, S. S. H. Mao, P. B. Duval and S. J. Rettig, *Polyhedron*, 1995, **14**, 11.
143. H. El Hafa, C. Cordier, M. Gruselle, Y. Besace, G. Jaouen and M. J. McGlinchey, *Organometallics*, 1994, **13**, 5149.
144. W. Lin, S. R. Wilson and G. S. Girolami, *J. Am. Chem. Soc.*, 1993, **115**, 3022.
145. W. Lin, S. R. Wilson and G. S. Girolami, *Organometallics*, 1994, **13**, 2309.
146. C. P. Casey, R. A. Widenhoefer, S. L. Hallenbeck, R. K. Hayashi and J. A. Gavney, Jr, *Organometallics*, 1994, **13**, 4720.
147. M. Bergamo, T. Beringhelli, G. D'Alfonso, G. Ciani, M. Moret and A. Sironi, *Organometallics*, 1996, **15**, 3876.
148. T. Beringhelli, G. D'Alfonso, A. P. Minoja, G. Ciani and A. Sironi, *J. Organomet. Chem.*, 1992, **440**, 175.
149. T. Beringhelli, G. D'Alfonso, A. P. Minoja and M. Freni, *Gazz. Chim. Ital.*, 1992, **122**, 375.
150. S. Aime, M. Botta, R. Gobetto, L. Milone, D. Osella, R. Gellért and E. Rosenberg, *Organometallics*, 1995, **14**, 3693.
151. T. Chihara, A. Jesorka, H. Ikezawa and Y. Wakatsuki, *J. Chem. Soc., Dalton Trans.*, 1997, 443.
152. N. J. Heaton, *Mol. Phys.*, 1997, **92**, 251.
153. V. Gerardy-Montouillout, C. Malveau, P. Tekely, Z. Olender and Z. Luz, *J. Magn. Reson. A*, 1996, **123**, 7.
154. D. Reichert, H. Zimmermann, P. Tekely, R. Poupko and Z. Luz, *J. Magn. Reson.*, 1997, **125**, 245.
155. A. Detken, H. Zimmermann, U. Haeberlen and Z. Luz, *J. Magn. Reson.*, 1997, **126**, 95.
156. Z. Luz, R. Poupko and S. Alexander, *J. Chem. Phys.*, 1993, **99**, 7544.
157. S. A. Vierkoetter, C. E. Barnes, G. L. Garner and L. G. Butler, *J. Am. Chem. Soc.*, 1994, **116**, 7445.
158. A. E. Aliev, K. D. M. Harris and F. Guillaume, *J. Phys. Chem.*, 1995, **99**, 1156.
159. D. O'Hare, S. J. Heyes, S. Barlow and S. Mason, *J. Chem. Soc., Dalton Trans.*, 1996, 2989.
160. P. J. Barrie, C. A. Mitsopoulou and E. W. Randall, *J. Chem. Soc., Dalton Trans.*, 1995, 2125.
161. P. J. Barrie, C. A. Mitsopoulou, M. Motevalli and E. W. Randall, *J. Chem. Soc., Dalton Trans.*, 1997, 353.
162. D. F. Brougham, P. J. Barrie, G. E. Hawkes, I. Abrahams, M. Motevalli, D. A. Brown and G. J. Long, *Inorg. Chem.*, 1996, **35**, 5595.
163. D. C. Maus, V. Copié, B. Sun, J. M. Griffiths, R. G. Griffen, S. Luo, R. R. Schrock, A. H. Liu, S. W. Seidel, W. M. Davis and A. Grohmann, *J. Am. Chem. Soc.*, 1996, **118**, 5665.
164. J. Kuemmerlen, I. Lange, W. Milius, A. Sebald and A. Blaschette, *Organometallics*, 1993, **12**, 3541.
165. J. Kuemmerlen and A. Sebald, *Magn. Reson. Chem.*, 1994, **32**, 173.
166. J. Kuemmerlen, A. Sebald, and E. Sendermann, *Organometallics*, 1994, **13**, 802.

167. A. E. Aliev, K. D. M. Harris, D. C. Apperley and R. K. Harris, *J. Solid State Chem.*, 1994, **110**, 314.
168. J. Kuemmerlen and A. Sebald, *Organometallics*, 1997, **16**, 2971.
169. X. Helluy, J. Kuemmerlen and A. Sebald, *Organometallics*, 1997, **16**, 5218.
170. K. G. Orrell, in *Encyclopedia of Nuclear Magnetic Resonance*, Vol. 8, Wiley, Chichester, 1996, p. 4850.
171. X.-A. Mao, *Chem. Phys.*, 1993, **175**, 237.
172. V. S. Dimitrov and N. G. Vassilev, *Magn. Reson. Chem.*, 1995, **33**, 739.
173. V. L. Yarnykh and Y. A. Ustynyuk, *J. Magn. Reson. A*, 1993, **102**, 131.
174. S. Macura, *J. Magn. Reson. A*, 1995, **112**, 152.
175. H. Gesmar, N. Faester and J. J. Led, *J. Magn. Reson. B*, 1994, **103**, 10.
176. Z. Zolnai, N. Juranic, J. L. Markley and S. Macura, *Chem. Phys.*, 1995, **200**, 161.
177. B. Boulet and M. Rance, *J. Chem. Phys.*, 1994, **101**, 7273.
178. K. Zangger and H. Sterk, *J. Phys. Chem.*, 1996, **100**, 11198.
179. C. Zwahlen, S. J. F. Vincent, M. Schwager and G. Bodenhausen, *Chem. Eur. J.*, 1996, **2**, 45.
180. J. H. Lee, C. Labadie, C. S. Springer and G. S. Harbison, *J. Am. Chem. Soc.*, 1993, **115**, 7761.
181. W. Lee and N. R. Krishna, *J. Magn. Reson.*, 1992, **98**, 36.
182. J.-L. Yan, X.-A. Mao and L.-F. Shen, *Chem. Phys. Lett.*, 1997, **272**, 278.
183. H. Desraux, P. Berthault, N. Birlirakis and M. Goldman, *J. Magn. Reson. A*, 1994, **108**, 219.
184. R. Shukla, *Magn. Reson. Chem.*, 1996, **34**, 545.
185. C. S. Johnson, Jr, *J. Magn. Reson. A*, 1993, **102**, 214.
186. G. A. Barrall, K. Schmidt-Rohr, Y. K. Lee, K. Landfester, H. Zimmermann, G. C. Chingas and A. Pines, *J. Chem. Phys.*, 1996, **104**, 509.
187. L. Frydman, S. Vallabhaneni, Y. K. Lee and L. Emsley, *J. Chem. Phys.*, 1994, **101**, 111.
188. L. Frydman, Y. K. Lee, L. Emsley, G. C. Chingas and A. Pines, *J. Am. Chem. Soc.*, 1993, **115**, 4825.
189. Y. K. Lee, L. Emsley, R. G. Larsen, K. Schmidt-Rohr, M. Hong, L. Frydman, G. C. Chingas and A. Pines, *J. Chem. Phys.*, 1994, **101**, 1852.
190. D. Schaefer, J. Leisen and H. W. Spiess, *J. Magn. Reson. A*, 1995, **115**, 60.
191. E. W. Abel, E. S. Blackwall, K. G. Orrell and V. Šik, *J. Organomet. Chem.*, 1994, **464**, 163.
192. E. W. Abel, E. S. Blackwall, P. J. Heard, K. G. Orrell, V. Šik, M. A. Mazid and K. M. A. Malik, *J. Chem. Soc., Dalton Trans.*, 1994, 445.
193. E. W. Abel, P. J. Heard, K. G. Orrell and V. Šik, *Polyhedron*, 1994, **13**, 2907.
194. E. W. Abel, P. J. Heard, K. G. Orrell, M. B. Hursthouse and K. M. A. Malik, *J. Chem. Soc., Dalton Trans.*, 1995, 3165.
195. E. W. Abel, P. J. Heard and K. G. Orrell, *Inorg. Chim. Acta*, 1997, **255**, 65.
196. A. Gelling, K. G. Orrell, A. G. Osborne and V. Šik, *J. Chem. Soc., Dalton Trans.*, 1994, 3545.
197. E. W. Abel, A. Gelling, K. G. Orrell, A. G. Osborne and V. Šik, *Chem. Commun.*, 1996, 2329.
198. A. Gelling, K. G. Orrell, A. G. Osborne and V. Šik, *J. Chem. Soc., Dalton Trans.*, 1998, 937.
199. K. G. Orrell, A. G. Osborne, V. Šik and M. Webba da Silva, *J. Organomet. Chem.*, 1997, **530**, 235.
200. K. G. Orrell, A. G. Osborne, V. Šik, M. Webba da Silva, M. B. Hursthouse, D. E. Hibbs, K. M. A. Malik and N. G. Vassilev, *J. Organomet. Chem.*, 1997, **538**, 171.
201. K. G. Orrell, A. G. Osborne, V. Šik, M. Webba da Silva, M. B. Hursthouse, D. E. Hibbs, K. M. A. Malik and N. G. Vassilev, *J. Organomet. Chem.*, 1998, **555**, 35.
202. A. Gelling, K. G. Orrell, A. G. Osborne and V. Šik, *J. Chem. Soc., Dalton Trans.*, 1996, 3371.

203. A. Gelling, D. R. Noble, K. G. Orrell, A. G. Osborne and V. Šik, *J. Chem. Soc., Dalton Trans.*, 1996, 3065.
204. A. Gelling, M. D. Olsen, K. G. Orrell, A. G. Osborne and V. Šik, *Chem. Commun.*, 1997, 587.
205. A. Gelling, M. D. Olsen, K. G. Orrell, A. G. Osborne and V. Šik, *Inorg. Chim. Acta*, 1997, **264**, 257.
206. P. J. Heard and K. Kite, *J. Chem. Soc., Dalton Trans.*, 1996, 3543.
207. S. J. Franklin and K. N. Raymond, *Inorg. Chem.*, 1994, **33**, 5794.
208. N. V. Shokhirev, T. Kh. Shokhireva, J. R. Polam, C. T. Watson, K. Raffii, U. Simonis and F. A. Walker, *J. Phys. Chem. A*, 1997, **101**, 2778.
209. V. Jacques and J. F. Desreux, *Inorg. Chem.*, 1994, **33**, 4048.
210. S. Aime, M. Botta, G. Ermondi, E. Terreno, P. L. Anelli, F. Fedeli and F. Uggeri, *Inorg. Chem.*, 1996, **35**, 2726.
211. S. Friedrich, L. H. Gade, A. J. Edwards and M. McPartlin, *Chem. Ber.*, 1993, **126**, 1797.
212. E. Alessio, L. Hansen, M. Iwamoto and L. G. Marzilli, *J. Am. Chem. Soc.*, 1996, **118**, 7593.
213. H. El Amouri, J. Vaissermann, Y. Besace, K. P. C. Vollhardt and G. E. Ball, *Organometallics*, 1993, **12**, 605.
214. I. D. Salter, V. Šik, S. A. Williams and T. Adatia, *J. Chem. Soc., Dalton Trans.*, 1996, 643.
215. A. Gogoll, J. Oernebro, H. Grennberg and J.-E. Baeckvall, *J. Am. Chem. Soc.*, 1994, **116**, 3631.
216. P. S. Pregosin, R. Salzmann and A. Togni, *Organometallics*, 1995, **14**, 842.
217. U. Burckhardt, U. Gramlich, P. Hofmann, R. Nesper, P. S. Pregosin, R. Salzmann and A. Togni, *Organometallics*, 1996, **15**, 3496.
218. J. Herrmann, P. S. Pregosin, R. Salzmann and A. Albinati, *Organometallics*, 1995, **14**, 3311.
219. P. Barbaro, P. S. Pregosin, R. Salzmann, A. Albinati and R. W. Kunz, *Organometallics*, 1995, **14**, 5160.
220. P. S. Pregosin and H. Ruegger, *Magn. Reson. Chem.*, 1994, **32**, 297.
221. A. Albinati, J. Eckert, P. S. Pregosin, H. Ruegger, R. Salzmann and C. Stössel, *Organometallics*, 1997, **16**, 579.
222. B. Crociani, S. Antonaroli, M. Paci, F. Di Bianca and L. Canovese, *Organometallics*, 1997, **16**, 384.
223. M. Tschoerner, G. Trabesinger, A. Albinati and P. S. Pregosin, *Organometallics*, 1997, **16**, 3447.
224. N. Feiken, P. S. Pregosin, G. Trabesinger and M. Scalone, *Organometallics*, 1997, **16**, 537.
225. D. S. Frohnapfel, P. S. White, J. L. Templeton, H. Ruegger and P. S. Pregosin, *Organometallics*, 1997, **16**, 3737.
226. D. M. Antonelli, P. T. Gomes, M. L. H. Green, A. M. Martins and P. Mountford, *J. Chem. Soc., Dalton Trans.*, 1997, 2435.
227. M. Stradiotto, S. S. Rigby, D. W. Hughes, M. A. Brook, A. D. Bain and M. J. McGlinchey, *Organometallics*, 1996, **15**, 5645.
228. D. C. Bradley, G. E. Hawkes, P. R. Haycock, K. D. Sales and D. H. Zheng, *Phil. Trans. R. Soc., London A*, 1994, **348**, 315.
229. C. L. Perrin, T. J. Dwyer and P. Baine, *J. Am. Chem. Soc.*, 1994, **116**, 4044.
230. C. J. Sleigh, S. B. Duckett and B. A. Messerle, *Chem. Commun.*, 1996, 2395.
231. M. S. Eisen, A. Haskel, H. Chen, M. M. Olmstead, D. P. Smith, M. F. Maestre and R. H. Fish, *Organometallics*, 1995, **14**, 2806.
232. G. Hilmersson and O. Davidsson, *Organometallics*, 1995, **14**, 912.
233. M. R. Sivik, W. Bauer, P. von R. Schleyer and L. A. Paquette, *Organometallics*, 1996, **15**, 5202.
234. L. J. Farrugia, *J. Chem. Soc., Dalton Trans.*, 1997, 1783.
235. L. J. Farrugia, A. M. Senior, D. Braga, F. Grepioni, A. G. Orpen and J. G. Crossley, *J. Chem. Soc., Dalton Trans.*, 1996, 631.

236. R. D. Adams and J. H. Yamamoto, *Organometallics*, 1995, **14**, 3704.
237. T. Beringhelli, G. D'Alfonso, M. Freni and M. Panigati, *Organometallics*, 1997, **16**, 2719.
238. E. Rosenberg, L. Milone, R. Gobetto, D. Osella, K. Hardcastle, S. Hajela, K. Moizeau, M. Day, E. Wolf and D. Espitia, *Organometallics*, 1997, **16**, 2665.
239. M. J. Davis and R. Roulet, *Inorg. Chim. Acta*, 1992, **197**, 15.
240. A. Strawczynski, G. Suardi, R. Ros and R. Roulet, *Helv. Chim. Acta*, 1993, **76**, 2210.
241. M. P. Cifuentes, M. G. Humphrey, B. W. Skelton and A. H. White, *J. Organomet. Chem.*, 1996, **507**, 163.
242. K. Kite, K. G. Orrell, V. Šik and Y. Roger, *Polyhedron*, 1995, **14**, 2711.
243. J. A. Casares and P. Espinet, *Inorg. Chem.*, 1997, **36**, 5428.
244. C. L. Higgitt, A. H. Klahn, M. H. Moore, B. Oelckers, M. G. Partridge and R. N. Perutz, *J. Chem. Soc., Dalton Trans.*, 1997, 1269.
245. Z. Szabo and J. Glaser, *Magn. Reson. Chem.*, 1995, **33**, 20.
246. I. Bányai, J. Glaser, K. Micskei, I. Tóth and L. Zekány, *Inorg. Chem.*, 1995, **34**, 3785.
247. Z. Szabo, W. Aas and I. Grenthe, *Inorg. Chem.*, 1997, **36**, 5369.
248. R. E. Blumer, F. Lianza, P. S. Pregosin, H. Ruegger and A. Togni, *Inorg. Chem.*, 1993, **32**, 2663.
249. P. Barbaro, A. Currao, J. Herrmann, R. Nesper, P. S. Pregosin and R. Salzmann, *Organometallics*, 1996, **15**, 1879.
250. P. Leoni, M. Pasquali, M. Sommovigo, A. Albinati, P. S. Pregosin and H. Ruegger, *Organometallics*, 1996, **15**, 2047.
251. D. Li and R. N. Bose, *J. Chem. Soc., Dalton Trans.*, 1994, 3717.
252. I. Dellavia, J. Blixt, C. Dupressoir and C. Detellier, *Inorg. Chem.*, 1994, **33**, 2823.
253. J. Milne and A. J. Williams, *Inorg. Chem.*, 1992, **31**, 4534.
254. I. Pianet, E. Fouquet, M. Pereyre, M. Gielen, F. Kayser, M. Biesemans and R. Willem, *Magn. Reson. Chem.*, 1994, **32**, 617.
255. F. Kayser, M. Biesemans, F. Fu, H. Pan, M. Gielen and R. Willem, *J. Organomet. Chem.*, 1995, **486**, 263.
256. E. Fouquet, T. Roulet, R. Willem and I. Pianet, *J. Organomet. Chem.*, 1996, **524**, 103.
257. G. Batta, I. Banyai and J. Glaser, *J. Am. Chem. Soc.*, 1993, **115**, 6782.

Solid-state NMR Studies of Wood and Other Lignocellulosic Materials

A. M. GIL and C. PASCOAL NETO

Department of Chemistry, University of Aveiro, Campus de Santiago, Aveiro, Portugal

Solid-state NMR spectroscopy has been extensively applied to the structural characterization of the main components of wood, carbohydrate and lignin. The knowledge of the in situ *structure and behaviour of such components is, however, of extreme importance since they determine the properties of wood materials under a variety of conditions. Some of the first applications of NMR to the direct study of wood involved the use of low-resolution measurements for the study of water within the wood fibre. With the development of high-resolution NMR techniques, an increasing number of* in situ *studies of wood have been carried out in order to investigate the behaviour of wood and wood-derived systems upon conditions such as stage of tree growth, susceptibility to biodegradation, response to pulping and bleaching and use in composite materials. Reference is also made to cork, another lignocellulosic material of economic interest to which solid-state NMR has been applied in an attempt to understand the origins of cork functional properties.*

1. INTRODUCTION

Woody plants are constituted of different types of cells organized in three main morphological regions: wood (xylem), bark (phloem) and cambium, the region between wood and bark, where cell wall division and plant growing takes place.[1–5] The main components of wood are cellulose (45–50%), hemicelluloses (20–25%), lignin (20–30%) and a family of low-molecular-mass compounds

ANNUAL REPORTS ON NMR SPECTROSCOPY
VOLUME 37 ISBN 0-12-505337-1

(extractives) that may be isolated from wood by solvent extraction (1–10%).[1–5] Cellulose is a linear homopolysaccharide composed of anhydro-D-glucopyranose units linked by $\beta(1 \rightarrow 4)$ glycosidic linkages, bearing regions of well-organized supramolecular domains (crystalline) and disordered domains (amorphous).[1–7] Hemicelluloses are branched and amorphous heteropolysaccharides composed of glucose and other sugars such as xylose, mannose, galactose and arabinose.[1–5] Lignin is a reticulated macromolecule composed of phenylpropane-derived units.[1–5,8,9] In barks, the biopolyester suberin, composed of aliphatic and aromatic domains, may also be present in significant amounts.

In its many applications, wood may be used as such or after suitable chemical modification intended to tailor the material properties to those desired in the end-product. Besides the use of wood and new wood composite materials in building and furniture, wood is also extensively used as a source of fibres for pulp and paper and a source of chemicals for new materials and applications. In order to understand fully the properties of wood and the functional changes resulting from its natural or industrial transformations, it is crucial to acquire knowledge about the structural properties of wood components, their interaction within the cell wall and their behaviour when submitted to physical, chemical or biological processes. This knowledge is particularly important for the development of new applications of wood and wood-derived materials. Solid-state NMR spectroscopy has proved to be a very useful analytical tool for achieving this, as evidenced by the many scientific papers published during the past two decades on wood and wood components as well as on wood composites and chemical derivatives of wood components.

To our knowledge, no comprehensive review of solid-state NMR studies of wood and other lignocellulosics has been published in recent years. With this chapter, we hope to meet this lack in the literature. The aspects covered include, in Section 2, the study of the individual wood components (mainly cellulose and lignin) and then, in Section 3, the study of whole wood. In the latter Section, attention is focused on the *in situ* structural characterization and quantification of wood components and their transformations upon wood growth and wood biodegradation. In Section 4, we focus our attention on the application of NMR to studies of wood pulping and pulp bleaching. Pulp and paper production constitutes one of the major industrial applications of wood involving its chemical treatment. It is not surprising, therefore, that the most relevant literature on solid-state NMR of wood chemical transformations is related to this topic. Section 5 describes a few solid-state NMR studies carried out on barks and non-woody plants. The scarce number of papers found about this subject is related to the lower economic and industrial importance of these materials, with the obvious exception of cork. Finally, in Section 6, a brief overview of some selected papers on solid-state NMR studies in wood composite materials is presented. This is an emerging research area with an increasing number of published papers involving the use of solid-state NMR

techniques. It is not, however, the scope of this paper to describe exhaustively this topic, which should best be presented in a separate communication dedicated solely to wood composite materials. Derivatives of wood components,[6–10] particularly cellulose derivatives[6,7,10] have been known and investigated for many decades, having at present an extremely wide range of practical uses. Since its early days, solid-state NMR has been one of the analytical techniques most used in the study of such systems but, owing to their high number, publications on this topic are not included in this paper, again deserving to be presented in the form of a separate communication.

2. SOLID-STATE NMR OF THE COMPONENTS OF WOOD

2.1. Polysaccharides

A very wide range of solid-state NMR studies has been carried out on the main wood polysaccharide, cellulose, and on an enormous variety of cellulose derivative systems. It is not the aim of the present chapter to review the subject exhaustively but, rather, to select those studies of polysaccharide fractions with most relevance for the understanding of cellulose and hemicellulose structure in wood. In Section 3, the work that investigated polysaccharide properties within the natural environment of wood is presented and, in Section 4, the polysaccharide changes observed upon pulping and bleaching are discussed. The formulae presented in Fig. 1 represent cellulose and the most representative of the hemicelluloses.

During the early 1970s, proton NMR in the solid state was used extensively to gain insight into the interaction of water with cellulose.[11–14] Continuous-wave NMR studies determined the linewidth changes of the proton signal with increasing water content in softwood dissolving pulp and hardwood semi-chemical pulps.[11] Two environments were observed with increasing water content, one where the width at half-height decreased rapidly and another where it decreased slowly. The first was identified with bound water and the latter with free water. The effects of treatments such as beating, which increase the hydrophilicity of the sample, on the water behaviour showed that the bound water became more strongly held. The effect of temperature on the water behaviour was also investigated[11,12] and found to be dependent on the nature of the pulp, the degree of beating and the water content. Further, the lower the temperature of the measurement, the greater the accuracy of water content determination by NMR. The glass transition temperatures of hydrated cellulose samples were determined from the curve representing the linewidth at half-height as a function of temperature and, as expected, were found to depend strongly on the water content.[12] A few years later, pulsed proton NMR was used to measure T_1 and T_2 relaxation times of bleached sulfite pulps, as

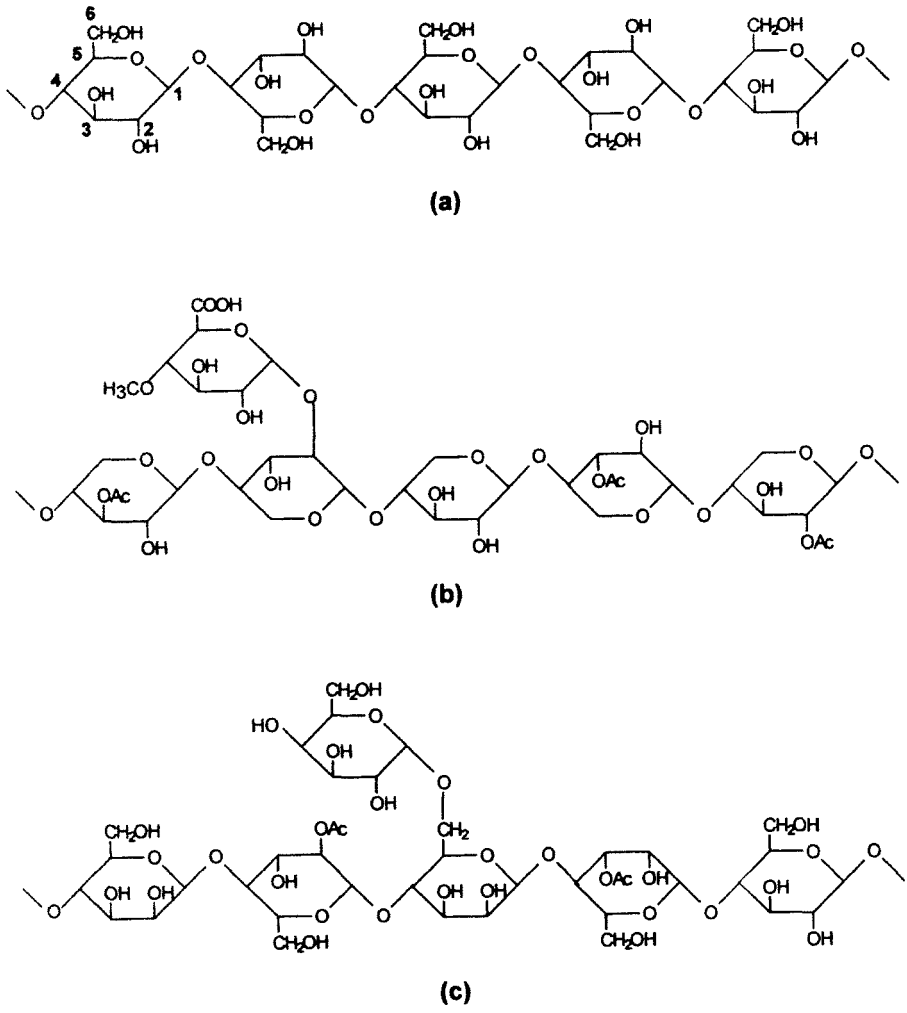

Fig. 1. Formulae of cellulose (a) and of the most representative wood hemicelluloses: glucuronoxylan from hardwood (b) and galactoglucomannan from softwood (c).

well as of highly crystalline fibrous cellulose, at different water contents.[13] Molecular motion of sorbed water was found to be strongly dependent on the degree of cellulose crystallinity, and the strength of water binding was largely dependent on the heterogeneity of the cellulose surface. The dependences of relaxation times on water content were extensively discussed in terms of a bridging network of water molecules in the cellulose matrix. A similar study applied to cotton linters, hydrated to different extents, showed that the resulting free induction decay (FID) curve enables the contributions from four

types of water to be identified: primary bound, secondary bound, free and bulk water.[14] From the T_2 values of each component, measured as a function of water content, a point of plasticization was identified and associated with the swelling of the structure, which allows increased mobility of cellulose chains. This study showed clearly that large changes in the physical properties of cellulose are expected above the plasticization point.[14]

It is well known that cellulose may exist in a variety of allomorphs distinguishable by x-ray diffraction. A great variety of work has applied ^{13}C CP-MAS NMR to the study of these allomorphs. Cellulose I is the native form of cellulose. Cellulose II is formed by regenerating cellulose from solution or by mercerizing (alkali swelling) of cellulose. Cellulose III is prepared by treatment with liquid ammonia or organic amines. Cellulose IV_I is prepared from III_I by, for example, heat treatment in glycerol at 260°C. Cellulose IV_{II} is formed from cellulose II and III_{II} by thermal treatment.[15,16]

Some of the first accounts of ^{13}C CP-MAS NMR spectra of cellulose allomorphs date from 1980.[17,18] The spectra of the two most common cellulose allomorphs, celluloses I and II, showed distinct differences in the C1 and C4 regions. The C1 and C4 splittings for the II form were first interpreted as indicative of two types of glycosidic linkages arising from an anhydrocellobiose repeating unit.[17] Comparison of the CP-MAS NMR spectrum of cellulose II with those of several oligosaccharides, however, suggested a different explanation for the C1 and C4 doublets: a crystalline structure composed of two independent chains in the unit cell.[19] Further investigations of the ^{13}C CP-MAS NMR spectrum of the I form[18,20] showed a second broad C4 resonance at 81–88 ppm and an upfield shoulder on C6 signal. Carbon T_1 and T_2 relaxation times measurements helped to establish that such features arise from amorphous cellulose regions or from cellulose molecules on the outer faces of the elementary fibrils.[18,20] Studies of several native cellulosic materials[21,22] and of low-DP (degree of polymerization) cellulose I[22] suggested that the C4 and C6 broad wings are associated with anhydroglucose moieties arising both from chains in three-dimensional regions of disorder and from crystallite surfaces. The narrower spectral features were assigned to crystallite interiors.

On the basis of the variability of multiplicity patterns for different cellulose I samples (Fig. 2) and the linear combination of some of the spectra, it was suggested that two crystalline forms exist in cellulose I: cellulose Iα and cellulose Iβ. All the native celluloses investigated were suggested to be composed of a mixture of Iα and Iβ forms in different proportions.[22] At that point, no further information on the structural differences of those forms was advanced but characteristic chemical shifts for Iα, Iβ and cellulose II were obtained (Table 1). The question at this stage was whether the two forms Iα and Iβ represented true solid-state allomorphs, with molecules possessing identical conformations, or whether they contained molecules with different conformations as well as different lattices. Numerous studies have followed aiming at gaining further insight on the crystal structures of celluloses through

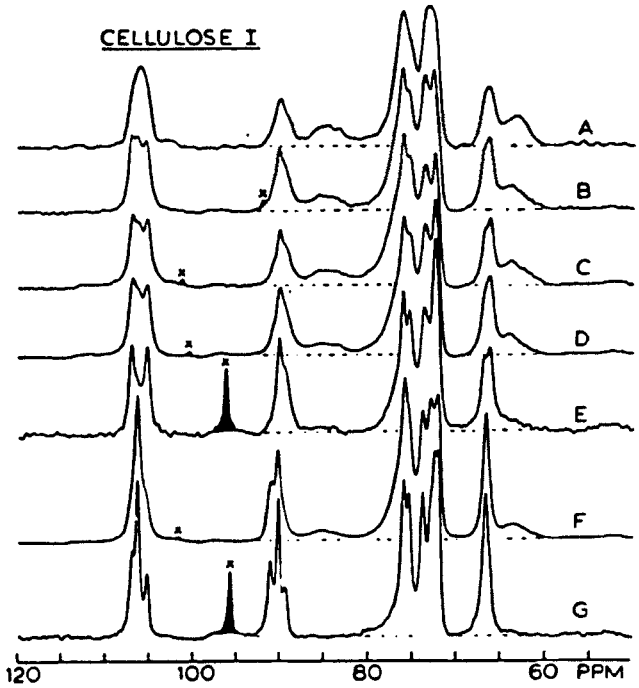

Fig. 2. ^{13}C CP-MAS NMR spectra of various cellulose I materials: A, Norway spruce kraft pulps; B, ramie; C, cotton linters; D, hydrocellulose made from cotton linters; E, a low-DP regenerated cellulose I; F, *Acetobacter xylinum* cellulose; G, *Valonia ventricosa* cellulose. (Reproduced with permission from reference 22.)

their ^{13}C CP-MAS spectra. In the light of x-ray studies, cellulose I ^{13}C CP-MAS spectra have been interpreted as reflecting the presence of both 2-chain and 8-chain unit cells[23] and, in another study, the spectral features of cellulose I and II have been found to be strongly sensitive to the number and type of intramolecular hydrogen bonds.[24] The C1 and C4 spectral regions were characterized using T_{1C} relaxation times to differentiate between crystalline and noncrystalline components.[25] These studies suggested that the crystalline spectra of hydrated native cellulose may be classified into two groups, cotton-ramie type and bacterial-valonia type, which seem significantly rich in cellulose Iβ and Iα, respectively.[22,26] To obtain further information about these crystal forms, the possibility of their interconversion was examined. It was apparent that both cotton-ramie-type and bacterial-valonia-type celluloses are converted into a cellulose richer in Iβ by annealing with saturated steam or in aqueous alkaline solution at high temperatures.[27] Conversion of cellulose I to cellulose III, and its reversion to cellulose I upon boiling in water, was followed by ^{13}C CP-MAS NMR and also showed an increase in Iβ content. The above

Table 1. ^{13}C Chemical shifts of the sharp features in the ^{13}C CP-MAS NMR spectra of cellulose I and cellulose II.

Crystal form	Chemical shifts (ppm)			
Cellulose Iα	66.5	72.0	90.2 (doublet)	106.3
		73.0	91.0	
		73.8		
		75.8		
Cellulose Iβ	66.1 (doublet)	72.4	89.3 (doublet)	105.2 (doublet)
	66.8	73.7	90.1	107.0
		75.3		
		76.1		
Cellulose II	63.6 (doublet)	73.8		
	64.2	75.9	88.7 (doublet)	106.0
		77.8	89.8	108.3

Adapted from reference 22.

results were interpreted as evidence that Iβ is the more stable of the two Iα and Iβ forms of cellulose.[28] The Iα → Iβ crystal transformation induced for valonia cellulose produced significant changes in the C1 and C4 regions of the ^{13}C CP-MAS NMR spectra.[29,30] The characteristic C1 and C4 multiplets undergo marked changes in relative intensities with increasing annealing temperature. Those lines are finally converted into doublets and such changes were interpreted in terms of the composite crystal model of cellulose in which Iα and Iβ are constituent allomorphs.

A delayed acquisition pulse sequence enabled ^{13}C NMR subspectra of crystalline and noncrystalline cellulose to be obtained based on differences between T_{1pH} relaxation times.[31–33] Spectra associated with long T_{1pH} times contained sharper peaks and were, thus, interpreted as relating to crystalline domains. Chemical shift variations and T_{1C} relaxation times helped to distinguish further subpopulations. For instance, in the subspectra of cellulose I, peaks at 88.5–90.2 ppm were identified with Iα and Iβ forms, whereas peaks at 83.9 and 84.9 ppm were assigned to C4 on surfaces of cellulose I crystals.[33] Within the crystal surface subspectrum, differences in C4 linewidths were interpreted in terms of 'well ordered' and 'poorly ordered' categories. The percentages of the different categories of crystal order could then be estimated in terms of the measured areas under each peak or range of chemical shifts.[33]

A variety of other studies[16,34–39] has applied ^{13}C CP-MAS NMR to the characterization of several other cellulose allomorphs. It was observed that most of the forms of cellulose I, II, III_I, III_{II}, IV_I and IV_{II} differed in the C4 and C6 features, thus suggesting that the mechanisms of their formation involve conformational/environmental changes of C4 and C6. III_I and III_{II} forms differ more clearly in the C1 region and in the C2, C3 and C5 region.[38]

The use of chemometric methods has proved very useful in detecting small changes in the supramolecular structure of cellulose that cause only slight differences in the ^{13}C CP-MAS NMR spectra.[40,41] Partial least-squares (PLS) and principal component analysis (PCA) have enabled the quantitation of Iα and Iβ, cellulose I and II, for different lignocellulosic samples such as different types of wood pulps.

Many of the spectral features of hemicelluloses are similar to those of cellulose, but signals tend to be broader owing to their heteropolymeric nature.[42] *In situ* identification of hemicellulose through the ^{13}C CP-MAS NMR spectrum of wood is, generally, hindered by the much stronger cellulose signals in the 60–110 ppm region of the spectra. The peaks at ~180 and 22 ppm are, however, good indications of the presence of hemicellulose acetate groups. Hemicellulose fractions of wood may be obtained through alkaline treatment of the so-called chlorite holocellulose fractions that consist mainly of carbohydrate with some residual lignin. Treatment of pine wood chlorite holocellulose with 5% aqueous KOH and subsequent treatment with 24% aqueous KOH give, respectively, hemicelluloses A and B.[42] Hemicellulose A was found to contain mainly arabino (4-*O*-methylglucurono)xylans[43,44] with a few uronic units that resonate at 180 ppm. Some galactoglucomanan acetate groups contribute to the weak peak at 22 ppm. The spectrum of hemicellulose B showed much more intense 180 and 22 ppm peaks since it is mostly composed of acetylated glucomannans. Signals from 50 to 110 ppm were assigned analogously to those of cellulose, with hemicellulose C1 and C6 carbons resonating, respectively, at 103 and 64 ppm. Further characterization of the hemicellulose fraction by NMR has been carried out in solution[45] rather than in the solid state.

2.2. Lignin

Lignin is a major component of wood materials and one of the most abundant organic materials and renewable resources on earth. It is technologically very important in the production of pulp for paper, and the knowledge of its structure within the original wood or wood-like systems and after wood delignification has become an important scientific goal. Because the nature of lignin is strongly dependent on its origin, lignins are usually classified according to their source, e.g. hardwoods or softwoods, and method of isolation, e.g. kraft, sulfite, milled wood, etc.[46]

Liquid-state NMR has been used since the early 1970s to characterize extracted lignin preparations. Comprehensive NMR characterization of lignins extracted by various techniques[47–52] has been invaluable to the elucidation of lignin structure. However, it has also become apparent that the common extraction procedures may cause significant modifications in the structure of lignin so that *in situ* studies by solid-state NMR have acquired considerable

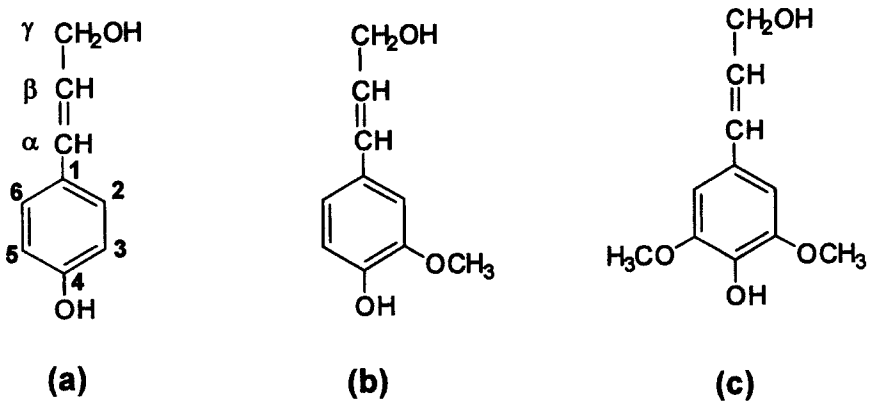

Fig. 3. Formulae of the main wood lignin precursors: (a) *p*-coumaryl alcohol, (b) coniferyl alcohol and (c) sinapyl alcohol. Natural random end-wise polymerization of these phenylpropane-type units leads to the formation of the lignin macromolecular network. This network involves interunit linkages such as *β-O*-4, *α-O*-4, *β*-5, *β*-1, 4-*O*-5 and *β-β*. Lignin units derived from (a), (b) and (c) are called respectively *p*-hydroxyphenyl- (H), guaiacyl- (G) and syringyl-propane (S) units.

interest. In addition, some isolation procedures produce insoluble lignins, which may thus be characterized by solid-state NMR. In the present subsection, the use of solid-state NMR in the study of lignin extracts is reviewed as well as the study of lignins obtained by specific synthetic or biosynthetic pathways. The latter studies bring significant aid in assigning lignin ^{13}C CP-MAS NMR spectra. The work described here will be extrapolated, in Section 3, to the *in situ* study of wood lignin, whereas the chemical changes that occur in lignin, through pulping and bleaching will be reviewed in detail in Section 4. Figure 3 represents the formulae of the wood lignin precursors.

The earliest application of solid-state NMR to lignin dates from 1970 and it made use of proton wideline NMR.[53] Dioxane lignin, thiolignin and calcium lignosulfonate prepared from a softwood were studied by following the changes in linewidth and in the second moment with temperature. An abrupt decrease in second moment at 120 K was assigned to the onset of methyl group motion. A decrease at 190–220 K indicated the onset of side-chain motion and decreases at 270–290 K and 330–370 K indicated onsets of motions of hydroxyl groups involved in weaker and stronger hydrogen bonds, respectively. On the basis of these results, a glass transition temperature of 430–450 K was estimated. The study of the variation of the second moment with temperature was combined with viscoelastic measurements in order to investigate lignin molecular motions further.[54] The results again suggested the existence of two kinds of molecular motions in non-hydrogen-bonding and tight-hydrogen-bonding regions.

The application of ^{13}C CP-MAS NMR for the characterization and quantitation of solid lignins has seen a very considerable development during the last two decades and the subject has been reviewed recently.[55,56] Early ^{13}C CP-MAS NMR spectra of lignins showed that the structure of that component depends strongly on the preparation method as well as on the type of wood.[42,57–59] The spectra of lodgepole pine wood lignins, isolated by different methods, were obtained.[42] Dioxane lignin, periodate lignin, enzymatic lignin and Braun's native lignin exhibited identical spectra to the lignin spectrum in whole pine wood. However, the Klason method was found to produce a lignin with a changed aromatic structure.

Many applications of ^{13}C CP-MAS NMR to the study of lignin have made use of the interrupted decoupling sequence, a method that selects only the quaternary carbons, along with the methyl carbons, producing a clearer spectrum in the lignin aromatic region. Resolution enhancement of the spectra has also been applied to improve the appearance of spectra and aid in their assignment.[60] The two techniques have often been combined to determine several structural properties of extracted lignin fractions such as lignin/tannin ratio, methoxyl content and syringyl(S)/guaiacyl(G) ratio.

Tannins are aromatic moieties, generally present in small amounts in wood, that are often associated with lignin and lignin extracts, thus complicating the interpretation of spectra. Examination of the aromatic region of the CP-MAS NMR spectra of lignin extracts enabled the identification of tannin contributions at 145 and 154 ppm and the estimation of lignin/tannin ratios for a range of softwoods and hardwoods.[61] In another work, lignin methoxyl content and S/G ratio were estimated after considering the quantitative ability of the ^{13}C CP-MAS experiment. For that purpose, T_{1H}, $T_{1\rho H}$ and T_{CH} times were registered for each peak in the spectra of lodgepole pine (*Pinus contorta*, softwood) and red oak (*Quercus rubra*, hardwood) lignins.[62] For each sample, these parameters covered a large range of values, thus making it difficult to extract reliable quantitative information. The authors consider, however, that quantitative arguments might be made within a range of error of about 20% and often better. Also, corrections of intensities may be applied since the values of the relaxation parameters are known. The total methoxyl content was estimated from the 56 ppm intensity for both lignin types but was found to give rather low values (5.8% and 7.4% for lodgepole and red oak, respectively), relatively to those expected (7–11% and 12–15% for lodgepole and red oak, respectively). These discrepancies may be related to the strong signal overlap, which hinders accurate quantitation. In the same work, the S/G ratio was estimated, semi-quantitatively, for extracted lignins, considering the ratio of intensities at 148 and 56 ppm.[62] Since the former peak should arise from C4 in syringyl sites (S4) and C4 carbon in guaiacyl sites (G4) and the latter peak should arise from two syringyl Ar—OCH_3 sites and one guaiacyl Ar—OCH_3 site, the I_{56}/I_{148} ratio was taken to reflect the (G + 2S)/(G + S) ratio. The S/G ratios calculated in this way for lodgepole and red oak lignins were 0.2 and 0.5,

respectively. These results were consistent with the concept that softwoods, such as lodgepole wood, contain mainly guaiacyl-derived lignins whereas hardwoods, such as red oak wood, contain a mixture of G and S. In whole wood, overlap with polysaccharide resonances may, however, severely hinder these calculations.

In a recent comparative study of the solution and solid-state ^{13}C NMR spectra of monomer and dimer lignin model compounds, it was found that the interrupted decoupling spectra of such compounds, with total sideband suppression, enabled semi-quantitative information to be extracted from the aromatic region, within a 10% error.[63] In the method used, spectral areas were determined, by tracing and weighting, for chemical shift ranges defined according to the chemical shift values observed in solution for each carbon site. The same quantitation method was then applied to lignins obtained from aspen wood and spruce wood by different extraction methods, as well as for eucalyptus kraft lignin.[63] The spectral areas of interest were 120–142 ppm (A) and 142–160 ppm (B). The quaternary resonances contributing for area B include G3, G4, S3, S5 and H4 (where H = *p*-hydroxyphenyl). The resonances contributing for area A are H1, G1, S1 and S4. Therefore, G contributes twice for area B and once for area A, whereas H and S contribute equally for A and B. The authors claim that a ratio B/A = 1 would thus indicate all H or S and a ratio of B/A = 2 would indicate all G. The values of B/A were also predicted for different percentage G residues. This method may, however, be significantly affected by the possible formation of condensation products. The resulting increase in carbon-substituted aromatic rings, during the process of lignin extraction, would result in an enhanced signal for area A. Changes such as these in the B/A ratio of lignins obtained by different extraction methods were discussed in terms of the chemical changes originated by each treatment.

The ^{13}C CP-MAS NMR spectra of Klason lignins obtained from six wood varieties, including conifer, eucalyptus and rainforest species, were examined.[64] Most of the eucalyptus and rainforest lignin spectra showed two extra peaks at 60 ppm and 152.5 ppm compared to the softwood lignins. The authors assigned the former peak to rotationally hindered methoxyl carbons brought about by lignin condensation, whereas the latter peak was assigned to aromatic carbons of syringyl units. Spectral assignment may be significantly aided by using specific isotope enrichment[65,66] or specific chemical derivation.[62] ^{13}C-labelling of various lignin precursors, at Cγ, Cβ, Cβ,γ or Cα sites, has enabled the study of the structure of a synthetic lignin, known as dehydrogenatively polymerized (DHP) lignin.[66] Much of the understanding of lignin structure comes from the comparison of isolated lignins with this artificial preparation, which has for a long time been considered to be representative of native lignin. The enhanced ^{13}C resonances in the spectra of the enriched materials enabled the establishment of the major bonding patterns, namely sub-structures containing coniferyl alcohol, β-*O*-(4–aryl)glycerol and pinoresinol moieties. In order to establish the minimum detectable level of enrichment

needed to observe lignin signals in a lignin/cellulose matrix, a mixture of DHP lignin/cellulose 24% (w/w) was examined, showing that lignified tissue enriched to >4% in ^{13}C will clearly show the bonding patterns of lignin in the CP-MAS NMR spectrum. The use of ^{13}C-labelling has also been applied to natural lignin by administering specifically labelled ferulic acid units to the plant species *Triticum aestivum*[67] and to a rapidly growing hardwood *Leucaena leucocephala*.[68] In the latter study, ^{13}C-labelled phenylalanine was also administered. The major changes observed in the spectra were enhanced signals at about 75 and 82 ppm, respectively assigned to C3 and β-O-4 linkages in the substructures in Fig. 3. Interestingly, spectral features observed for the ^{13}C-enriched natural lignins were found to be somewhat different from those observed for DHP lignin,[67,68] thus suggesting that some care is needed in assuming identical structures for the latter system and native lignin.

Chemically modified lignins from lodgepole pine and red oak[62] were obtained by HCl hydrolysis and then *O*-methylated or acetylated. The *O*-methylated samples were studied at natural ^{13}C abundance and also by using ^{13}C-enriched CH_3I. *O*-Methylation of red oak lignin caused a marked increase at 56 ppm and a relative decrease at 148 ppm reflecting the conversion of Ar—OH groups to Ar—OCH_3. An increase at 61 ppm was assigned to methylation of S-type hydroxy sites, whereas methylation of G-type hydroxyls gave rise to intensity at 55–56 ppm. Changes at 63 and 75 ppm also showed that methylation of Cγ—OH (resonating at 63 ppm in untreated lignin) causes a shift to 75 ppm. Methylation of lodgepole lignin leads to much less marked spectral changes than for red oak lignin, reflecting the differences in lignin composition of the two woods. Acetylation of red oak lignin led to more complex spectral changes than did methylation. A marked increase at 21 and 171 ppm reflected the methyl and carbonyl carbons of the resulting esters. Acetylation of phenolic OH groups caused a decrease of intensity at 148 ppm and 106 ppm and a corresponding increase at 139–142 ppm. Changes at 85–90 ppm also showed that acetylation of the aliphatic side-chain occurs primarily at the Cγ position. The same changes were observed for lodgepole lignin, although less marked.

The validity of the ^{13}C assignments of lignin has, more recently, been checked by a systematic comparison of solution-state and solid-state ^{13}C chemical shifts of 33 monomer and dimer lignin models.[63] The solution ^{13}C NMR spectra of all the compounds were assigned and the chemical shift positions were compared to those measured in the solid state for the same compounds. Chemical shift changes, $\Delta\delta$, greater than 4.0 ppm were taken as significant and were observed mainly for the carbons of the substituent at C1 and for the C2 and C6 carbons of the aromatic ring. This indicated that the conformation of the C1 substituent is particularly determinant for solution–solid-state differences. Furthermore, the cinnamic acid derivatives showed a very large negative $\Delta\delta$ for the carboxyl carbon, which was interpreted as hydrogen bonding involving this group in the solid state.

The effects of pyrolysis of *Eucalyptus grandis* lignin on its structure were investigated by ^{13}C CP-MAS.[69] A decrease in the signals in the 0–100 ppm region and an increase at 100–150 ppm at temperatures higher than 200°C showed that an increase of aromaticity occurs. Simultaneously, C—C and C—OCH_3 bonds, resonating between 41 and 92 ppm, are broken and α,β-unsaturations and carbonyl groups are formed. The low-temperature pyrolysis of two lignins derived from sweetgum[56] resulted in a marked change in relative intensities at 148 and 153 ppm. This indicated that the β-*O*-4 linkages in syringyl units are readily cleaved under the pyrolysis conditions used. A simultaneous increase in intensity in the 52–15 ppm region, assigned to aliphatic carbons not adjacent to oxygen, was consistent with alkyl chain dehydration. These dehydration reactions should produce alkenes that rapidly react to give alkyl chains. Further, it was observed that, under the conditions studied, no carbonyl groups accumulate in the solid residue and methoxyl groups were not cleaved below 335°C.[56]

2.3. Lignin/carbohydrate complex

The nature of the interactions between polysaccharides and lignin in the wood matrix has been the subject of a few studies, particularly because covalent linkages may be promoted not only through biosynthesis, but also by important practical processes such as high-temperature drying, wood plasticization, hydrothermal treatment and pulp production.

One of the first applications of ^{13}C CP-MAS NMR to the study of extracted lignin and carbohydrate fractions showed that the spectra of all lignin samples, obtained using different extraction methods, exhibited carbohydrate peaks, and vice versa.[42] The authors interpreted these observations as evidence of a lignin–carbohydrate complex existing in wood. Some years later, the use of ^{13}C CP-MAS NMR was extended to the characterization of wheat (*Triticum aestivum* L.) root tissue, grown in a medium enriched in ^{13}C-labelled lignin precursors.[70] The enhanced signals could not, however, be readily explained on the basis of bonding patterns in synthetic lignins. For instance, a very intense peak at 81–82 ppm was tentatively assigned to bonding of the C3 carbon in ferulic acid with carbohydrate-, phenolic- or ferulic acid-like moieties. This possibility was confirmed in a similar study applied to a rapidly growing hardwood *Leucaena leucocephala*.[68]

A variety of studies have indicated that the formation of lignin–carbohydrate linkages may give rise to a benzyl ester- and benzyl ether-type bonds.[71–74] A ^{13}C CP-MAS NMR study of residual lignins in softwood kraft pulps showed the presence of large amounts of galactose in all lignin samples. This was interpreted as an indication of the establishment of covalent carbohydrate–lignin linkages established through galactose.[75] In a recent study, the solid-phase reactions between kraft cellulose and lignin models (vanillyl

alcohol and veratryl alcohol) were performed at 120°C and the resulting products were characterized by ^{13}C CP-MAS.[76] The authors observed the appearance of peaks at 130.3 and 131.6 ppm, respectively, for the products of the reactions involving the two models, both peaks shifted to higher field relatively to those in solution. These observations were interpreted as indicating the formation, during thermal treatment, of a linkage between cellulose C6 hydroxyl and one of the ring substituents of the model compound, reflecting the favouring of primary hydroxyls in esterification reactions.[74] This was confirmed by measuring T_{1pH} relaxation times for the product of the reaction between cellulose and veratryl alcohol to check the efficiency of spin diffusion and, hence, proximity of those moieties. The complete and homogeneous spin diffusion found between them gave an estimate of 9 nm for the separating distance, which is consistent with the existence of a chemical bond linking cellulose and the alcohol.

3. SOLID-STATE NMR OF NATURAL WOOD

3.1. Low-resolution NMR studies

Some of the earliest NMR work on whole wood aimed at determining moisture content.[77,78] This is a very important measurement since many operations in the wood-based industries are closely related to it. However, it must be taken into account that an accurate moisture measurement relies not only on the precision of the technique employed but also on the definition of the boundary between bound and free water. Therefore, moisture content (M) is usually closely related to the method employed. Following some earlier results,[77] the moisture content of pine, beech and oak woods, as well as several types of pulp samples, was measured by pre-weighting the samples and recording the continuous-wave proton spectrum at 15 MHz.[78] The area under the narrower peak was integrated assuming that it arose only from water molecules. The accuracy of this NMR method was comparable to that of the gravimetric method with a standard deviation of approximately 0.6%. Pulps exhibited a non-linear calibration curve, as opposed to the wood samples and, while suitable M ranges for measurements in wood were in the range 0–60%, in pulps accuracy of the NMR determination was only in the 0–15% range.[78] Further attempts to use continuous-wave NMR to evaluate M in wood were made,[79,80] but, soon after, pulse NMR began to be used for the measurement of M with much higher efficiency.[81] More recently, pulsed NMR was used to determine the absolute moisture content below the fibre saturation point (FSP) of aspen wood.[82] The FSP is the usual moisture content of wood in commercial products and is considered to be about 30%. By recording the proton FID of the hydrated wood sample and knowing the relative spin density of the wood

relative to water (RSD), the absolute moisture content was calculated through

$$M_{NMR} = S_{water} \times \frac{1}{S_{wood} \times RSD} \times 100 \quad (1)$$

where S_{water} is the signal intensity of the slow-decaying FID component and S_{wood} is the signal intensity of the fast-decaying FID component. The RSD is the ratio of the proton spin density of wood and that of water. The proton spin density of wood (or water) is proportional to the signal intensity of the dry wood (or of water) divided by its mass. However, it was observed that the M_{NMR} results depended significantly on the procedure used to hydrate the wood. For instance, for samples prepared by liquid water adsorption, NMR predicted a higher moisture content than the M determined gravimetrically. A similar discrepancy was found for the water vapour adsorption samples with M near the FSP. Such deviations were interpreted as reflecting the effects of chemical exchange between the wood and water phases but, in addition, possible effects of mobilization due to swelling of the wood matrix were considered. A possible connection between these effects and the formation of water clusters was also discussed.

The calculation of the second moment of the proton NMR lineshape in the spectrum of solid wood, together with the recording of T_2 of the water in the sample, enabled the study of water binding in lodgepole pine heartwood, as a function of hydration below the FSP.[83] The FID signal was fitted to the second-moment expansion equation and used to calculate the water content in the sample in terms of the intensity ratio of the liquid and solid signals, as defined in a previous report.[84] The NMR method measured an FSP of 27%, which agreed with the value calculated by the isotherm model. The second moment for dry wood was about 23% lower than that obtained by the rigid lattice calculation, indicative of a rigid structure with some anisotropic molecular motion occurring. Above 5% hydration, the second moment decreased by 13–16% indicating a loosening of the molecules with increased moisture content. The T_2 of the water in the sample increased with water content but provided no evidence of the separate water fractions predicted by isotherm theory. An explanation was advanced in terms of water exchange occurring on a time scale faster than the measured T_2 time.

The interpretation of water T_2 relaxation in biological systems is typically complicated by a number of factors such as heterogeneity, chemical exchange, presence of paramagnetic species, compartmentalization, diffusion and magnetic susceptibility.[85] The regular and robust nature of wood structure was found, however, to help in simplifying the interpretation of such relaxation data. The proton NMR signal obtained for green wood was separated into solid wood, cell-wall water and lumen water. The first component decays completely in tens of microseconds; the cell-wall water signal has a T_2 of a few milliseconds, and the lumen water decays in tens to hundreds of milliseconds.[86–88] Proton

NMR has been used to follow the extraction of water from wood as wood dries, and it showed that lumen water is extracted first, followed by cell-wall water.[89,90] A number of physical properties of wood are found to change as the cell-wall water is removed: the heat required to remove cell-wall water is significantly higher than that used to remove lumen water; wood mechanical strength increases as cell-wall water is removed but is independent of lumen water content; thermal and electrical conductivity are altered by removal of cell-wall water but independent of lumen water content.[91]

A diffusion model for spin–spin relaxation of compartmentalized water with a relaxation surface was verified for lumen water in wood.[92] Spin–spin relaxation time measurements were recorded for water in redwood sapwood, spruce sapwood and spruce compression-wood samples, which possessed different cell-lumen radius distributions as evaluated by scanning electron microscopy. For redwood, NMR measurements were made for temperatures in the 4–55°C range over which the average lumen-water T_2 decreased from 177 to 103 ms. The lumen-water theory was in agreement with the experimental results and evidence of higher-order relaxation modes was found. The model was extended to two water regions to characterize the surface relaxation in terms of spin–spin relaxation, the diffusion coefficient of the cell-wall water and the partition coefficient. Using the measured T_2 times and the relative populations of lumen and cell-wall water, estimates of cell-wall water diffusion rates were obtained. The activation energy for cell-wall water diffusion was also estimated and found to be about 40% higher than the free water value.

3.2. High-resolution NMR studies

Extensive characterization of cellulose and lignin fractions in the solid state has enabled the assignment of a typical wood ^{13}C CP-MAS NMR spectrum (Fig. 4) to be made. Table 2 summarizes the assignments of the different peaks observed.

3.2.1. Study of wood growth

Earlywood and latewood *Pinus radiata* samples were studied by ^{13}C CP-MAS NMR as a function of number of growth rings away from the pith (41 growth rings).[93] Samples of earlywood and latewood were removed from several of the growth rings along with samples of compression wood, opposite wood, root and bark wood. Polysaccharide C4 signals were used to estimate crystallinity of the various samples.[60] This showed that only small changes in crystallinity exist for the various growth rings and between earlywood and latewood, except for the growth ring closest to the pith, which showed a higher content of amorphous polysaccharides. This is consistent with other studies that suggest that an increase of 2–4% pentosan occurs near the pith. In addition, the pith

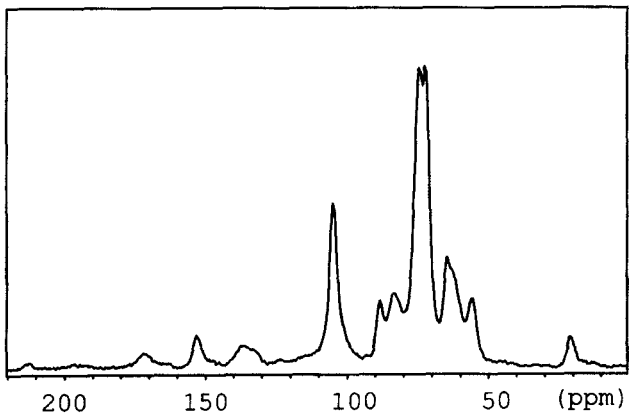

Fig. 4. ^{13}C CP-MAS NMR spectrum of *Eucalyptus globulus* wood (hardwood).

Table 2. General assignments of the ^{13}C CP-MAS NMR spectrum of wood.[16,42,55,56,62,98]

	Assignments	
Chemical shift (ppm)	Functional group	Component[a]
22	$\underline{C}H_3-COO-$	Carbohydrate
56	$Ar-O\underline{C}H_3$, $-O\underline{C}H_3$	Lignin and carbohydrate
60	$-\underline{C}_\gamma-OH$	Lignin
65	$-\underline{C}H_2OH$	C6: carbohydrate
72	$-\underline{C}HOH-$	C2,3,5: carbohydrate
74	$-\underline{C}_\alpha-OR$	Lignin
75	$-\underline{C}HOH-$	C2,3,5: carbohydrate
84	$-\underline{C}_\beta-OR$	Lignin
84	$-\underline{C}HOH-$	C4: carbohydrate
89	$-\underline{C}HOH-$	C4: carbohydrate
105	$-\underline{C}H-$	C1: carbohydrate
106	$-\underline{C}H-$	S2, S6: lignin
112	$-\underline{C}H-$	G2: lignin
115	$-\underline{C}H-$	G5: lignin
120	$-\underline{C}H-$	G6: lignin
134	quaternary C	S1(ne), S4(ne), G1(e): lignin
137	quaternary C	S1(e), S4(e), G1(e): lignin
148	quaternary C	S3(ne), S5(ne), G1,G4: lignin
153	quaternary C	S3(e), S5(e): lignin
173	$-\underline{C}OO-R$, $CH_3-\underline{C}OO-$	Carbohydrate

[a]e: etherified units in C4; ne: non-etherified units in C4 (phenolic).

and the bark samples were shown to have a high content of amorphous polysaccharides, consistent with their very friable nature. Lignin contents were determined from the ^{13}C CP-MAS NMR spectra using methods previously described.[94] The lignin content was found to be highest near the pith. Otherwise, lignin contents seemed uniform, although the latewood samples had slightly less lignin than the earlywood. Branch compression wood was found to be more lignified than wood from the trunk. High lignin contents were found for the samples of branch opposite wood. The degree of etherification was calculated by curve-fitting of the interrupted-decoupling spectra and indicated that all growth rings had the same etherified guaiacyl fraction (0.8 ± 0.1) except for the most recent growth, the earlywood of ring 41, which had a lower etherified guaiacyl fraction of 0.61 ± 0.1. For branch compression, opposite and root wood, relatively low values (0.70 ± 0.1) were found. The authors took the peaks at 145 ppm and 154 ppm as indicative of the presence of tannins and estimated tannin contents by curve fitting of the spectra and spectral simulation. Bark was estimated to have 24% tannins, whereas the pith sample contained about 10% tannins. No significant tannin contents were found in the ring section woods.

3.2.2. In situ *study of wood and wood components*

Some of the first ^{13}C CP-MAS NMR spectra of wood were reported in the early 1980s.[42,95,96] The effects of wood pyrolysis were investigated for spruce and oak woods and the changes in the ^{13}C NMR spectra showed that cellulose started decomposing before lignin. Above 615 K, both components decompose, resulting in a variety of aromatic compounds.[95,96] At about the same time, an extensive ^{13}C CP-MAS study of lodgepole pine wood was carried out[42] with the goal of initiating the investigation of how wood components, by then considerably well characterized in the solid state, interact *in situ*. A comparison between the spectra of ground and ball-milled wood showed that milling broadens the spectrum dramatically, indicating a significant increase in the amorphous material. Dimethyl sulfoxide extraction and steam swelling produced relative intensity changes in the 70–80 ppm region and decrease in the 174, 84, 63 and 22 ppm peaks. These changes were interpreted as conversion of amorphous cellulose into crystalline cellulose and removal of some hemicelluloses. The same work investigated the effects of enzymatic treatment of extractive-free wood for the preparation of lignin. After treatment of a wood sample with cellulysin, the resulting ^{13}C CP-MAS NMR spectrum showed that almost all cellulose had been removed. The spectra of solid ash wood and spruce wood[97] were compared and differences were mainly observed at the carbonyl and acetyl methyl regions, thus indicating different relative contents of hemicellulose. Evidence of a small quantity of hemicellulose was found in the spectrum of extractive-free pine wood,[98] expressed by the broad, poorly resolved shoulder on the high-field side of the 105 ppm C1

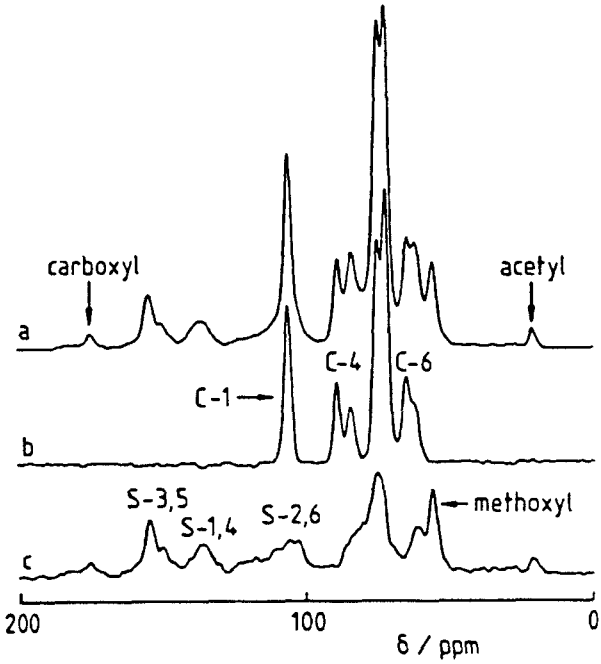

Fig. 5. (a) ^{13}C CP-MAS NMR spectrum of *Beilschmiedia tawa* wood and separate subspectra of (b) cellulose and (c) non-cellulosic components, i.e. (c) represents the difference between (a) and (b). S represents syringyl lignin units. (Reproduced with permission from reference 99.)

peak. The observed cellulose features indicated the predominance of native natural cellulose, cellulose I, as indicated by C1 at 105 ppm, C4 at 89 ppm with a broad shoulder at 84 ppm, and C6 at 66 ppm with a broad shoulder at 63 ppm. The broad shoulders on the C4 and C6 resonances were indicative of amorphous cellulose or less ordered surface cellulose molecules.

Natural differences in proton spin–lattice relaxation times, due to restricted spin diffusion, helped to differentiate the spectra of cellulose and non-cellulosic domains and determine the degree of crystallinity of cellulose in moistened wood.[99] The delayed acquisition pulse sequence enabled subspectra relating to moieties with different $T_{1\rho H}$ values to be obtained and this resulted in a subspectrum of cellulose and a second one of non-cellulosic components (lignin and hemicellulose) (Fig. 5). Cellulose crystallinity was then estimated through the ratio of the areas measured in the subspectrum of cellulose at

89 ppm (C4, crystalline) and 84 ppm (C4, amorphous). This study found lower crystallinities for hardwoods than for softwoods. Further investigation of the crystalline cellulose subspectra of seven different tree species involved digital resolution enhancement of the subspectra and enabled the 90 and 88 ppm peaks, characteristic of crystalline cellulose C4 in Iα and Iβ forms, to be distinguished.[101] The ratio of the intensities of those peaks enabled estimates of the relative proportions of Iα and Iβ to be obtained. Interestingly, it was found that softwood celluloses have a higher relative amount of Iα, whereas hardwood have a higher amount of the Iβ form.

The lignin content of wood was initially estimated from the wood ^{13}C CP-MAS NMR spectrum by measuring the area under the 141–159 ppm region, relative to the total area of the spectrum. This band is associated with G3, G4, S3 and S5, however, if tannins are present an interfering band will appear at 145 ppm and hinder an accurate estimation of lignin.[55,102] Quantitation of lignin and cellulose was also attempted by first investigating the CP signal intensity build-up and decay of each peak in the spectrum of pine wood.[98] Equivalent CP dynamic conditions were found for lignin and polysaccharide peaks so that a 1 ms contact time was suitable to quantify both.[94,98] For cellulose, the average empirical formula $C_6H_{10}O_5$ was assumed with an average molecular mass of 162 g mol^{-1}. Corrections for the amount of hemicellulose needed to be considered in some cases. For lignin, the representative empirical formula of conifer lignin was assumed, $C_9H_{7.95}O_{2.4}(OCH_3)_{0.92}$, and a molecular mass of 183 g mol^{-1} was taken. The integrated areas in the 160–109 ppm (A_{low}) and 109–20 ppm (A_{high}) regions were used to represent, respectively, lignin aromatics and carbohydrate sites overlapped with lignin alkyl and methoxyl carbons. The areas relating to lignin and carbohydrate, A(lig) and A(carb), were related to the measured areas by

$$A(\text{lig}) = (9.92/6)A_{\text{low}} \qquad \text{and} \qquad A(\text{carb}) = A_{\text{high}} - (3.92/6)A_{\text{low}}$$

since only 6 carbons are accounted for by A_{low}, of the total 9.92 lignin carbons. Thus, the contribution of the remaining carbons of lignin must be subtracted from A_{high} to obtain a good indication of the carbohydrate area. After normalization of the A(lig) and A(carb) areas, the percentage lignin was obtained from

$$\%\text{lignin (w/w)} = 100 \times \frac{183/9.92 \times A'(\text{lig})}{183/9.92A'(\text{lig}) + 162/6A'(\text{carb})}$$

where A'(lig) and A'(carb) are the normalized areas for lignin and carbohydrate. The percentage lignin in pine wood obtained by NMR, 26.5%, was found to be in very good agreement with the percentage lignin obtained by the Klason method, 25.5%. This approach may, however, involve considerable error if the assumed empirical formulae, particularly for lignin, do not reflect

the actual nature of the components. In this case, adjusted formulae must be used.

A similar quantitation procedure has been applied in a comparative study of softwoods and hardwoods.[94] Spectral areas assigned to polysaccharides, lignin aromatics and methoxyls and hemicellulose acetyl groups were measured by cutting out and weighting. In order to quantify the aromatic lignin content, account was taken of spinning sidebands contribution by introducing a correction factor obtained from studies of sideband intensities for pure model compounds, such as syringic acid and vanillyl alcohol. After this correction, the ratio of polysaccharides to aromatic lignin spectral areas was calculated and, hence, used to calculate the percentage lignin. This was done again by assuming average empirical formulae for each component, but a distinction was made between the softwood sample and the hardwood sample since they contain different relative amounts of guaiacyl and syringyl units: $C_9H_{7.92}O_{2.40}(OMe)_{0.92}$ with molecular mass of 183 for the softwood and $C_9H_{7.72}O_{2.75}(OMe)_{1.54}$ with molecular mass of 207 for the hardwood. For the softwood, the percentage of lignin determined by NMR was somewhat inflated relatively to the chemical method determination, probably owing to loss of soluble lignin in the latter.

In a typical CP-MAS NMR spectrum of a hardwood, a sharp peak at 153 ppm and a broader peak at 149 ppm are assigned, respectively, to S3 and S5 and to G3 and G4. In the spectrum of a softwood, it may be assumed that only G contributes for the aromatic region and an S/G ratio may be estimated from the two 153 and 149 ppm peaks.[103] The procedure consisted in subtracting the softwood (G) spectrum from the hardwood spectrum so that the intensity is nulled in the 146–149 ppm region. The remaining area at 153 ppm reflects the S content and the ratio of this to the original area at 146–149 ppm gives the S/G ratio.

The signal observed at 140–156 ppm in the interrupted decoupling spectra of softwoods often shows partially resolved structure that has been used to estimate the abundance of β-*O*-4 ether linkages.[93] The NMR spectra were simulated by adding four Gaussian lineshapes so that two peaks of equal intensity at 152.6 and 148.4 ppm reflected contributions from etherified units and two peaks at 148.4 and 145.0 ppm, reflected non-etherified units. For spruce wood (*Picea abies*), the best fit gave 60% etherification. The same approach is hindered, for hardwoods, by the intense peaks of both G and S structures.[60]

To facilitate quantitative analysis based on ^{13}C CP-MAS NMR spectra of wood, the effect of hydration in increasing the signal-to-noise ratio and resolution of white spruce wood was investigated.[104] Improvement of resolution was particularly significant for polysaccharide peaks in the spectrum of a wood sample containing 2 ml of water per gram of wood. However, the linewidth of lignin aromatic peaks did not change upon hydration, which indicated that, owing to the condensed spatial nature of lignin, relaxation to more ordered conformations is hindered. In addition, the signal-to-noise ratio

improved more than 50% for aliphatic carbons compared to the aromatic carbons. The authors suggested that water may assist the cross-polarization process through hydrogen bonding which, naturally, would involve preferentially the polysaccharide C6 carbons and the lignin aliphatic carbons of lignin, relative to lignin aromatic carbons. Accordingly, the cross-polarization rate constants were found to increase more with water content for the aliphatic carbons than for the aromatic carbons.

Differences in relaxation times for the different wood components have been explored to elucidate the spatial relationships of cellulose and lignin. Both proton spin–lattice relaxation times, T_{1H}, and proton spin–lattice relaxation times in the rotating frame, $T_{1\rho H}$, are determined by spin diffusion. T_{1H} values are usually of the order of 1 second and hence they may be used to study domain sizes larger than 30 nm. On the other hand, $T_{1\rho H}$ is typically of the order of milliseconds and so can be used for domain sizes in the 2–30 nm range. A variation of the ^{13}C CP-MAS NMR experiment was used to obtain direct evidence of spin diffusion between domains in wood, and a time constant of 14 ms for mixing of proton spins between cellulose and lignin of *Eucalyptus regnans* wood was found.[105] This time scale should be short enough for averaging of T_{1H} through spin diffusion but long enough to prevent averaging of $T_{1\rho H}$ values, so that similar T_{1H} values and distinct $T_{1\rho H}$ values would be expected for a wood sample. However, apparently conflicting results were obtained for proton spin relaxation times in wood, with some studies indicating distinct T_{1H} values[106] and indistinguishable $T_{1\rho H}$ values[98,107] for wood cellulose and lignin. These apparent inconsistencies were, in a subsequent work, explained in terms of the very high sensitivity of T_{1H} and $T_{1\rho H}$ to the different water contents in the samples studied.[100] Water content in wood should, therefore, be carefully monitored when proton relaxation times are to be measured and compared. Moistening wood was found to enhance T_{1H} relaxation and improve discrimination between $T_{1\rho H}$ relaxation times of cellulose and lignin. A detailed proton spin diffusion study of moistened *P. radiata* wood was then carried out. Comparison with computer-simulated relaxation curves showed that the experimental relaxation values are consistent with a model in which microfibrils of cellulose about 14 nm thick are encrusted with a mixture of hemicelluloses and lignin. Evidence was also found for relatively intimate mixing of crystalline cellulose with disordered cellulose and of acetylated hemicelluloses with lignin. The presence of paramagnetic impurities, such as some metal ions, may seriously affect T_{1H} values in wood and, although this effect has been explored to gain information on the structural connectivity of polysaccharides and lignin,[108] the importance of removing those ions has been demonstrated.[109–111] T_{1H} values of wood components were also found to be strongly dependent on the static magnetic field and a qualitative relationship between T_{1H}^{-1} and ω_0^{-2} was found.[110]

Additional information on the spatial proximity of wood components has been obtained through the application of the spin-exchange experiment to

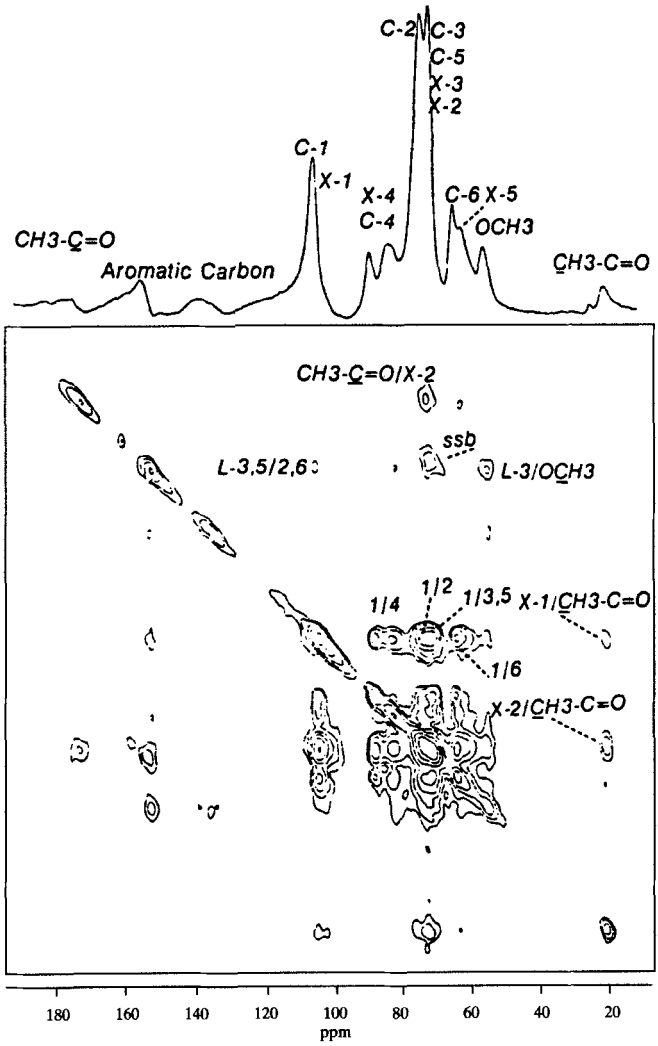

Fig. 6. 2D CP-MAS ^{13}C NMR spin-diffusion spectrum obtained with a 2 s mixing time. The horizontal projection corresponds to the normal 1D recorded under CP-MAS conditions. (Reproduced with permission from reference 112: Solid State NMR, 8, M. Bardet, L. Emsley and M. Vincendon, Two-dimensional spin-exchange solid state NMR studies of ^{13}C-enriched wood, 25, 1997, with kind permission of Elsevier Science-NL, Sara Burgerhartstraat 25, 1055 KV Amsterdam. The Netherlands.)

^{13}C-enriched wood.[112] Figure 6 shows a 2D ^{13}C CP-MAS NMR spin-diffusion spectrum of aspen wood (*Populus euramericana*), grown under a $^{13}CO_2$-enriched atmosphere. Dipolar coupling correlations between spins at progressively longer distances were obtained as the mixing time increased, and this enabled the sequential assignment of all cellulose resonances. The same

approach also enabled structural considerations regarding hemicellulose to be made. Since no correlations were observed between the three main wood components, it was concluded that, at least on a scale of some nanometres (corresponding to the time scale of the experiment), the three components are situated in separate phases. This is consistent with previous NMR studies[100] and with the existing models of wood structure in which different phases are at least of the order of 3–10 nm.

The investigations of the behaviour and structural changes of wood upon specific processing conditions are of great interest, particularly if new technologies are under development. Following this line of research, the effects of shear deformation and high-pressure (SDHP) treatment on wood, cellulose and paper have been investigated.[113] Besides indicating a decrease of cellulose crystallinity, the ^{13}C CP-MAS NMR spectrum of the wood sample subjected to SDHP showed the appearance of a peak at 98 ppm (assigned to C1 of the chain reducing end), which has been associated with cellulose depolymerization. The treatment also induces changes in the lignin spectral region, namely, an increase at 148 ppm that was interpreted as indicating the breaking of aryl ether β-*O*-4 bonds of syringyl units. Proton spin–lattice relaxation times measured for wood and steam-exploded wood samples, previously subjected to SDHP, suggested that some degree of separation between cellulose and lignin occurs in the process.

Many studies of polymer systems have aimed at finding a correlation between molecular phenomena and the macroscopic performance of the material. Such a relationship is also particularly important in the field of wood composites performance. Such work has been initiated recently by combining dynamic mechanical analysis (DMA) results with solid-state ^{13}C CP-MAS parameters.[114] Samples of yellow poplar (*Liriodendron tulipifera*) and hard maple, subjected to a range of treatments known to alter the dynamic modulus of the material (varying moisture content, densification, chemical treatments), were studied by using an inversion recovery CP experiment. This enabled cross-polarization times, T_{CH}, to be obtained and an average $\langle T_{CH}\rangle^*$ was estimated, with basis on the different responses of protonated and non-protonated carbons. A correlation between $\langle T_{CH}\rangle^*$ and the dynamic storage modulus (E') was established for dry treated and untreated wood:

$$E' \propto \frac{\omega^2 (1/\langle T_{CH}\rangle^*)^2}{1 + \omega^2 (1/\langle T_{CH}\rangle^*)^2} \tag{2}$$

which indicated that both parameters are determined by similar near-static molecular motions in wood. Interestingly, the relationship was found not to be valid for wet wood samples, owing to plasticization rendering the CP process less efficient. This work is a significant step forward in relating molecular phenomena with macroscopic performance of wood and wood composites.

3.2.3. Study of wood biodegradation

The effects of microbial or enzymatic degradation on the structure of wood have attracted a great deal of scientific interest, not only in order to gain insight into the resulting structural damage to the material, so that a way to slow down or prevent undesirable changes may be devised, but also in order to use biodegradation as a technique for converting wood and similar materials into value-added products. Factors such as lignin content, structure and distribution as well as surface area and porosity of the cellulose fibre[115–117] affect the accessibility to bioconversion processes and the rate of enzymatic hydrolysis.

The white-rot fungus *Ganoderma australe* causes decay of hardwood in Chilean rain-forest producing a delignified material that is used as cattle feed.[118,119] Since it is known that differences in hardwood lignin characteristics can affect the decay produced by fungi, lignin composition of a range of Austral hardwoods was studied by solid-state ^{13}C NMR.[120] ^{13}C CP-MAS was used to estimate syringyl(S)/guaiacyl(G) ratios for the different woods as well as their variation with decay. S/G ratios were calculated by subtraction of a cedar wood spectrum (G-rich lignin) from the wood spectra. The S/G lignin ratio was found to be relatively high for the initial ulmo wood (*E. cordifolia* wood) which was also one of the most biodegradable woods under study. The authors concluded that the high S/G ratio is the main factor conferring a high biodegradability to lignins from *E. cordifolia* and other Chilean woods, relative to the *G. australe* fungus. The S/G ratio was seen to decrease during decay, as a result of the delignification process. Changes in wood and straw constituents after solid-state fermentation with ligninolytic fungi, *Trametes versicolor* and *Pleurotus eryngii*, were less marked than those resulting from *G. australe* decay.[121] In addition, the spectra of the fermented samples showed that, instead of only lignin being removed, both cellulose and lignin are removed.

White-rot fungi other than *G. australe* degrade both lignin and polysaccharides,[122,123] reflecting the fact that rates of removal of lignin and polysaccharides depend not only on the wood species but also on the choice of white-rot fungus. Application of ^{13}C CP-MAS to the decay of the softwood Colorado blue spruce (*Picea pungens*) by a variety of white-rot fungi (*Phanerochaete chrysosporium*, *Trametes versicolor* and *Dichomitus squalens*)[122] enabled percentage lignin, percentage OCH_3 and cellulose crystallinity to be estimated as a function of decay. These determinations were based on the deconvoluted spectra after correction of spectral intensities by taking into account the different parameters of cross-polarization dynamics. The spectral changes provoked by the white rots indicated that both lignin and polysaccharides are removed almost evenly. This has been confirmed by more recent studies of softwood white rot.[123] However, a slight preference of the fungi for amorphous polysaccharides relative to crystalline cellulose has also been observed.[123] Intensity increases at 124 and 153 ppm were interpreted in

terms of the softwood biodegradation mechanism as reflecting an increase in vanillic acid-type moieties formed by Cα—Cβ bond cleavage and oxidation of lignin. An analogous approach was taken in studying the effects of the same fungi on the hardwood paper birch (*Betula papyrifera*).[124] The decay of the hardwood was similar to that of the softwood, in the sense that lignin and polysaccharides are equally removed and there is a slight preference for amorphous polysaccharides. A decrease in the S/G ratio was noted for the hardwood at higher stages of decay, which has been interpreted as reflecting a direction of decay from the cell lumen towards the cell wall. In addition, and unlike the case of the softwood, no indication was found of Cα—Cβ cleavage, which showed that this type of reaction is not as prominent in hardwoods as in softwoods. Alternatively, it may be the case that the products of this reaction are more quickly removed from the bulk of the wood.[124]

Similar studies have investigated the action of brown-rot fungi on both softwoods and hardwoods,[121,123,125,126] mainly spruce and birch woods. Although taxonomically similar to white rots, brown rots are known to remove the polysaccharide fraction of the wood, leaving the lignin fraction behind. In fact, brown-rot decay of *E. cordifolia* wood produces a ^{13}C NMR spectrum that is reminiscent of a hardwood lignin sample.[121] Figure 7 shows the ^{13}C CP-MAS NMR spectra of untreated *E. cordifolia* wood and wood after brown-rot and after white-rot decay. Estimates of the S/G ratio showed minimal modifications relative to the untreated wood. As with white-rot, brown-rot decay is related to this ratio, it having been found that the strong resistance of *A. punctatum* wood may relate to the low S/G value characterizing this Austral wood.[125] The decays of birch and spruce woods by brown rot are, however, somewhat distinct, as viewed by ^{13}C CP-MAS NMR.[126] For spruce, mainly polysaccharides are removed from the wood and hemicelluloses are removed at a higher rate than cellulose. In addition, spruce lignin structure changes during decay by loss of methoxyl groups and formation of vanillic acid-type structures and α-carbonyl groups. On the other hand, the most prominent reaction affecting birch wood lignin was suggested to be β-*O*-4 cleavage rather than demethoxylation. Also, and contrary to what was observed for spruce wood, cellulose crystallinity in birch wood does not change during the process, thus indicating no preference for the amorphous component.

Changes in cellulose crystallinity upon brown-rot decay have been investigated in detail for *Pinus koraiensis* softwood using the fungus *Gloeophyllum trabeum*.[127] Proton spin relaxation measurements were carried out to obtain separated subspectra upon spectral editing, and resolution enhancement was used to improve the quality of the spectra. This achieved not only separation of the cellulose subspectrum from the lignin subspectrum but also separation of subspectra of cellulose with different degrees of crystallinity. Relative areas were used to estimate the quantities of the different components and, interestingly, the authors found no evidence of degradation of the non-

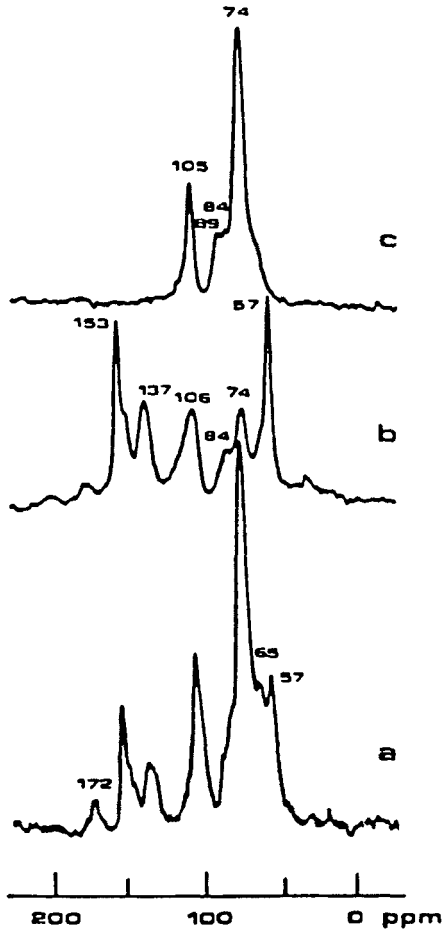

Fig. 7. ^{13}C CP-MAS NMR spectra of *Eucryphia cordifolia* wood (a) prior to degradation, (b) after natural brown-rot decay, (c) after white-rot decay (showing near complete delignification by *Ganoderma australe*). (Reproduced with permission from reference 121.)

crystalline cellulose. In addition, the loss of partly ordered cellulose on crystal surfaces (reflected by the 84 and 62 ppm peaks) exceeded the loss of crystal-interior cellulose (represented by the 89 and 65 ppm peaks). Further, the proportion of monoclinic Iβ crystalline form increased, as shown by the increase of the 88.5 ppm peak relative to that of the 90.2 ppm peak.[22,29] This was interpreted in terms of preferential degradation of crystallites that are relatively narrow and/or of the triclinic Iα form.

4. SOLID-STATE NMR OF WOOD PULPING AND PULP BLEACHING

High-resolution solid-state NMR has been extensively applied to the characterization of lignin structural changes upon different pulping processes and during bleaching processes.

Kraft cooking is the most worldwide used method of chemical pulp production. It involves the selective removal of lignin in wood by sodium hydroxide and sodium sulfide aqueous solutions. Kraft cooking is known to promote ether cleavage reactions leading to delignification. Towards the end of the process, a number of different condensation reactions may become important, as indicated by the considerable difficulty in removing residual lignin from the pulp. In order to investigate the structural changes affecting lignin during the process, kraft lignin samples withdrawn at different cooking times have been analysed by solution-state ^{13}C NMR as well as by elemental and methoxyl analysis.[128] However, many of the major changes were found to take place in the solid phase and solid-state NMR is thus a suitable technique to investigate such changes, circumventing the dependence of the results on the isolation procedure. Since pulping removes most wood extractives, extractive-free wood is often used as a basis of comparison for the study of spectral changes upon pulping. The effect of different cooking times on the lignin of pine wood was studied by ^{13}C CP-MAS.[56,98] The spectrum of short-cook pulp showed substantial, but incomplete, loss of lignin and selective depletion of hemicellulose.[56] The spectrum of the kraft pulp obtained at an intermediate-cook time demonstrated that a significant further reduction in lignin content occurs. In addition, no apparent changes in the structure and morphology of cellulose were observed, even under long-cook time conditions.[56,98] Lignin contents in pine wood and pulps determined by NMR were in good agreement with those determined by chemical methods.[98] However, NMR quantitation of lignin for intermediate-cook and long-cook kraft pulps was hindered by the very low signal-to-noise ratio of the resulting spectra. White spruce kraft pulps were studied by ^{13}C CP-MAS NMR in order to study the kinetics of the pulping process in more detail.[129] Six pulp samples obtained under different conditions were investigated and lignin quantitation was carried out in terms of the normalized area at 150 ppm, taking the 105 ppm polysaccharides peak as intensity reference. Percentage lignin estimated by NMR gave a linear correlation with the Klason lignin percentage values, within a 10% error. The authors noted, however, that the ^{13}C CP-MAS technique was not sensitive to lower lignin contents. Generally, lignin content was seen to decrease rapidly with the yield of pulp, whereas the peak intensities for polysaccharides decreased much more slowly. In fact, intensity changes in the polysaccharide region, 65–105 ppm, were very slight, confirming that little cellulose is lost during the process. A more significant decrease of the C6 carbon, at 65 ppm, compared to the decreases of the ring-carbon peaks, suggested the occurrence

of cleavage in the carbohydrate reducing end-groups. Generally, these results were in agreement with those previously observed for kraft pulping by traditional methods. The strong signal overlap in the polysaccharide region is, however, a major stumbling-block to the use of NMR as a fully quantitative technique unless, for instance, multivariate analysis is used, as indicated below.

Multivariate data analysis of the ^{13}C CP-MAS NMR spectra has been applied for the study of birch pulping kinetics.[130,131] Samples were taken at regular times during processing and their ^{13}C CP-MAS NMR spectra were analysed by principal components (PC) and partial least-squares (PLS) analysis. PC analysis gave a model with two components that could explain 90% of the total variance in the available data set. The major component, describing 85% of variance, was clearly related to the extent of delignification. PLS analysis enabled a correlation between the ^{13}C CP-MAS data matrix and the chemical analysis (CA) matrix to be established. The CA data matrix, containing percentage lignin values determined by the Klason method, correlated clearly with the percentage of lignin predicted by the NMR method, proving the method very efficient for predicting lignin content of new samples. Such predictive ability was efficient for lignin contents lower than 5%, even under conditions of strong overlap. This multivariate method has been extended to predict polysaccharide content, and its combination with Fourier transform mid-infrared (FTIR) and near-infrared (NIR) data has been investigated.[131] Although NIR was the spectroscopic method that gave the best model in terms of predictive ability, the combination of ^{13}C CP-MAS, FTIR and NIR resulted in a model with better predictive ability.

As mentioned in the beginning of this subsection, residual lignin of kraft pulps is strongly resistant to removal during pulping and also during pre-bleaching. Besides the possible occurrence of lignin condensation reactions, another possible explanation for this resistance is the existence of covalent bonds between lignin and carbohydrate, which may originate either from lignin biosynthesis or from the effects of pulp processing. To investigate this possibility, residual lignins in unbleached and chlorine semi-bleached softwood *Pinus taeda* L. kraft pulps were isolated by enzymatic hydrolysis of the carbohydrate fraction and characterized by ^{13}C CP- MAS.[75] Results indicated that bleaching gives rise to extensive degradation of residual lignin. This was indicated by a significant decrease in methoxyl content and an increase in carboxyl content as shown by the CP-MAS NMR spectra, consistent with the occurrence of extensive oxidation and demethoxylation. Interestingly, appreciable amounts of carbohydrates were found in all residual lignins, with galactose being the most abundant monomer. The authors interpreted such findings as evidence of covalent carbohydrate–lignin linkages established through galactose and claim the possible importance of these bonds in determining the resistance of lignin to removal.

Structural changes in wood cellulose during pulping have been the subject of a large number of investigations, which made extensive use of x-ray

diffraction techniques. Solid-state ^{13}C CP-MAS NMR has been used to follow the cellulose changes upon kraft cooking of radiata pine wood and showed that, initially, the degree of cellulose crystallinity increased owing to the preferential loss of disordered cellulose.[132] At a later stage of the process, the degree of crystallinity dropped owing to formation of physically damaged cellulose. More recently, solid-state NMR has been combined with data from mid-infrared spectroscopy (IR) and x-ray diffraction[133] and all three methods have confirmed the relative increase of cellulose crystallinity during the process, reflecting the removal of less ordered carbohydrate. While x-ray and IR studies suggested that the actual amount of crystalline cellulose remained constant throughout the process, NMR studies confirmed previous reports that showed an increase in crystal-interior cellulose in the early stages of pulping, followed by some degree of cellulose damage. The relative sensitivities of the methods were discussed and attention was drawn to the fact that, while x-ray diffraction is sensitive to long-range order, NMR is sensitive to crystallite size.

Solid-state NMR has provided evidence of conversion of the metastable Iα crystalline form of cellulose to the more stable Iβ form at temperatures typical of the pulping processes.[134] The evidence was based on the relative intensities at 90.2 and 88.5 ppm, assigned to C4 in Iα and Iβ crystallite interiors, respectively. The use of chemometric methods has proved very useful in detecting small changes in the supramolecular structure of cellulose through the ^{13}C CP-MAS NMR spectra.[40,135,136] Partial least- squares (PLS) analysis enabled the quantitation of Iα and Iβ for different types of wood pulps. The effects of different kraft pulping conditions were studied by a PCA model, which showed that the main spectral changes relate to the changes in temperature and reflect changes in the proportion of cellulose Iα and Iβ. The PCA model has also enabled the estimation of cellulose II content in several cellulose and lignocellulosic samples,[40,135] proving applicable for particularly low cellulose II contents.[135] Relative amounts of cellulose I, cellulose II and amorphous cellulose were estimated and the effects of sample treatments such as decrystallization, regeneration, mercerization, drying and hydrolysis were investigated.

High-yield chemimechanical pulping (CMP) is another approach for pulp production that combines chemical and mechanical treatments. The pulp obtained in this way retains a large fraction of the initial lignin content of wood and the response of CMP to non-delignifying bleaching agents is therefore of great importance. ^{13}C CP-MAS NMR has been used to investigate the chemimechanical pulping of sound and spruce budworm-killed balsam fir[137] and the effect of subsequent peroxide bleaching.[137,138] This work reported no effect of pulping on the cellulose component but evident changes in lignin and in hemicelluloses. However, no differences were observed between the responses of sound wood and spruce budworm-killed balsam fir wood to both pulping and bleaching.

The type and amount of carbonyl groups in mechanical and high-yield pulps have an important influence on the colour of lignin-containing papers. It is therefore important to characterize the chemical environment of those groups. ^{13}C CP-MAS NMR enabled their observation and characterization to some extent, but an alternative approach was devised involving the use of the ^{31}P nucleus.[139] ^{31}P was inserted in some high-yield pulps, previously treated with Fremy's salt, through a condensation reaction of the carbonyl groups with trimethyl phosphite to produce phosphite esters. Assignment of the ^{31}P NMR spectra was aided by study of model compounds. The spectra of freshly oxyphosphorylated pulp samples exhibit peaks at 10 ppm and between 20 and 40 ppm. The peak at 10 ppm was mainly assigned to cyclic phosphite esters of orthoquinones present in lignin in high-yield pulps. The signals situated between 20 and 40 ppm were assigned to trimethyl phosphite adducts of α,β-unsaturated aldehydes and ketones present in lignin. ^{31}P lineshapes were found to depend significantly on sample ageing. Although orthoquinones are removed by alkaline peroxide bleaching, residual signals at 10 ppm were observed in the spectra of bleached oxyphosphorylated pulps. The possibility of signal overlap, at 10 ppm, with the signal of an adduct of trimethyl phosphite with carboxylic acid groups, thus hindering the determination of orthoquinones, in pulps, was investigated.[140] It was found that hydroxypropylation or complete ionization of the carboxylic acid group prevents formation of such an adduct. In such conditions, the orthoquinone content may be calculated through the ratio of the area of the ^{31}P NMR signal at 10 ppm to the total area of all signals, multiplied by the phosphorus content.

High-yield and ultra-high-yield mechanical pulps undergo photoinduced brightness reversion, which limits their use to short-life products. The prevention of this process is industrially important in order to enable pulps to be used in a wider range of products. Brightness reversion is associated with the photodegradation of lignin and the resulting chemical changes in that component were studied by ^{13}C CP-MAS NMR.[141] Unbleached and alkaline hydrogen peroxide-bleached stoneground wood pulps were subjected to severe light irradiation and the dipolar diphasing ^{13}C CP-MAS NMR spectra of the pulps were obtained. The spectra showed signals from hemicellulose carbonyls and methyls, at 173 ppm and at 22 ppm respectively; C3 and C4 of the guaiacyl structures, at 153, 149 and 146 ppm; C1 of guaiacyl structures, at 134 ppm and lignin methoxyls, at 57 ppm. Some residual cellulose signals were still present and were taken as intensity reference since they are not expected to be affected by irradiation. NMR spectral changes, together with FTIR data, indicated that irradiation results in the formation of α-carbonyl groups, carboxylic groups, ketonic and aldehydic groups, as well as in an increase in condensed lignin structures. Hydrogen peroxide bleaching of non-irradiated samples was found to hydrolyse hemicellulose acetyl groups and ether linkages in etherified guaiacyl structures, resulting in no significant loss of lignin aromaticity. However, the spectra of irradiated pulps showed that irradiation

alone resulted in significant loss of lignin aromaticity, relating to loss of etherified and non-etherified guaiacyl structures, and this loss of aromaticity was larger for the bleached sample than for the unbleached one. Cold soda pulp and stone-ground wood pulp, bleached with calcium hypochlorite and with hydrogen peroxide, respectively, were studied by ^{13}C CP-MAS.[142] Little effect on the ketonic structures was observed and no effect was seen on the etherified aryl units for both treatments. However, hypochlorite degraded most lignin units which were not linked in β-*O*-4 ethers.

T_{1H} values may be used to probe the microstructure of wood pulps and several factors affecting T_{1H} have been investigated: paramagnetic relaxation,[109] temperature and magnitude of static magnetic field.[110] T_{1H} was measured for spruce high-yield pulps at two magnetic static fields and a qualitative relationship of $T_{1H}^{-1}(\omega_0^{-2})$ was suggested. An average domain size of about 15 nm was estimated in terms of the T_{1H} values measured at 100 MHz. Measurements made at a variety of temperatures, at 300 MHz, showed that the T_{1H} minimum was close to room temperature.

The steam explosion treatment is a relatively new alternative approach for wood refining and pulp production. It involves brief contact of wood chips with superheated steam (30–40 bars at 230–250°C) in a reactor, followed by explosion due to rapid decompression. This treatment leads to physical and chemical modification, permitting greater accessibility of its different components to solvents and to chemical or enzymatic hydrolysis. The effect of wood explosion on the ^{13}C CP-MAS NMR spectrum has been studied for spruce wood, resulting in a pronounced signal narrowing for exploded wood.[97] The spectrum shows a sharp intense polysaccharide C4 peak, whereas in native wood the C4 peak adopts a broad, weaker feature. Similar observations were registered in the polysaccharide C6 region. This has been interpreted as an increase in cellulose crystallinity, as a result of the explosion treatment, and this has been confirmed by x-ray powder diffraction. The same authors suggested that their results are consistent with the proposal that the process causes segregation of lignin and polysaccharides into separate domains. Following some previous studies,[143] $T_{1\rho H}$ relaxation times of untreated and treated wood samples were compared with those observed for the separated components: cellulose, hemicellulose and lignin.[107] As expected, intimate mixing averages the relaxation parameter in most samples but, after prolonged treatment, an increase of $T_{1\rho H}$ is registered for cellulose relative to lignin. This was interpreted as reflecting the removal of non-crystalline carbohydrate or a change in lignin molecular mobility probably due to condensation.

Steam explosion is known to be less successful when applied to softwoods, relative to hardwoods, and the possible reasons for this difference have been investigated by ^{13}C CP-MAS.[94] The softwood *Pinus radiata* and the hardwood *Eucalyptus regnans* have been examined before and after treatment by two steam explosion processes, the Canadian Iotech process (IC) and the Australian Siropulper (SP) process. For the softwood, both processes lower the

carbohydrate/lignin ratio (C/L), as measured by ^{13}C CP-MAS, indicating degradation of carbohydrate, particularly hemicellulose. On the other hand, for extracted exploded wood, the C/L ratio rises to near the original value, which reflects removal of lignin. Study of the carbohydrate spectral region confirmed the previously observed increase in cellulose crystallinity upon steam explosion, which may arise partly from cleavage of interunit linkages in amorphous regions and destruction of bonding interactions of surface cellulose with the matrix components. Extraction of the exploded wood leads to further crystallinity increase, which was more marked for IC-treated samples. Lignin changes were monitored through the signals of etherified plus free phenolic C4 carbons, in the 141–158 ppm region. Steam treatment results in reduction of intensity of the signals of C4 in etherified guaiacyl units reflecting lignin de-etherification with extensive cleavage of the β-*O*-4 linkages and release of free phenolic groups. For the hardwood sample, the C/L ratio also falls upon steam explosion and rises upon extraction, but, in contrast to the softwood, to values that are much higher than those for untreated wood. Accordingly, hardwood lignin proved to be more easily extracted than softwood lignin. The more favourable C/L ratio and the higher extractability of lignin contribute to the better accessibility to bioconversion of hardwood substrates, relative to softwood. The effect of both steam explosion treatments on the hardwood proved to be similar to those on the softwood. Hemicellulose content was clearly higher in the hardwood, as shown by the 21 and 173 ppm peaks, but, as with the softwood, it is significantly reduced by explosion. Structural changes in lignin are much clearer in the spectra of hardwoods than in the spectra of softwoods. The SP process gives rise to greater cleavage and a more condensed lignin than the IC process, which may be a cause of process-related differences in the accessibility to bioconversion and rate of enzymatic hydrolysis of the treated wood substrates. The products of SP steam explosion were further examined by ^{13}C CP-MAS NMR using a spin-locking sequence to suppress protonated carbons and select lignin aromatic signals only.[144] Residual lignin was suggested to be either partly depolymerized or repolymerized, rather than unreacted. This lignin may be responsible for the observed greater hindrance of enzyme access to polysaccharides. In addition, the β-*O*-4 ether content of the lignin seems also to be related to the ease of the enzymatic action. It is suggested, therefore, that enzymatic action is related not to lignin content but rather to residual lignin structure and location. The steam explosion of aspen wood[145] and poplar wood *Populus tremula* has also been studied.[107,146] Figure 8 clearly shows the effect of steam explosion on the CP-MAS NMR spectrum of poplar wood. Disappearance of the 21 and 172 ppm peaks, accompanied by a general signal sharpening, indicated the almost complete removal of hemicelluloses. After prolonged treatment, the increase of the peaks at 56 and 143 ppm was interpreted as indicative of recondensation of degradation products such as furfural or hydroxymethylfurfural. Intensity changes in the polysaccharide C4 region and in the 60–65 ppm region have been explained by

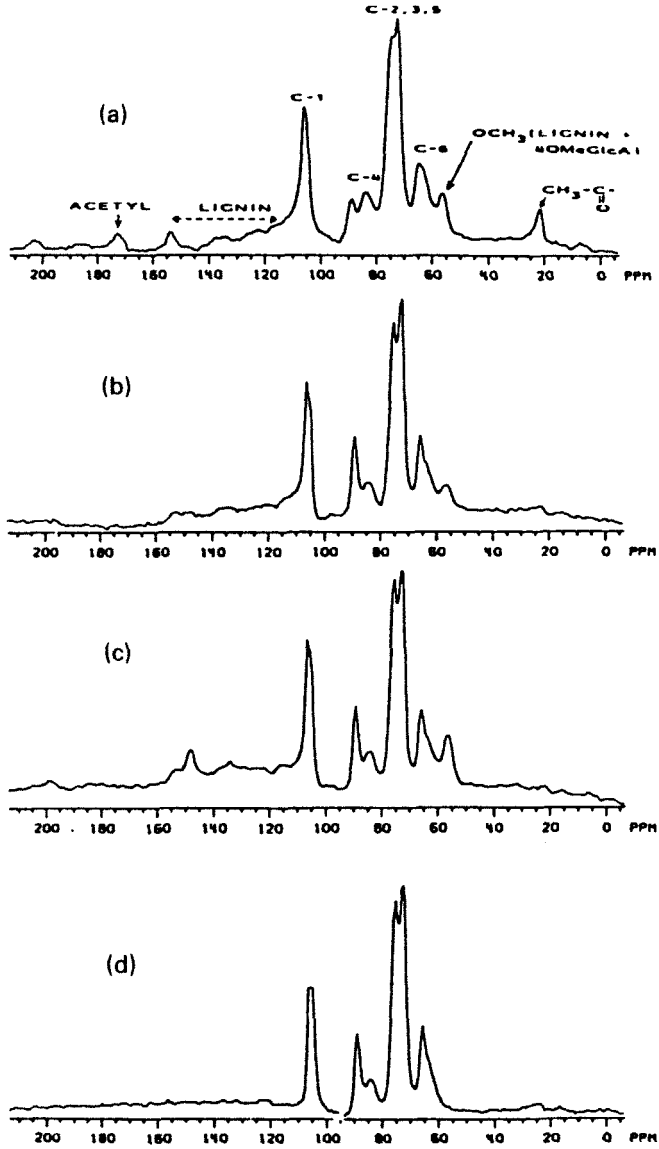

Fig. 8. ^{13}C CP-MAS NMR spectra of poplar wood recorded for (a) coarsely divided untreated chips, (b) and (c) water-extracted exploded samples pre-treated at 40 bars during 90 and 165 s, respectively, (d) water extracted samples pre-treated at 40 bars during 165 s with additional chlorite bleaching. (Reproduced with permission from reference 107 by courtesy of Marcel Dekker, inc.)

hemicellulose removal and also by preferential hydrolysis of amorphous cellulose, relative to crystalline cellulose. Water extracts resulting from steam treatment have also been analysed by CP-MAS together with an insoluble fraction that separated during centrifugation of the water extracts. The water extracts were identified as hemicelluloses and lignin, whereas the insoluble fraction was found to give both lignin and carbohydrate signals. This fraction was identified as a lignin–carbohydrate complex.

5. SOLID-STATE NMR OF NON-WOODY LIGNOCELLULOSIC MATERIALS

Cork, the outer bark of *Quercus suber* L., is a material widely used for stoppers, insulating and decorative panels, floors and walls. Cork is composed of 40% suberin, 22% lignin, 20% polysaccharides and about 15% of waxes and other extractives.[147] The major component of cork, suberin, has been extensively studied and characterized as a biopolyester composed of aliphatic domains, mainly C_{16}–C_{24} hydroxyacids, and possibly some aromatic domains.[148–150] The structural characterization of suberin has been significantly aided by close comparison with the very similar system of intact cutin,[151–156] a biopolyester that forms the structural component of the protective cuticle in terrestrial plants. ^{13}C CP-MAS NMR spectra and depolarization spectra of cutin enabled different dynamic environments to be probed[151,153] and proton and carbon relaxation times showed that cutin is mainly composed of long, mobile methylene chains and some shorter and more hindered methylene segments. Cutin structure includes considerably rigid cross-links constituted by esters of secondary alcohols.[151,153] ^{13}C CP-MAS studies of the cutin-like biopolymer suberin supported the suggestion that suberin and cell-wall components are chemically bonded via aromatic groups.[153] In potato tissue, aliphatic suberin and other cell-wall components were, however, found to be spatially separated, as shown by proton and carbon relaxation times.[155] Enzymatic and chemical isolation of cutin and suberin have recently been optimized and the processes have been followed by ^{13}C CP-MAS NMR.[156]

The first solid-state NMR study of whole cork dates from only a few years ago.[157] ^{13}C CP-MAS NMR was used, along with FTIR, to follow the thermal degradation of cork. Figure 9 shows the changes in the 15–35 ppm aliphatic region where aliphatic suberin resonates and in the carbohydrate and lignin regions. The changes observed showed that degradation is initiated at about 150°C with decomposition of polysaccharides, waxes and other extractives. It is suggested that partial degradation of suberin begins at 150°C, starting probably at points of attachment to the cell wall. The major structural modifications of cork components take place between 200 and 350°C. The decomposition of lignin begins at 250–300°C and, even at temperatures as high as 350–400°C, traces of partially decomposed suberin are present, as shown by

the 30 ppm peak in Fig. 9. This interesting point has been suggested to be potentially related to the well-known thermal resistance of the basic cellular structure of cork. The changes in the aromatic region reflect the formation of significant amounts of coke as thermal decomposition proceeds.[157]

A more recent work has involved the use of relaxation time measurements to gain some insight into the proximity and interaction between cork components, with particular interest in the structural changes brought about by removal of suberin.[158] T_{1pH} relaxation times showed that aliphatic suberin, in cork, is spatially separated from carbohydrate and lignin, and T_{1C} and T_{1pC} relaxation times indicated that suberin experiences higher motional freedom in the MHz and in the kHz ranges of motion frequencies. Stepwise removal of suberin through alkaline treatment caused considerable changes in the ^{13}C CP-MAS NMR spectra and in the relaxation times of the components. Such changes suggested that desuberization induces the breakage of ester linkages of suberin to phenylpropane units and/or carbohydrate C6 carbons. Shorter aliphatic chains seemed to be removed preferentially during the process. Changes in the relaxation times showed that removal of suberin leads to a motionally restricted and more compact environment, on the MHz and kHz time scales.[158]

^{13}C CP-MAS NMR has been compared with the popular method of near-infrared spectroscopy as a rapid nondestructive method for analysis of grass species.[159] Spectral areas in the 60–110 ppm and 100–160 ppm regions and the carbonyl peak at 175 ppm were used to obtain polysaccharide, lignin and protein ratios, respectively. Although the CP-MAS technique is unlikely to replace NIR owing to the much higher rapidity of the latter, it proved to be useful in aiding the assignment of the components present and their relative quantities.

In recent years, the possibilities of using products derived from oil palm trees in a variety of industrial applications have attracted considerable interest, particularly in Asiatic countries. Oil palm trunks are anatomically different from wood and are taxonomically close to grasses and cereals. ^{13}C CP-MAS NMR has been used to study lignin content and structure in palm cell walls.[160] These factors are believed to be important in determining mechanical,

Fig. 9. Selected regions of the ^{13}C CP-MAS NMR spectra of cork calcined in air for 20 min at the temperatures indicated. In both spectral regions peak heights were normalized to the intensity of the 30 ppm suberin peak. (Reproduced with permission from reference 157: Solid State NMR, 4, C. Pascoal Neto, J. Rocha, A. Gil, N. Cordeiro, A. P. Esculcas, S. Rocha, I. Delgadillo, J. D. P. Jesus and A. J. F. Correia, ^{13}C Solid State NMR and FTIR studies of the thermal decomposition of cork, 143, 1995, with kind permission of Elsevier Science-NL, Sara Burgerhartstraat 25, 1055 KV Amsterdam, The Netherlands.)

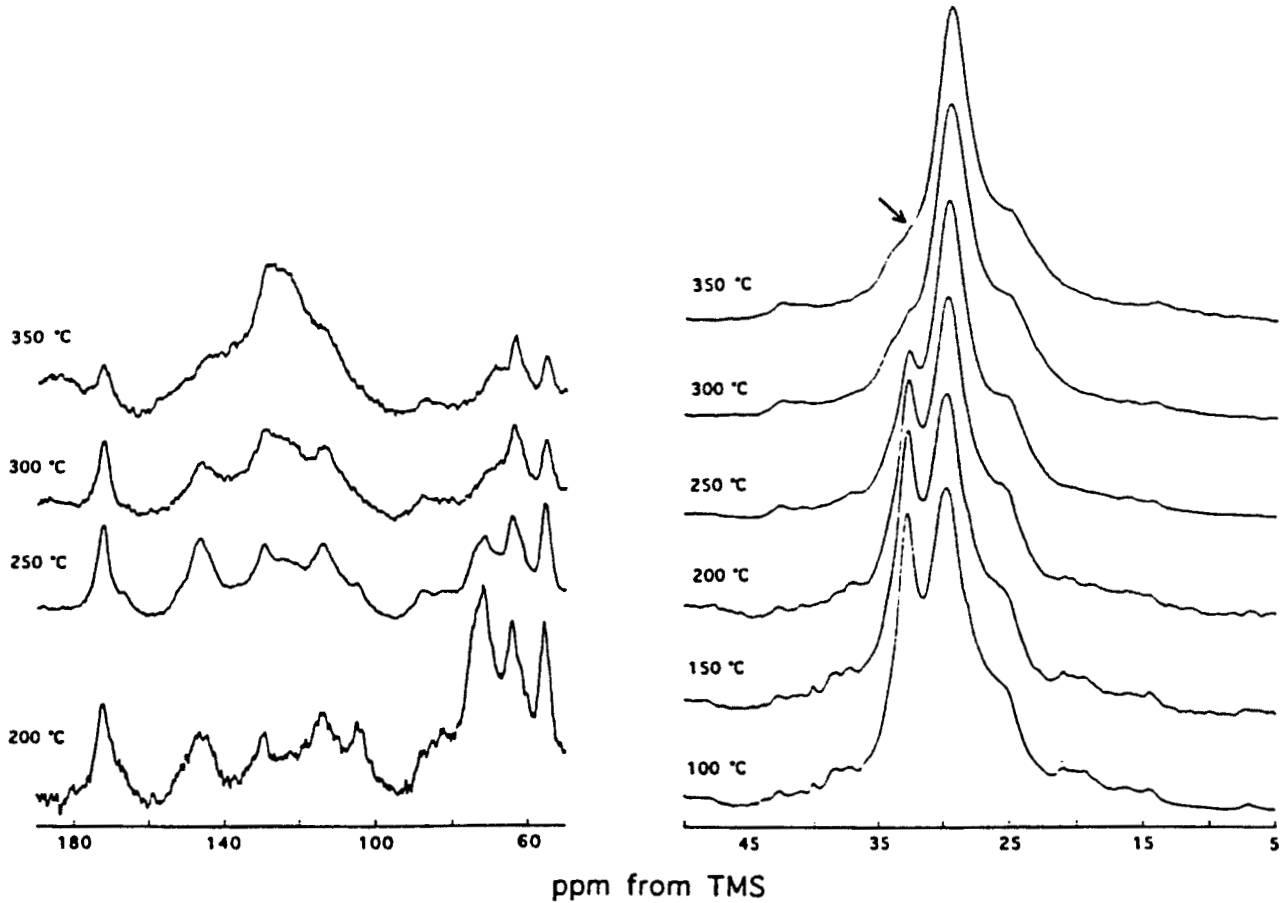
350 °C
300 °C
250 °C
200 °C
180
140
100
60
350 °C
300 °C
250 °C
200 °C
150 °C
100 °C
45
35
25
15
5
ppm from TMS

nutritional and pulping properties. Spectra were obtained with the interrupted decoupling sequence and lignin contents were estimated, for the parenchyma and vascular bundles, through the spectral area between 125 and 156 ppm. It is proposed that palm trunk lignin contains a high proportion of aryl ether-linked syringyl units but little ferulic or *p*-coumaric acid.[160]

6. SOLID-STATE NMR OF WOOD COMPOSITES

Wood and wood–polymer composites have been increasingly developed and applied to an enormous variety of uses. Composite performance can be bettered by improving the interfacial shear strength between the thermoplastic matrix and the wood fibre through the formation of chemical bonds across the interface. Physical characterization of wood and wood–polymer composites (WPC) has involved a variety of tests in order to define the properties needed to establish product design and strength criteria. In a recent update of new and reliable test methods,[161] the use of solid-state NMR, along with scanning electron microscopy and x-ray analysis, to obtain information about the interaction between wood components and the *in situ* formed polymer has been discussed. A good example of a WPC is the composite of balsa wood and poly(EHMA) (the homopolymer of ethyl α-hydroxymethylacrylate). Balsa wood is a low-density wood that is extensively used commercially, and the potential use of balsa wood/EHMA WPC as a lightweight material has been investigated by NMR.[161,162] $T_{1\rho H}$ measurements have been used to gain insight into the extent of the interaction between the two components[161] and the results showed two separate $T_{1\rho H}$ values for polymer signals and wood signals in the ^{13}C CP-MAS NMR spectrum. This suggested that the region of interaction is small, compared to the individual components. The same result is reflected by the biexponential relaxation observed for the peak at 61 ppm which results from the overlap of wood cellulose with poly(EHMA) carbons. The ^{13}C CP-MAS NMR spectrum of the resulting WPC showed a combination of peaks found in the spectra of untreated balsa wood and poly(EHMA). The observations that spectral subtraction (WPC minus wood) does not null all wood peaks and that the difference spectrum is not identical to that of poly(EHMA) were interpreted as indicating the existence of strong interactions that provoked chemical shift changes in some peaks.

^{11}B NMR has been used, along with ^{13}C NMR, to study the reaction of boric acid with wood in a polystyrene melt.[163] This study aimed at investigating the possibility of performing reactive extrusion in the development of wood–polymer composites. ^{11}B NMR and ^{13}C CP-MAS NMR suggested that boron bonds chemically to wood during the preparation of the WPC wood/polystyrene/boric acid. ^{11}B is a quadrupolar nucleus with spin $I = 3/2$ and the lineshape observed is highly sensitive to local geometry. ^{11}B NMR spectra indicated that tetrahedral complexes may form between boron and wood

polysaccharides, however, trigonal geometries may also occur. Dynamic mechanical analysis and differential scanning calorimetry characterization of the composite material indicated that no significant changes in the WPC properties are caused by the reaction with boric acid.[163]

REFERENCES

1. E. Sjostrom, *Wood Chemistry: Fundamentals and Applications*, 2nd edn, Academic Press, San Diego, 1993.
2. D. Fengel and G. Wegener, *Wood: Chemistry, Ultrastructure, Reactions*, Walter de Gruyter, Berlin, 1984.
3. D. N.-S. Hon and N. Shiraishi (eds), *Wood and Cellulosic Chemistry*, Marcel Dekker, New York, 1991.
4. R. Rowell (ed.), *The Chemistry of Solid Wood*, Advances in Chemistry Series 207, American Chemical Society, Washington, DC, 1984.
5. M. Lewin and I. S. Goldstein (eds), *Wood Structure and Composition*, Marcel Dekker, New York, 1991.
6. H. A. Krassig, *Cellulose: Structure, Accessibility and Reactivity*, Gordon and Breach Science Publishers, Yverdon, 1993.
7. J. F. Kennedy, G. O. Philips, D. J. Wedlock and P. A. Williams (eds), *Cellulose and Its Derivatives*, Ellis Horwood, Chichester, 1985.
8. W. G. Glasser and S. Sarkanen (eds), *Lignin: Properties and Materials*, ACS Symposium Series 397, American Chemical Society, Washington, DC, 1992.
9. K. V. Sarkanen and C. H. Ludwig (eds), *Lignins. Occurrence, Formation, Structure and Reactions*, Wiley-Interscience, New York, 1971.
10. T. P. Nevell and S. H. Zeronian (eds), *Cellulose Chemistry and Its Applications*, Ellis Horwood, Chichester, 1985.
11. Y. Ogiwara, H. Kubota, S. Hayashi and N. Mitomo, *J. Appl. Polym. Sci.*, 1969, **13**, 1689.
12. Y. Ogiwara, H. Kubota, S. Hayashi and N. Mitomo, *J. Appl. Polym. Sci.*, 1970, **14**, 303.
13. T. F. Child, *Polymer*, 1972, **13**, 259.
14. M. F. Froix and R. Nelson, *Macromolecules*, 1975, **8**, 726.
15. A. K. Kulshreshitha, *J. Text. Inst.*, 1979, 15.
16. G. Torri, P. Sozzani and B. Focher, in *From Molecular Materials to Solids. Applications of Nuclear Magnetic and Electron Paramagnetic Resonance Spectroscopies* (ed. F. Morazzoni), p. 71, Polo Editoriale Chimico, Milano, 1993.
17. R. H. Atalla, J. C. Gast, D. W. Sindorf, V. J. Bartuska and G. E. Maciel, *J. Am. Chem. Soc.*, 1980, **102**, 3249.
18. W. L. Earl and D. L. Vanderhart, *J. Am. Chem. Soc.*, 1980, **102**, 3251.
19. R. L. Dudley, C. A. Fyfe, P. J. Stephenson, Y. Deslandes, G. K. Hamer and R. H. Marchessault, *J. Am. Chem. Soc.*, 1983, **105**, 2469.
20. F. Horii, A. Hirai and R. Kitamaru, *Polym. Bull.*, 1982, **8**, 163.
21. R. H. Atalla, *Proceedings of ISWPC*, Tsukuba, 1983, Vol. 1, p. 42.
22. D. L. Vanderhart and R. H. Atalla, *Macromolecules*, 1984, **17**, 1465.
23. J. J. Cael, D. L. W. Kwoh, S. S. Bhattacharjee and S. L. Patt, *Macromolecules*, 1985, **18**, 821.
24. K. Kamide, K. Okajima, K. Kowsaka and T. Matsui, *Polymer J.*, 1985, **17**, 701.
25. F. Horii, A. Hirai and R. Kitamaru, *Macromolecules*, 1987, **20**, 2117.
26. R. H. Atalla, and D. L. Vanderhart, *Science*, 1984, **223**, 283.
27. A. Hirai, F. Horii and R. Kitamaru, *Macromolecules*, 1987, **20**, 1440.
28. R. H. Atalla and D. L. VanderHart, *Proceedings of ISWPC*, Paris, 1987, Vol. 1, p. 215.

29. E. M. Debzi, H. Chanzy, J. Sugiyama, P. Tekely and G. Excoffier, *Macromolecules*, 1991, **24**, 6816.
30. H. Yamamoto and F. Horii, *Macromolecules*, 1993, **26**, 1313.
31. R. Teeäär, A. N. Zhilkin, P. M. Valov and O. A. Terentiev, *Polym. Bull.*, 1987, **17**, 231.
32. R. H. Newman, J. A. Hemmingson and I. D. Suckling, *Holzforschung*, 1993, **47**, 234.
33. R. H. Newman and J. A. Hemmingson, *Cellulose*, 1994, **2**, 95.
34. D. S. Himmelsbach, F. E. Barton and D. E. Akin, *Appl. Spectrosc.*, 1986, **40**, 1054.
35. F. Horii, H. Yamamoto, R. Kitamaru, M. Tanahashi and T. Higuchi, *Macromolecules*, 1987, **20**, 2946.
36. H. Yamamoto, F. Horii, H. Odami, *Macromolecules*, 1989, **22**, 4130.
37. H. Chanzy, B. Henrissat, M. Vincendon, S. F. Tanner and P. S. Belton, *Carbohydr. Res.*, 1987, **160**, 1.
38. A. Isogai, M. Usuda, T. Kato, T. Uryu and R. H. Atalla, *Macromolecules*, 1989, **22**, 3168.
39. C. A. Fyfe, R. L. Dudley, P. J. Stephenson, Y. Deslandes, G. K. Hamer and R. H. Marchessault, *JMS–Rev. Macromol. Chem-Phys.*, 1983, **C23**, 187.
40. H. Lennholm and T. Iversen, *Proceedings of EWLP '94*, Stockholm, 1994, p. 1.
41. H. Lennholm and T. Iversen, *Holzforschung*, 1995, **49**, 119.
42. W. Kolodziedjski, J. S. Frye and G. E. Maciel, *Anal. Chem.*, 1982, **54**, 1419.
43. B. L. Browning, *The Chemistry of Wood*, R. E. Krieger, New York, 1975.
44. T. W. Timell, *Adv. Carbohydr. Chem.*, 1965, **20**, 409.
45. D. J. Brasch and A. L. Wilkins, *Appita*, 1985, **38**, 353.
46. G. Fengel and D. Wegener, *Wood: Chemistry, Ultrastructure, Reactions*, p. 132, Walter de Gruyter, Berlin, 1984.
47. C.-L. Chen and D. Robert, in *Methods in Enzymology* Part B (ed. W. A. Wood and S. T. Kellog), **161**, p. 137, Academic Press, Orlando, 1988.
48. M. Drumond, M. Aoyama, C.-L. Chen and D. Robert, *J. Wood Chem. Technol.*, 1989, **9**, 421.
49. D. Robert and C.-L. Chen, *Holzforschung*, 1989, **43**, 323.
50. L. L. Landucci, *Holzforschung*, 1991, **45** (Suppl.), 55.
51. L. L. Landucci, *Holzforschung*, 1991, **45**, 425.
52. D. Robert, in *Methods of Lignin Chemistry* (ed. S. Y. Lin and C. W. Dence), p. 250, Springer-Verlag, Berlin, 1992.
53. H. Hatakeyama and J. Nakano, *Tappi J.*, 1970, **53**, 472.
54. S. Yano, T. Hatakeyama and H. Hatakeyama, in *Proceedings of ISWPC*, Tsukuba, 1983, Vol. 1, p. 76.
55. G. J. Leary and R. H. Newman, in *Methods of Lignin Chemistry* (ed. S. Y. Lin and C. W. Dence), p. 146, Springer-Verlag, Berlin, 1992.
56. J. F. Haw, in *Nuclear Magnetic Resonance in Agriculture* (ed. P. E. Pfeffer and W. V. Gresimowicz), p. 355, CRC Press, Boca Raton, 1989.
57. V. J. Bartuska, G. E. Maciel, H. I. Bolker and B. I. Fleming, *Holzforshung*, 1980, **34**, 214.
58. G. E. Maciel, D. J. O'Donnell, J. J. H. Ackerman, B. L. Hawkings and V. J. Bartuska, *Makromol. Chem.*, 1981, **182**, 2297.
59. J. Schaefer, M. D. Sefcik, E. O. Stejskal, R. A. McKay and P. L. Hall, *Macromolecules*, 1981, **14**, 557.
60. G. J. Leary, R. H. Newman and K. Morgan, *Holzforshung*, 1986, **40**, 267.
61. R. H. Newman, K. R. Morgan and G. J. Leary, *Proceedings of ISWPC*, Vancouver, 1985, p. 53.
62. G. R. Hatfield, G. E. Maciel, O. Erbatur and G. Erbatur, *Anal. Chem.*, 1987, **59**, 172.
63. G. E. Hawkes, C. Z. Smith, J. H. P. Utley, R. R. Vargas and H. Viertler, *Holzforschung*, 1993, **47**, 302.
64. L. Doimo and R. L. Frost, *Holzforschung*, 1990, **44**, 305.
65. M. Bardet, D. Gagnaire, R. Nardin, D. Robert and M. Vincendon, *Holzforschung*, 1986, **40** Suppl., 17.

66. N. G. Lewis, J. Newman, G. Just and J. Ripmeister, *Macromolecules*, 1987, **20**, 1752.
67. N. G. Lewis, E. Yamamoto, J. B. Wooten, G. Just, H. Ohashi and G. H. N. Towers, *Science*, 1987, **237**, 1344.
68. N. G. Lewis, R. A. Razal, E. Yamamoto and J. B. Wooten, *Proceedings of ISWPC*, Raleigh, 1989, p. 349.
69. D. Pilo-Veloso, S. A. L. Morais and E. A. Nascimento, *Proceedings of ISWPC*, Raleigh, 1989, p. 233.
70. N. G. Lewis, E. Yamamoto, J. B. Wooten, G. Just and G. H. N. Towers, *Proceedings of ISWPC*, Paris, 1987, Vol. 1, p. 245.
71. Y. Z. Lai and K. V. Sarkanen, in *Lignins: Occurrence, Formation, Structure and Reactions* (ed. K. V. Sarkanen and C. H. Ludwig), p. 165, Wiley Interscience, New York, 1971.
72. K. Tanaka, F. Nakatsubo and T. Higuchi, *Mokuzai Gakkaishi*, 1979, **25**, 653.
73. J. A. Hemmingson, G. J. Leary, I. J. Miller, W. A. Thomas and A. D. Woodhouse, *J. Chem. Soc. Chem. Commun.*, 1978, 92.
74. D. Joniak, B. Kosíková and M. Matulová, *Chem. Papers*, 1991, **45**, 817.
75. J. Jiang, H. Chang, S. S. Bhattacharjee and D. L. Kwoh, *J. Wood Chem. Technol.*, 1987, **7**, 81.
76. B. Kosíková, M. Hricovíni and R. Simonutti, *Holzforschung*, 1996, **50**, 335.
77. H. Magnusson and T. Konradsoonm, *Svensk Papperstidn.*, 1971, **74**, 835.
78. H. Magnusson, L. Eriksson and L.-O. Andersson, *Svensk Papperstidn.*, 1972, **75**, 619.
79. A. J. Nanassay, *Wood Sci.*, 1973, **5**, 187.
80. A. J. Nanassay, *Wood Sci.*, 1974, **7**, 61.
81. A. R. Sharp, M. T. Riggin, R. Kaiser and M. H. Schneider, *Wood and Fiber*, 1978, **10**, 74.
82. I. D. Hartley, F. A. Kamke and H. Peemoeller, *Holzforschung*, 1994, **48**, 474.
83. C. D. Araujo, S. Avramidis and A. L. MacKay, *Holzforschung*, 1994, **48**, 69.
84. C. D. Araujo, A. L. MacKay, J. R. T. Hailey and K. P. Whittall, *Wood Sci. Technol.*, 1992, **26**, 101.
85. P. S. Belton and R. G. Ratcliffe, *Prog. NMR Spectrosc.*, 1985, **17**, 241.
86. E. His, R. Hossfeld and R. G. Bryant, *J. Colloid Interface Sci.*, 1977, **62**, 389.
87. M. T. Riggin, A. R. Sharp, R. Kaiser and M. H. Schneider, *J. Appl. Polym. Sci.*, 1979, **23**, 3147.
88. R. S. Menon, A. L. MacKay, J. R. T. Hailey, M. Bloom, A. E. Burgess and J. S. Swanson, *J. Appl. Polym. Sci.*, 1987, **33**, 1146.
89. R. S. Menon, A. L. MacKay, J. R. T. Hailey, M. Bloom, A. E. Burgess and J. S. Swanson, *J. Appl. Polym. Sci.*, 1987, **33**, 1146.
90. M. T. Riggin, A. R. Sharp, R. Kaiser and M. H. Schneider, *J. Appl. Polym. Sci.*, 1979, **23**, 3147.
91. J. G. Haygreen and J. L. Bowyer, *Forest Products and Wood Science: An Introduction*, Iowa State University Press, Ames, IA, 1982.
92. C. D. Araujo, A. L. MacKay, K. P. Whittall and J. R. T. Hailey, *Journal of Magnetic Resonance, Series B*, 1993, **101**, 248.
93. G. J. Leary. K. R. Morgan and R. H. Newman, *Appita*, 1987, **40**, 181.
94. J. A. Hemmingson and R. H. Newman, *J. Wood Chem. Technol.*, 1985, **5**, 159.
95. W. L. Earl, *Proc. Int. Conf. Residential Solid Fuels Environ. Impacts & Solns*, Portland, OR, 1982, p. 772.
96. P. G. Hatcher, I. A. Breger and W. L. Earl, *Org. Geochem.*, 1981, **3**, 49.
97. M. G. Taylor, Y. Deslandes, T. Bluhm, R. H. Marchessault, M. Vincendon and J. Saint-Germain, *Tappi J.*, 1983, **66**, 92.
98. J. F. Haw, G. E. Maciel and H. A. Schroeder, *Anal. Chem.*, 1984, **56**, 1323.
99. R. H. Newman and J. A. Hemmingson, *Holzforschung*, 1990, **44**, 351.
100. R. H. Newman, *Holzforschung*, 1992, **46**, 205.
101. R. H. Newman, *J. Wood Chem. Technol.*, 1994, **14**, 451.

102. K. R. Morgan and R. H. Newman, *Appita*, 1987, **40**, 450.
103. W. F. Manders, *Holzforschung*, 1987, **41**, 13.
104. J. M. Willis and F. G. Herring, *Macromolecules*, 1987, **20**, 1554.
105. R. H. Newman, G. J. Leary and K. R. Morgan, *Proceedings of ISWPC*, Raleigh, 1989, p. 221.
106. P. Tekeley and M. R. Vignon, *J. Polym. Sci., Part C: Polym. Lett.*, 1987, **25**, 257.
107. P. Tekeley and M. R. Vignon, *J. Wood Chem. Technol.*, 1987, **7**, 215.
108. W. V. Gerasimowicz, K. B. Hicks and P. E. Pfeffer, *Macromolecules*, 1984, **17**, 2597.
109. D. S. Argyropoulos and F. G. Morin, *Wood Sci. Technol.*, 1995, **1**, 29.
110. D. S. Argyropoulos, F. G. Morin and L. Lapeik, *Holzforschung*, 1995, **49**, 115.
111. D. S. Argyropoulos and F. G. Morin, *Wood Sci. Technol.*, 1995, **29**, 19.
112. M. Bardet, L. Emsley and M. Vincendon, *Solid State NMR.*, 1997, **8**, 25.
113. R. Teeäär, E. Lippmaa, J. Gravitis, A. Kokorevics, A. Kreituss and A. Zharov, *J. Appl. Polym. Sci.*, 1994, **54**, 697.
114. J. Ni and C. E. Frazier, *Holzforschung*, 1996, **50**, 327.
115. S. B. Lee, I. H. Kim, D. D. Y. Ryu and H. Taguchi, *Biotechnol. Bioeng.*, 1983, **25**, 33.
116. M. M. Chang, T. Y. C. Chou and G. T. Tsao, in *Advances in Biochemical Engineering* (ed. A. Fiechter), Vol. 20, p. 15, Springer-Verlag, Berlin, 1981.
117. J. N. Sadler, H. H. Brownell, L. P. Clermont and N. Levitin, *Biotechnol. Bioeng.*, 1982, **24**, 1389.
118. F. Zadrazil, J. Grinbergs and A. E. González, *Eur. J. Appl. Microbiol. Biotechnol.*, 1982, **15**, 167.
119. I. Dill and G. Kraepelin, *Appl. Environ. Microbiol.*, 1986, **52**, 1305.
120. A. T. Martínez, A. E. González, A. Prieto, E. J. González-Vila and R. Fründ, *Holzforschung*, 1991, **45**, 279.
121. A. T. Martínez, A. E. González, M. Valmaseda, B. E. Dale, M. J. Lambregts and J. F. Haw, *Holzforschung*, 1991, **45** (Suppl.), 49.
122. M. F. Davis, H. R. Schroeder and G. E. Maciel, *Holzforschung*, 1994, **48**, 99.
123. G. Gilardi, L. Abis and A. E. G. Cass, *Enzyme and Microbial Technology*, 1995, **17**, 268.
124. M. F. Davis, H. R. Schroeder and G. E. Maciel, *Holzforschung*, 1994, **48**, 186.
125. V. Pérez, M. T. de Troya, A. T. Martinez, F. J. González-Vila, E. Arias and A. E. González, *Wood Sci. Technol.*, 1993, **27**, 295.
126. M. F. Davis, H. R. Schroeder and G. E. Maciel, *Holzforschung*, 1994, **48**, 301.
127. Y. S. Kim and R. H. Newman, *Holzforschung*, 1995, **49**, 109.
128. D. R. Robert, M. Bardet, G. Gellerstedt and E. L. Lindfors, *J. Wood Chem. Technol.*, 1984, **4**, 239.
129. J. M. Willis, N. R. Jagannathan and F. G. Herring, *J. Wood Chem. Technol.*, 1986, **6**, 249.
130. L. Wallbäcks, U. Edlund and B. Nordén, *J. Wood Chem. Technol.*, 1989, **9**, 235.
131. L. Wallbäcks, U. Edlund, B. Nordén and I. Berglund, *Tappi J.*, 1991, **74**, 201.
132. R. H. Newman, J. A. Hemmingson and I. D. Suckling, *Holzforschung*, 1993, **47**, 234.
133. R. Evans, R. H. Newman, U. C. Roick, I. D. Suckling and A. F. A. Wallis, *Holzforschung*, 1995, **49**, 498.
134. R. H. Newman, J. A. Hemmingson, *Proceedings of ISWPC*, Helsinki, 1995, Vol. 1, p. 182.
135. H. Lennholm and T. Iversen, *Holzforschung*, 1995, **49**, 119.
136. H. Lennholm, T. Larsson and T. Iversen, *Carbohydr. Res.*, 1994, **261**, 119.
137. J. M. Willis and F. G. Herring, *Wood Sci. Technol.*, 1987, **21**, 373.
138. J. M. Willis and F. G. Herring, *Holzforschung.*, 1987, **41**, 379.
139. D. S. Argyropoulos, C. Heitner and F. G. Morin, *Holzforshung*, 1992, **46**, 211.
140. D. S. Argyropoulos and C. Heitner, *Holzforschung*, 1994, **48** (Suppl.), 112.
141. T. Kimura, F. Kimura, D. S. Argyropoulos and D. G. Gray, *Holzforshung*, 1992, **46**, 331.
142. L. A. Dunn, R. H. Newman and J. A. Hemmingson, *J. Wood Chem. Technol.*, 1991, **11**, 93.
143. R. E. Teejaer, E. T. Lippmaa, J. A. Gravitis, B. A. Andersons and P. P. Erins, *Khim. Drev.*, 1985, **6**, 106.

144. J. A. Hemmingson and R. F. H. Dekker, *J. Wood Chem. Technol.*, 1987, **7**, 229.
145. D. R. Robert, M. Bardet and D. Gagnaire, *Proceedings of ISWPC*, Paris, 1987, Vol. 1, p. 189.
146. G. Excoffier, M. Vignon and P. Tekeley, *Proceedings of ISWPC*, Paris, 1987, Vol. 2, p. 375.
147. H. Pereira, *Wood Sci. Technol.*, 1988, **22**, 211.
148. P. J. Kolattukudy, *Science*, 1980, **208**, 990.
149. P. J. Holloway, *Phytochemistry*, 1983, **22**, 495.
150. M. Arno, M. C. Serra and E. Seoane, *Anales de Quim.*, 1981, **77**, 82.
151. T. Zlotnik-Mazori and R. E. Stark, *Macromolecules*, 1988, **21**, 2412.
152. R. E. Stark, T. Zlotnik-Mazori, L. M. Ferrantello and J. R. Garbow, in *Plant Cell Wall Polymers* (ed. N. G. Lewis and M. G. Paice), p. 214, American Chemical Society, Washington, DC, 1989.
153. J. R. Garbow, L. M. Ferrantello and R. E. Stark, *Plant Physiol.*, 1989, **90**, 783.
154. J. R. Garbow and R. E. Stark, *Macromolecules*, 1990, **23**, 2814.
155. R. E. Stark and J. R. Garbow, *Macromolecules*, 1992, **25**, 149.
156. R. A. Pacchiano, Jr, W. Sohn, V. L. Chlanda, J. R. Garbow and R. E. Stark, *J. Agric. Food Chem.*, 1993, **41**, 78.
157. C. Pascoal Neto, J. Rocha, A. Gil, N. Cordeiro, A. P. Esculcas, S. Rocha, I. Delgadillo, J. D. P. Jesus and A. J. F. Correia, *Solid State NMR*, 1995, **4**, 143.
158. A. M. Gil, M. Lopes, J. Rocha and C. Pascoal Neto, *Int. J. Biol. Macromol.*, 1997, **20**, 293.
159. D. S. Himmelsbach, F. E. Barton and W. R. Windham, *J. Agric. Food Chem.*, 1983, **31**, 401–404.
160. J. Gallacher, C. E. Snape, K. Hassan and M. C. Jarvis, *J. Sci. Food Agric.*, 1994, **64**, 487.
161. J. R. Wright and L. J. Mathias, *J. Appl. Polym. Sci.*, 1993, **48**, 2225.
162. J. R. Wright and L. J. Mathias, *J. Appl. Polym. Sci.*, 1993, **48**, 2241.
163. Y. Wang, J. Simonsen, C. Pascoal Neto, J. Rocha, T. G. Rials and E. Hart, *J. Appl. Polym. Sci.*, 1996, **62**, 501.

This Page Intentionally Left Blank

NMR Structural Studies of Iron–Sulfur Proteins

BRIAN J. GOODFELLOW*† and ANJOS L. MACEDO*

*Departamento de Química, Faculdade de Ciências e Tecnologia, Universidade Nova de Lisboa, and †Departamento de Química, Universidade del Aveiro, Aveiro, Portugal

The use of NMR spectroscopy in the structural study of iron–sulfur proteins is reviewed. Some introductory theory of the electron-nucleus interaction and how it affects NMR parameters such as chemical shift and relaxation times is presented. Problems encountered in the determination of the solution structure of paramagnetic proteins are discussed and recent work in the field is extensively reviewed.

1. INTRODUCTION

Since the mid-1980s, when the first protein structure in solution was determined by NMR,[1] the area has seen an almost exponential growth. Nowadays

ANNUAL REPORTS ON NMR SPECTROSCOPY
VOLUME 37 ISBN 0-12-505337-1

protein structure determination by NMR is well established and the determination of structures for proteins of up to 200 amino acids is nearly routine. One area where progress has not been so rapid is that of metalloproteins, mainly owing to the presence of metal centres that can contain unpaired electrons, as is the case for cytochromes, Cu(II)-containing proteins and iron–sulfur proteins. In NMR, the presence of unpaired electrons causes nuclei in their vicinity to have short relaxation times and resonances shifted well outside the normal diamagnetic envelope. This can cause problems when using standard NMR methods to determine structures in solution. However, in the last 6 or 7 years a number of methods have been developed to overcome these problems and in fact nowadays the presence of metals centres (in certain cases) can be an advantage as extra constraints may be obtained between nuclei and the metal itself.

In the case of iron–sulfur proteins NMR has been invaluable for the elucidation of solution-state structures and also in the investigation of the electronic structure of the clusters. One major advantage NMR has over x-ray (the other major tool for structure elucidation) is that information can be obtained about the distribution of electron density at the centre, allowing conclusions to be drawn about structure–function relationships in these types of proteins.

This review of NMR structural studies of iron–sulfur proteins will present, (1) a description of the classes of proteins studied in the field, (2) an introduction from an NMR point of view of the electron–nucleus interaction, (3) the experiments used to assign spectra and obtain NMR constraints, (4) the methods for structure calculation, and (5) a description of current work in the field.

2. IRON–SULFUR PROTEINS

Iron–sulfur proteins are a group of non-haem-iron-containing proteins with iron atoms (either Fe^{2+} or Fe^{3+}) bound tetrahedrally by sulfur atoms which can be bridging or terminal in nature. There are four main types of centre found in iron–sulfur proteins: [Fe-4S], [2Fe-2S], [3Fe-4S] and [4Fe-4S]. In this review we will be focusing on the small iron–sulfur-containing proteins: rubredoxin (Rd), desulforedoxin (Dx), ferredoxin (Fd) and the high-potential iron proteins (HiPIPs).[2–4] The Fds can exist as 2Fe, 3Fe or 4Fe forms. They may also contain two clusters of the type 3Fe/4Fe or 4Fe/4Fe, giving 7Fe and 8Fe Fd proteins, respectively. Table 1 shows the possible oxidation states for each type of centre along with the corresponding oxidation and reduction potentials. In the case of the clusters the type of spin coupling model is also given.

The simplest iron–sulfur protein, isolated from sulfate-reducing bacteria, is rubredoxin (Rd). The Rds are low-molecular-mass (6–7 kDa) proteins containing one Fe centre.[5] The metal atom (oxidized native state high-spin Fe^{3+}

Table 1. Characteristic parameters for iron–sulfur clusters[2,3]

Centre	Global oxidation state[a]	E^0(mv)[b]	Iron formal oxidation states	S_{total}/spin coupling model[d]
[Fe-S] Rd, Dx type	3+	−60 to +20	Fe^{3+}	5/2
	2+		Fe^{2+}	2
[2Fe-2S] Fd	+2	−460 to −240	$2 \times Fe^{3+}$	$S_t = 0$: AF coupling between two $S = 5/2$ spins
	+1		Fe^{3+}, Fe^{2+}	$S_t = 1/2$: AF coupling between a $S = 5/2$ and a $S = 2$ spin
[3Fe-4S] Fd	+1	−420 to −50	$3 \times Fe^{3+}$	$S_t = 1/2$: AF coupling between a ferric pair, $S' = 2$ or 3, and a ferric ion $S = 5/2$
	0	−720 to −690	$2 \times Fe^{3+}$, Fe^{2+}	$S_t = 2$: AF coupling between a mvp, $S' = 9/2$, and a ferric ion $S = 5/2$
	−2		$3 \times Fe^{2+(c)}$	
[4Fe-4S] HiPIP	+3	+50 to +450	$3 \times Fe^{3+}$, Fe^{2+}	$S_t = 1/2$:AF coupling between a mvp, $S' = 9/2$, and a ferric pair $S' = 4$ or 3
	+2		$2 \times Fe^{3+}$, $2 \times Fe^{2+}$	$S_t = 0$: AF coupling between two mvp $S' = 9/2$
Fd	+1	−645 to 0	Fe^{3+}, $3 \times Fe^{2+}$	$S_t = 1/2$: AF coupling between a mvp, $S' = 9/2$, and a ferrous pair $S' = 4$

[a]Calculated based on the iron atom charges and inorganic sulfur, S^{2-}.
[b]Typical range.
[c]State produced at the electrode surface, by electrochemistry.
[d]mvp, mixed valence pair; AF, antiferromagnetic.

$S = 5/2$, reduced state high-spin Fe^{2+} $S = 2$) is bound by four cysteine residues with a conserved binding sequence of the type: -C-X-Y-C- . . . -C-X-Y-C-. The resulting centre has tetrahedral geometry. A large number of x-ray structures exists for Rds from various bacterial sources.[6–9]

Desulforedoxin (Dx), the other known [Fe-4S] protein, is a small homo-

dimer (4 kDa per monomer) containing four cysteinyl residues that bind a high-spin iron atom in each monomer. The binding sequence in Dx differs from that found in Rd in that the second pair of cysteines are consecutive: -C-X-Y-C- . . . -C-C-. The x-ray structure of *Desulfovibrio gigas* (*Dg*) Dx has been determined.[10]

Both of the Rd-type and Dx-type centres have been found in larger proteins. The protein rubrerythrin[11,12] contains an Rd centre along with an oxo-bridged octahedral Fe centre, while desulfoferrodoxin[13,14] has a Dx-type centre and an Fe centre with pentacoordination by one cysteine and four histidines.[15]

The [2Fe-2S] Fd cluster can be found in two redox states: $[2Fe\text{-}2S]^{2+}$ and $[2Fe\text{-}2S]^{1+}$. In the oxidized form the two iron atoms are in the ferric state, and their $S = 5/2$ spins are antiferromagnetically coupled, giving a total spin system of $S_t = 0$.[16] The system is diamagnetic in the ground state, but at room temperature the excited states can be populated and the system is paramagnetic. In the reduced state, the cluster, $[2Fe\text{-}2S]^{1+}$, has Mössbauer parameters indicative of the presence of two localized valence sites: one ferric, $S = 5/2$, and one ferrous, $S = 2$. The electron paramagnetic resonance (EPR) spectra, centred at $g = 1.94$, is characteristic of an $S = 1/2$ ground state system.

Of the four basic, well-established structures for iron–sulfur proteins, the [3Fe-4S] cluster is the latest entry discovered around 1980.[17,18] In the oxidized state, $[3Fe\text{-}4S]^{1+}$, the three high-spin ferric atoms ($S = 5/2$) are antiferromagnetically coupled, forming an electronic ground state with a spin system of 1/2. The one-electron reduced state, $[3Fe\text{-}4S]^{0}$, contains a mixed valence pair, $2 \times Fe^{+2.5}$, with $S' = 9/2$, and one Fe^{3+}, $S = 5/2$. The system is characterized by a global $S = 2$ spin state, arising from the antiferromagnetic coupling between the two spin systems.

The [4Fe-4S] cluster can be found in three redox states: $[4Fe\text{-}4S]^{3+}$, $[4Fe\text{-}4S]^{2+}$ and $[4Fe\text{-}4S]^{1+}$. The redox pair, $[4Fe\text{-}4S]^{3+}/[4Fe\text{-}4S]^{2+}$, is characteristic of the high-potential iron proteins, while the $[4Fe\text{-}4S]^{2+}/[4Fe\text{-}4S]^{1+}$ pair is found in 4Fe Fds. The three redox states all contain a mixed valence pair, $2 \times Fe^{2.5+}$, in conjunction with: a ferric pair for the 3+ state; another mixed valence pair for the 2+ state and a ferrous pair for the 1+ state. The cluster is paramagnetic with a total spin of $S = 1/2$ in the 3+ state and the 1+ state. The 2+ state has an $S = 0$ ground state, but is paramagnetic due to the occupancy of excited states at room temperature.[2,19]

3. PARAMAGNETISM AND NMR

When determining the structure of metalloproteins by NMR one of the drawbacks has been the presence of the metal centre, which can be paramagnetic owing to one or more unpaired electrons being present in at least one of its oxidation states.[20] These electrons interact with nuclei causing (1) efficient nuclear relaxation resulting in broadening of resonances, and (2) hyperfine

chemical shifts that place the signals well outside the normal diamagnetic envelope (0–10 ppm for ^{1}H). Paramagnetic interactions are most severe for protons close to the metal centre.

In this section, some theory of electron–nucleus interactions is presented. For a more detailed analysis, and for derivations of all equations, the reader is directed to a number of excellent articles and reviews by the group of Bertini.[21–25]

3.1. Electron–nuclear coupling

In diamagnetic compounds, the presence or absence of electrons and their motion in an external magnetic field determines the chemical shift of a proton. In the presence of unpaired electrons the magnetic moment, μ_S, of the electron will contribute to the shielding of a proton nucleus and in these cases we have paramagnetic shielding. If we consider that this shielding interaction is dipolar in nature, the coupling between the electron and a nucleus (hyperfine coupling) can be described as $H = I \cdot \hat{A} \cdot S$, where I is the nuclear spin and S the electron spin. The coupling tensor is described by A. The interaction energy is dependent on the angle between the nuclear and spin vectors (Fig. 1), the external magnetic field, and the distance between the two spins:

$$E = \frac{\mu_0}{4\pi} \frac{\mu_I \mu_S}{r^3} (3\cos^2\theta - 1)$$

In solution, where random molecular tumbling normally occurs, we can ignore terms involving $3\cos^2\theta - 1$ as they average to zero. However, if g for the electron (and μ_S, as $\mu_S = \sqrt{g_e^2 \mu_B^2 S(S+1)}$)) varies with molecular tumbling, the $3\cos^2\theta - 1$ term does not average to zero and hyperfine shifts will be seen. This through-space interaction is known as the pseudocontact shift and is given by

$$\delta_{pc} = \left(\frac{\Delta\nu}{\nu_0}\right) = \frac{1}{4\pi} \frac{1}{3N_A r^3} \left[\chi_{zz} - \tfrac{1}{2}(\chi_{xx} - \chi_{yy})(3\cos^2\theta - 1) + \tfrac{3}{2}(\chi_{xx} - \chi_{yy}) \sin^2\theta \cos^2 2\phi \right] \quad (1)$$

The average hyperfine shift is given by $\Delta\nu$ and ν_0 is the chemical shift of a reference nucleus, N_A is Avogadro's number and χ_{zz}, χ_{xx} and χ_{yy} are the principal components of the magnetic susceptibility tensor. This tensor is anisotropic in part owing to the anisotropy of the electron g values. The three χ direction cosines define the axis frame and the polar coordinates define the nucleus within that frame.

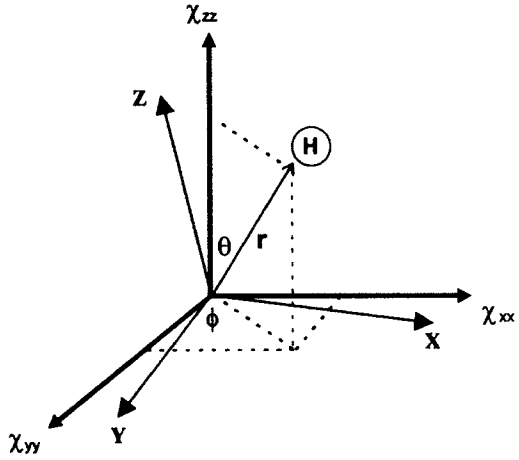

Fig. 1. Relationship between the M—H vector, the protein reference frame, and the axes of the three direction cosines defining the magnetic susceptibility tensor (χ).

In reality the spin of the unpaired electrons is not localized entirely on the metal ion since delocalization occurs via molecular orbitals. If delocalization occurs then the equation for the pseudocontact shift does not strictly hold true. There is also the possibility that unpaired spin density may reside on the resonating nucleus (if s-type orbitals are involved in the molecular orbital). This spin density can be described as $H = AI{\cdot}S$ where $A = K\rho/2S$ (the contact coupling constant) and K is the hyperfine splitting and ρ the spin density. In an external magnetic field the electron has M_s possible orientations and the transitions between these energy levels depends on the electron relaxation time. Almost always, the electron relaxation times are much faster than proton relaxation times, therefore the proton sees an average orientation. This results in a nonzero magnetic moment (some orientations are preferred);

$$\langle \mu \rangle = g\mu_B \langle S_z \rangle \qquad \text{where } \langle S_z \rangle = -S(S+1)\frac{g\mu_B B_0}{3kT} \tag{2}$$

The resulting shift, called the contact shift, due to this spin density delocalization (σ and π) is thus

$$\delta_{con} = \left(\frac{\Delta\nu}{\nu_0}\right) = \frac{A}{\hbar\gamma_1 B_0}\langle S_z \rangle = \frac{A}{\hbar}S(S+1)\frac{g\mu_B}{3\gamma_1 kT} \tag{3}$$

The contact shift is dependent on temperature and on S (informative about coupling in Fe clusters). Contact shifts are seen for protons up to 4 or 5 bonds removed from the metal atom on which the unpaired electron resides.

3.2. Nuclear relaxation

In general, relaxation of nuclei in NMR occurs via fluctuating magnetic fields at the correct frequency to cause transitions between nuclear energy levels. In the absence of unpaired electrons, there are four main relaxation mechanisms for $I = \frac{1}{2}$ nuclei:[26] dipole–dipole, spin rotation, chemical shift anisotropy and scalar relaxation (two kinds). In the presence of unpaired electrons, nuclear relaxation is normally dominated by fluctuating fields created by the magnetic moment of the unpaired electron; this therefore is a fifth relaxation mechanism. These fluctuating fields arise by (1) relaxation of the electron, (2) molecular tumbling and (3) chemical exchange. Electron relaxation in metal ions is fast, of the order of 10^{-8} to 10^{-13} s, and provides magnetic field variations that in turn cause nuclear relaxation. In the case of iron–sulfur proteins, the electron relaxation time (τ_s) varies from 10^{-9} to 10^{-11}s for Fe^{3+} high-spin and is $\sim 10^{-11}$s for Fe^{2+} high-spin, resulting in line broadening that varies from 200 to 12 000 Hz for Fe^{3+} high-spin and is of the order 150 Hz for Fe^{2+} high-spin.[25] Molecular tumbling, which changes the relative orientation of the electron–nucleus vector with respect to the external magnetic field, results in the nucleus sensing a tumbling electron with associated magnetic moment, which in turn relaxes the nucleus. Another relaxation pathway due to molecular tumbling arises from the fact that $\langle S_z \rangle$ (see above) is populated via the Boltzmann distribution and is nonzero, therefore S_z has an induced magnetic moment. Rotation of this magnetic moment causes relaxation, known as Curie relaxation. The final mechanism by which unpaired electron cause nuclear relaxation is chemical exchange.

The availability of mechanisms occurring at the correct frequency to induce transitions between nuclear energy levels is of great importance. The spectral density function represents the availability of these frequencies in the environment of the nucleus; $1/T_{1,2} = (E^2)_{av} f(\omega, \tau_c)$.

For relaxation, as for the electron–nucleus hyperfine shifts, two contributions are present, dipolar and contact. For the dipolar case, the following relaxation equations are given for spin–lattice (T_1), spin–spin (T_2, dipolar and Curie) and spin–lattice relaxation in the rotating frame ($T_{1\rho}$):

$$\left(\frac{1}{T_1}\right) = \frac{2}{15}\left(\frac{\mu_0}{4\pi}\right)^2 \frac{\gamma_I^2 g_e^2 \mu_B^2 S(S+1)}{r^6}\left[\frac{\tau_c}{1+(\omega_I-\omega_S)^2\tau_c^2} + \frac{3\tau_c}{1+\omega_I^2\tau_c^2} + \frac{6\tau_c}{1+(\omega_I+\omega_S)^2\tau_c^2}\right] \tag{4}$$

$$\left(\frac{1}{T_2}\right) = \frac{1}{15}\left(\frac{\mu_0}{4\pi}\right)^2 \frac{\gamma_I^2 g_e^2 \mu_B^2 S(S+1)}{r^6}\left[4\tau_c + \frac{\tau_c}{1+(\omega_I-\omega_S)^2\tau_c^2} + \frac{3\tau_c}{1+\omega_I^2\tau_c^2} + \frac{6\tau_c}{1+(\omega_I+\omega_S)^2\tau_c^2} + \frac{6\tau_c}{1+\omega_S^2\tau_c^2}\right] \tag{5}$$

$$\left(\frac{1}{T_2}\right)\text{Curie} = \frac{1}{5}\left(\frac{\mu_0}{4\pi}\right)^2 \frac{\omega_I^2 g_e^4 \mu_B^4 S^2(S+1)^2}{(3kT)^2 r^6}\left[4\tau_c^2 + \frac{3\tau_c}{1+\omega_I^2\tau_c^2}\right] \tag{6}$$

$$\left(\frac{1}{T_{1\rho}}\right) = \frac{1}{15}\left(\frac{\mu_0}{4\pi}\right)^2 \frac{\gamma_I^2 g_e^2 \mu_B^2 S(S+1)}{r^6}\left[\frac{4\tau_c}{1+\omega_I^2\tau_c^2} + \frac{\tau_c}{1+(\omega_I-\omega_S)^2\tau_c^2} + \frac{3\tau_c}{1+\omega_I^2\tau_c^2}\right.$$

$$\left. + \frac{6\tau_c}{1+(\omega_I+\omega_S)^2\tau_c^2} + \frac{6\tau_c}{1+\omega_S^2\tau_c^2}\right] \tag{7}$$

The correlation time, τ_c, is a sum of the various correlation times active for nuclear relaxation:

$$\frac{1}{\tau_c} = \frac{1}{\tau_s} + \frac{1}{\tau_r} + \frac{1}{\tau_m}$$

where τ_s is the electron relaxation time, τ_r the rotation correlation time and τ_m the exchange time. For contact relaxation the equations are

$$\left(\frac{1}{T_1}\right) = \frac{2}{3}\left(\frac{A}{\hbar}\right)^2 S(S+1)\left[\frac{\tau_e}{1+(\omega_I-\omega_S)^2\tau_e^2}\right] \tag{8}$$

$$\left(\frac{1}{T_2}\right) = \frac{1}{3}\left(\frac{A}{\hbar}\right)^2 S(S+1)\left[\frac{\tau_e}{1+(\omega_I-\omega_S)^2\tau_e^2} + \tau_e\right] \tag{9}$$

$$\left(\frac{1}{T_{1\rho}}\right) = \frac{1}{3}\left(\frac{A}{\hbar}\right)^2 S(S+1)\left[\frac{\tau_e}{1+(\omega_I-\omega_S)^2\tau_e^2} + \frac{\tau_e}{1+\omega_I^2\tau_e^2}\right] \tag{10}$$

As contact coupling is independent of molecular rotation,

$$\frac{1}{\tau_e} = \frac{1}{\tau_s} + \frac{1}{\tau_m}$$

Dipolar and Curie relaxation are related to the distance between the metal and the proton, and can provide constraints if they can be determined independently. This is often possible, as relaxation of a nucleus is normally dominated by one mechanism only. In general, the dipolar relaxation mechanism is dominant for most systems of interest, unless there is some unpaired electron density at the nucleus.

The important factors, which control the relaxation of nuclei, outlined above

will dictate whether high-resolution NMR can be performed and whether structural information can be obtained from the spectra, i.e. whether NMR signals can be observed.

3.3. The nuclear Overhauser enhancement

The nuclear Overhauser enhancement (NOE) is a through-space dipolar interaction and is the basis for all NMR structural work in solution. The theory of the NOE is highly developed for diamagnetic systems.[27,28] The effect of paramagnetism on the NOE is encountered via T_1 effects. At steady state (irradiation time is long compared to the T_1 of the observed proton) for irradiation of proton J, the NOE at proton I is: $\eta = \sigma_{IJ}/\rho_I$. The σ_{IJ} term is the cross-relaxation ($\sigma_{IJ} = \omega_2 - \omega_0$) rate and is given by

$$\sigma_{IJ} = \left(\frac{\mu_0}{4\pi}\right)^2 \frac{\hbar^2 \gamma_I^2 \gamma_J^2}{10r^6}\left[\frac{6\tau_c}{1+(\omega_I+\omega_J)^2\tau_c^2} - \frac{\tau_c}{1+(\omega_I+\omega_J)^2\tau_c^2}\right] \tag{11}$$

The relaxation rate $\rho_I = \omega_0 + 2\omega_1^I + \omega_2$ contains both paramagnetic and diamagnetic contributions; $\rho_I = \sum_M \rho_{IM}^{para} + \sum_J \rho_{IJ}$ where,

$$\rho_{IJ} = \left(\frac{\mu_0}{4\pi}\right)^2 \frac{\hbar^2 \gamma_I^2 \gamma_J^2}{10r^6}\left[\frac{\tau_c}{1+(\omega_I+\omega_S)^2\tau_c^2} + \frac{3\tau_c}{1+\omega_I^2\tau_c^2} + \frac{6\tau_c}{1+(\omega_I+\omega_S)^2\tau_c^2}\right] \tag{12}$$

$$\rho_{IM}^{para} = \frac{2}{15}\left(\frac{\mu_0}{4\pi}\right)^2 \frac{\gamma_I^2 g_e^2 \mu_B^2 S(S+1)}{r_{IM}^6}\left[\frac{7\tau_c}{1+\omega_S^2\tau_c^2} + \frac{3\tau_c}{1+\omega_I^2\tau_c^2}\right] \tag{13}$$

This last equation is the same as that for T_1 dipolar relaxation only written for the case where electron relaxation is dominant. If ρ_I (the measured $1/T_1$ of the nucleus) is dominated by ρ_{IM}^{para} then $\eta_{IJ} = \sigma_{IJ} T_{1M}^{-1}$. The dependence of the steady-state NOE on H–H distance and molecular mass for hyperfine shifted resonances is illustrated in Table 2.[29] It can be seen that as protein molecular mass increases so does the NOE enhancement, and the smaller the T_1 the smaller the NOE. For paramagnetic species, as the NOE is independent of the T_1 of the irradiated proton, observation of an NOE is easier when the faster relaxing proton is saturated. The 2D NOESY experiment is an example of a transient NOE: in this case the simplified equation relating the NOE enhancement to the cross-relaxation rate is $\eta_{IJ} = \exp[-(\rho - \sigma_{IJ})t][1 - \exp(-2\sigma_{IJ}t)]$ where the initial slope of the NOE build-up curve is $2\sigma_{IJ}$.

Table 2. NOEs enhancements for some iron–sulfur protein hyperfine shifted resonances[29]

Group	Distance (Å)	NOE (%)	T_1 (ms)	Molecular mass (kDa)	τ_r (ns)
H–C–H	1.8	6	8.4	9	4
(Cys)		5	3.6	11	5
		7	5.6	11	5
		43	120	16	9
H–C–H		7.7	2.4	32	14
(Asp, Glu, Cys,		60	100	36	21
and His)		50	80	42	22
Hα–C–C–Hβ	2.2–2.4	4.5	34	9	4
(Cys)		1.8	5.6	11	5

4. NMR EXPERIMENTS FOR SPIN ASSIGNMENT

The first step in the determination of structures in solution by NMR is the complete assignment of the spectra, that is, the chemical shift of every proton in the protein must be obtained. The standard procedure is to use a combination of 2D COSY[30,31] (correlation spectroscopy) and TOCSY[32] (total correlation spectroscopy) spectra (scalar interactions) to identify the type of spin systems present and then use 2D NOESY[33] spectra (dipolar interactions) to identify sequentially these spin systems.[34] This methodology was developed for diamagnetic systems and relies on suitable ^3J coupling values and dipolar–dipolar through-space interactions. In the presence of unpaired electrons, as outlined above, hyperfine shifted signals are observed along with short T_1 and T_2 values for nuclei in their vicinity. This requires experiments tailored for the detection of these signals.

Hyperfine shifted resonances can appear at both high and low fields and, therefore, in order to observe J coupling or NOE effects between hyperfine shifted protons and protons that are not affected by electron–nuclear interactions, larger spectral windows need to be employed. The use of large spectral windows can result in a loss of resolution (if the same number of data points in t_2 is used) and in extreme cases may require the use of fast digitizers to record spectra with large hyperfine shifted resonances (e.g. Rd(Fe) and Dx(Fe), Section 6.1). Normally, two sets of spectra are recorded to characterize separately the diamagnetic (small spectral window) and paramagnetic regions (large spectral window) of the spectrum. Associated problems are those of baseline distortion and uneven excitation of resonances across the spectral window. Baseline distortion can be severe for large spectral windows although the use of digital filtering and backwards linear prediction can help. To obtain

a uniform 90° pulse over a large spectral window requires high-power pulses; where this is not possible, excitation can be performed only in certain regions of the spectrum to overcome the problem.

The short nuclear relaxation times present other problems. Short T_2 values mean large linewidths in NMR, therefore problems involving peak overlap and low peak intensity will be encountered in the spectra. In severe cases, peaks may be broadened beyond detection. Experimental considerations, such as acquisition times in t_2 and t_1, have to be taken into account. In COSY-type experiments the time taken for cross-peaks to develop is related to T_2 and it has been found that, for short T_2, the acquisition times (t_1 and t_2) should be set to $2T_2$.[35] In DQF-COSY (double-quantum filtered COSY) experiments, large linewidths can result in the cancellation of antiphase cross-peaks and so M-COSY (magnitude correlation spectroscopy) experiments are often used where short T_2 values are encountered. In the case of TOCSY-type experiments similar problems occur. Large sweep widths require spin lock pulses of higher power than normally used in order to ensure all resonances are locked in the x–y plane during the mixing period. The relaxation time related to cross-peak build-up is $T_{1\rho}$. Therefore, if $T_{1\rho}$ is of the order of T_2, the spin lock mixing time should be $\sim T_{1\rho}$. A $t_{2\max}$ value of T_2 should also be used.[24]

For paramagnetic systems the 1D NOE experiment is very useful: in terms of signal intensity it is often superior to 2D NOESY experiments and it allows the detection of connectivities between the resonances in the paramagnetic and diamagnetic regions of the spectrum. These types of experiments normally use a super-WEFT[36]-type sequence to suppress water and slowly relaxing protons. The super-WEFT difference 1D NOE experiment[37] has been found to be particularly useful. In 2D NOESY experiments the parameters $t_{1\max}$ and $t_{2\max}$ should not exceed T_2, while the mixing time, τ_m, should be of the order of T_1 of the signal of interest. A set of experiments with short mixing times and large spectral windows are normally needed to characterize the hyperfine shifted and/or broadened signals. Other NOE-type experiments that have been used for assignment include NOE-NOESY-type experiments where a 1D NOE sequence is placed before a NOESY experiment for spectral simplification.[38] The resulting spectra only display cross-peaks for those protons with NOEs to the irradiated proton of the 1D sequence.

Although not normally used to assign spectra, relaxation times are often required. Measurement of T_1 relaxation times is determined using the inversion recovery (IR) sequence. A non-selective 1D version or an IR sequence, placed before a 2D experiment such as a NOESY, TOCSY or COSY, can be used. For fast relaxing resonances T_2 can be measured directly from the linewidth ($1/T_2 = \pi\Delta\nu$), while for slowly relaxing resonances the Carr, Purcell, Meiboom, Gill (CPMG) sequence is used.

For isotopically labelled samples, heteronuclear experiments may be used for assignment purposes, and can be of great use owing to the favourable, i.e small, magnetogyric ratios of heteronuclei such as ^{13}C, ^{15}N and ^{2}H

(as paramagnetic relaxation is related to γ^2; Section 3.2.). Experiments such as heteronuclear multiple-quantum filtered correlation spectroscopy (HMQC)[39–41] or heteronuclear single-quantum filtered correlation spectroscopy (HSQC)[42,43] can be used with the fixed delays being set to $1/2T_2$ of the fast relaxing protons to assign both ^{1}H and heteronuclear chemical shifts. It should be noted that, although in Fe-S proteins low-intensity signals can be a problem, as T_1 and T_2 are normally short, recycle times can be reduced significantly, when compared to normal diamagnetic recycle times, and a larger number of scans can be accumulated in the same time period.

5. STRUCTURE CALCULATION FROM NMR DATA

The ways in which structures are calculated in solution by NMR are essentially the same for diamagnetic and paramagnetic proteins. The major differences are that the experiments needed to record spectra, and detect spin systems and NOEs for hyperfine shifted or broadened resonances, are more demanding. Distance constraints (^{1}H–^{1}H, M–^{1}H) and J coupling constants are the basis by which structures are calculated. These constraints are usually derived from the NOE, and both 1D and 2D spectra may be used. Initially, a qualitative assessment is normally made of the NOE data as regular secondary structure can be identified early on in a structure determination. Sequential NOEs are dependent on the local backbone conformation, as are $^3J_{\mathrm{NH\text{-}H\alpha}}$ coupling constants. Medium-range NOEs are also indicative of regular structure such as β-turns and α-helices.[44] It has also been found that Hα and Cα chemical shifts are indicative of secondary structure.[45,46] In D_2O spectra, NHs that are solvent protected often appear, and are usually taken as an indication of the presence of H-bonding. Thus, the combination of all the above qualitative data can identify structure at an early stage in the process.

5.1. Distance constraints

The 1D NOE or 2D NOESY spectrum, once fully assigned, is the starting point for the determination of distance constraints. The theory of the NOE tells us that the area of a peak, or the volume of the cross-peak, is inversely proportional to the 6th power of the distance between the protons that give rise to the peak: $\eta = c/r^6$.[27,28] Calibration with a known distance, or distances, is needed to obtain the constant c. Normally, the area or volume of a cross-peak between protons that are a fixed distance apart (Hβ or aromatic protons) can be used as a calibration. As an example, the program DYANA[47] uses a method in which the distances are calibrated using different distance classes. Cross-peaks for all NH/Hα–NH/Hα and NH/Hα–Hβ protons between residues less

than 5 residues apart are calibrated using a function where $V = A/d^6$. Side-chain protons, i.e. not backbone and not methyl, use $V = B/d^4$, and methyl protons use $V = C/d^4$. A problem may occur with the overestimation of distances for protons affected by the paramagnetism of the metal centre, as short relaxation times give rise to cross-peaks with reduced intensity. This problem can be overcome by back-calculating NOE intensities from initial structures using no explicit term for the paramagnetic influence. Comparison of NOE intensities in the experimental and back-calculated spectra allow correction factors to be determined and 'tighter' distance constraints obtained for the affected proton pairs.[48] After the complete calibration process, a list of distances between various protons in the protein is obtained. These distances are in the format of distance ranges as there is a number of problems with the precise quantitative determination of NOE cross-peaks. Studies have shown that it is the number of constraints and not the precision that determines the quality of a structure determined by NMR.[49]

For metalloproteins, constraints can also be obtained between the metal atom and nearby protons. Using the equations given in Sections 3.1 and 3.2, pseudocontact shifts and relaxation time values can be used to derive M—H distances while the contact shift can be empirically used to constrain Hβ—Cβ—Sγ—M dihedral angles.

Distance constraints from relaxation data can be obtained by assuming pseudo-exponential behaviour and that $\rho^{\text{eff}} = \rho^{\text{eff}}_{\text{dia}} + \rho^{\text{eff}}_{\text{para}}$. In this case $\rho^{\text{eff}}_{\text{dia}}$ needs to be estimated (an upper limit for $\rho^{\text{eff}}_{\text{dia}}$ can normally be taken between 4 and 5 s^{-1}, or a T_1 of 200 or 250 ms). The resulting $\rho^{\text{eff}}_{\text{para}}$ value can be used to extract a distance that is an upper limit. Owing to the magnetic moment of the electron, these are long-range distance constraints (5–15 Å).

The pseudocontact shift can be extracted assuming $\delta = \delta^{\text{con}} + \delta^{\text{pc}} + \delta^{\text{dia}}$. If the protons experiencing the pseudocontact shift are more than 4 bonds removed from the metal, δ^{con} can be assumed to be negligible, leaving the problem of estimating δ^{dia}. Literature values for δ^{dia}, or a diamagnetic equivalent of the protein under study, can be used to provide diamagnetic chemical shift values. Extraction of distances from δ^{pc} shifts requires the principal components of the magnetic susceptibility tensor to be known along with the direction cosines, which define the magnetic susceptibility tensor within an internal axis frame, as well as the position of the proton within that frame. Initial NMR structure calculations (or an x-ray structure) can be used to determine these values. The differences between experimental and calculated δ^{pc} values can then be minimized by varying the atomic coordinates. It should be noted that new molecular susceptibility tensors need to be calculated, when the atomic coordinates are changed, until a best fit is obtained. The r^{-3} dependence of the δ^{pc} means that longer-range distance constraints are obtained from pseudocontact shifts than from NOE constraints.[50,51] The introduction of pseudocontact shift constraints will be implemented as a module of DYANA.

Contact shifts can also be used to obtain angle constraints, although they have been implemented only for $[4Fe\text{-}4S]^{2+}$ cluster proteins and in an empirical way.[52,53] Using a δ versus dihedral angle curve, contact shifts can be input and dihedral angles read out and used, with suitable tolerance range, in NMR structure calculations.

5.2. Methods for structure calculations

All NMR structures for Fe-S proteins have been calculated using distance geometry (DG) or by simulated annealing (SA) methods. The term distance geometry describes a general methodology, which formulates conformational problems in terms of distance and chirality constraints. The constraints used to derive conformation may come from various sources. The molecular formula (bonds, etc.) is one source, since covalent bond lengths and 3-atom angles are determined exactly by this information. Experimentally, in solution, the richest source of constraints is the 1D/2D/3D NOESY NMR experiment. Each cross-peak represents a constraint between a pair of protons, with the maximum distance normally being 5 Å (in diamagnetic cases). The major problem to be overcome is that of local minima encountered during the minimization process. Methods such as metric matrix,[54] variable target functions in dihedral angle space[55,56] and simulated annealing in torsion angle space[47] have been used to search for protein conformations obeying the experiment upper (and lower) experimental NMR distance constraints, avoiding local minima.

The programs DIANA and XPLOR have been used almost exclusively to calculate NMR structures of Fe-S proteins. As an example, the DG program DIANA (and its newer version DYANA which employs torsion angle dynamics) uses a variable target function (VTF) algorithm developed specifically for the calculation of protein structures from NMR.[47,56] Structures are calculated many times starting from randomly chosen torsion angles, ensuring a large sampling of conformational space. The essential idea behind the method is that it avoids being trapped in local minima by initially minimizing a target function that restrains only the torsion angles with the 'short range' distances between sequential residues. The longer-range distance constraints are then introduced gradually. This ensures that the short-range secondary structure is formed first, followed by the interaction of the secondary structural elements in a manner analogous to the way proteins are thought to fold in solution.

The program XPLOR[161] uses restrained molecular dynamics (RMD), normally in conjunction with an SA protocol, to calculate structures from NMR data. RMD involves minimizing the energy of the system while exploring conformational space using the experimental NOE constraints. In SA, the temperature of the whole system is raised to overcome local energy barriers

and then slowly cooled in the hope of encountering the global energy minimum.

Once initial structures have been calculated, an iterative procedure is normally carried out, as many ambiguous NOE cross-peaks can only be assigned using initial structures. The results from DG or SA calculations do not give one definite structure, because a single result, although compatible with the distance constraints, may not be unique. The calculations are normally carried out from different starting conditions and each result, or convergence, is judged by the residual violations of the distance constraints. All solutions that satisfy the constraints are included in a 'family' of structures. The final quality of this family is determined by the root mean square deviation (RMSD) between all the conformers in the family. Global backbone RMSDs of ~1 Å are considered as good. Normally, however, the RMSD will vary along the protein backbone: low RMSDs in the protein core and high RMSDs at the termini and surface residues. Often low RMSDs are also seen near the metal centre or cluster in iron–sulfur proteins owing to the lack of NOEs (the residues nearby are 'bleached out').

5.3. Including the metal centre in structure calculations

A problem encountered for iron–sulfur metalloproteins is how to include the metal centres in the calculations. The protein is essentially described in the calculations by fixed distances (chemical bonds, angles, etc.) and the distance constraints are obtained from NMR experiments. The actual metal, or metal cluster, in metalloproteins has no protons, therefore no distance constraints can be obtained. The nearest protons, for Fe-S proteins, are normally the β-CH_2 protons of the cysteine residues that bind the metal. The question is how to obtain the distances and angles between the metal and the cysteine sulfurs, and between the sulfurs and the rest of the protein. It would be possible to introduce no constraints for the metal centre and calculate structures relying on the 'natural' constraints of the protein fold about the metal centre. The problem in using this approach, however, is that the paramagnetism of the centre usually means the protons near the centre are 'bleached out' resulting in few NOE constraints near the centre. Another approach is to use data from x-ray crystallographic studies. Structures already solved by x-ray can be used to obtain Fe-S distances and Cβ—S—Fe angles and Cα—Cβ—S—Fe torsion angles. These data can then be introduced into the NMR calculations as extra distance constraints. The added problem with this approach is that we are assuming that the structure of the centre is the same in solution and the solid state. However, this last assumption is usually valid as the majority of protein structures solved by NMR and x-ray show that the overall folds are very similar, and therefore the transfer or extrapolation of x-ray data to NMR can usually be made. As an example, the way in which metal centres are introduced

in the DG program DIANA will be used. The metal–sulfur centres are included by defining an additional 'special' amino acid.[57] The M—S bond length and angles are defined using distance constraints for the M, S and C atoms identical to those seen in the x-ray structure. Special covalent bonds between the M of the 'new' amino acid and the sulfurs of the other cysteine residues are defined along with special covalent linkages between cysteinyl sulfurs (to fix the cluster geometry).

Recent advances in structure calculation that introduce M—H distance constraints from relaxation data, for example, may eventually, when sufficient constraints are available, allow the metal centre to be defined by experimental constraints only, which is essentially the goal of the NMR spectroscopist.

6. NMR STRUCTURAL STUDIES OF IRON–SULFUR PROTEINS

This section will be divided into cluster types, although within each section similar techniques will be discussed. Within each section, work will be reviewed by protein and in chronological order, where possible. Most of the work reviewed here, for the paramagnetic proteins, starts with identification and characterization of the hyperfine shifted signals and the identification of those protons near the binding cysteines (using 1D NOE experiments). Sequential assignment of the diamagnetic spin systems is then carried out allowing in many cases the determination of a structure in solution. Almost all of the NMR structural work carried out for Fe-S proteins has taken place within the last 8 years, so most of the references will be from these years.

6.1. Rubredoxin-type proteins

One of the first NMR studies of Rd(Fe) was carried out on a Rd from *Desulfovibrio gigas* (*Dg*) to identify the hyperfine shifted signals.[58] A group of four broad signals, for the reduced form of the protein (Fe^{2+}, $S = 2$), were seen between 100 and 300 ppm (Fig. 2) and were assigned to the four sets of β-CH_2 protons of the iron binding cysteines by analogy with model compounds. Under the experimental conditions used, no hyperfine shifted signals above 50 ppm were seen for the native oxidized form of the protein (Fe^{3+}, $S = 5/2$). For the other known [Fe-4S] protein, *Dg* Dx, as for *Dg* Rd, only the reduced form shows a set of hyperfine shifted signals in the low-field region of the spectrum (Fig. 3).[59]

The hyperfine shifted signals for *Clostridium pasteurianum* (*Cp*) Rd were identified unequivocally using site-specific labelling.[60] The cysteines that bind the Fe in the protein were labelled with $^2H\alpha$Cys and $^2H\beta$Cys and ^{15}NCys. ^{2}H NMR spectra indicated, for the reduced protein, that the β-CH_2 protons appear as a group of signals between 280 and 120 ppm. For the Hα protons, in

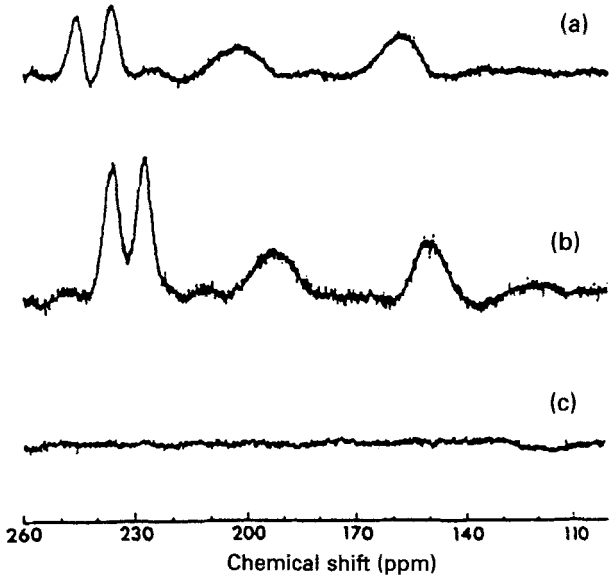

Fig. 2. 300 MHz ^{1}H NMR spectrum of *Dg* Rd in the 260–100 ppm region: (a) reduced, 40°C; (b) reduced 55°C; (c) oxidized, 55°C. 64 000 transients of 16 K data points were collected with a recycle delay of 120 ms. (Reprinted with permission from Werth *et al.*, *J. Am. Chem. Soc.*, 1987, **109**, 273. Copyright 1987 American Chemical Society).

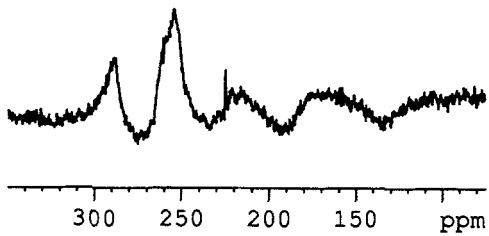

Fig. 3. 400 MHz ^{1}H NMR spectrum of the 100–300 ppm region for *Dg* DxWt(Fe) reduced form at 303 K and pH 7.2. A sweep width of 800 ppm was used and 2 K transients were collected.[59]

the reduced form, two of the four resonances appear at 19 and 16 ppm, with the other pair appearing at 0 ppm (overlapped). In the oxidized form, the cysteine β-CH_2 protons were seen in the ^{2}H spectrum between 900 and 300 ppm (Fig. 4) while two Hα protons appeared at 180 and 150 ppm and two at -10 ppm (overlapped). The upfield shift for two of the Hα protons in the oxidized form of *Cp* Rd was suggested to be a result of differing contact and pseudocontact contributions at different atoms near the Fe centre, or electron–

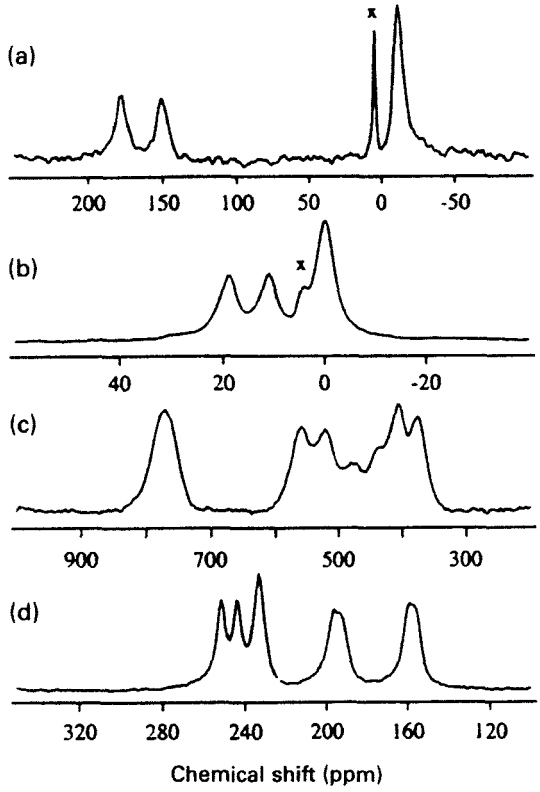

Fig. 4. ^{2}H NMR spectra of [^{2}H]cysteine-labelled *Cp* Rd at 35°C, pH 6.0: (a) oxidized [$^2H^{\alpha}$]Cys-labelled Rd; (b) reduced [$^2H^{\alpha}$]Cys-labelled Rd; (c) oxidized [$^2H^{\beta 2,\beta 3}$]Cys-labelled Rd; (d) reduced [$^2H^{\beta 2,\beta 3}$]Cys-labelled Rd. The peak labelled 'x' arises from residual $^1H^2HO$. (Reprinted with permission from Xia *et al.*, *J. Am. Chem. Soc.*, 1995, **117**, 5347. Copyright 1995 American Chemical Society.)

nuclear hyperfine coupling constants of differing signs for two of the four Hα protons. These labelling studies confirm the tentative assignments postulated for the hyperfine shifted signals seen in the ^{1}H spectra of reduced *Dg* Rd(Fe) and reduced *Dg* Dx(Fe).[58,59] The large hyperfine shifts and linewidths and the increased gyromagnetic ratio of ^{1}H compared to ^{2}H, resulting in an increased relaxation enhancement, probably result in the non-observation of any hyperfine shifted signals in the ^{1}H spectra of oxidized *Dg* Rd(Fe) and oxidized *Dg* Dx(Fe).

The use of a combination of 2D and 3D heteronuclear experiments allowed the almost complete assignment of the ^{1}H, ^{13}C and ^{15}N chemical shifts in *Cp* Rd.[61,62] In the oxidized form, due to the paramagnetism of the Fe, 12 ^{15}N signals from the binding motifs (CXXCGX) experienced hyperfine shifts and no

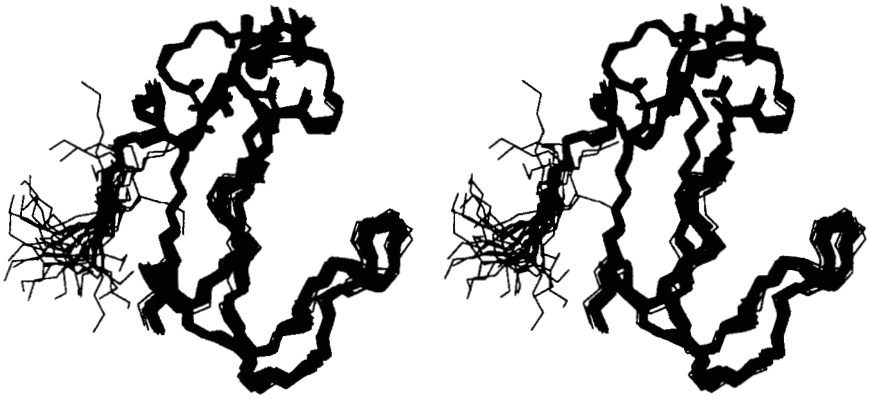

Fig. 5. Stereoplot of the backbone atoms of the NMR family of 40 structures calculated for *Pf* Rd(Zn) (Brookhaven access code: 1zrp). The cysteine side-chains are shown and the Zn atoms are displayed as space filling.[64]

resonances from these amino acids could be identified in the 2D or 3D spectra. These resonances are within 11 Å of the Fe and experience severe line broadening and hyperfine shifting. The residues which could be identified were K2–Y4, N14–W37 and E51–E54. In the reduced form, as the paramagnetism is reduced, more spin systems could be identified, K2–T5, I12–V38 and G45–E54. By combining these assignments with T_1 and/or pseudocontact shift constraints, these data should enable a solution structure of *Cp* Rd(Fe) eventually to be determined.

The first structure of an Rd determined by NMR used metal replacement to overcome the problems of paramagnetic line broadening. The native Fe was replaced by Zn in *Pyrococcus furiosus* (*Pf*) Rd and standard NMR methods were used to assign the 200 ms NOESY spectrum,[63] giving 403 distance constraints.[64] The metal centre was modelled by introducing Zn—S distance and Cβ—S—Zn angle constraints to keep sp^3 hybridization of the sulfurs. Slowly exchanging NHs were introduced as additional H-bond constraints. Distance geometry/simulated annealing (DG/SA) calculations gave a family of 40 structures (30 from molecular replacement and 10 from random starting structures) with a backbone RMSD of 0.42 (Fig. 5). The structures were found to be similar to the x-ray structure of *Cp* Rd(Fe).[65,66]

The only other NMR structure of an [Fe-4S]-type protein is that of *Dg* Dx. The active site of Dx was reconstituted with Zn, and its solution structure was determined using 2D ^{1}H NMR methods.[59] DG calculations using 687 constraints gave a family of 16 structures with a low target function violation for the Dx dimer and backbone RMSD of 0.59 Å. The metal centre was introduced using distances from the x-ray structure. Secondary structural elements identical to those seen in the x-ray structure were observed. The amide protons

Fig. 6. A stereoplot of the superimposed family of 16 low-target-function *Dg* DxWt(Cd) dimer structures derived from NMR data. The protein backbone is displayed along with the cysteine side-chains. The Cd atoms are shown as space filling.[67]

for G4, D5, G13, L11 and Q14 NHε, H-bonded in the x-ray structure,[10] were not seen by NMR as slowly exchanging, while structural disorder at the N-terminus, for the backbone at E10 and for the section G22–*T*25, was observed. Comparison between the Fe (x-ray) and Zn (NMR) forms of Dx suggests that metal substitution does not have an effect on the structure of the protein. A study of the ^{113}Cd derivative of Dx also produced a family of structures (Fig. 6) with a global fold very similar to the Zn and Fe forms of the protein.[67]

The geometry at the metal centre in [Fe-4S]-type proteins cannot normally be determined accurately owing to the lack of constraints in the vicinity. The nearest protons to the metal are the β-CH_2 of the binding cysteines and normally the centre is near the surface of the protein (for functional reasons). However, by replacing the metal with an 'NMR active' nucleus, information about the centre geometry can be obtained. This approach was used in *Pf* Rd substituted with ^{113}Cd and ^{199}Hg where small ^{1}H–M couplings were identified.[68,69] A heteronuclear spin-echo difference (HSED) experiment was used with ^{1}H–^{1}H *J* coupling removed and antiphase magnetization purged at the start of the data acquisition. Interestingly, apart from the expected ^3J Hβ–Cβ–S–^{113}Cd couplings, a number of H-bond-mediated couplings were seen (Fig. 7) as well as a novel through-space coupling between A43(CH_3) and the metal. These non-^3J couplings ranged from 0.3 to 1.8 Hz. Similar results were obtained for the ^{199}Hg derivative of *Pf* Rd, although the couplings were larger (0.4 to 4 Hz) owing to the smaller magnetogyric ratio of Hg. The results indicated that NH—S H-bonds at the metal centre have covalent character and that the through-space coupling involves orbital overlap between a proton and an Sγ atom. A more extensive study of the same protein indicated, by

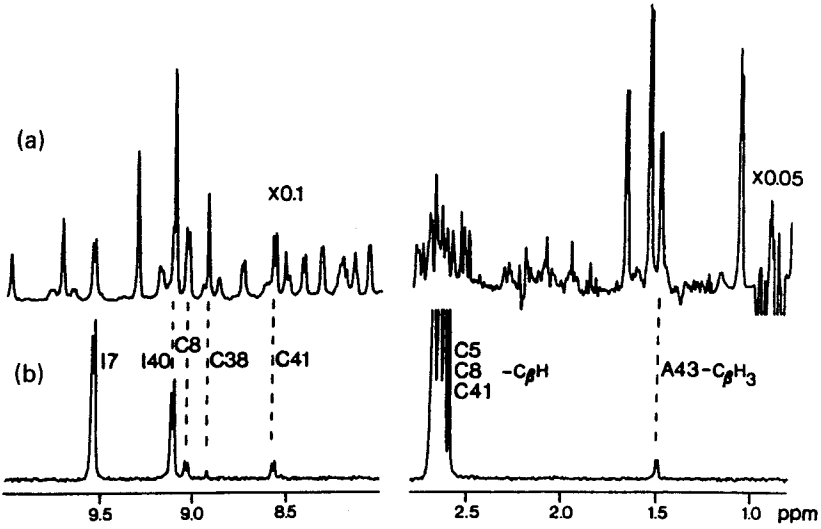

Fig. 7. Selected regions of the ^{1}H NMR spectrum (600 MHz) of ^{113}Cd-substituted Rd, acquired with the HSED sequence. (a) spectrum obtained using the first four steps of the phase cycle, i.e. without affecting the ^{113}Cd spin state. The spectrum results from 1200 transients. (b) spectrum obtained using the full 8-step phase cycle with identical parameters to (a) except the number of transients (120 000 total, 60 000 with $\phi_2 = +x$ and 60 000 with $\phi_2 = -x$). The total measuring time was 36 h. The downfield and upfield regions of the ^{1}H spectrum shown in (a) are displayed at five- and 2.5-fold higher magnification compared to (b), and 0.1- and 0.05-fold after correcting for the number of transients. The sample concentration was 3 mmol l^{-1} in 90% H_2O, pH 6.3 and temperature 45°C. (Reprinted from P. R. Blake *et al.*, *J. Biomol. NMR*, **2**, 1992, p. 529, with kind permission of Kluwer Academic Publishers.)

comparing 2D NOESY spectra, that no extensive structural perturbations occurred for the ^{113}Cd and ^{199}Hg substituted proteins.[70] By using ^{113}Cd–^{1}H and ^{199}Hg–^{1}H HMQC experiments, it was also possible to identify those protons ^{3}J scalar coupled to the metal and obtain coupling constants that ranged from 0.5 to 38 Hz.

A HSED experiment was also used to probe the ^{113}Cd derivative of *Dg* Dx. Metal–proton ^{3}J couplings were observed for cysteine β-CH_2 protons and for those NHs involved in NH—S H-bonds (Fig. 8). Additionally a through-space coupling was identified between an L26 CH_3 group and the ^{113}Cd. Interestingly, this coupling was found to be across the Dx dimer interface[67] and involved the Sγ atom of C28.

In another study, the ^{113}Cd form of *Dg* Rd was also used to probe the metal centre geometry.[71,72] A combination of 1D HMQC-TOCSY and 2D COSY experiments identified the β-CH_2 protons of the binding cysteines and their coupling constants with the ^{113}Cd were measured. A comparison with the

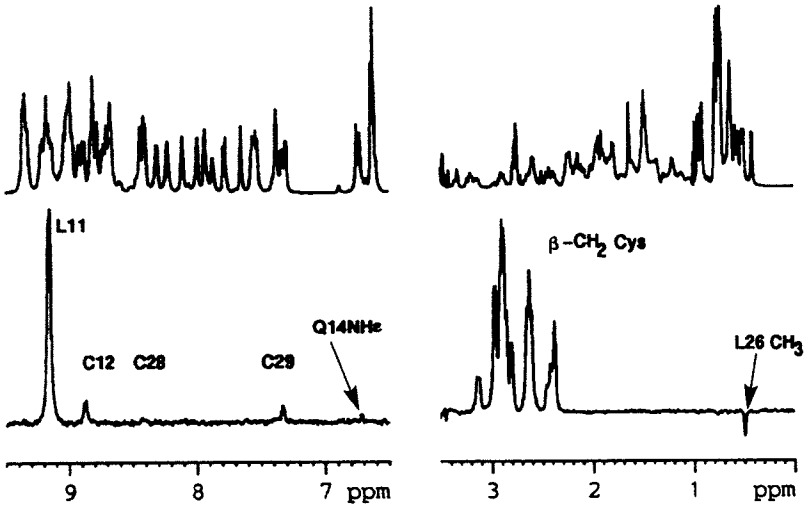

Fig. 8. Selected regions of the ^{1}H NMR spectrum (600 MHz) of an 8 mmol l^{-1} sample of Dx(^{113}Cd), at 303 K and pH 7.2 in 90% H_2O, acquired using the HSED experiment. 60 000 transients were acquired. The assignments of the observable peaks are indicated.[67]

x-ray structure allowed a Karplus-type relationship to be traced out for Hβ–Cβ–S–^{113}Cd angles versus J.

Instead of using a diamagnetic metal or an 'NMR active' derivative it is also possible to substitute native Fe by other paramagnetic metals that have better ^{1}H NMR characteristics. This is the case for *Dg* Rd substituted with Ni^{2+} ($S = 1$) and Co^{2+} ($S = 3/2$ high-spin, $S = 1/2$ low-spin). For the Ni derivative, 8 hyperfine shifted signals between 300 and 100 ppm for *Dg* Rd (Fig. 9) were observed and the resonances were assigned to the 8 β-CH_2 cysteine protons.[73] The Co derivative of *Dg* Rd also showed sets of hyperfine shifted signals between 300 and 100 ppm. These cysteine β-CH_2 proton signals, for the Ni and Co forms of Rd, are much sharper than those seen in the Fe form owing to the reduced paramagnetism and favourable electron relaxation properties.

Mutants of a number of Rds have been studied to probe specific interactions in this protein. Wild-type *Cp* Rd(Zn) and a mutant that mimics the N-terminal sequence of the hyperthermophillic *Pf* Rd were studied by NMR and the 2D NOESY spectra were assigned.[74] The global structure of the mutant was found to be similar to the wild-type (WT) protein based on a comparison of cross-peak intensities in the NOESY spectra. Extra H-bonds in the mutant, at the N-terminus, were observed between residues in a similar position to those seen for the hyperthermophillic *Pf* Rd. However, the *Cp* Rd mutant is not

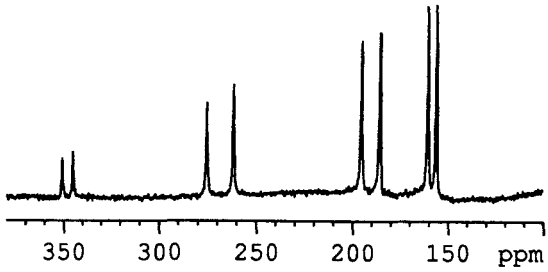

Fig. 9. 400 MHz ^{1}H NMR spectrum of the hyperfine shifted β-CH_2 protons for the binding cysteines in *Dg* Rd(Ni). The spectrum was recorded at 308 K in D_2O. The variation in peak intensity is due to the large spectral window used (900 ppm) and the uneven excitation of the resonances.[73]

thermostable, leading to the conclusion that these specific H-bonds of the N-terminus in *Pf* Rd do not contribute to the stability of the protein.

Cp Rd was also the object of a study that mutated residues near the metal binding site.[75] The conserved glycines at positions 10 and 43 were mutated to alanine and valine to give four single and two double mutants. The ^{113}Cd derivatives of the WT and three of the mutants (G10V, G43V, and G10V/G43V) were studied by NMR. The results indicated that the G10V mutant had perturbations in the environment of the mutation (residues 5–11) while the V44–C42 NH—S H-bond was found to be perturbed in the G43V mutant. The perturbations were additive as the G10V/G43V double mutant displayed both types of changes localized in each of the binding loops.

NMR has also been used to determine electron self-exchange rates in *Cp* Rd.[76,77] The electron self-exchange rate constant was determined by monitoring the perturbation introduced by increasing concentrations of the Rd oxidized form on the T_1 and T_2 relaxation times of hyperfine-shifted ^{1}H NMR signals (200, 11.8, 10.4, 10.2, −2.4, −3.6, and −4.2 ppm) of the Rd reduced form.[76] Similar measurements using signals at 11.8, 10.4, 10.2, and −1.1 ppm, carried out on a mutant, V8Q to probe the electron transfer site, gave a significantly smaller value. This was ascribed to the negatively charged Q8 near the exposed C9 and C42 residues.

6.2. 2Fe ferredoxins

Pseudomonas putida (*Pp*) putidaredoxin (Pdx) is a [2Fe-2S] Fd containing 106 amino acid residues. The sequential assignment of the diamagnetic regions of the 2D NMR spectra of the oxidized form has been carried out.[78,79] The solution structure of the oxidized form of *Pp* Pdx was determined by 2D NMR methods.[80] Of the 106 residues present in the protein, the spin systems for residues 36–48 and 84–86 could not be identified owing to paramagnetic

broadening. Some of the protons of spin systems 24, 25, 49, 70, 71 and 87 were also unidentified. The position of the metal cluster in the protein was determined using information from similar proteins and from mutagenesis studies, leading to the ligating cysteines being identified as C39, C45, C48 and C86. The cluster was constrained, in the structure calculations, using distances found in the x-ray structure of *Anabaena* [2Fe-2S] Fd.[81] Backbone dihedral angles for the residues 38–48 and 84–87 were also constrained to the x-ray values. An upper distance limit of 8 Å from the cluster Fe atoms was used for the residues S22, M70, L71, V74 and Q105, which were broadened in the 2D NMR spectra. A total of 878 constraints plus 66 dihedral angle and 5 paramagnetic broadening constraints gave, after a SA protocol, a family of 10 structures with a backbone RMSD of 1.14 Å (Fig. 10). The protein was found to have a similar folding topology to other known [2Fe-2S] Fds.

A redox study of *Pp* Pdx showed that the reduced form of Pdx (Fe^{3+}–Fe^{2+}) has increased unpaired electron density at the metal cluster and shows increased line broadening for the resonances of protons near the cluster.[82] The pattern of broadening was studied to give information on placement of the cluster within the protein frame. Studies of the function of the protein have shown that the C-terminal W106 residue is implicated in binding interactions with cytochrome $P450_{cam}$. Spectral changes between the oxidized and reduced forms were found mostly to be concentrated at the C-terminus where changes in NOE patterns were seen for W106. The indole protons of this residue also experienced the largest chemical shift changes on reduction of the protein.

The dynamics of *Pp* Pdx was probed using ^{15}N-labelling of the protein and the determination of amide proton exchange rates.[83] The ^{15}N assignments, in both oxidation states, were made using NOESY-HMQC and TOCSY-HSQC experiments. Owing to the paramagnetism of the cluster, residues 36–48 and 84–87 in the vicinity could not be identified. Amide proton exchange rates were determined from the peak intensities of cross-peaks in 2D ^{1}H–^{15}N HSQC spectra after exchange into deuterated buffer. Nonselective ^{1}H T_1 values were also measured and it was found that the protons that exchange most slowly in Pdx correlate with the regions of the protein with regular secondary structure. A comparison of the results for the oxidized and reduced forms of Pdx indicated that proton exchange is slowed significantly in reduced Pdx compared to oxidized Pdx. This effect was particularly noticeable near the cluster and for residues involved in the C-terminal cluster.

In order to probe the paramagnetic domain of *Pp* Pdx, ^{15}N-labelling was performed and a number of 1D and 2D ^{1}H and ^{15}N experiments were utilized.[84] Standard 2D NMR experiments were carried out to characterize the protein and comparisons were made with previous studies.[79,83] In total, 16 broadened ^{15}N resonances, which are close to the [2Fe-2S] centre, were detected along with a number of ^{15}N resonances that had not previously been detected. ^{15}N T_1 relaxation times and NOEs were measured and distances between ^{15}N nuclei and the Fe atoms were calculated. To obtain these distances the weighted

average spin quantum number for the populations of the various spin states and the correlation time τ_c, must be known. These values were estimated and reduced distances

$$d_r = \sqrt[6]{\frac{d_1^6 d_2^6}{d_1^6 + d_2^6}}$$

were obtained (between 4 and 7 Å, where contact relaxation can be ignored). A comparison between these calculated reduced distances, reduced distances obtained using[85]

$$\frac{1}{T_1} \times 10^2 = \frac{a}{d_r^6} \times 10^4 + b$$

and distances from an NMR structure of Pdx[80] showed that the values were comparable to although smaller (0.3–0.6 Å) than those obtained in the study of Chae[85] (which included information from published x-ray structures of related proteins). These results suggest that ^{15}N studies may be used to provide M–H constraints for NMR structure calculations.

The metal gallium, has been used as a replacement in the [2Fe-2S] cluster of *Pp* Pdx in order to circumvent paramagnetic line broadening.[86] A combination of standard 2D homonuclear NMR experiments and heteronuclear 3D experiments allowed sequential assignment of the spin systems. This process was helped by the availability of the resonance assignments of native oxidized Pdx.[79,83] A qualitative study of the 2D and 3D NOE data suggested that secondary structural elements found in native Pdx are also present in the Ga-substituted protein. A larger number of NOE constraints for Ga Pdx allowed a more precise determination of the relative position of the structural elements in the protein, indicating that one of the helices (helix G) appears to be tilted relative to its position in the native protein.[80] The use of ^{15}N NOE and ^{15}N T_1 measurements indicated that the overall protein mobility is higher for GaPdx than for the native Pdx and that the C-terminal W106, implicated in binding interactions with cytochrome P450, is mobile.

A ^{15}N and ^{2}H NMR study of uniformly ^{15}N and selectively ^{2}H labelled *Anabaena* 7120 [2Fe-2S] Fd detected and assigned many of the hyperfine shifted signals.[85] By using ^{15}N-labelled serine, glycine, cysteine and leucine it was possible to investigate 12 of the 17 amino acids within 8.5 Å from the cluster. ^{15}N T_1 relaxation measurements were also used, in conjunction with distances from the x-ray structure[87] to attempt some assignments. A plot of $1/T_1$ versus $1/d_r^6$ showed that the labelled serines and leucines fall on a straight line while the cysteines and glycines lie off this line. The differences were ascribed to a possible breakdown of the dipolar approximation used to fit the T_1 data (the cysteines and glycines are less than 4.2 Å from the iron atoms and may have contact contributions to relaxation).

Fig. 10. A stereoplot of the superimposed family of 10 low-target-function *Pp* Pdx structures derived from NMR data (Brookhaven access code: 1put). The Fe atoms are shown as space filling and the cysteine side-chains are displayed. The disorder in the vicinity of the cluster (Fe atoms are space filling) can clearly be seen.[80]

Using the same method, site-specific labelling and uniform ^{15}N-labelling of the same [2Fe-2S] *Anabaena* 7120 Fd,[88] previous assignments[89] for the binding cysteinyl protons were confirmed. The ^{1}H NMR spectra of ^{2}HαCys and ^{2}HβCys labelled protein identified the β-CH_2 protons as a group of four resonances between 150 and 90 ppm and a further four resonances between 25 and 15 ppm. The Hα protons were identified as signals at ~44, 17, 5 and 3 ppm (Fig. 11). It was also possible to identify the ^{13}C and ^{15}N resonances of the four cysteine Cβ and N backbone atoms for both the reduced and oxidized forms of the protein. A study of the temperature dependence of the cysteinyl ^{1}H, ^{13}C and ^{15}N resonances showed that $\Delta\delta/\Delta T^{-1}$ was different for different atom types within a given residue.

The [2Fe-2S] Fd from *Anabaena* 7120 had its four ligating cysteine residues mutated individually to serine in order to probe whether serine could replace cysteine in [2Fe-2S] Fds.[90] The four oxidized mutants showed ^{1}H NMR spectra with hyperfine shifted signals between 20 and 30 ppm with anti-Curie temperature dependences. Each of the mutants gave spectra different from each other and different from the wild-type protein. Only two of the reduced forms of the mutants were stable; the C46S mutant showed hyperfine shifted signals similar to the WT while C49S did not. Assignment of the C46S hyperfine shifted signals was carried out on the basis of the temperature dependences and results from a β-$C^{2}H_2$ labelled sample. The results suggested that serine substitution as a cluster ligand is possible, although cluster ligation by cysteine is more stable.

Metal replacement studies have been carried out for the [2Fe-2S] Fd from

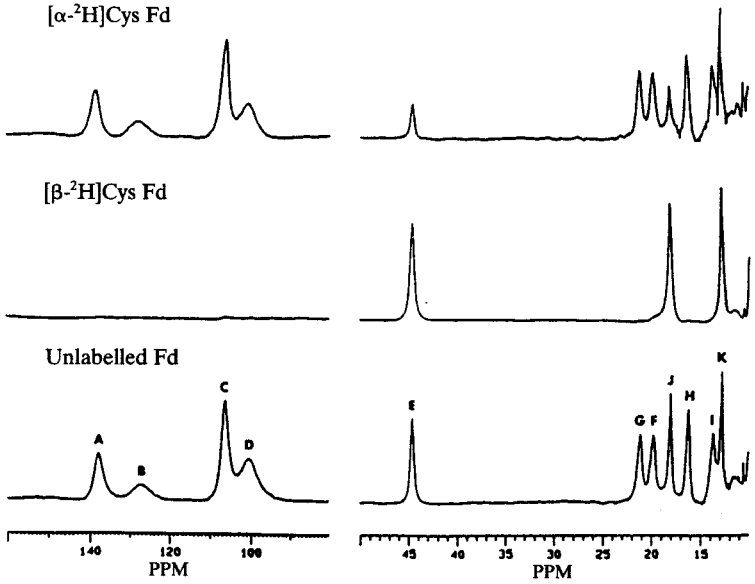

Fig. 11. ^{1}H NMR spectrum (500 MHz), of reduced, recombinant *Anabaena* 7120 vegetative Fd: (top) labelled with [$^{2}H^{\alpha}$]Cys, (middle) labelled with [$^{2}H^{\beta 2,\beta 3}$]Cys, and (bottom) at natural abundance. Samples contained 3–5 mmol l^{-1} protein in 100 mmol l^{-1} sodium pyrophosphate buffer and 100 mmol l^{-1} NaCl; the pH was 8.5; the solvent was 90% $^{2}H_2O$/10% $^{1}H_2O$. The spectra were recorded at 283 K. A total of 20 000 transients were collected as 8 K data points over 333.44 ppm. (Reprinted from H. Cheng *et al.*, *Arch. Biochem. Biophys.*, 1995, **316**, 619, by permission of the publisher Academic Press Ltd, London.)

Anabaena 7120 where Ga(III) was used to replace the Fe atoms in the cluster.[91] The apo-protein was reconstituted with Ga(III) and sulfide ion under argon. Comparison of the 2D NMR spectra of the native Fd indicated that those protons, unaffected by the paramagnetism of the cluster, appeared at the same chemical shifts in the Ga-containing protein. New spin systems could be identified that were sequentially assigned and found to be due to those protons near the cluster, now detectable as a result of the presence of the diamagnetic Ga. A qualitative study of the NOE patterns in the Ga protein indicated that the structure is similar to the native Fe-containing form.

In a NMR study of the [2Fe-2S] Fd from *Synechocystis* sp. PCC 6803, the protein was uniformly labelled with ^{15}N and sequential assignment of resonances from protons further than 8 Å from the cluster was performed using 2D HMQC and HSQC ^{1}H–^{15}N experiments.[92] Unassigned spin systems included 23–25, 35–49, 61–66 and 74–79 (the cysteines that bind the cluster are 39, 44, 47 and 77). Structures were calculated using NOE constraints and allowed the identification of secondary structural elements. The cluster was included in the calculations using distance constraints obtained from the x-ray

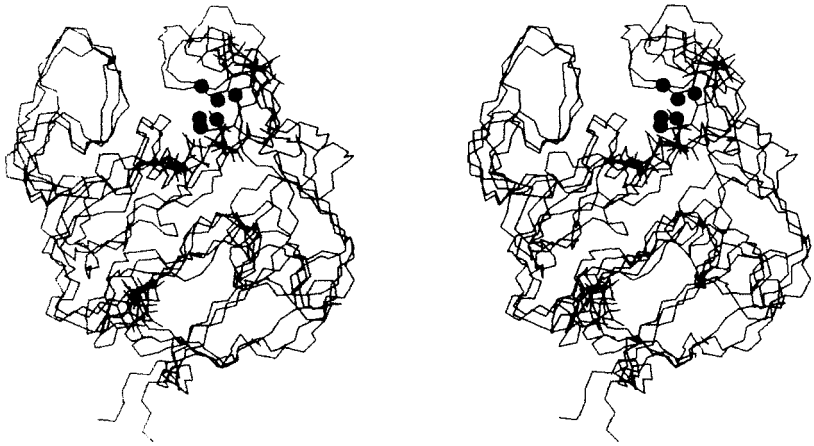

Fig. 12. A stereoplot of the backbone atoms of the superimposed family of three NMR structures of *Synechocystis* 2Fe Fd (Brookhaven access code: 1doy). The Fe atoms of the cluster are displayed as space filling.[92]

structure.[93] Paramagnetic constraints were also used: those protons not seen, or exhibiting broadened lines, were constrained to distances that ranged between 3 and 11 Å from the cluster and those Hα protons not seen as broadened in the NMR spectra were constrained to be 9–30 Å from the cluster. A total of 831 constraints was used in the structure calculations. A qualitative study of the NOE patterns indicated a disulfide bridge, between C85 and C18. In order to test this hypothesis, two sets of NMR families were calculated using a SA protocol, with and without a S—S bridge. It was found that both families exhibited similar tertiary folds (RMSD 2.2 Å), suggesting that the disulfide bridge may be present in solution. The region near the cluster was poorly defined (owing to a lack of NOEs) but the sections of secondary structure with much higher NOE densities were well defined (Fig. 12).

The solution structure of a [2Fe-2S] Fd from *Synechococcus elongatus* (Se) was determined using standard 2D NMR experiments and assignments were obtained for 79 out of 97 amino acids.[94] The sections containing the binding cysteines were unobserved (38–49, 76–79, 62 and 64). The number of constraints used in the calculations was 1784, including H-bond and dihedral angle constraints. The cluster was included in a similar manner to that in the study by LeLong *et al.*,[92] although no paramagnetic constraints were used. A family of 20 structures was obtained with backbone RMSD of 0.87 Å after RMD calculations. The problem of definition of the protein near the cluster, where no NOEs were obtained, is clearly illustrated in Fig. 13. The global fold of the solution structure was found to be similar to the x-ray structures of homologous Fds; *Anabaena* Fd;[81] *E. arvense* Fd[95] and *Synechocystis* Fd.[93]

In the following year, 2D ^{1}H NMR was used to determine a 3D structure of

Fig. 13. A stereoplot of the superimposed family of 10 NMR structures of *Se* 2Fe Fd (Brookhaven access code: 1roe). The backbone atoms are displayed along with the cysteine side-chains and the Fe atoms (space filling). The lack of NOEs in the vicinity of the cluster result in the observed increase in disorder in the region.[94]

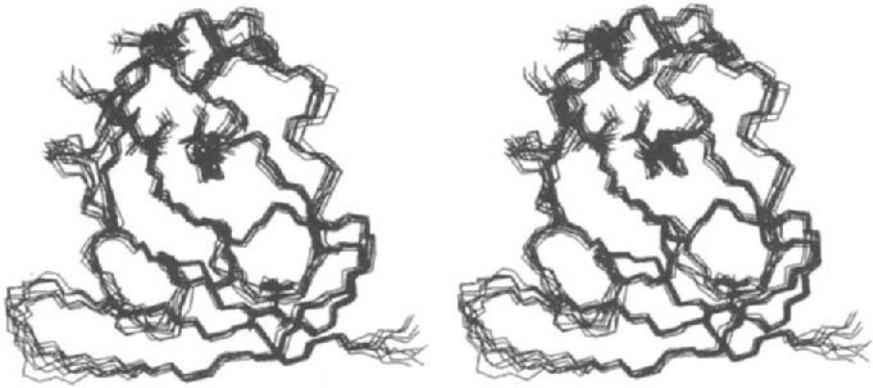

Fig. 14. A stereoplot of the superimposed family of 10 NMR structures of *Se* 2Fe Fd (Brookhaven access code: 2cjo). The use of a large number of distance constraints from the x-ray structure allowed much improved definition in the region of the 2Fe cluster (cf. Fig. 13).[96]

the same protein (Se Fd).[96] Standard methods were used to assign NOESY spectra, resulting in 946 distance constraints being obtained. Owing to the disappearance, as a result of the paramagnetism, of 21 spin systems near the [2Fe-2S] cluster (L26, P37–A49, Q62–F64, and L76–V79), 241 distance constraints (between 1.8 and 5 Å), derived from the crystal structure of *Spirulina platensis* Fd,[97] were also used. The RMSD of the 10 low-energy structures (Fig. 14), derived from SA calculations, was 0.61 Å for the backbone atoms. During

the calculations, the Fe atoms of the [2Fe-2S] cluster were replaced by H atoms. The RMSD of selected regions of the protein, without using the x-ray constraints, was 0.81 Å. The RMSD of the complete backbone, without x-ray constraints, was not given. The global folding of *Se* Fd was similar to the crystal structures of other mesophile Fds. Differences between solution and solid state included an extension of the hydrophobic core, a unique hydrophobic patch on the surface of the large β-sheet, and two unique charged networks that were postulated as possible contributors to the thermostability of this protein. A comparison between the calculated NMR family and the results from Baumann *et al.*[94] was also carried out. The RMSD between the two families was 4.3 Å, and a number of major differences were found. These differences were suggested to arise from the NOESY assignment procedure. The use of x-ray restraints was suggested as being very helpful in the assignment of degenerate NOESY peaks outside the cluster region, as most of the differences between the two studies were located near the cluster.

6.3. 3Fe ferredoxins

A ^{1}H NMR study of *Dg* [3Fe-4S] FdII analysed the temperature dependences of the hyperfine shifted signals and recorded 1D NOE difference spectra.[98] For the four sets of resonances, between 30 and 12 ppm, assumed to be from the β-CH_2 protons of the ligating cysteines, two showed Curie and two anti-Curie temperature dependences (Fig. 15c). A theoretical model of the coupling between the Fe atoms of the cluster explained the differences between the temperature dependences and obtained values for the *J* coupling constants. A 1D NOE between two of the hyperfine shifted signals indicated that they belonged to the same β-CH_2 proton pair (with Curie temperature dependence) and by using dihedral angles from the x-ray structure of *Dg* FdII[99] an assignment to C50 was made. A more detailed NMR study of this protein identified geminal pairs of hyperfine shifted signals using a combination of M-COSY, NOESY and 1D NOE experiments.[100] Figure 15a,b shows the 1D ^{1}H NMR spectra of *Dg* FdII, which is typical of a 3Fe-containing protein, along with a 1D NOE difference spectrum. The complete sequence-specific assignment of the hyperfine shifted resonances was carried out by identifying a NOE between C14 and the single aromatic residue F22. These residues are found in close proximity in the x-ray structure.[99] It was also concluded that C11 is not bound to the cluster in FdII.

The [3Fe-4S] form of Fd from *Pf* was studied by NMR via a combination of 1D and 2D NOE and COSY experiments that allowed the assignment of the three aromatic residues, a conserved valine and the β-CH_2 and Hα protons of the three cysteines bound to the cluster.[101] Specific NOEs were detected that indicated that the overall folding was similar to that seen for the x-ray structure of *Dg* Fd. Sequence-specific assignment of C14 was achieved by observing

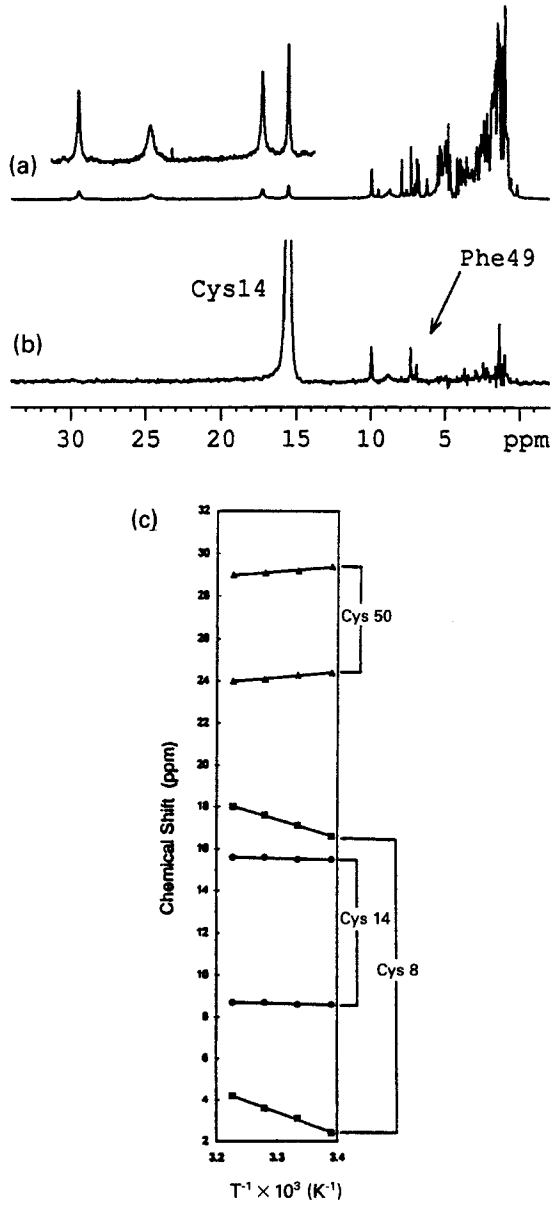

Fig. 15. 600 MHz ^{1}H NMR spectra of (a) *Dg* FdII acquired using the super-WEFT sequence; (b) 1D NOE difference spectra after irradiation of a β-CH_2 proton of Cys14; and (c) the temperature dependence of the three pairs of β-CH_2 signals of the cysteinyl cluster ligands, in the oxidized state.[98,100]

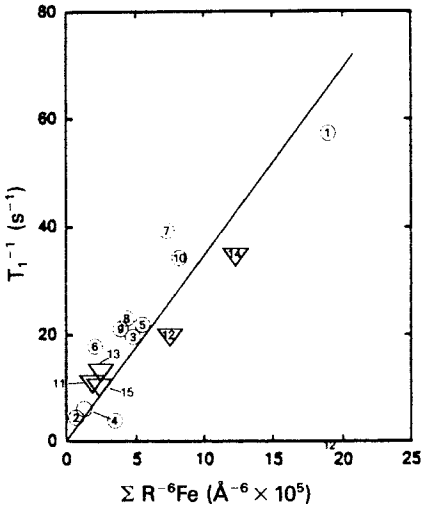

Fig. 16. Plot of the estimated relaxation rate (T_1^{-1}) for resolved/partially resolved and paramagnetically relaxed protons of *Pf* 3Fe Fd in ^1H_2O as a function of the sum of the inverse sixth power of the distance to each of the three iron (ΣR_i^{-6}) for the homologous protons in the crystal structure of *Dg* 3Fe Fd_{ox}. The numbered points are as follows: 1, $Ala^{18}NH$; 2, $Leu^{20}NH$; 3, $Phe^{25}C\beta 2H$; 4, $Leu^{32}NH$; 5, $Ala^{33}C\alpha H$; 6, $Val^{58}C\alpha H$; 7, $Leu^{61}NH$; 8, $Cys^{11}NH$; 9, $Cys^{56}NH$; 10, $Cys^{17}C\alpha H$; 11, $Cys^{11}C\beta H$; 12, $Cys^{11}C\beta' H$; 13, $Cys^{56}C\beta H$; 14, $Cys^{56}C\beta' H$; 15, $Cys^{17}C\beta H$. The horizontal scale for peaks 1–10 is that shown; both scales for peaks 11–15 (the hyperfine shifted peaks) are reduced by ×10 compared to those for peaks 1–10. (Reprinted with permission from C. M. Gorst *et al.*, *Biochemistry*, 1995, **34**, 600. Copyright 1995 American Chemical Society.)

NOEs to the conserved F22 residue. Analysis of the temperature dependence of the hyperfine shifted resonances indicates asymmetry in the coupling between the Fe atoms, as was found for *Dg* FdII.[98] Secondary structural elements in *Pf* [3Fe-4S] Fd were subsequently identified using 2D NMR methods.[102] 2D COSY, TOCSY and NOESY spectra were recorded and the spin systems were assigned using standard procedures. Protons for 65 of the 66 spin systems were identified, but not all were assigned. Proximity to the cluster could account qualitatively for the loss of some signals. The 2D NOESY spectrum was qualitatively analysed and elements of secondary structure were identified. A comparison with the x-ray structure of *Dg* Fd showed that although most structural elements were present in both proteins, *Pf* Fd exhibited some extended structures.

In an attempt to characterize the tertiary structure of *Pf* [3Fe-4S] Fd and to sequence-specifically assign the hyperfine shifted cysteine resonances, a number of experiments tailored to detect fast relaxing signals were carried out.[103] By determining relaxation rates of hyperfine shifted signals in *Pf* [3Fe-4S] Fd and by using x-ray structures of analogous [3Fe-4S] proteins it was shown that

a correlation exists between the distance from the Fe atoms in the cluster and the relaxation rate of hyperfine shifted signals (Fig. 16).

A redox study of the *Dg* FdII identified a stable intermediate state ($FdII_{int}$) with characteristic hyperfine shifted signals at 24, 21.5, 21 and 14 ppm.[104] The oxidized and reduced states exhibit signals at 29, 24, 18 and 15.5, and 18.5 and −11 ppm, respectively. Three electrons were required to reduce fully the protein and, as only one electron is needed to reduce the $[3Fe\text{-}4S]^{1+}$ cluster to $[3Fe\text{-}4S]^{0}$, it was proved that the two remaining electrons were used to reduce a disulfide bridge present between C18 and C42. The intermediate state was therefore postulated to be the protein with the cluster oxidized and the S—S bridge broken. The change in the hyperfine shifted signals during the redox cycle between $FdII_{ox}$ and $FdII_{int}$ was assumed to result from a small change in the cluster environment on breakage of the disulfide bridge.

6.4. 4Fe proteins

6.4.1. Ferredoxins

The characteristic hyperfine shifts of a [4Fe-4S] containing Fd were identified in a study of *Dg* FdI.[100] Figure 17 shows the ^1H NMR spectrum of *Dg* FdI, where four pairs of β-CH_2 protons were identified in both oxidation states of the protein, indicating that C11 is the fourth cluster ligand.

The assignment of the β-CH_2 and Hα protons of the four binding cysteines of a [4Fe-4S] containing Fd from *Thermococcus litoralis* (*Tl*) was carried out using 1D and 2D NMR experiments in combination with the interpretation of relaxation data for the oxidized and reduced forms.[105] Correlation of hyperfine shifted signals in the reduced and oxidized states was achieved using 2D EXSY experiments. Anti-Curie temperature dependence was seen for two of the binding cysteines and Curie dependence for the other two, which was indicative of the presence of a mixed-valence pair of $Fe^{2.5+}$ atoms ($S = 9/2$) and a ferrous Fe^{2+} pair ($S = 4$). In a further study, the identification of 58 of the 59 spin systems was achieved using TOCSY and NOESY spectra tailored to detect fast and slowly relaxing resonances.[106] Steady-state 1D NOE experiments utilizing the super-WEFT sequence were also used. Secondary structural elements were detected and the NOE patterns observed suggested that the overall fold of the protein in solution is similar to that for the x-ray structure of [3Fe-4S] *Dg* Fd II.[99] A plot of T_1^{-1} versus the sum of the distances (obtained from crystal structures, and using $1/T_1 = D\sum_q R_{Fe}^{-6}$,[22,103]) from the proton under study to the Fe atoms in the cluster, showed a linear relationship for those protons affected by the paramagnetism of the Fe atoms, indicating that the relaxation properties of these protons correlate with distance from the Fe atoms.

A molecular model has been proposed for *Tl* Fd using NOESY data.[107] Approximately 295 NOE distance constraints were used, from a 300 ms

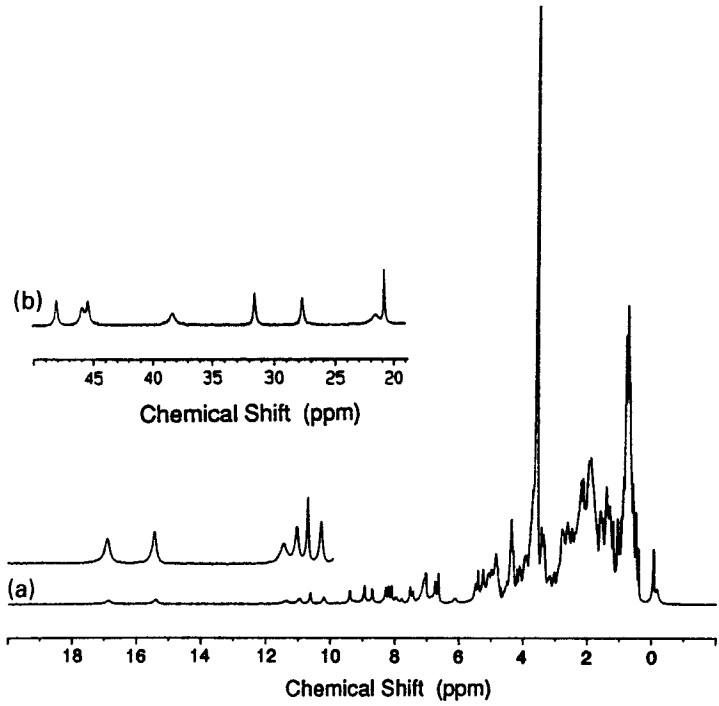

Fig. 17. 500 MHz ^{1}H NMR spectrum of oxidized *Dg* FdI (a) and the low-field region of reduced *Dg* FdI (b).[100]

NOESY spectrum, and 30 used from steady-state 1D NOE experiments where distances were extracted by considering T_1 relaxation times and NOE intensities. Recalibration, due to enhanced relaxation, was carried out for 17 protons less than 6 Å from an Fe atom in initial structures. Paramagnetic constraints of less than 4.5 Å from the Fe atoms were introduced for those protons with T_1 values of less than 10 ms. Those backbone protons not detected were restricted to less than 4 Å from the Fe atoms. This gave an extra 32 constraints in total. Dihedral constraints for the β-CH_2 cysteine protons were also used, as was a S—S disulfide bridge between C20 and C43. DG and SA was used to calculate a final family of 10 structures (Fig. 18). A global backbone RMSD of less than 1 Å was observed. The global fold of the protein was similar to known cubane cluster Fds. The major difference between the *Tl* Fd NMR structure and other Fds is that a turn, present in the x-ray structures of *Dg* FdII,[99] *Bacillus thermoproteolyticus* (*Bt*) Fd[108] and *Desulfovibrio atrucanus* (*Da*) Fd,[109] is replaced by a short segment that forms a third antiparallel strand in a β-sheet at the N-terminus.

A ^{1}H NMR study of *Desulfovibrio africanus* (*Da*) Fd I showed the presence of His and Trp residues, which indicated that the original amino acid sequence

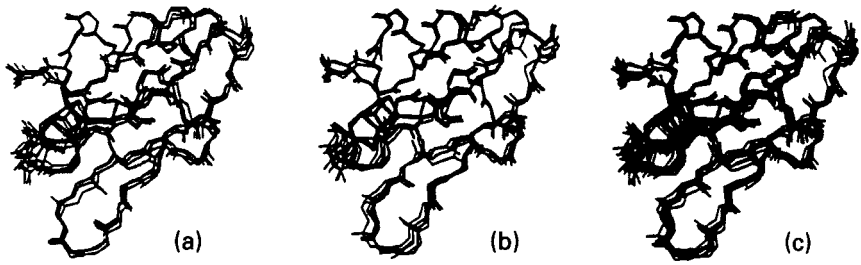

Fig. 18. Superposition of backbones for accepted structures of *Tl* 4Fe Fd from the DG restrained SA structure calculations. (a) Five structures obtained with Cys χ_2 as constraints; (b) five structures obtained without using Cys χ_2 as constraints; (c) superposition of the two sets of five structures for (a) and (b) above. (Reprinted with permission from P.-L. Wang *et al.*, *Biochemistry*, 1996, **35**, 11319. Copyright 1996 American Chemical Society.)

was in error. The secondary structure of the protein was investigated using 2D NOESY experiments in which sections of α-helix and β-sheet were identified.[110] The temperature dependence of the hyperfine shifted resonances was measured and indicated that contributions from pseudocontact interactions were negligible. The sequential assignment of the β-CH_2 cysteine protons was subsequently carried out (using a combination of 1D NOE and TOCSY experiments and comparison with known Fd structures) and the cluster geometry was probed by analysing the hyperfine shifts.[111] Using dihedral Hβ—Cβ—S—Fe angles from the x-ray structures of *Dg* Fd and *Bt* Fd, and the relaxation properties of the β-CH_2 proton pairs, a plot of the two β-CH_2 hyperfine shifts versus the ratio of their relaxation rates was obtained. The results for *Da* Fd indicated that the dihedral angles were similar to those of other Fds.

The solution structure of *Da* Fd was determined using standard 2D NMR and 1D NOEs difference experiments.[112] Of the 64 spin systems present in *Da* Fd, only 53 appeared in the NH—Hα region of the 2D spectra and sequence-specific assignments of 59 amino acids were obtained. The majority of the distance constraints (588) were determined using a 150 ms NOESY spectra. Shorter mixing time experiments were used to obtain further NOEs (180) giving a total of 768. Dihedral angle constraints (4) were also used. The cluster was incorporated using the method of Banci *et al.*[57] A family of structures was calculated using the DG program DIANA.[56] Further refinement was carried out using XPLOR to give a final family of 19 structures (Fig. 19). The global backbone RMSD was 0.61 Å. Comparison with the published x-ray structure[109] gave an RMSD of 1.18 Å (residues 4–62) with all structural elements observed in both structures. Deviations occurred for the sections 8–10 and 29–32. Poor definition in the NMR family was given as the reason for differences in the region 8–10, while it was suggested that the region 29–32, as it is well defined

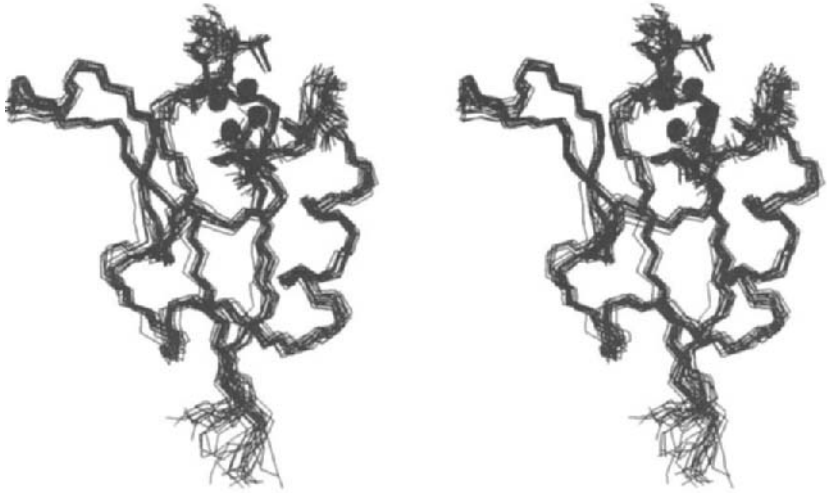

Fig. 19. A stereoplot of the backbone atoms of the superimposed family of 19 NMR structures of *Da* 4Fe Fd (Brookhaven access code: 1dfd). The Fe atoms are shown as space filling.[112]

in the NMR family, shows genuine differences between the solution and solid states.

Sequence-specific assignment of the cysteine binding ligands for *Desulfovibrio desulfuricans* (*Dd*) Norway Fd_{ox} I was obtained[113] using TOCSY and NOESY experiments in conjunction with x-ray structures (*Dg* Fd, *Bt* Fd) of related Fds. EXSY experiments were also utilized to assign hyperfine shifted signals in the reduced form of *Da* Fd. Two of these resonances show a Curie temperature dependence while the other two exhibit anti-Curie, indicating that C9 and C15 are ligated to the mixed-valence Fe ions.

The [4Fe-4S] form of native *Pf* Fd, which has an unusual coordination configuration of 3 cysteines and an aspartic acid binding the cluster, was studied, by NMR, in its reduced and oxidized forms.[114] ^{1}H NMR 1D experiments used the super-WEFT sequence to suppress slowly relaxing signals and T_1 values were estimated from the null point in IR experiments. 2D NOESY and TOCSY experiments were also used to identify the chemical shifts of some non-coordinated resonances. Four distinct redox states could be identified for the [4Fe-4S] form of the protein, Fd_A^{ox}, Fd_B^{ox}, Fd_A^{red} and Fd_B^{red}. The hyperfine shifted resonances for the two oxidized states of the Fd appeared between ~14 and 11 ppm (4 resonances) while those for the two reduced states appeared between ~50 and 20 ppm (6 resonances). The two distinct states for the oxidized and reduced forms were proposed to involve the presence or absence of a C21–C48 disulfide bridge as was observed in the case of [3Fe-4S] from *Dg* FdII.[104]

In order to identify the non-cysteinyl ligand binding the cluster in the four redox states of [4Fe-4S] *Pf* Fd, a combination of 1D and 2D experiments tailored to identify resonances with short relaxation times was used.[115] The use of standard 2D NOESY and TOCSY experiments initially identified several residues unaffected by the paramagnetism of the cluster. Scalar connectivities, in conjunction with quantitative analysis of 1D NOEs and relaxation times, allowed individual cysteines to be identified in both the reduced and oxidized forms. The fourth ligand was identified, using the size of the hyperfine shifts, the AMX spin topology and the conserved nature of the cluster environment in these types of proteins, as being D14 in Fd_{red}. In the oxidized form large contact shifts, anti-Curie temperature dependence and an AMX topology suggest that the same ligand, D14, binds the cluster.

A study of two mutants (D14C and D14S) of *Pf* Fd was carried out to attempt to identify the oxidation state of the individual Fe ligated by a particular protein ligand.[116] Comparison of 2D spectra in the 'diamagnetic region' indicated that the oxidized form of the two mutants and the oxidized wild-type protein have very similar cross-peak patterns and thus similar global folds. Using an assignment protocol similar to that used in Gorst *et al.*[114] and Calzoali *et al.*[115] (1D and 2D experiments optimized for fast relaxing protons), and in conjunction with EXSY experiments, the assignments for the cluster ligand resonances in the mutants was carried out for the four oxidation states. It was found that, by analysing the magnitude of the contact shifts, the relaxation properties and the temperature dependence of the protons of the cluster binding residues, the reduced cluster D14C protein has C11 and C17 ligated to a mixed-valence pair ($S = 9/2$) $2Fe^{2.5+}$ and C14 and C56 ligated to $2Fe^{2.0+}$. The D14S mutant has the sequence positions of the $2Fe^{2.5+}$ and $2Fe^{2.0+}$ ion pairs interchanged. The wild-type protein has D14 ligated to a $Fe^{2.5+}$ and C11 ligated to $Fe^{2.0+}$ in each state, while the other two ligands have oxidation states between $Fe^{2.5+}$ and $Fe^{2.0+}$. It was also found that the mixed-valence pair bound to C11 and C17 was significantly stabilized for the disulfide-bridged C21–C48 form of the protein, indicating the presence of a C17—C21 H-bond (also seen in x-ray structures of homologous proteins).

Following the assignment of the resonances (85% of the amino acid residues) using 1D and 2D NMR experiments, and the identification of secondary structural elements,[117] the solution structure of *Thermotoga maritima* (*Tm*) Fd was published in 1996.[118] 2D NOESY spectra gave a total of 637 distance constraints to which were added 13 H-bond constraints, a disulfide bond (C20—C43) and 35 $^3J_{NH-H\alpha}$ dihedral angle constraints. The cluster was incorporated in the model using distances and backbone dihedral angles taken from x-ray data (mainly *Da* Fd[109]). A family of 10 structures was calculated using a SA protocol giving a global backbone RMSD of 0.78 Å (Fig. 20). An unrestrained molecular dynamics (MD) calculation was run (200 ps) to test the stability of the secondary and tertiary structural elements. No loss of structure was seen over this time period, suggesting that these structural

Fig. 20. A stereoplot of the backbone atoms of 10 structures of *Tm* Fd with lowest internal energy and smallest experimental distance violations obtained from restrained MD calculations. (Brookhaven access code: 1rof.)[118]

elements are stable. Structural similarities between the protein fold and that of Fds from *Dg* and *Da* were observed. No definite conclusions as to the origin of the thermostability of *Tm* Fd could be drawn.

6.4.2. High-potential iron proteins

One of the first paramagnetic protein structures to be determined in solution by NMR was the reduced high-potential iron protein (HiPIP) I from *Ectothiorhodospira halophila* (*Eh*), a recombinant protein (of 8 kDa) similar to the WT but containing two extra amino acids at the N-terminal, A1, and S2.[57] Of the 73 residues, 60 were found not to be affected by hyperfine interactions and could be assigned by 'standard' NOESY, COSY, and TOCSY 2D and 3D experiments (using a ^{15}N-enriched sample).[119] The detection of connectivities involving fast relaxing protons, from eight other residues, was made using 1D NOE and 2D NOESY experiments (tailored for fast relaxing nuclei, Section 4). The x-ray structure of *Eh* HiPIP[120] was also used to assign three more residues, giving a final assignment tally of 71 of the 73 residues and 88% of the protein protons. A family of 15 structures was generated by DG calculations using 948 relevant interproton NOEs and 40 additional constraints involving protons in the vicinity of the cluster. The cluster was introduced by adding an artificial amino acid[57] to the residue library of the DIANA program. The backbone RMSD for the NMR family, calculated for residues 4–71, was 0.67 Å

Fig. 21. A stereoplot of the superimposed family of 15 low-target-function reduced *Eh* HiPIP I structures derived from NMR data. The Fe atoms are shown as space filling (Brookhaven access code: 1pih).[57]

(Fig. 21). Refinement of the structure was carried out using REM calculations giving a RMSD of 0.6 Å. RMD calculations were found to give a substantial improvement in the quality of the NMR family (RMSD of 0.51 Å).

The investigation of the ligand cysteine protons of oxidized *Eh* HiPIP I (Fig. 22) showed that the difference found in the 1D proton spectrum (the β-CH_2 protons of C66 were found in the diamagnetic envelope) was consistent with an equilibrium between two valence distributions (a ratio of 4:1) for the Fe atoms of the cluster.[121] Using the data obtained for other HiPIPs[19] it was possible to obtain an empirical relationship between the hyperfine shifts of the β-CH_2 cysteinyl ligands and the percentage of each electronic species.

The solution structure of the oxidized form of *Eh* HiPIP I was determined using standard COSY, TOCSY and NOESY experiments along with ^{1}H–^{15}N HMQC experiments to assign the ^{15}N resonances.[122] Almost all of the proton resonances were assigned (90%) and 1437 NOEs were detected. Of these, 10% were between fast relaxing signals and after DG calculations a family of 18 structures with a backbone RMSD of 0.65 Å was obtained. The cluster was introduced as for the reduced form. The structure was found to be similar to the reduced form of the protein. Interestingly, the oxidized form, although it has increased paramagnetism, was more amenable to NMR study owing to the shorter electronic relaxation times.

A refinement of the structure of the reduced form of *Eh* HiPIP I was carried out using isotope ^{13}C- and ^{15}N-labelling of the protein, in order to obtain further constraints in the vicinity of the paramagnetic metal cluster.[123] Heteronuclear 3D experiments were performed to detect ^{3}J coupling constants involving slow and fast relaxing protons, which were then used as new

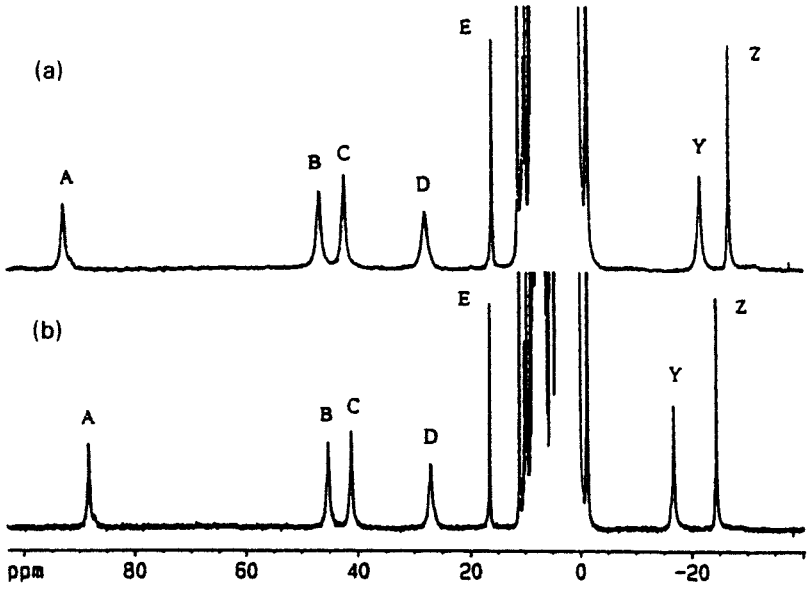

Fig. 22. 600 MHz ^{1}H NMR spectra of oxidized HiPIP I from *E. halophila* at 288 K (a) and 298 K (b). The spectra were recorded in H_2O solutions, 50 mmol l^{-1} phosphate buffer at pH 5.1. (Reprinted with permission from Bertini *et al.*, *Inorg. Chem.*, 1995, **34**, 2516. Copyright 1995 American Chemical Society.)

constraints allowing the assignment of 94% of the total proton resonances. Inversion-recovery HSQC (^{13}C and ^{15}N) experiments allowed the measurement of 200 nonselective T_1 values and T_1 values of protons with broad linewidths (no scalar couplings were detected), but only 70 were short enough ($T_1^{\text{eff}} < 100$ ms) to be introduced as proton–metal distance constraints. The procedure used was to subtract a diamagnetic T_1 value (assumed to be equal for all protons) from those T_1 values < 100 ms, giving an upper distance limit (which overestimates the diamagnetic contribution to T_1 relaxation). These distances were subsequently calibrated using initial structures generated from DG runs. As a solution structure had been obtained with a low RMSD,[57] the effect of the paramagnetic contributions to nuclear relaxation started to become important. The reduction in intensity of the NOESY cross-peaks and subsequent overestimation of the distances were compensated for using by a relaxation matrix analysis.[48,124] In a modified version of CORMA, an iterative procedure was used to correct the NOE intensities. Back-calculation of the NOE intensities was carried out using an NMR family of structures and then compensation for electron–nucleus interactions introduced to the diagonal elements of the matrix. The corrected NOE intensities were then used to obtain new distance constraints. The backbone RMSD for the newly refined structures and the original set was 0.87 Å. The regions closest to the cluster

showed the largest improvement as these regions were most affected by the paramagnetism. The new family of structures clearly showed that the aromatic ring of Y14 is rotated and the side-chain of V60 is positioned differently, with respect to the x-ray structure.[120] A similar methodology was also applied to reduced *Chromatium vinosum* HiPIP.[125] Using IR-TOCSY experiments it was possible to determine T_1 values for protons with resonances in the diamagnetic envelope.

A similar structural refinement was also carried out for oxidized *Eh* HiPIP using ^{1}H relaxation data.[126] An HSQC experiment preceded by a ^{1}H 180° pulse allowed the nonselective ^{1}H T_1 values to be obtained. The effective paramagnetic contributions to the nuclear relaxation rates, ρ_i^{para}, were obtained by subtracting the average diamagnetic contributions ($3.5\ s^{-1}$ for the amide protons and $1.3\ s^{-1}$ for all other protons) from the observed relaxation rates. A modified version of the equation for T_1 relaxation, given in Section 3.2, and an equation that describes the electron–nucleus dipolar interaction, modified for the presence of four metal ions and an equilibrium between two species (in a ratio of 80/20) were utilized to extract M—H distances

$$R_1^{(I)} = K_1 \mathbf{r}_{I1}^{-6} + (0.8K_2 + 0.2K_4)\, \mathbf{r}_{I2}^{-6} + K_3 \mathbf{r}_{I3}^{-6} + (0.2K_2 + 0.8K_4)\, \mathbf{r}_{I4}^{-6}$$

The constants K_J were calculated using the solution structure of *Eh* HiPIP I[122] as input along with the experimental ρ_i^{para} values. The metal-to-proton distances were back-calculated, and the solution structure was solved again using NOEs and ρ_i^{para} constraints, simultaneously. All protons with $T_1 < 150$ ms were used (with some exceptions), giving a total of 27 constraints. The definition of the families obtained with and without ρ_i^{para}-derived constraints is essentially the same, while the definition of the polymetallic centre is improved by the introduction of the new paramagnetic constraints (Fig. 23).

Eh HiPIP I was subject to mutation studies at the Y12 position in order to probe the role of this conserved aromatic residue.[127] Five mutants were prepared and chemical shift differences of the hyperfine shifted residues were compared. The mutants Y12F, Y12H and Y12W were destabilized compared to the wild-type protein. The structural differences between Y12F and WT were found to be the loss of two H-bonds of the Y12 OH group. A mutation at F48R and F48H was also found to destabilize the cluster, as shown by ^{1}H–^{15}N HMQC experiments, as a result of increased solvent access.[128] The conserved F66 was also mutated, with the conclusion that protection of the cluster from solvent was the main role of the residue.[129]

The NMR solution structure of *Chromatium vinosum* (*Cv*) HiPIP (85 amino acids) has been solved in both oxidized and reduced states. Using the assignments for the proton resonances of the reduced form of the protein[130] and results from 3D ^{1}H–^{1}H TOCSY/^{1}H–^{15}N HMQC and ^{1}H–^{1}H NOESY/^{1}H–^{15}N HMQC experiments, the assignment was extended to 85% of the protons and to 90% of the ^{15}N resonances.[131] Only two amino acids (L65 and S79) close

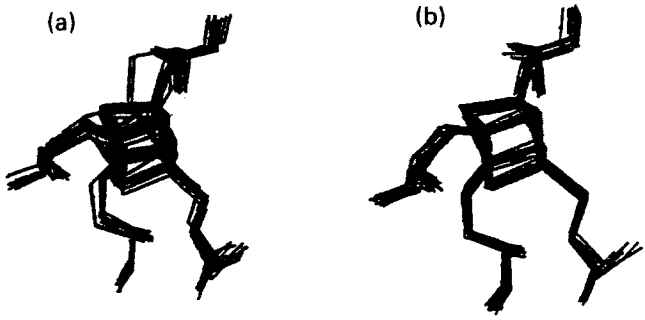

Fig. 23. Close-ups of the polymetallic centre in the DYANA families obtained without (a) and with (b) the use of p_1^{para} constraints. (Reprinted with permission from I. Bertini *et al.*, *Inorg. Chem.*, 1997, **36**, 4798. Copyright 1997 American Chemical Society.)

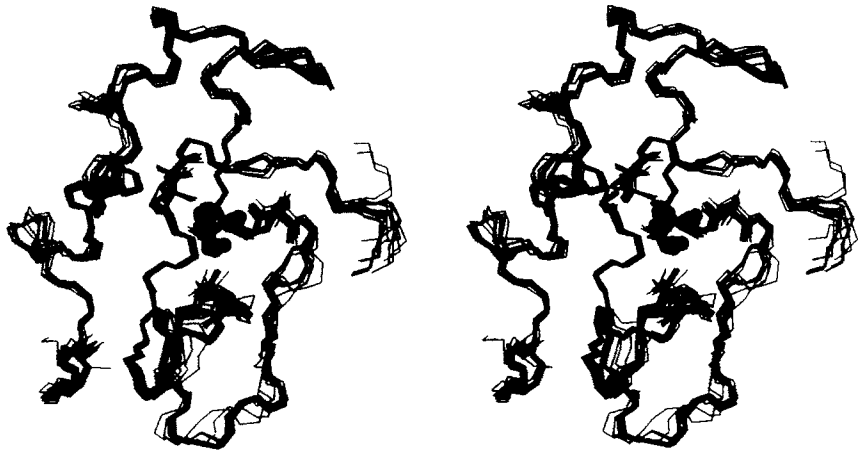

Fig. 24. A stereoplot of the superimposed family of 15 low-target-function reduced *Cv* HiPIP I structures derived from NMR data. The Fe atoms are shown as space filling (Brookhaven access code: 1hrr).[131]

to the iron–sulfur centre could not be assigned. The DG calculations for the reduced form were made using 1147 NOE constraints (including 28 1D NOEs) and the family of 15 structures showed a backbone RMSD of 0.73 Å (Fig. 24). REM and RMD calculations gave a final family of NMR structures with RMSD of 0.69 Å and 0.62 Å, respectively. For the oxidized form, 85% of the ^{1}H resonances were assigned and 1142 constraints obtained, of which 39 were obtained from 1D NOE experiments and by irradiation of the hyperfine shifted cysteine resonances.[132] The final family of 15 structures had a RMSD of 0.67 Å from DG calculations, and 0.59 Å and 0.57 Å for REM and RMD calculations,

respectively. The chemical shifts of the majority of the protons for the protein in the oxidized state,[132,133] were found to be identical to those seen in the reduced state. The differences in chemical shift that were detected were suggested to be a reflection of structural changes taking place on protein oxidation, although the structural resolution for the oxidized and reduced NMR families was not sufficient to confirm this. It was also concluded that pseudocontact shifts were not a source of the observed chemical shift differences.

One of the binding cysteines of *Cv* HiPIP was mutated to a serine (C77S), where analysis of hyperfine shifts and 1D NOE experiments indicated that in both the reduced and oxidized forms minimal structural rearrangements take place.[134] The temperature dependences of the hyperfine shifted signals indicated that the ligating residues C46 and C77 were Curie and anti-Curie, the opposite of that found in the WT. The solution structure of the C77S mutant of reduced *Cv* HiPIP was subsequently determined[135] using the assignments for the WT reduced *Cv* HiPIP. Most spin systems, 70 of 85, were identified from an 80 ms TOCSY spectrum and 67 of these were sequentially assigned via standard methods. Combining assignments from 1D NOE experiments allowed 87% of the protein protons to be identified. Analysis of the NOESY spectra gave 1092 distance constraints to which were added 24 from 1D NOE experiments, 46 from *J* coupling constants and 8 H-bond constraints. The cluster was introduced using the method of Banci *et al.*[57] and DG calculations gave a family of 15 structures with a global backbone RMSD of 0.71 Å. REM calculations reduced the RMSD to 0.62 Å. The structure of the C77S mutant was found to be very similar to that of the WT protein. Hyperfine shifts suggest that the serine Oγ atom is coordinated to the cluster.

The residues Y19, F48 and F66 (conserved aromatic residues) of *Cv* HiPIP were mutated to test their role in controlling the redox potential of the protein.[136] The self-exchange rate of the wild type and the mutants were calculated using 2D EXSY experiments (Fig. 25), where it was found that neither solvent accessibility nor aromatic side-chains have a defining role in determining redox potentials of this protein.

To probe the solvent accessibility of the cluster in native and mutant *Cv* HiPIP, multinuclear NMR spectroscopy was used.[137] A previous study[138] had shown that mutations at Y19 destabilized the cluster, therefore two mutants were prepared, Y19L and Y19H. The native and mutant proteins were uniformly labelled with ^{15}N and selectively labelled with [3-^{19}F]phenylalanine. ^{1}H–^{15}N HMQC experiments were used to probe solvent accessibility as cross-peak intensities in these types of experiments are directly related to the backbone NH exchange rate. Lyophilized samples were dissolved in D_2O and 2D ^{1}H–^{15}N HMQC experiments were acquired every 12–15 min (2K × 256 with 4 scans per increment). Exchange rates were classified as very slow, moderate and very fast and comparisons between the native and mutant proteins were made. It was found that reduced and oxidized native HiPIP show no significant

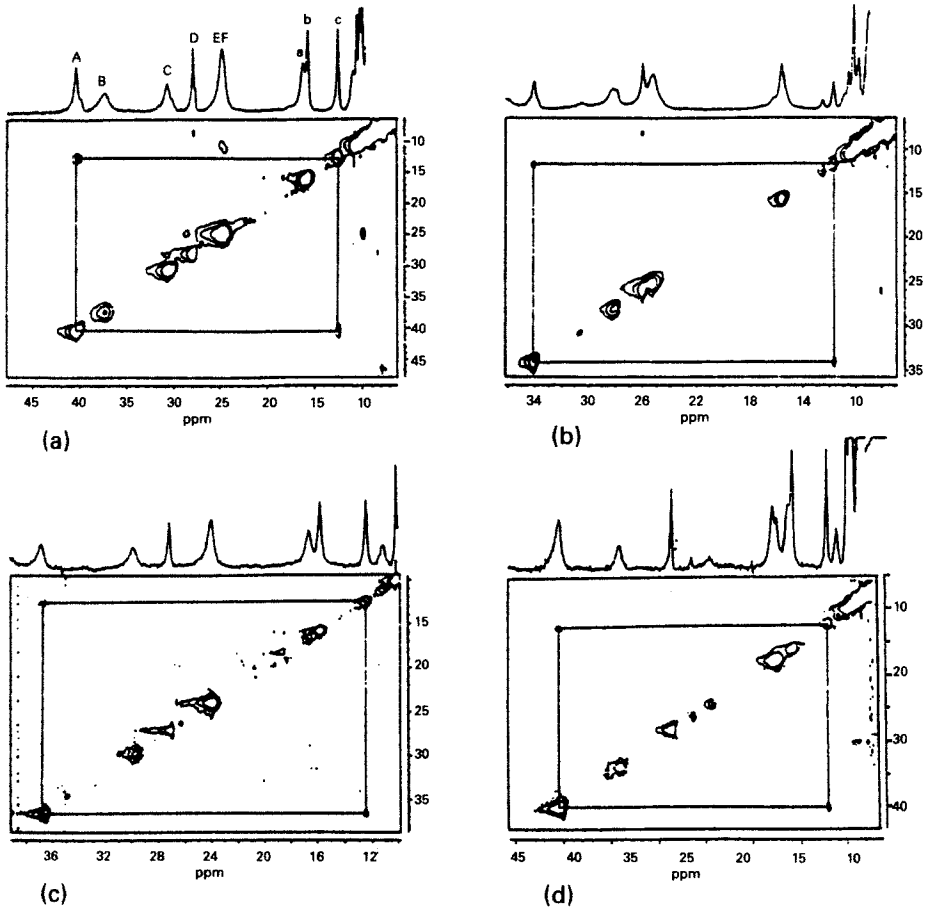

Fig. 25. 500 MHz ^{1}H NMR EXSY spectra of a redox mixture of the recombinant-native and mutant *Cv* HiPIPs at 288 K: (a) rec-nat; (b) Y19L; (c) F48H; (d) F48R. (Reprinted with permission from A. Soriano *et al.*, *Biochemistry*, 1996, **35**, 12479. Copyright 1996 American Chemical Society.)

differences. For the mutants, it was found that residues in the vicinity of Y19 are in the slow exchange regime for the native protein but switch to the fast regime for the mutants, confirming the hypothesis that Y19 is important in protecting the cluster from solvent. ^{19}F NMR was also used to probe solvent accessibility as ^{19}F relaxation times and chemical shifts are sensitive to interaction with solvent. It was found that one of the mutant proteins, Y19H, showed isotopic shifts indicative of increased solvent exposure while the native and Y19L mutant did not.

In a more extensive ^{19}F NMR study of *Cv* HiPIP, relaxation times, chemical shift variations and temperature dependences of ^{19}F-labelled Phe and Trp

protein were investigated.[139] Changes in ^{19}F chemical shifts, measured using EXSY experiments, and relaxation times, for the oxidized and reduced forms of the protein were interpreted as resulting from a conformational change rather than a change in the pseudocontact contribution from the cluster.

NMR has also been used to study the folding process in *Cv* HiPIP by monitoring the changes that occur in 1D and 2D ^{1}H–^{15}N HSQC spectra on the addition of concentrated solutions of guanadinium chloride (GdmCl).[140] It was found that the addition of 3.3–4.4 mol l^{-1} GdmCl produced a new set of hyperfine shifted signals with a concomitant decrease in the native hyperfine shifted signals. The equilibrium was reversible and, by utilizing 1D NOE experiments, the geminal partners for the new (intermediate) species could be identified and, by comparison with the native species, assigned. Further 1D NOE experiments indicated that there were only minor rearrangements in the vicinity of the cluster while larger changes occurred for aromatic residues around the cluster. The ^{1}H–^{15}N HSQC experiments showed that, as the GdmCl concentration is increased, the spectral dispersion in the ^{1}H dimension decreases significantly, indicating a loss of structure and the adoption of a more random coil conformation. The relaxation properties of the ^{15}N backbone atoms were also studied and it was found that the intermediate state had increased mobility when compared to the native state. H_2O/D_2O exchange experiments also confirmed the 'unfolded' nature of the intermediate state. This state was suggested to have a possible role in the folding process of *Cv* HiPIP.

A methodology similar to that used in Bertini *et al.*,[121] which correlates hyperfine chemical shifts with the electron density at the metal centre, was applied to the oxidized and reduced forms of HiPIP from *Rhodoferax fermentans*.[141] Two different electronic distributions, which interconvert rapidly on the NMR time scale, were detected, indicating that one Fe atom has a formal 3+ charge and one electron is delocalized over the remaining three Fe atoms. Analysis of the T_1 rates and dihedral angles (from x-ray sources) of the cysteine β-CH_2 protons gave a semi-quantitative method for extracting structural data from relaxation time measurements.

6.5. 7Fe and 8Fe ferredoxins

One of the earliest high-resolution NMR studies of a 8Fe Fd from *Cp* was carried out in 1989. The 1D NMR spectra of the oxidized and reduced forms were recorded and significant differences were observed.[142] In a later study, the use of 2D M-COSY and NOESY spectra with fast recycle times (~50 ms) and short mixing times (10 and 25 ms) allowed the eight cysteine β-CH_2 proton pairs to be identified.[53] The relaxation properties of these protons were analysed and allowed the stereospecific assignments of each β- CH_2 proton pair to be obtained. A comparison with the x-ray structure of *Peptococcus*

aerogenes (*Pa*) Fd_{ox}[143] indicated that the contact shifts of the cysteine β-CH_2 protons are qualitatively in agreement with the Hβ–Cβ–S–Fe angles. A study by Bertini *et al.*[144] also sequentially identified the hyperfine shifted signals in *Cp* Fd.

Preliminary assignments of the aromatic spin systems F30 and Y2 in the diamagnetic region of oxidized *Cp* Fd using TOCSY spectra were carried out.[145] Subsequently, sequential assignments for the diamagnetic part of oxidized *Cp* Fd and *Clostridium acidi urici* (*Cau*) Fd, using standard 2D NMR methods, was carried out[146] and a preliminary study of some long-range NOEs indicated that the N- and C-termini were in close proximity (as observed in the x-ray structure of *Cau* Fd). A pH-dependent NMR study, in *Cp* Fd, of the hyperfine shifted cysteine β-CH_2 protons found that at high pH values the resonances associated with cluster II showed some shifts, while those associated with cluster I did not.[147] These changes were attributed to deprotonation of a phenolic OH group of Y2 that is situated near cluster II. The complete sequence-specific assignment for all the binding cysteine protons of *Cp* Fd was also published in 1994 along with those for *Cau* Fd.[52] The assignments were carried out using M-COSY, TOCSY and NOESY spectra with fast recycle times and short mixing delays. Natural abundance ^1H–^{13}C HMQC spectra were also used to assign the Cβ and Cα chemical shifts of the cysteines. By comparison with the x-ray structure of Fd from *Pa* it was possible to obtain a correlation between the Hβ–Cβ–S–Fe torsion angle and the cysteine β-CH_2 chemical shifts and Cα cysteine chemical shifts. A Karplus-type relationship was used for the fitting: $\delta = a \sin^2\theta + b \cos\theta + c$. Figure 26 shows the resulting curve with the shifts from the proteins *Cau* Fd_{ox}, *Cp* Fd_{ox}, *Cv* $HiPIP_{red}$, and *Eh*

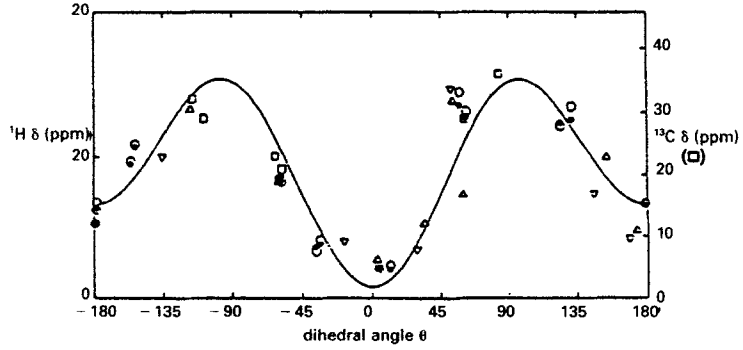

Fig. 26. Plot of the hyperfine shifts of cysteine β-CH_2 protons (left-hand scale) and Cα carbon (right-hand scale) for some proteins containing $[4Fe\text{-}4S]^{2+}$ clusters as a function of the dihedral angles θ, Fe–S–Cβ–H and Fe–S–Cβ–Cα, respectively. The hyperfine shifts of β-CH_2 protons from different proteins are reported as follows: (●) oxidized *C. acidi urici* Fd, (○) oxidized *Cp* Fd, (Δ) reduced *Cv* HiPIP, (▽) reduced *Eh* HiPIP II. (Reprinted with permission from I. Bertini *et al.*, *J. Am. Chem. Soc.*, 1994, **116**, 651. Copyright 1994 American Chemical Society.)

$HiPIP_{red}$ II. The results (large positive a value of 11.5) suggest that the spin delocalization mechanism is dominated by $p\pi$ spin-transfer and that contact shifts may be used to obtain structural information about dihedral angles in these types of proteins.

Mutation studies were also used to obtain the complete sequence-specific assignment of the eight hyperfine shifted binding cysteine β-CH_2 protons in *Cp* Fd. The mutants G12A, G41A and double mutant G12A/G41A were prepared to produce minor local structural changes in either cluster I (G12) or cluster II (G41). TOCSY, NOESY and ^1H–^{13}C HMQC spectra were used along with the crystal structure of a related protein (*Pa* Fd) to carry out the assignment.[148]

Multinuclear NMR was used to identify the ^{15}N resonances in labelled *Cp* Fd.[149] All the 61 ^{15}N resonances were detected in a ^1H-decoupled ^1H–^{15}N INEPT experiment along with all side-chain ^{15}N signals. This was in comparison with only 41 of the possible 51 backbone ^1H protons being detected owing to the smaller γ of ^{15}N being less affected by the paramagnetism of the clusters. It was suggested that classical ^{15}N-detected experiments may yield better results than inverse detected experiments.

The complete solution structure of *Cp* Fd_{ox} by NMR was published in 1995.[150] A combination of standard 2D NMR experiments was used to assign the diamagnetic and paramagnetic parts of the spectrum and 1D super-WEFT NOE experiments were used to provide the link between the two regions. The x-ray structure of *Cau* Fd[151] was also used to provide some assignments. Almost 80% of the protons were assigned. The constraints used in the structure calculations were derived from NOE experiments (478 and 58 from 1D NOEs), H-bonds (12), $^3J_{HN\text{-}H\alpha}$ coupling constants (16) and Hβ—Cβ—S—Fe cysteine dihedral angles (8). The clusters were included by introducing 'special' amino acids[57] in the DG calculations (Section 5.3). A family of 16 structures was obtained with a backbone RMSD of 0.75 Å. Restrained energy minimization (REM) followed by RMD resulted in a family with RMSD of 0.66 Å (Fig. 27). The global folding, secondary structural elements and side-chain orientations of the protein were found to be similar to those seen in the x-ray structure of the 8Fe *Cau* Fd[151] although the section G26–D28 differed significantly in the solution state and x-ray structures.

2D NMR has been used to study the role of conserved proline residues in *Cp* Fd.[152] The mutants P19K, P48K and the double mutant P19D/N21D were cloned to probe the functional effect of the conserved prolines. The TOCSY and NOESY spectra of the mutants were compared with the spectra of the native protein. The spin systems that were perturbed by the P19K mutation were very few in number and point to a very localized change in protein structure — the folding of the section of amino acids following C18 appears to depend on the presence of P19 and the conserved prolines appear to stabilize the active site.

The sequential assignment of the NMR spectra of *Cv* Fd was carried out

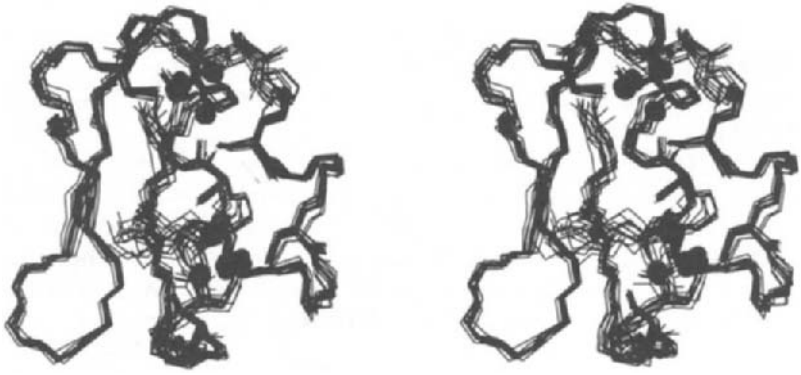

Fig. 27. A stereoplot of the superimposed family of 16 low-target-function *Cp* 8Fe Fd structures derived from NMR data. The Fe atoms are shown as space filling (Brookhaven access code: 1clf).[150]

using steady-state 1D NOE and 2D NOESY and TOCSY experiments with fast recycle times for the hyperfine shifted signals and 'standard' delays for the protons unaffected by the paramagnetism of the clusters.[153] Figure 28 shows the 1D spectrum of *Cv* Fd where the hyperfine shifted signals characteristic of an 8Fe Fd can be seen. Of the 82 spin systems only 55 appeared in the fingerprint region of the TOCSY spectrum and 14 could not be detected in any spectra. ^{1}H–^{13}C HMQC experiments were also used, which identified some side-chain carbons of cysteinyl residues. The eight spin systems of the binding cysteines were also detected. The qualitative study of NOESY cross-peak patterns indicates that this protein folds in a similar manner to smaller 8Fe containing proteins. Differences were detected, however, in that an extra turn seems to be present between C40 and C49 and the extended C-terminal in *Cv* Fd has an α-helix. An angular dependence of β-CH_2 cysteine hyperfine shifts with the Hβ–Cβ–S–Fe angle was seen. Interestingly, C40 appeared off the curve, possibly as a result of extra spin density on this residue.

The native oxidized 7Fe Fd protein from *Bacillus schlegelii* (*Bs*) was studied by NMR[154] and the assignment of the hyperfine shifted resonances was carried out using 1D NOE and TOCSY experiments and by using a model based on the x-ray structure of *Azotobacter vinelandii* (*Av*) Fd.[155] The reduced form of the protein showed a loss of some hyperfine shifted signals. An analysis of the temperature dependences of the hyperfine shifted signals in the oxidized form gave estimates for the three different J coupling values of the [3Fe-4S] cluster.

A mutant of 7Fe *Bs* Fd, where an Asp residue at position 13 has been substituted by a Cys, was prepared in order to engineer an 8Fe protein.[156] A comparison of the NMR results indicated that the mutant contained two [4Fe-4S] clusters rather than a [4Fe-4S] and [3Fe-4S] cluster. The diamagnetic

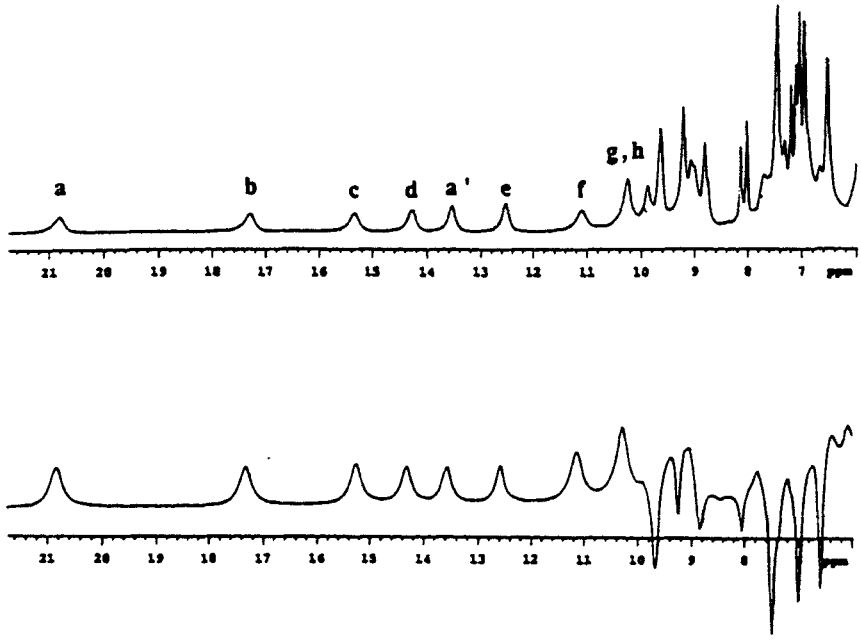

Fig. 28. Downfield part of the ^{1}H NMR spectra of oxidized *Cv* Fd. (Upper trace) Obtained with a selective presaturation of water followed by a nonselective 90° pulse. (Lower trace) Obtained with the sequence 180°–32 ms delay–90° with selective irradiation of water during the 32 ms delay. The slowly relaxing signals with $T_1 \geq 50$ ms have been inverted or suppressed. (Reprinted with permission from J. G. Huber *et al.*, *Biochemistry*, 1995, **34**, 194. Copyright 1995 American Chemical Society.)

part of the ^{1}H NMR spectrum was similar in the two proteins; however, the D13C mutant showed numerous hyperfine shifted resonances that were indicative of a 8Fe protein where C13 is binding one of the clusters. TOCSY and NOESY experiments with fast recycle times and 1D NOE difference experiments identified geminal partners for the β-CH_2 protons. Comparison with *Cv* Fd and *Cau* Fd NMR spectra allowed sequence-specific assignments to be made.

NMR was used to characterize a 7Fe Fd from *Rhodopseudomonas palustris* (*Rp*) and to identify hyperfine shifted signals that indicated that the protein contains a [4Fe-4S] and [3Fe-4S] cluster.[157] A study of the oxidized form of the protein, using 1D and 2D NOE experiments, COSY and TOCSY spectra, and the analysis of NMR results for analogous proteins, enabled the sequence-specific assignment of the cysteine β-CH_2 protons in the absence of the amino acid sequence.[158]

The 7Fe Fd from *Pseudomonas nautica* was characterized by NMR and five hyperfine shifted signals were identified (Fig. 29).[159] The three downfield

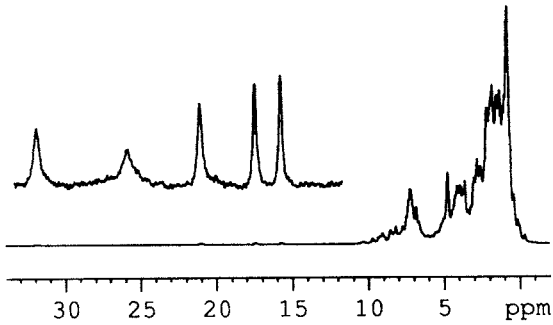

Fig. 29. 400 MHz ^{1}H NMR spectrum of native 7Fe Fd from *P. nautica*. The low-field region is expanded.[159]

shifted signals were assigned to the ligand protons of the 3Fe centre, with the other two assigned to the 4Fe ligands, as is seen for *Av* FdI[160] and *Rp* Fd.[157] The β-CH_2 cysteine proton pairs could be identified in a 2 ms mixing time NOESY experiment and by analogy with NMR results from *Dg* FdI and FdII, and *Av* FdI.

7. CONCLUSIONS

Since 1992, when the first solution structure of an iron–sulfur protein was determined (*Pf* Rd[64]), and 1994, when the first structure of paramagnetic iron–sulfur proteins (*Eh* HiPIP[57] and Pdx[80]) were determined, the number of iron–sulfur protein NMR structures published has expanded to 15, including all the main types of cluster with the exception of [3Fe-4S] (Table 3). The methods used to determine the structures of these types of proteins in solution have evolved over the years. Assignment methods have been generally consistent, with the hyperfine shifted signals being assigned first via 1D/2D NOE experiments (and comparison with x-ray structures) followed by assignment of the diamagnetic regions of the spectrum using standard 2D experiments. Isotopic labelling has also aided the assignment process; in the case of ^{15}N, ^{1}H–^{15}N correlation experiments have identified ^{1}H resonances, and for ^{2}H site-specific labelling has directly identified some hyperfine shifted signals. In some cases, mutation studies have also contributed to the assignment process. The determination of distance constraints for NMR structure calculations in iron–sulfur proteins has mirrored standard procedures used for diamagnetic proteins although, additionally, 1D NOE difference experiments have been used and have proved to be essential in providing correlations between the paramagnetic and diamagnetic parts of the protein. The introduction of the metal centre or cluster into the structure calculations has generally been

Table 3. Published NMR structures for iron–sulfur proteins including backbone RMSDs (as a measure of the quality of the NMR family), number of structures included in the family, number of amino acids for each protein, the number of constraints and method of calculation. The PDB code and the reference are also given.

Protein	RMSD[a]	Number of structures	Number of amino acids	Constraints	Method	PDB code (References)
[Fe-4S]						
Pf Rd(Zn)	1.13	10	53	436	XPLOR	1zrp (64)
Dg Dx(Zn)	0.57	15	36	687	DIANA	(59)
Dg Dx(Cd)	0.45	16	36	866	DIANA	(67)
[2Fe-2S]						
Pp Pdx	1.01	12	106	948	XPLOR	1put (80)
Synechocystis Fd	2.96	3	96	848	XPLOR	1doy (92)
Se Fd	1.01	10	97	1815	XPLOR	1roe (94)
Se Fd	0.81	10	97	1187	XPLOR	2cjo (96)
[4Fe-4S]						
Eh HiPIP I red	0.81	15	73	1444	DIANA	1pih (57)
Eh HiPIP I ox	0.33[b]	15	73	1437	DIANA	(122)
Cv HiPIP red	0.83	15	85	1515	DIANA	1hrr (131)
Cv HiPIP ox	0.67[c]	15	85	1567	DIANA	1neh (132)
Cv HiPIP red C77S	0.72	15	55	1668	DIANA	1noe (135)
Tm Fd	0.81	10	60	759	XPLOR	1rof (118)
Da Fd I	0.85	19	64	786	DIANA/ XPLOR	1dfd (112)
2x[4Fe-4S]						
Cp Fd	0.72	16	55	703	DIANA	1clf (150)

[a]Pairwise RMSD values for all residues.
[b]For residues 4–71.
[c]For residues 2–82.

carried out via the use of distance and angle constraints, taken from available x-ray data. The structure calculations themselves have been carried out using the programs DIANA and/or XPLOR. Generally, the quality of the NMR structures has been good for the diamagnetic regions of the iron–sulfur proteins, while the regions near the metal centres show increased disorder, mainly due to the lack of NOE constraints. This problem (and the problem of introducing the metal centre into structure calculations) has been approached in various ways:

(1) where metal replacement was possible, a diamagnetic metal has been used to avoid the 'bleaching' effect of the unpaired electron at the Fe

atoms, although the possibility that structural changes may take place upon metal substitution have to be considered;

(2) where no spin systems are observed or where broad lines are seen, distance constraints have been introduced between these protons and the Fe atoms using x-ray data: in this case the biasing of the structures towards the x-ray structure has to be considered;

(3) other sources of distance constraints are starting to be used, such as relaxation data, contact shifts and pseudocontact shifts.

This last approach appears to be the way forward in that only experimental NMR data are used and, in theory, no bias is introduced from solid-state x-ray data. Also, the metal centre or cluster can be 'linked' to the protein via experimental constraints.

Relaxation data from both ^{1}H, ^{13}C and ^{15}N nuclei allow M—H(C or N) distances to be obtained from experimental relaxation times;[123,126] however, in order to use these data a number of steps need to be taken. First, the diamagnetic contribution to the relaxation rate needs to be evaluated (normally an upper limit is used) and subtracted from the experimental relaxation to give the relaxation due solely to paramagnetic effects (Section 3.2). Distance constraints are then extracted using either the maximum possible distance between the metal ion and the proton or, if initial structures (or an x-ray structure) are available, the distance seen in these structures. Structure recalculation is then carried out using both the new constraints and the original set.

Contact shifts allow Hβ—Cβ—S—M dihedral angles to be estimated, but up until now this has been carried out only for 4Fe Fds and in an empirical way using calibration via x-ray structures.[52,53] No theoretical basis exists because of the problem of spin delocalization, i.e. how much unpaired spin density resides on each nucleus.

Pseudocontact shifts, as for relaxation constraints, allow M—H distances to be obtained (Section 3.3.1) although the method has not yet been applied to iron–sulfur proteins only to a cytochrome *c*.[50] The first step, in extracting distances from pseudocontact shifts, is to obtain the diamagnetic shift of the proton under study (more than 5 bonds remove from the metal) and subtract it from the observed pseudocontact shift. This is achieved by measuring chemical shifts in a diamagnetic equivalent of the system (e.g. reduced cytochrome *c*) or in a system where the paramagnetic metal has been replaced by a diamagnetic equivalent (Zn, Cd, Hg, etc.). The problems that arise from structural differences that may occur between the diamagnetic and paramagnetic forms of the protein have been overcome by giving a tolerance (proportional to the value of the pseudocontact shift) to the experimental pseudocontact shifts. The next step involves the problem of obtaining the orientation of the M—H vectors, in the protein, with respect to the internal magnetic susceptibility tensor. This is achieved by using an initial family of

NMR structures calculated with only diamagnetic constraints (or an x-ray structure) and varying the magnetic susceptibility tensor to fit the observed pseudocontact shifts. The protein structure/coordinates are then varied to fit the experimental pseudocontact shifts and a new magnetic susceptibility tensor is calculated. This is a 5-parameter fit if the metal is assumed to be the centre of the axis system or an 8-parameter fit if the metal is allowed to move. The process is repeated until self-consistency is achieved. The introduction of diamagnetic distance constraints and pseudocontact shifts constraints at the same time during the minimization procedure is found to be the optimal method.

As the number and nature of structural constraints near the cluster are the determining factors in obtaining an accurate molecular model, these recent advances, which allow experimental constraints to be introduced at the centres or clusters, are improving the quality of the solution-state structures of paramagnetic iron–sulfur proteins and are leading to the determination of solution-state structures totally independently from x-ray data.

In general, the NMR solution structures of iron–sulfur proteins have not shown major differences when compared to solid-state x-ray structures of the same, or homologous, proteins even when the metal has been replaced by a diamagnetic equivalent. This suggests that the use of x-ray distances and angles as constraints for the metal centres may not be so problematic, as is often thought, and that metal replacement, especially in the case of [Fe-4S] proteins, may be a viable alternative. The absence of observed differences between NMR and x-ray structures may also be a result of a lack of 'resolution' in the NMR family not allowing the detection of subtle differences between the solution and solid state.

The importance of the position of the paramagnetic cluster relative to the protein as a whole has an effect on the number of 'available' NOE constraints. The HiPIPs have their [4Fe-4S] cluster buried, while the Fds and Rd-type proteins have their clusters very near the surface of the protein. This results in a larger number of observable dipolar contacts between each of the cluster ligands and the 'diamagnetic' protein matrix in the HiPIPs, while for the Fds and Rds there are many fewer dipolar contacts to the diamagnetic part and hence fewer structural constraints for the cluster environment. This is reflected in the RMSD of the backbones near the cluster for the Fds and Rds.

At a more subtle level, differences between the oxidized and reduced forms of the same protein (*Cv* and *Eh* HiPIP I) have not been seen at a global level, although differences in the hyperfine shifted signals indicate that coupling between the Fe atoms varies. This demonstrates the utility of NMR in probing the electronic structure of the clusters in iron–sulfur proteins.

During the last 7–8 years, the goal of determining the structure of metalloproteins in solution by NMR has begun to be realized. Advances in experimental techniques and the application of new theoretical methods have allowed constraints near the metal centre (or cluster) to be introduced,

improving markedly the quality of the solution structures. NMR studies of iron–sulfur proteins have demonstrated the versatility of this method of structure determination and have shown how practical and theoretical challenges posed by the paramagnetism of these systems have driven forward experimental methods and produced theoretical advances in the field.

ACKNOWLEDGEMENTS

The authors would like to acknowledge José and Isabel Moura for introducing us to this fascinating field of NMR and iron-sulfur proteins.

NOTE ADDED IN PROOF

The solution structures of the Fe^{2+} form of the [Fe-4S] protein *Cp* Rd (I. Bertini, D. M. Kurtz Jr, M. K. Eidness, G. Liu, C. Luchinat, A. Rosato and R. A. Scott, *J. Biol. Inorg. Chem.*, 1998, **3**, 401) and the oxidized 7Fe Fd from *Bs* (S. Aono, D. Bentrop, I. Bertini, A. Donaire, C. Luchinat, Y. Niikura and A. Rosato, *Biochem.*, 1998, **37**, 9812) have recently been published.

REFERENCES

1. M. P. Williamson, T. F. Havel and K. Wüthrich, *J. Mol. Biol.*, 1985, **182**, 295.
2. R. Cammack, in *Advances in Inorganic Chemistry 38. Iron–Sulfur Proteins* (ed. R. Cammack and A. G. Sykes), p. 281, Academic Press, 1992.
3. R. H. Holm, *Advances in Inorganic Chemistry 38. Iron–Sulfur Proteins* (ed. R. Cammack and A. G. Sykes), p. 1, Academic Press, 1992.
4. J. J. G. Moura, A. L. Macedo and P. N. Palma, *Methods Enzymol.*, 1994, **243**, 165.
5. L. C. Sieker, R. E. Stenkamp and J. LeGall, *Methods Enzymol.*, 1994, **243**, 203.
6. R. E. Stenkamp, L. C. Sieker and L. H. Jensen, *Proteins*, 1990, **8**, 352.
7. M. Frey, L. C. Sieker, F. Payan, R. Haser, M. Bruschi, G. Pepe and J. LeGall, *J. Mol. Biol.*, 1987, **197**, 525.
8. Z. Dauter, L. C. Sieker and K. S. Wilson, *Acta Crystallogr.*, Sect. B, 1992, **48**, 42.
9. K. D. Watenpaugh, L. C. Sieker and L. H. Jensen, *J. Mol. Biol.*, 1980, **138**, 615.
10. M. Archer, R. Huber, P. Tavares, I. Moura, J. J. G. Moura, M. A. Carrondo, L. C. Sieker, J. LeGall and M. J. Romão, *J. Mol. Biol.*, 1995, **251**, 690.
11. I. Moura, P. Tavares and N. Ravi, *Methods Enzymol.*, 1994, **243**, 216.
12. J. LeGall, B. C. Prickril, I. Moura, A. V. Xavier, J. J. G. Moura and B.-H. Huynh, *Biochemistry*, 1988, **27**, 1636.
13. I. Moura, P. Tavares, J. J. G. Moura, N. Ravi, B. H. Huynh, M. Y. Liu and J. LeGall, *J. Biol. Chem.*, 1990, **265**, 21596.
14. P. Tavares, N. Ravi, J. J. G. Moura, J. LeGall, Y. H. Huang, B. R. Crouse, M. J. Johnson, B. H. Huynh and I. Moura, *J. Biol. Chem.*, 1994, **269**, 10504.
15. A. V. Coelho, M. Pedro, V. Fülöp, A. Thompson, A. Gonzalez and M. A. Carrondo, *J. Biol. Inorg. Chem.*, 1997, **2**, 680.

16. W. R. Dunham, G. Palmer, R. H. Sands and A. H. Bearden, *Biochim. Biophys. Acta*, 1971, **253**, 373.
17. M. H. Emptage, T. A. Kent, B. H. Huynh, J. Rawlings, W. H. Orme-Johnson and E. Münck, *J. Biol. Chem.*, 1980, **255**, 11793.
18. B. H. Huynh, J. J. G. Moura, I. Moura, T. A. Kent, J. LeGall, A. V. Xavier and E. Münck, *J. Biol. Chem.*, 1980, **255**, 3242.
19. I. Bertini, S. Ciurli and C. Luchinat, *Structure and Bonding*, 1995, **83**, 1.
20. H. Cheng and J. M. Markley, *Annu. Rev. Biophys. Biomol. Struct.*, 1995, **24**, 209.
21. I. Bertini and C. Luchinat, *NMR of Paramagnetic Molecules in Biological Systems*, Menlo Park, Benjamin/Cummings, 1986.
22. L. Banci, I. Bertini and C. Luchinat, *Nuclear and Electron Relaxation*, VCH, Weinheim, 1991.
23. I. Bertini, P. Turano and A. J. Vila, *Chem. Rev.*, 1993, **93**, 2833.
24. I. Bertini, C. Luchinat and A. Rosato, *Prog. Biophys. Mol. Biol.*, 1996, **66**, 43.
25. I. Bertini and C. Luchinat, *Coord. Chem. Rev.*, 1996, **150**, complete volume.
26. R. K. Harris, *Nuclear Magnetic Resonance Spectroscopy*, Wiley, New York, 1986.
27. J. H. Noggle and R. E. Schirmer, *The Nuclear Overhauser Effect*, Academic Press, New York, 1971.
28. D. Neuhaus and M. P. Williamson, *The Nuclear Overhauser Effect in Structural and Conformational Analysis*, VCH Publishers, New York, 1989.
29. L. Banci, in *Biological Magnetic Resonance* (ed. L. J. Berliner and J. Reuben), Vol. 12, pp. 79–111, Plenum, New York, 1993.
30. A. Bax, R. Freeman and G. Morris, *J. Magn. Reson.*, 1981, **42**, 164.
31. A. Bax and R. Freeman, *J. Magn. Reson.*, 1981, **44**, 542.
32. L. Braunschweiler and R. R. Ernst, *J. Magn. Reson.*, 1983, **53**, 521.
33. S. Macura and R. R. Ernst, *Mol. Phys.*, 1980, **41**, 95.
34. K. Wüthrich, *NMR of Proteins and Nucleic Acids*, Wiley, New York, 1986.
35. I. Bertini, C. Luchinat, M. Piccioli and D. Tarchi, *Concepts Magn. Reson.*, 1994, **6**, 307–335.
36. T. Inubushi and E. D. Becker, *J. Magn. Reson.*, 1983, **51**, 128.
37. I. Bertini, F. Briganti, C. Luchinat, A. Scozzafava and M. Sola, *J. Am. Chem. Soc.*, 1991, **113**, 1237.
38. I. Bertini, A. Dikiy, C. Luchinat, M. Piccioli and D. Tarchi, *J. Magn. Reson. Ser. B*, 1994, **103**, 278.
39. L. Müller, *J. Am. Chem. Soc.*, 1979, **101**, 4481.
40. M. R. Bendall, D. T. Pegg and D. M. Doddrell, *J. Magn. Reson.*, 1983, **52**, 81.
41. A. Bax, R. H. Griffey and B. L. Hawkins, *J. Magn. Reson.*, 1983, **55**, 301.
42. G. Bodenhausen and D. J. Ruben, *Chem. Phys. Lett.*, 1980, **69**, 185.
43. D. Brühwiler and G. Wagner, *J. Magn. Reson.*, 1986, **69**, 546.
44. G. Wagner, *Prog. NMR Spec.*, 1990, **22**, 101.
45. D. S. Wishart, F. M. Richards and B. D. Sykes, *Biochemistry*, 1992, **31**, 1647.
46. D. S. Wishart, C. G. Bigam, J. Yao, F. Abildgaard, H. J. Dyson, E. Oldfield, J. L. Markley and B. D. Sykes, *J. Biomol. NMR*, 1995, **6**, 135.
47. P. Guntert, C. Mumenthaler and K. Wuthrich, *J. Mol. Biol.*, 1997, **273**, 283.
48. I. Bertini, A. Donaire, I. C. Felli, A. Rosato and C. Luchinat, *Magn. Reson. Chem.*, 1996, **34**, 948.
49. T. F. Havel, G. M. Crippen and I. D. Kuntz, *Biopolymers*, 1979, **18**, 73.
50. L. Banci, I. Bertini, K. L. Bren, M. A. Cermonini, H. B. Gray, C. Luchinat and P. Turano, *J. Biol. Inorg. Chem.*, 1996, **1**, 117.
51. L. Banci, I. Bertini, G. G. Savellini, A. Romagnoli, P. Turano, M. A. Cremonini, C. Luchinat and H. B. Gray, *Proteins Struct., Funct. Genet.*, 1997, **29**, 68.
52. I. Bertini, F. Capozzi, C. Luchinat, M. Piccioli and A. J. Villa, *J. Am. Chem. Soc.*, 1994, **116**, 651–660.

53. S. C. Busse, G. N. LaMar and J. B. Howard, *J. Biol. Chem.*, 1991, **266**, 23714.
54. T. F. Havel and K. Wüthrich, *Bull. Math. Biol.*, 1984, **46**, 673.
55. W. Braun and N. Go, *J. Mol. Biol.*, 1985, **186**, 611.
56. P. Güntert, W. Braun and K. Wüthrich, *J. Mol. Biol.*, 1991, **217**, 517.
57. L. Banci, I. Bertini, L. D. Eltis, I. C. Felli, D. H. W. Kastrau, C. Luchinat, M. Piccioli, R. Pierattelli and M. Smith, *Eur. J. Biochem*, 1994, **225**, 715.
58. M. T. Werth, D. M. Kurtz Jr, I. Moura and J. LeGall, *J. Am. Chem. Soc.*, 1987, **109**, 273.
59. B. J. Goodfellow, P. Tavares, M. J. Romao, C. Czaja, F. Rusnak, J. Legall, I. Moura and J. J. G. Moura, *J. Biol. Inorg. Chem.*, 1996, **1**, 341.
60. B. Xia, W. M. Westler, H. Cheng, J. Meyer, J. M. Moulis and J. L. Markley, *J. Am. Chem. Soc.*, 1995, **117**, 5347.
61. B. F. Volkmann, A. M. Prantner, S. J. Wilkens, B. Xia and J. L. Markley, *J. Biomol. NMR*, 1997, **10**, 409.
62. A. M. Prantner, B. F. Volkmann, S. J. Wilkens, B. Xia and J. L. Markley, *J. Biomol. NMR*, 1997, **10**, 411.
63. P. R. Blake, J.-B. Park, F. O. Bryant, S. Aono, J. K. Magnuson, E. Eccleston, J. B. Howard, M. F. Summers and M. W. W. Adams, *Biochemistry*, 1991, **30**, 10885.
64. P. R. Blake, J.-B. Park, Z. H. Zhou, D. R. Hare, M. W. W. Adams and M. F. Summers, *Protein Sci.*, 1992, **1**, 1508.
65. M. W. Day, B. T. Hsu, L. Joshua-tor, J.-B. Park, Z. H. Zhou, M. W. W. Adams and D. C. Rees, *Protein Sci.*, 1992, **1**, 1494.
66. P. R. Blake, M. W. Day, B. T. Hsu, L. Joshua-Tor, J.-B. Park, D. R. Hare, M. W. W. Adams, D. C. Rees and M. F. Summers, *Protein Sci.*, 1992, **1**, 1522.
67. B. J. Goodfellow, F. Rusnak, I. Moura, T. Domke and J. J. G. Moura, *Protein Sci.*, 1998, **7**, 928.
68. P. R. Blake, B. Lee, M. F. Summers, M. W. W. Adams, J.-B. Park, Z. H. Zhou and A. Bax, *J. Biomol. NMR*, 1992, **2**, 527.
69. P. R. Blake, J.-B. Park, M. W. W. Adams and M. F. Summers, *J. Am. Chem. Soc.*, 1992, **114**, 4931.
70. P. R. Blake, B. Lee, M. F. Summers, J. B. Park, H. Z. Zhi and M. W. W. Adams, *New J. Chem.*, 1994, **18**, 387.
71. C. J. Henehan, D. L. Pountney, O. Zerbe and M. Vasak, *Protein Sci.*, 1993, **2**, 1756.
72. O. Zerbe, D. L. Pountney, W. von Philipsborn and M. Vasak, *J. Am. Chem. Soc.*, 1994, **116**, 377.
73. I. Moura, M. Teixeira, J. LeGall and J. J. G. Moura, *J. Bioinorg. Chem.*, 1991, **44**, 127.
74. K. A. Richie, Q. Teng, C. J. Elkin and D. M. Kurtz, Jr, *Protein Sci.*, 1996, **5**, 883.
75. M. Ayhan, X. Xiao, M. J. Lavery, A. M. Hamer, K. W. Nugent, S. B. D. Scrofani, M. Guss and A. G. Wedd, *Inorg. Chem.*, 1996, **35**, 5902.
76. S.-C. Im, H.-Y. Zhuang-jackson, T. Kohzuma, P. Kyritsis, W. Mcfarlane and A. G. Sykes, *J. Chem. Soc., Dalton Trans.*, 1996, **22**, 4287.
77. J. Gaillard, H.-Y. Zhuang-jackson and J. M. Moulis, *Eur. J. Biochem.*, 1996, **238**, 346.
78. T. C. Pochapsky and X. M. Ye, *Biochemistry*, 1991, **30**, 3850.
79. X. M. Ye, T. C. Pochapsky and S. S. Pochapsky, *Biochemistry*, 1992, **31**, 1961.
80. T. C. Pochapsky, X. M. Ye, G. Ratnaswamy and T. A. Lyons, *Biochemistry*, 1994, **33**, 6424.
81. W. R. Rypniewski, D. R. Breiter, M. W. Benning, G. Wesenberg, B.-H. Oh, J. L. Markley, I. Rayment and H. M. Holden, *Biochemistry*, 1991, **30**, 4126.
82. T. C. Pochapsky, G. Ratnaswamy and A. Patera, 1994, *Biochemistry*, **33**, 6433.
83. T. A. Lyons, G. Ratnaswamy and T. C. Pochapsky, *Protein Sci.*, 1996, **5**, 627.
84. B. Coxon, N. Sari, M. J. Holden and V. L. Vilker, *Magn. Reson. Chem.*, 1997, **35**, 743.
85. Y. K. Chae and J. L. Markley, *Biochemistry*, 1995, **34**, 188.
86. S. Kazanis and T. C. Pochapsky, *J. Biomol. NMR*, 1997, **9**, 337.
87. B. L. Jacobson, Y. K. Chae, J. L. Markley, I. Rayment and H. M. Holden, *Biochemistry*, 1993, **32**, 6788.

88. H. Cheng, W. M. Westler, B. Xia, B. H. Oh and J. L. Markley, *Arch. Biochem. Biophys.*, 1995, **316**, 619.
89. L. Skjeldal, W. M. Westler, B.-H. Oh, A. M. Kretzel, H. M. Holden, B. L. Jacobson, I. Rayment and J. L. Markley, *Biochemistry*, 1991, **30**, 7363.
90. H. Cheng, B. Xia, G. H. Reed and J. L. Markley, *Biochemistry*, 1994, **33**, 3155.
91. E. Vo, H. C. Wang and J. P. Germanas, *J. Am. Chem. Soc.*, 1997, **119**, 1934.
92. C. Lelong, P. Setif, H. Bottin, F. Andre and J. M. Neumann, *Biochemistry*, 1995, **34**, 14462.
93. T. Tsukihara, K. Fukuyama, M. Mizushima, T. Harioka, M. Kusunoki, Y. Katsube, T. Hase and H. Matsubara, *J. Mol. Biol.*, 1990, **216**, 399.
94. B. Baumann, H. Sticht, M. Schärpf, M. Sutter, W. Haehnel and P. Rösch, *Biochemistry*, 1996, **35**, 12831.
95. S. Ikemizu, M. Bando, T. Sato, Y. Morimoto and T. Tsukihara, *Acta Crystallogr.*, **D50**, 1994, 167.
96. H. Hatanaka, R. Tanimura, S. Katoh and F. Inagaki, *J. Mol. Biol.*, 1997, **268**, 922.
97. K. Fukuyama, N. Ueki, H. Nakamura, T. Tsukihara and H. Matsubara, *J. Biochem.*, 1995, **117**, 1017.
98. A. L. Macedo, I. Moura, J. J. G. Moura, J. Legall and B. H. Huynh, *Inorg. Chem.*, 1993, **32**, 1101.
99. C. R. Kissinger, L. C. Sieker, E. T. Adman and L. H. Jensen, *J. Mol. Biol.*, 1991, **219**, 693.
100. A. L. Macedo, P. N. Palma, I. Moura, J. Legall, V. Wray and J. J. G. Moura, *Magn. Reson. Chem.*, 1993, **31**, S 59.
101. S. C. Busse, G. N. LaMar, L. P. Yu, J. B. Howard, E. T. Smith, Z. H. Zhou and M. W. W. Adams, *Biochemistry*, 1992, **31**, 11952.
102. Q. Teng, Z. H. Zhou, E. T. Smith, S. C. Busse, J. B. Howard, M. W. W. Adams and G. N. LaMar, *Biochemistry*, 1994, **33**, 6316.
103. C. M. Gorst, Y. H. Yeh, YQ. Teng, L. Calzolai, Z. H. Zhou, M. W. W. Adams and G. N. LaMar, *Biochemistry*, 1995, **34**, 600.
104. A. L. Macedo, I. Moura, K. K. Surerus, V. Papaefthymiou, M. Y. Liu, J. Legall, E. Münck and J. J. G. Moura, *J. Biol. Chem.*, 1994, **269**, 8052.
105. A. Donaire, C. M. Gorst, Z. H. Zhou, M. W. W. Adams and G. N. LaMar, *J. Am. Chem. Soc.*, 1994, **116**, 6841.
106. A. Donaire, Z.-H. Zhou, M. W. W. Adams and G. N. LaMar, *J. Biomol. NMR*, 1996, **7**, 35.
107. P.-L. Wang, A. Donaire, Z.-H. Zhou, M. W. W. Adams and G. N. LaMar, *Biochemistry*, 1996, **35**, 11319.
108. K. Fukuyama, Y. Nagahara, T. Tsukihara and Y. Katsube, *J. Mol. Biol.*, 1988, **199**, 183.
109. A. Sery, D. Housset, L. Serre, J. Bionicel, C. Hatchikian, M. Frey and M. Roth, *Biochemistry*, 1994, **33**, 15408.
110. S. L. Davy, J. Breton, M. J. Osborne, A. J. Thomson, A. P. Thurgood, L. Y. Lian, Y. Petillot, C. Hatchikian and G. R. Moore, *Biochim. Biophys. Acta*, 1994, **1209**, 33.
111. S. L. Davy, M. J. Osborne, J. Breton, G. R. Moore, A. J. Thomson, I. Bertini and C. Luchinat, *FEBS Lett.*, 1995, **363**, 199.
112. S. L. Davy, M. J. Osborne and G. R. Moore, *J. Mol. Biol.*, 1998, **277**, 683.
113. E. Lebrun, C. Simenel, F. Guerlesquin and M. Delepierre, *Magn. Reson. Chem.*, 1996, **34**, 873.
114. C. M. Gorst, Z. H. Zhou, K. Ma, Q. Teng, J. B. Howard, M. W. W. Adams and G. N. LaMar, *Biochemistry*, 1995, **34**, 8788.
115. L. Calzolai, C. M. Gorst, Z. H. Zhou, Q. Teng, M. W. W. Adams and G. N. LaMar, *Biochemistry*, 1995, **34**, 11373.
116. L. Calzolai, C. M. Gorst, K. L. Bren, Z. H. Zhou, M. W. W. Adams and G. N. LaMar, *J. Am. Chem. Soc.*, 1997, **119**, 9341.

117. G. Wildegger, D. Bentrop, A. Ejchart, M. Alber, A. Hage, R. Sterner and P. Rosch, *Eur. J. Biochem.*, 1995, **229**, 658.
118. H. Sticht, G. Wildegger, D. Bentrop, B. Darimont, R. Sterner and P. Rosch, *Eur. J. Biochem.*, 1996, **237**, 726.
119. I. Bertini, I. C. Felli, D. H. W. Kastrau, C. Luchinat, M. Piccioli and M. S. Viezzoli, *Eur. J. Biochem.*, 1994, **225**, 703.
120. D. R. Breiter, T. E. Meyer, I. Rayment and H. M. Holden, *J. Biol. Chem.*, 1991, **266**, 18660.
121. I. Bertini, F. Capozzi, L. D. Eltis, I. C. Felli, C. Luchinat and M. Piccioli, *Inorg. Chem.*, 1995, **34**, 2516.
122. I. Bertini, L. D. Eltis, I. C. Felli, D. H. W. Kastrau, C. Luchinat and M. Piccioli, *Chem. — Eur. J.*, 1995, **1**, 598.
123. I. Bertini, M. M. J. Couture, A. Donaire, L. D. Eltis, I. C. Felli, C. Luchinat, M. Piccioli and A. Rosato, *Eur. J. Biochem.*, 1996, **241**, 440.
124. I. Bertini, I. C. Felli, C. Luchinat and A. Rosato, *Proteins Struct. Funct. Genet.*, 1996, **24**, 158.
125. J. G. Huber, J. M. Moulis and J. Gaillard, *Biochemistry*, 1996, **35**, 12705.
126. I. Bertini, A. Donaire, I. C. Felli; C. Luchinat and A. Rosato, *Inorg. Chem.*, 1997, **36**, 4798.
127. S. G. Iwagami, A. L. Creagh, C. A. Haynes, M. Borsari, I. C. Felli, M. Piccioli and L. D. Eltis, *Protein Sci.*, 1995, **4**, 2562.
128. A. Soriano and J. A. Cowan, *Inorg. Chim. Acta*, 1996, **251**, 285.
129. S. M. Bian, C. F. Hemann, R. Hille and J. A. Cowan, *Biochemistry*, 1996, **35**, 14544.
130. J. Gaillard, J.-P. Albrand, J.-M. Moulis, D. E. Wemmer, *Biochemistry*, 1992, **31**, 5632.
131. L. Banci, I. Bertini, A. Dikiy, D. H. W. Kastrau, C. Luchinat and P. Sompompisut, *Biochemistry*, 1995, **34**, 206.
132. I. Bertini, A. Dikiy, D. H. W. Kastrau, C. Luchinat and P. Sompornpisut, *Biochemistry*, 1995, **34**, 9851.
133. D. G. Nettesheim, S. R. Harder, B. A. Feinferg and J. D. Otvos, *Biochemistry*, 1992, **31**, 1234.
134. E. Babini, I. Bertini, M. Borsari, F. Capozzi, A. Dikiy, L. D. Eltis and C. Luchinat, *J. Am. Chem. Soc.*, 1996, **118**, 75.
135. D. Bentrop, I. Bertini, F. Capozzi, A. Dikiy, L. D. Eltis and C. Luchinat, *Biochemistry*, 1996, **35**, 5928.
136. A. Soriano, D. W. Li, S. M. Bian, A. Agarwal and J. A. Cowan, *Biochemistry*, 1996, **35**, 12479.
137. D. W. Li, A. Agarwal and J. A. Cowan, *Inorg. Chem.*, 1996, **35**, 1121.
138. A. Agarwal, D. Li and J. A. Cowan, *Proc. Natl. Acad. Sci. USA*, 1995, **92**, 9440.
139. D. W. Li, A. Soriano and J. A. Cowan, *Inorg. Chem.*, 1996, **35**, 1980.
140. I. Bertini, J. A. Cowan, C. Luchinat, K. Natarajan and M. Piccioli, *Biochemistry*, 1997, **36**, 9332.
141. S. Ciurli, M. A. Cremonini, P. Kofod and C. Luchinat, *Eur. J. Biochem.*, 1996, **236**, 405.
142. L. Skejeldal, J. Krane and T. Ljones, *Int. J. Biol. Macromol.*, 1989, **11**, 322.
143. E. T. Adman, L. C. Sieker and L. H. Jensen, *J. Biol. Chem.*, 1973, **248**, 3987.
144. I. Bertini, F. Briganti, C. Luchinat, L. Messori, R. Mannonni, A. Scozzafava and G. Vallini, *FEBS Lett.*, 1991, **289**, 253.
145. M. L. Ganadu, F. Bonomi, S. Pagani and R. Boelens, *Biochem. Int.*, 1992, **26**, 577.
146. J. Galliard, J.-M. Moulis, R. Kummerle and J. Meyer, *Magn. Reson. Chem.*, 1993, **31**, S27.
147. L. Calzolai, L. Messori and R. Monnanni, *FEBS Lett.*, 1994, **350**, 41.
148. S. D. B. Scrofani, P. S. Brereton, A. M. Hamer, M. J. Lavery, S. G. Mcdowall, G. A. Vincent, R. T. C. Brownlee, N. J. Hoogenraad, M. Sadek and A. G. Wedd, *Biochemistry*, 1994, **33**, 14486.

149. M. Sadek, S. D. B. Scrofani, R. T. C. Brownlee and A. G. Wedd, *J. Chem. Soc., Chem. Commun.*, 1995, **105**.
150. I. Bertini, A. Donaire, B. A. Feinberg, C. Luchinat, M. Piccioli and H. Yuan, *Eur. J. Biochem.*, 1995, **232**, 192.
151. E. D. Duée, E. Fanchon, J. Vicat, L. C. Sieker, J. Meter and J.-M. Moulis, *J. Mol. Biol.*, 1994, **243**, 683.
152. I. Quinkal, V. Davasse, J. Gaillard and J. M. Moulis, *Protein Eng.*, 1994, **7**, 681.
153. J. G. Huber, J. Gaillard and J.-M. Moulis, *Biochemistry*, 1995, **34**, 194.
154. S. Aono, I. Bertini, J. A. Cowan, C. Luchinat, A. Rosato and M. S. Viezzoli, *J. Biol. Inorg. Chem.*, 1996, **1**, 523.
155. C. D. Stout, *J. Biol. Chem.*, 1993, **268**, 25920.
156. S. Aono, D. Bentrop, I. Bertini, C. Luchinat and R. Macinai, *FEBS Lett.*, 1997, **412**, 501.
157. G. Battistuzzi, M. Borsari, S. Ferretti, C. Luchinat and M. Sola, *Arch. Biochem. Biophys.*, 1995, **320**, 149.
158. I. Bertini, A. Dikiy, C. Luchinat, R. Macinai, M. S. Viezzoli and M. Vincenzini, *Biochemistry*, 1997, **36**, 3570.
159. A. L. Macedo, S. Besson, C. Moreno, G. Fauque, J. J. G. Moura and I. Moura, *Biochem. Biophys. Res. Commun.*, 1996, **229**, 524.
160. H. Cheng, K. Grohmann and W. Sweeney, *J. Biol. Chem.*, 1990, **265**, 12388.
161. A. T. Brunger, *X-PLOR, A System for X-ray Crystallography and NMR*, Yale University, New Haven, CT, 1987.

This Page Intentionally Left Blank

NMR Studies of Wine Chemistry and Wine Bacteria

ANA RAMOS and HELENA SANTOS

Instituto de Tecnologia Química e Biológica, Universidade Nova de Lisboa, Oeiras, Portugal

Given the powerful analytical capabilities of NMR spectroscopy it is not surprising that this is a first-choice technique for the analysis and characterization of wine components as well as for the elucidation of the physiology and metabolism of microorganisms involved in wine fermentation. The non-destructive nature of NMR is one of its most attractive features in this field of application, allowing rapid on-line measurements or analysis of wine samples involving virtually no sample preparation, and non-invasive studies of wine bacteria in vivo. *In this report, several examples are given illustrating recent applications of NMR to study wine chemistry or to elucidate key metabolic traits of wine bacteria.*

1. INTRODUCTION

Wine is here defined as a complex mixture of compounds resulting from the fermentation of the juice of grapes of *Vitis vinifera*. In addition to the major component, ethanol, several hundred organic and inorganic substances contribute to the texture and organoleptic characteristics of this ancient and highly appreciated beverage.

Tartaric, malic, succinic, lactic, acetic and citric acids are the major organic

ANNUAL REPORTS ON NMR SPECTROSCOPY
VOLUME 37 ISBN 0-12-505337-1

acids found in wine. For detailed information on wine composition, see references 1 and 2. Of these organic acids, tartaric acid is present in the highest amounts (1.5–4.0 $g\,l^{-1}$), whereas citric acid is often a minor component (0–0.5 $g\,l^{-1}$) except when added to wines as a metal chelating agent at the time of bottling. Among nitrogenous compounds, amino acids are the predominant components, present in concentrations as high as hundreds of milligrams per litre; however, proline, the most abundant amino acid in wine, can reach very high amounts (3.5 $g\,l^{-1}$). More than 20 amines have been identified in wine, but the concentrations of nonvolatile amines, such as histamine and tyramine, have been the object of tight control in wines because of their potential biogenic effects.[3] Residual sugars from microbial fermentations are present in highly variable amounts and contribute significantly to the organoleptic characteristics of the final product; glucose, fructose and rhamnose are the predominant hexoses, while arabinose, xylose and ribose are the major pentoses. Polyols form another class of compounds with relevant contribution to the taste and structure of wine: glycerol is often the third major wine component after water and ethanol, but the contents of 2,3-butanediol, inositol, mannitol, arabitol and erythritol can also reach significant values. Several hundred minor components contribute to the wine 'bouquet' and play a definitive role in the quality of the wine. Carbonyl compounds include acetaldehyde, hydroxymethyl furfural and diacetyl: the last compound, a product of citric acid metabolism during malolactic fermentation, is an important flavour conferring a 'buttery' taste that can be undesirable when in excess. Phenolic compounds play a decisive role in the make-up of a wine's character; for instance, the myriad shades of colour in red wines are largely due to the presence of anthocyanins in different proportions. Finally, the wine may contain several chemicals added at different stages of wine production, such as sulfur dioxide and sorbic and benzoic acids which are used as preservatives.

This brief description of wine composition is far from exhaustive but serves the purpose of acquainting the reader with the great chemical complexity of this alcoholic beverage, even though only the major low-molecular-mass organic components have been mentioned here.

Chemical analysis of wine is essential to guarantee the authenticity of the product and to protect the consumer. Furthermore, during the process of wine making, chemical analysis allows reliable predictions to be made about the evolution of the vinification process and enables timely interventions to correct unfavourable chemical or microbiological conditions. Wine is primarily the result of biological processes carried out by yeast and bacteria and, therefore, the success of these interventions and the quality of the final product depend critically on in-depth knowledge of the physiology of these organisms under complex environmental conditions.

Given the powerful analytical capabilities of the modern NMR techniques and their broad range of applications, it is not surprising that NMR has also been used successfully to identify and quantify many components of wine, to

study co-pigmentation phenomena, to detect adulteration and to determine its geographical origin, to detect traces of fluorinated pesticides, and even to investigate the metabolism of wine microbes *in vivo*. In addition to the power of sophisticated modern NMR techniques to determine chemical structures of wine constituents, the great advantage of NMR resides in its unique non-invasive and nondestructive characteristics that permit rapid on-line measurements or analysis involving virtually no sample preparation. Thus far, reports on the application of ultra-high-field NMR spectrometry to study wine samples are still scarce, but technical improvements have now been implemented that allow full exploitation of the immense potential of this analytical technique to examine such a complex biological sample as wine.

2. NMR STUDIES OF WINE CHEMISTRY

2.1. NMR for structure determinations of wine components

The remarkable advances in NMR spectrometers and pulse techniques over the last two decades have made NMR spectroscopy the first choice for structure determination of small molecules. Many wine components have been isolated and characterized by NMR, but phenolic compounds are the class of wine chemicals most often examined. Apart from the great importance that these compounds have in the characteristics of the wine, namely with regard to chemical transformations associated with ageing, recent clinical studies ascribe the benefit of wine to human health to the antioxidant properties of phenolic substances.[4–6] This hypothesis has generated renewed interest into the investigation of these compounds.

Norisoprenoids are important aroma constituents in some *V. vinifera* cultivars. The structures of two monoglucosides and two diglucosides of norisoprenoids isolated from Gewürztraminer wine were established by NMR[7] as well as those of five major glycosides of C_{13}-norisoprenoids isolated from the leaves of *V. vinifera* cv. Riesling.[8] The use of NMR to identify 2-ethyl-3-methylmaleimide *N*-β-D-glucopyranoside, an aroma precursor, from Riesling wine was also reported.[9] Resveratrol monomers have also been isolated and characterized, and their evolution in red wine vinification was monitored.[10] Several stilbene glycosides accumulating in cell cultures of *V. vinifera* were isolated and characterized by 1D and 2D NMR techniques,[11] and NMR was also used to determine the structures and absolute configurations of two C_{13}-norisoprenoid glucosidic precursors of wine flavour.[12]

Anthocyanins constitute the most important group of plant pigments. In wine, they are derived from the grape skin and are responsible for the colour of red wines. They are considered to be safe colour additives in the food industry and this potential application led to considerable research efforts to discover novel and more stable anthocyanins. A major obstacle to their

immediate application is related to the loss of colour in slightly acidic aqueous solutions (pH values higher than 4). NMR has been used extensively to determine the chemical structures of anthocyanins in solution,[13,14] but it is especially useful for studying multiequilibria in solution and characterizing exchange processes among the different species. NMR spectroscopy has been applied to the study of aqueous solutions of malvidin 3,5-diglucoside, one of the major anthocyanins present in wine.[15] In addition to the flavylium cation, two hemiacetal forms and both *cis* and *trans* forms of chalcone were identified and quantified as a function of the solution pH, allowing the calculation of equilibrium constants as well as enthalpy and entropy changes for the interconversion processes. Two-dimensional exchange correlation spectroscopy was crucial for the assignment of the several forms that interconvert in solution. More recently, the same methodology was used to characterize the aggregation processes leading to colour stabilization of the natural anthocyanin malvidin 3-glucoside.[16] The data provide evidence for the occurrence of multimeric aggregates of flavylium cations at very acidic pH and co-pigmentation of flavylium cations with the *trans*-chalcone form at moderately acidic pH, a process that results in desirable colour enhancement.

The distribution of anthocyanins in grape skin has been evaluated and the structures of the malvidin derivatives have been elucidated by Bakker and Timberlake.[17] Recently, the identification of vitisin A, an anthocyanin occurring in some wines, was also reported.[18] The structures of new malvidin-derived wine pigments were recently identified by ^{1}H NMR and mass spectrometry.[19]

Procyanidins, another class of phenolic compounds, consist of polymers of (+)-catechin and (−)-epicatechin units and are responsible for the astringency of young red wines; subsequent chemical conversions involving these polymers are believed to occur during wine ageing, with beneficial consequences for the quality of wine. NMR spectroscopy has proved to be useful in the study of the structure of one of the dimers resulting from (+)-catechin–acetaldehyde condensation.[20]

2.2. NMR for wine analysis

2.2.1. Testing the authenticity of wine

NMR is a powerful technique for determining specific isotopic abundances of several elements, such as H, C, N, O, S. In a particularly relevant application, the fate of specifically labelled carbon atoms throughout metabolism in intact cells is monitored by *in vivo* NMR techniques and valuable information on the nature and contribution of different metabolic pathways can be obtained.[21,22] Thus far, perhaps, the most important application of NMR in the field of wine

takes advantage of the ability of this technique to determine isotopic ratios in major ingredients of wine, namely ethanol, glycerol, water and organic acids. Comparison of isotopic enrichments at specific sites in the molecule with a suitable isotopic database enables the authenticity of a foodstuff to be judged. In this way, information on the botanical species, the climate and the fermentation medium can be drawn from the isotopic composition. The methodology is designated SNIF-NMR[23] (site-specific natural isotopic fractionation–nuclear magnetic resonance) and has been adopted officially by the European Union for the quality control of wine and fruit juices.[24] Various forms of adulteration can be detected, including dilution with water, addition of sugar, mislabelling of provenance or age and undeclared additions of flavours, organic acids and colouring substances.[25] Despite the importance of this practical application, SNIF-NMR will not be covered in detail here since a large number of reviews and detailed papers on the subject are available in the literature. The inventors of the technique, Gérard and Maryvonne Martin, have written an especially useful introduction to the method.[26] The interested reader is referred to the list of recent references provided.[27–35]

2.2.2. *Analysis of natural wine*

Applications using ^1H NMR. One of the main advantages of ^{1}H NMR in the study of wine and other complex mixtures derives from its ability to provide a complete representation of all the proton-containing low-molecular-mass components without requiring separation or the set-up of special experimental conditions for detection of individual compounds. In other words, NMR provides an easy way to detect the unexpected. Very high levels of sensitivity and resolution can be achieved in modern ultra-high-field spectrometers (600, 750, 800 MHz), and a large number of components can be detected routinely and rapidly. Therefore, ^{1}H NMR is most useful for analysis of very large numbers of samples, providing a rapid means to determine sample variability and semi-quantitative information on composition. Obviously, the complexity of the spectra increases as a consequence of improved sensitivity, a situation that demands the implementation of adequate assignment techniques. An important effort has been made in the areas of toxicology, drug metabolism and diagnosis of inborn errors of metabolism to develop strategies for exploring the analytical potential of ^{1}H NMR in the analysis of biological fluids.[36–40] The two-dimensional *J*-resolved technique, when performed at very high field, was found particularly efficient in the identification of small molecules in urine and blood plasma.[41] The application of combined techniques, the so-called hyphenated techniques, such as LC-NMR (liquid chromatography coupled to NMR) or HPLC coupled to NMR and mass spectrometry, proved very useful for the identification of compounds in complex mixtures, but once again the examples in the literature refer largely to urine or blood plasma.[42,44] Only one

example of on-flow LC-NMR of a wine concentrate was found.[45] The doubly phenated method HPLC-NMR-MS,[44] is very powerful for the characterization of components in complex mixtures, combining the high efficiency of HPLC for the resolution of components with the structural information available from the complementary NMR and MS techniques. Optimal results demand the purchase of dedicated LC-NMR commercial probes, but an adaptation of standard probes to LC-NMR was recently reported.[46]

Surprisingly, we could not find similar applications involving high-field ^{1}H NMR for the analysis of wine in the literature, although several reports of ^{1}H NMR for the analysis of fruit juices have appeared in recent years.[47–50] Probably the main reasons for the lack of applications of ^{1}H NMR to wine analysis stem from the high cost of the equipment and the existence of well-established standard analytical methods.[1,2] As expected, the ^{1}H NMR spectrum of a sample of natural wine is dominated by two multiplet resonances at 1.2 and 3.6 ppm due, respectively, to the methyl and methylene protons of ethanol (Fig. 1). The presence of these two strong resonances and respective ^{13}C-satellites, in addition to the water resonance, obliterates a significant frequency range in the spectrum and, for some applications, such as 2D spectroscopy, the use of techniques that permit simultaneous suppression of three resonances is essential. This is easily achieved with modern high-field spectrometers prepared to generate shaped pulses (Fig. 2). However, useful information can still be extracted from a standard 1D spectrum acquired with water presaturation such as that shown in Fig. 3. The spectrum provides a representative picture of the organic components of wine and can be used as a fingerprint, especially useful for the comparison of large numbers of wine samples or for the rapid detection of abnormal constituents. Resonances due to glycerol, succinic and acetic acids, 2,3-butanediol, isobutyl alcohol, proline, methanol and anomeric protons in sugars are easily recognized and can be used to quantify these ingredients. To facilitate resonance assignment, freeze-drying of the wine sample will significantly reduce the complexity of the spectrum (Fig. 4); information on the volatile fraction can still be obtained if the sublimated components are recovered in a cold trap. However, the procedure involves some degree of sample treatment, which may be undesirable when large numbers of samples need to be measured.

It has been shown that NMR spectroscopy of body fluids, such as urine or blood plasma, when combined with computer pattern-recognition approaches, allowed the generation and classification of toxicological or metabolic data that are considered to be valuable in clinical diagnosis.[38–40] Since pattern-recognition strategies for analysis of NMR spectra of complex mixtures have been developed over the last five years, there is no reason not to benefit from the application of similar approaches to the classification of wine samples.

Low-field (hence low-cost) NMR spectroscopy has also found application for the direct and rapid analysis of ethanol in wine and other alcoholic beverages.[51,52] In the low-resolution pulsed NMR technique proposed by

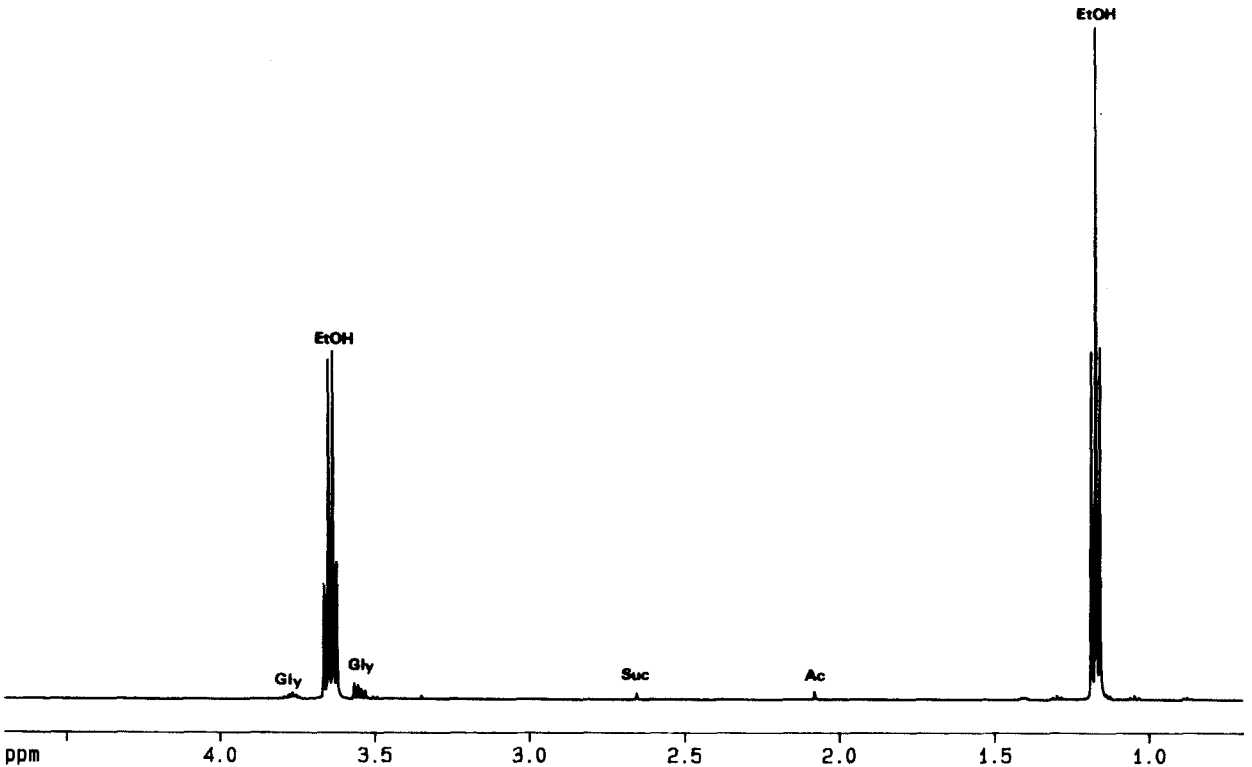

Fig. 1. Proton NMR spectrum of a red table wine. The spectrum was obtained at 500.13 MHz in a Bruker DRX500 spectrometer after a 1.7-fold dilution of wine with ^2H_2O. Spectral width, 5 kHz; data points 16K; acquisition time, 5.6 s; number of transients, 100; presaturation was used to suppress the water resonance. Key to assignments: EtOH, ethanol; Gly, glycerol; Suc, succinic acid; Ac, acetic acid. Chemical shifts are relative to 3-(trimethylsilyl)propanesulfonic acid (sodium salt).

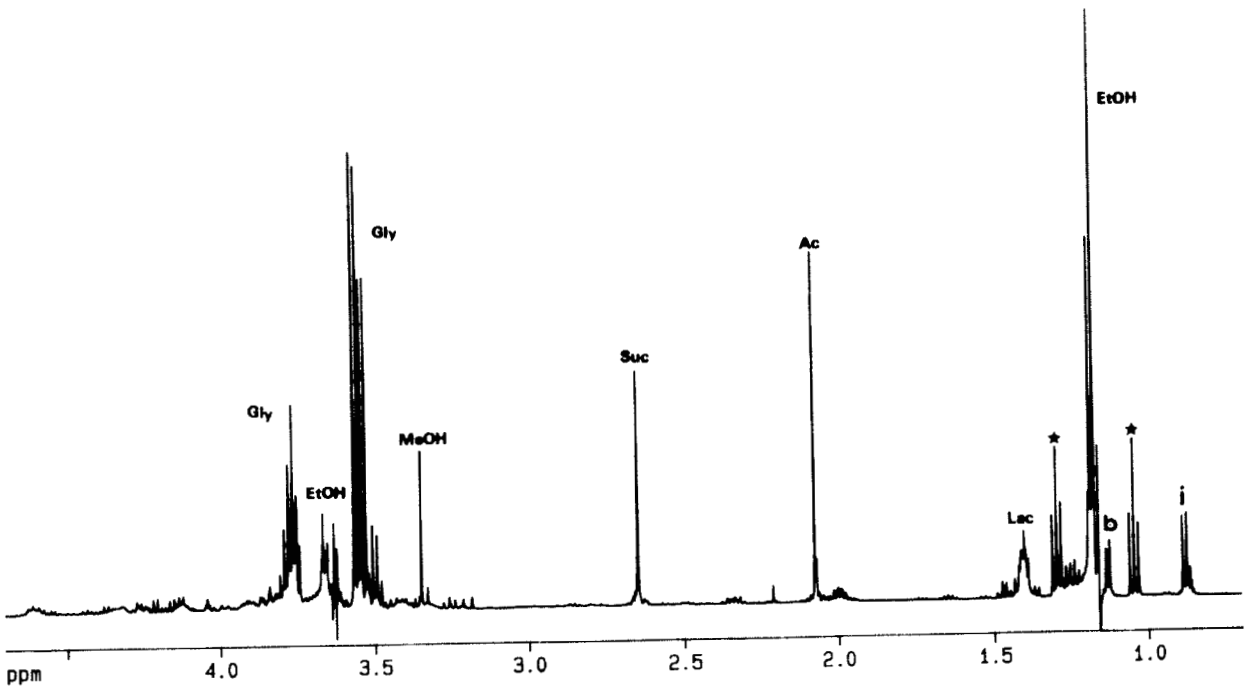

Fig. 2. 500 MHz ^{1}H NMR spectrum of the same wine sample used for Fig. 1. The water resonance was suppressed with a presaturation pulse while both resonances of ethanol were eliminated using a phase-modulated pulse. Key to assignments: EtOH, ethanol; Gly, glycerol; Suc, succinic acid; Ac, acetic acid; MeOH, methanol; Lac, lactic acid; b, 2,3-butanediol; i, isobutanol; ★, ^{13}C-satellite resonances.

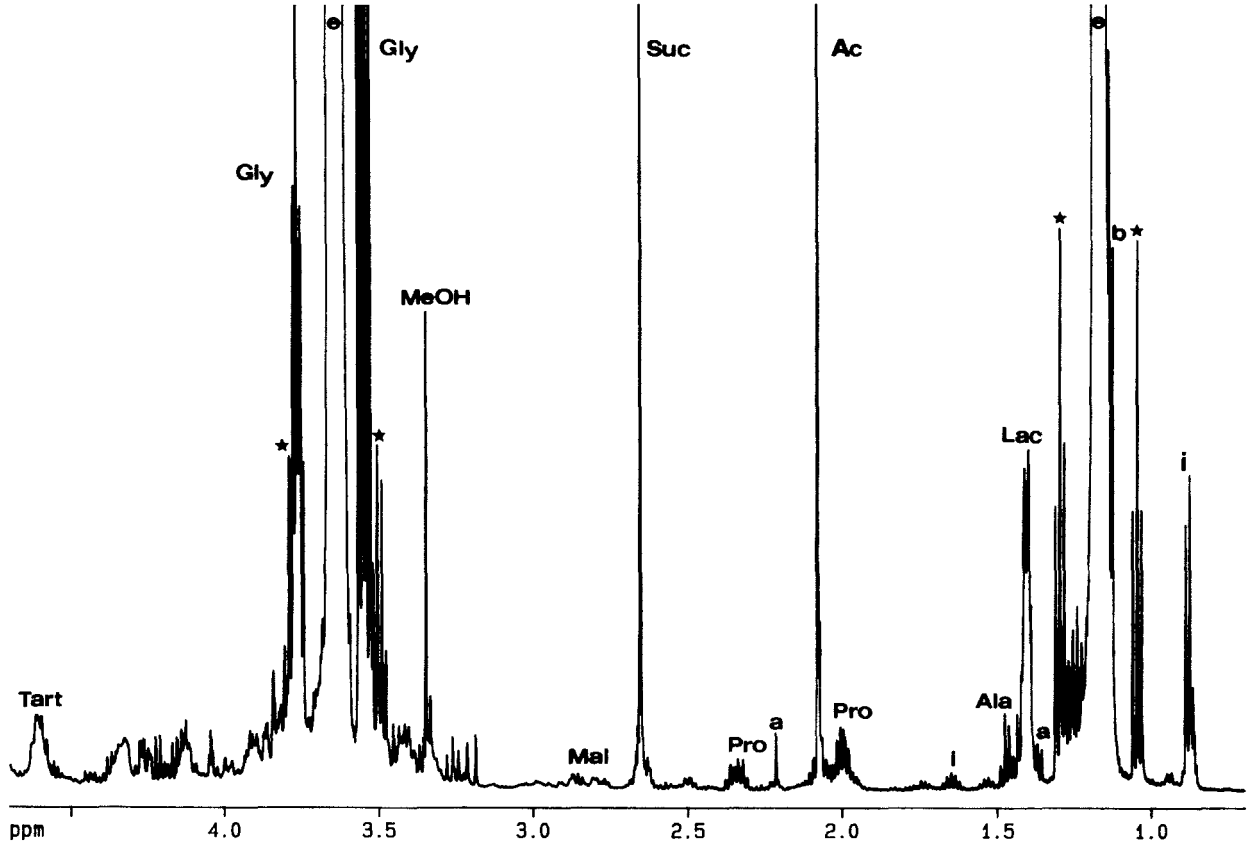

Fig. 3. Same 500 MHz ^{1}H NMR spectrum as in Fig. 1 but plotted with a 120 times higher vertical amplification. Assignment of resonances due to minor components of wine was made by addition of the pure compounds. Key to assignments: EtOH, ethanol; Gly, glycerol; Suc, succinic acid; Ac, acetic acid; MeOH, methanol; Lac, lactic acid; Tart, tartaric acid; Mal, malic acid; Pro, proline; Ala, alanine; a, acetoin; b, 2,3-butanediol; e, ethanol; i, isobutanol; ★, ^{13}C-satellite resonances.

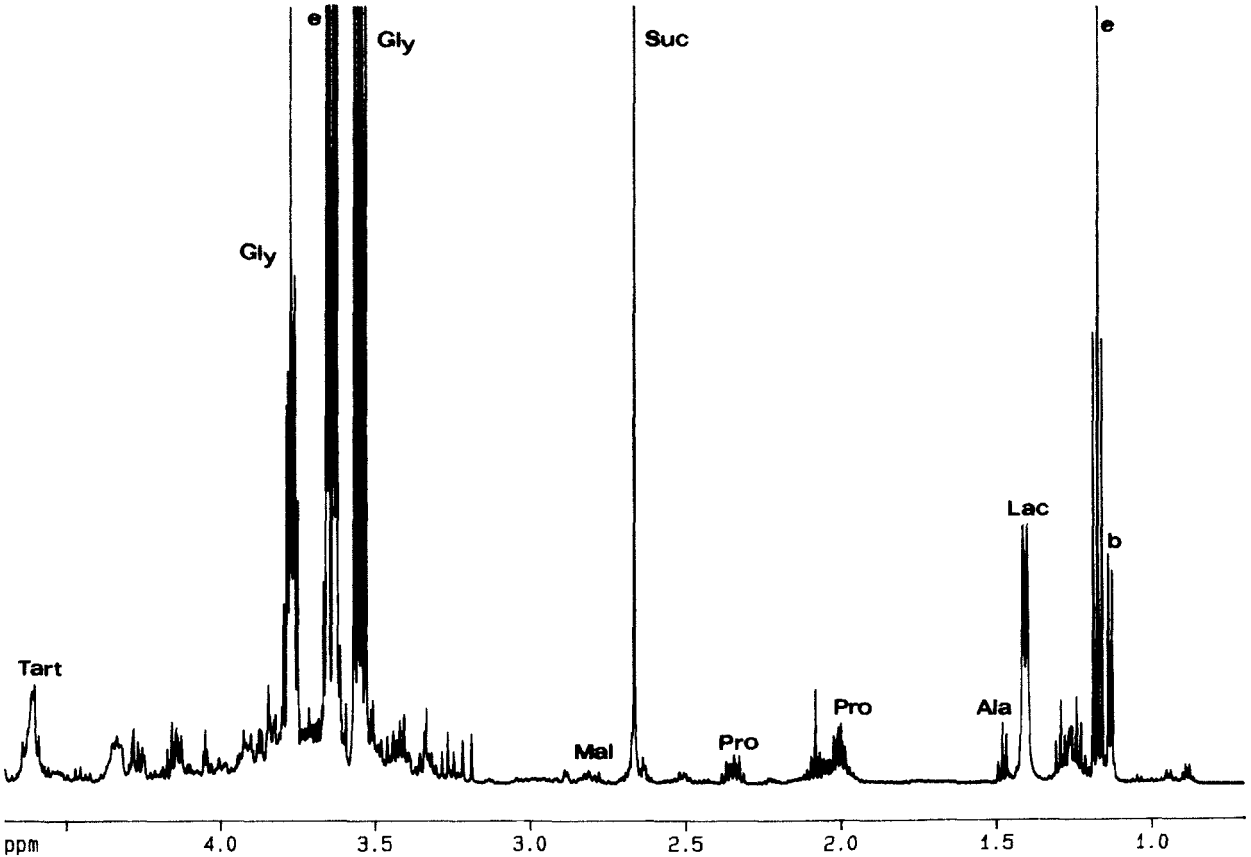

Fig. 4. 500 MHz ^1H NMR spectrum of the same red wine after freeze-drying and re-suspending in ^2H_2O. Key to assignments: Gly, glycerol; Suc, succinic acid; Lac, lactic acid; Tart, tartaric acid; Mal, malic acid; Pro, proline; Ala, alanine; e, ethanol; b, 2,3-butanediol.

Guillou and Tellier,[52] the measurement is based on the linear relationship between the percentage of ethanol and the amplitude of the echo modulation, either in a simple ethanol solution or in a more complex media such as wines and spirits. It is claimed that the accuracy of the method can be as high as 0.2 vol% and that it is suitable for on-line control of industrial fermentation processes.

Applications using heteronuclear NMR. ^{13}C NMR has often been used to analyse major components present in wine or wine extracts. Sugars (glucose, fructose, galactose, arabinose, rhamnose, trehalose, xylose, ribose) as well as alcohols (inositol, mannitol) and sugar acids (galacturonic, glucuronic and gluconic acids) can be quantified in a single run.[53] Amino acids (alanine, glycine, proline, glutamic, glutamine, methionine, aminobutyric acid, leucine, threonine and others) could also be identified and quantified by the same method in wine extracts obtained by vacuum distillation of wine.[54] A procedure to determine adulterations with diethylene glycol[55] or methanol[56] in natural wine was also described; the detection limit for diethylene glycol achieved with a 500 MHz spectrometer was 10 mg l^{-1}.[55] An interesting example of the application of solid-state ^{13}C NMR to investigation of the nature of undesirable insoluble deposits adhering to the inner glass surface of bottles of red wine has been reported by Waters and co-workers.[57] The deposits were found to be composed of a phenolic polymer of anthocyanins, procyanidins and proteins, and are believed to result from extensive cross-linking between the phenolic polymer and proteins.

^{11}B NMR has been used to determine boric acid esters in wine.[58,59] Boron was found in at least three different molecular species that occur in highly variable proportions.

Finally, the high sensitivity of fluorine was explored for the screening and analysis of fluorinated pesticides in food products.[60] Using a 5 mm diameter probe-head with a 400 MHz spectrometer it was possible to measure fluorine-containing compounds directly in wine with a detection limit of 1.0 mg l^{-1}.

3. NMR STUDIES OF WINE BACTERIA

3.1. Introducing malolactic fermentation

In natural wine fermentations, after a lag phase following the alcoholic fermentation by yeast, the residual lactic acid bacteria begin multiplication and perform a malolactic fermentation in which L-malic acid is decarboxylated to L-lactic acid and carbon dioxide. *Oenococcus oeni*, formerly *Leuconostoc oenos*[61] is the main species responsible for this process, since it is well adapted to the adverse conditions in wine after alcoholic fermentation, i.e. low pH (3–3.5) and high ethanol concentration.[62] Malolactic fermenta-

tion (MLF) results in deacidification and the consequent smoothing of the wine, with improvement in its microbiological stability owing to the utilization of potential nutrients that would otherwise be available for spoilage microorganisms. Furthermore, it contributes significantly to the organoleptic properties of wine, since the flavour changes associated with MLF are in general beneficial.[62,63]

The usage of bacterial starter cultures to initiate malolactic fermentation in wines is becoming widespread[64] and *O. oeni* is often the first-choice organism for the preparation of commercial starters.

In addition to malic acid, *O. oeni* metabolizes carbohydrates (hexoses and pentoses), organic acids (e.g. citric, tartaric and pyruvic acids), and amino acids. These substrates can be converted to a wide range of products, such as lactic acid, ethanol, acetic acid, mannitol (and other polyols), acetaldehyde, acetoin, diacetyl and 2,3-butanediol, in addition to other minor fermentation products.[63] The simultaneous utilization of citric acid (or pyruvic acid) and carbohydrates leads to the production of acetoin, 2,3-butanediol and diacetyl, important aroma components. Diacetyl is a butter-flavoured compound that has an extremely low aroma threshold. The amounts of diacetyl produced by malolactic bacteria (1–5 mg l^{-1}) are generally low enough to be beneficial to the sensorial properties of wine; however, in white wine production, even lower amounts of diacetyl may be detrimental.[65,66] Given the aforementioned diversity of fermentation end-products and their impact on the final quality of wine, a detailed knowledge of the regulatory mechanisms of the metabolic pathways in *O. oeni* is essential for the development of successful starter cultures that will permit the true control of wine production.

Despite numerous studies on the ecological and physiological behaviour of wine bacteria (for reviews see references 64 and 66), the biochemistry and regulation of the central metabolic pathways in *O. oeni* remained largely obscure until recently. In the past few years, *in vivo* and *in vitro* NMR spectroscopy was applied with success to the elucidation of several metabolic traits of *O. oeni*, namely the biosynthetic pathway for diacetyl production, the metabolism of carbohydrates and organic acids, and the effect of carbohydrate metabolism on the malolactic fermentation. An overview on NMR studies of wine bacteria is provided here, focusing on results that can be valuable for improving and modulating the characteristics of wine.

3.2. Biosynthetic pathway of diacetyl

The metabolic pathway leading to the synthesis of C_4 compounds (diacetyl, acetoin and 2,3-butanediol) in bacteria was a matter of controversy in the past. It had been suggested that diacetyl was synthesized from the condensation of one molecule of hydroxyethylthiamine pyrophosphate (PPi), derived from pyruvate, and one molecule of acetyl-Coenzyme A, in a reaction catalysed by

the enzyme diacetyl synthase.[67] ^{13}C NMR was used to elucidate the biosynthesis of diacetyl in the dairy bacterium *Lactococcus lactis*,[68,69] and contrary to that proposal, it was found that the intermediate metabolite in the synthesis of diacetyl is α-acetolactate. This unstable compound is formed by the condensation of one molecule of pyruvate with one molecule of hydroxyethylthiamine-PPi. A similar pathway was also found in *O. oeni* using ^{13}C NMR and labelling experiments.[70] The pathway involving condensation of acetyl-CoA with hydroxyethylthiamine-PPi would lead to labelling in the CH_3 and CO groups of diacetyl as well as in the CH_3 group and the CO or CH group of acetoin or 2,3-butanediol, respectively. However, no acetoin, diacetyl or 2,3-butanediol labelled on the methyl group was detected, and the label from acetyl-CoA was found only in the methyl group of acetic acid (Fig. 5). The C_4 compounds formed were acetoin labelled in CO and in the CHOH groups and diacetyl enriched on both CO groups. The labelling pattern on these metabolites is in agreement with a pathway involving the formation of α-acetolactate as intermediate (Fig. 6).

In vivo NMR experiments with cell suspensions of *O. oeni* also allowed the direct detection and quantification of the unstable compound diacetyl, showing that it is synthesized at physiological pH values, probably by chemical oxidative decarboxylation of α-acetolactate, provided oxygen is supplied.[70] In wine, under typical conditions of low oxygen tension, it is unlikely that high amounts of diacetyl are formed.[64] Thus, the presence of diacetyl in products resulting from anaerobic fermentations is most likely due to decarboxylation of the unstable intermediate α-acetolactate during manipulation processes following fermentation and/or decomposition of that compound during the conventional analytical procedures used in the determination of diacetyl.

3.3. Carbohydrate metabolism

3.3.1. Pathways of carbohydrate utilization

The metabolism of glucose in heterolactic lactic acid bacteria (LAB), such as *O. oeni*, is generally described as a fermentation initiated by the oxidation of glucose 6-phosphate to 6-phosphogluconate followed by decarboxylation and splitting of the resulting pentose 5-phosphate into acetyl phosphate and glyceraldehyde 3-phosphate. The latter is converted to pyruvate through a sequence of reactions of the Embden–Meyerhof–Parnas pathway, giving lactic acid as end-product, while acetyl phosphate is converted to ethanol through reactions catalysed by dehydrogenases where the reduced co-enzymes formed in the initial steps of glucose catabolism are re-oxidized. Consequently, equimolar amounts of CO_2, lactic acid and ethanol are expected from the heterofermentative metabolism of glucose.[71]

The pathway of glucose catabolism has been studied by ^{13}C NMR in

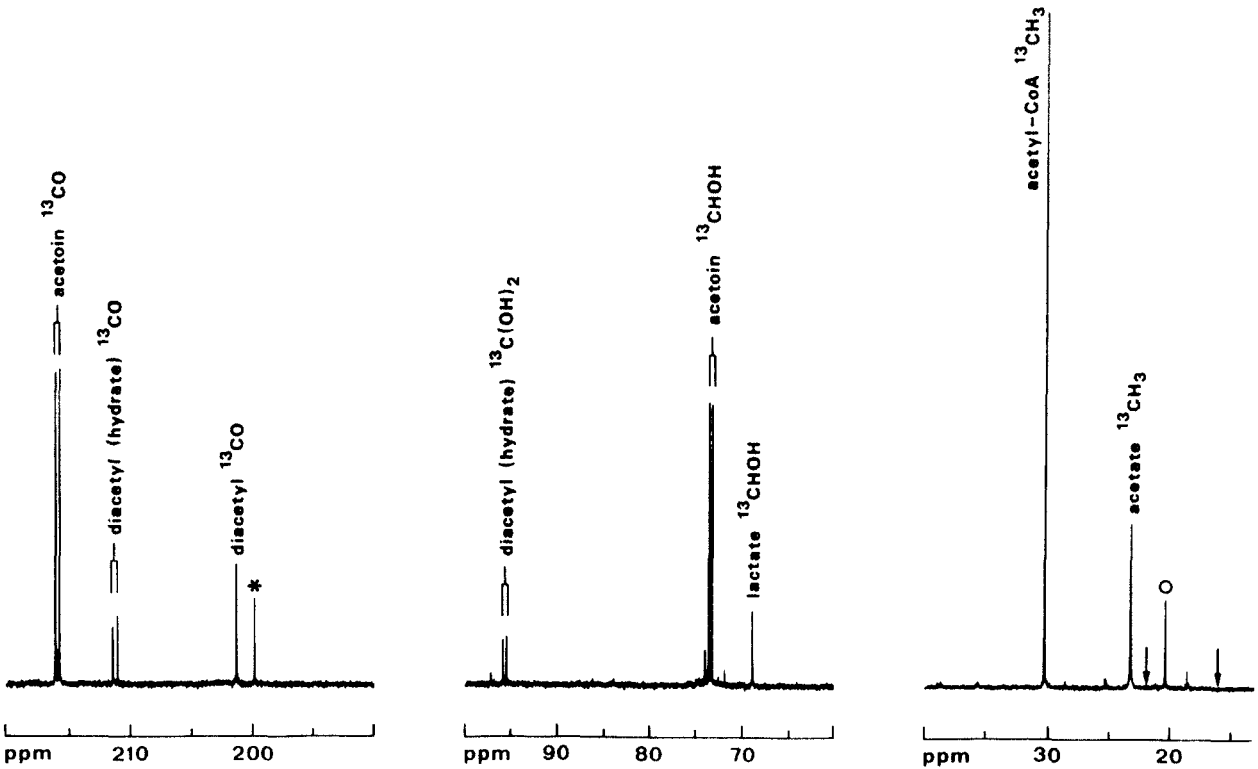

Fig. 5. ^{13}C NMR spectrum of a supernatant solution obtained after the co-metabolism of [2-^{13}C]pyruvate and [2-^{13}C]acetyl-CoA by permeabilized cells of *O. oeni*. The spectrum was obtained at 125.77 MHz using a Bruker AMX500 spectrometer, with the following acquisition parameters: spectral width, 38 kHz; data points, 32K; repetition delay, 21 s; number of transients, 2000. The arrows at higher field indicate the positions expected for the resonances of diacetyl, acetoin and 2,3-butanediol labelled on the methyl groups. Symbols: O, *N*-acetyl-CoA, impurity in the preparation of acetyl-CoA; *, unassigned resonance. (Reproduced from reference 70 with permission.)

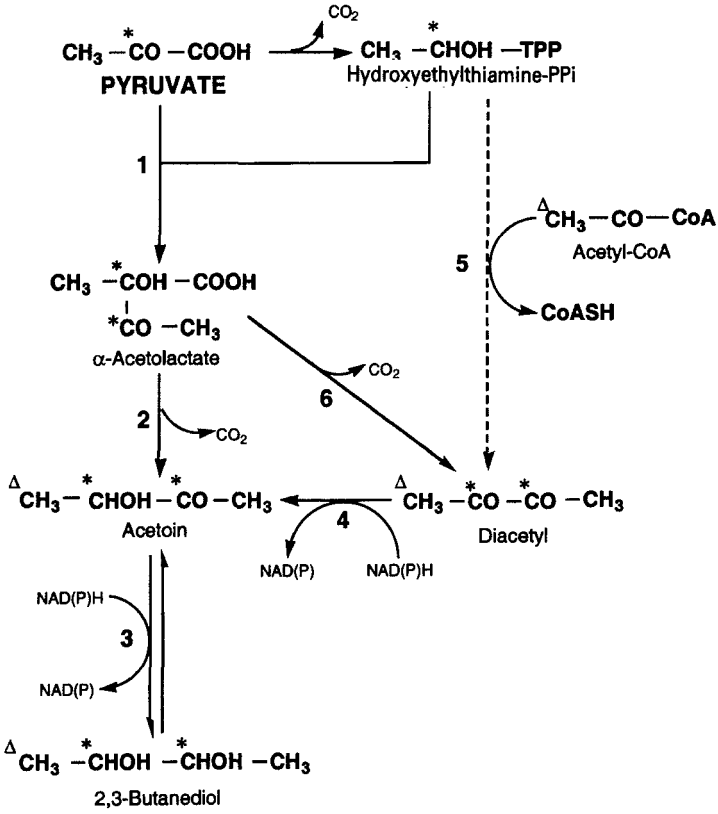

Fig. 6. Proposed pathways for acetoin, diacetyl and 2,3-butanediol production. The labelling patterns on the intermediates and end-products derived from [2-^{13}C]pyruvate (*) and [2-^{13}C]acetyl-CoA (Δ) are shown. Reaction numbers are as follows: 1, α-acetolactate synthase; 2, α-acetolactate decarboxylase; 3, acetoin reductase; 4, diacetyl reductase; 5, diacetyl synthase; 6, chemical oxidative decarboxylation of α-acetolactate.

non-growing cells of *O. oeni* strain GM, a commercially available bacterial starter culture used to initiate malolactic fermentation. The observations that the ^{13}C label supplied in the position 1 of glucose was not totally lost as $^{13}CO_2$, as would be expected from a typical heterolactic fermentation, and that acetate and ethanol labelled in the methyl groups were produced under these conditions, triggered further effort to elucidate the catabolism of glucose. If glucose is metabolized exclusively by the heterofermentative pathway described above, the enriched carbon from [2-^{13}C]glucose should be recovered in the methyl groups of ethanol and/or acetate. However, the label supplied in position 2 of glucose is also recovered in the COOH group of acetate and in the CH_2OH group of ethanol. From glucose labelled in position 6, erythritol

and glycerol labelled in the CH_2OH groups were formed, in addition to lactic acid labelled in the methyl group. The proton NMR spectrum of the supernatant solution from the experiment in which [2-^{13}C]glucose was supplied is shown in Fig. 7. The singlet at 1.9 ppm was assigned to the methyl protons of unlabelled acetate; $^{13}CH_3COOH$ gives rise to a doublet centred at the same position, whereas $CH_3{}^{13}COOH$ gives a doublet with a smaller coupling constant. The integration of the areas of the two doublet resonances led to the conclusion that approximately 75% of the glucose supplied was metabolized through the conventional phosphoketolase pathway; and that the remaining 25% was channelled to an alternative pathway that produced erythritol and glycerol as the main end-products. The non-labelled acetate, accounting for ~50% of the total acetate produced was derived from the metabolism of endogenous reserve compounds.[72] The biosynthesis of erythritol results from the reduction and subsequent dephosphorylation of erythrose 4-phosphate, itself resulting from splitting of the intermediate fructose 6-phosphate.[73]

The production of glycerol by *O. oeni* was previously reported,[74] and proceeds via a similar route to that occurring in yeast: glycerol is synthesized by the reduction of glyceraldehyde 3-phosphate to glycerol 3-phosphate, followed by dephosphorylation of the glycerol 3-phosphate to glycerol, with concomitant oxidation of NAD(P)H. Erythritol and glycerol were also produced by growing cells of *O. oeni* under anaerobic conditions,[72] and it is noteworthy that the amount of erythritol produced by growing cells of *O. oeni* (230 mg l^{-1} after 25 days of incubation) agrees well with the range of concentrations of this sweetener reported for table wines (90–700 mg l^{-1}). NMR data also revealed that the anaerobic metabolism of fructose by resting cells of *O. oeni* produced mannitol as the main end-product, in addition to acetic and lactic acids and small amounts of ethanol, while aerobically acetic acid was the main end-product. Lactic and acetic acids were the only two end-products formed from the anaerobic metabolism of ribose, whereas under aerobic conditions most of the lactic acid formed was replaced by acetic acid.[72]

3.3.2. Glucose/malic acid co-metabolism

Carbohydrate/malic acid co-metabolism by wine bacteria is largely dependent on the organism and on culture conditions, such as pH. As discussed by Henick-Kling,[64] some authors observed that the presence of malic acid had a clear effect on the pattern of end-products from carbohydrate metabolism, whereas others found the opposite. Despite these discrepancies, the relationships between the metabolism of carbohydrates and malic acid are generally described as follows. At low pH, malic acid is utilized at a high rate whereas carbohydrates are not utilized or their metabolism proceeds very slowly. The malolactic fermentation leads to an increase of the pH of the medium, allowing subsequent carbohydrate catabolism, thereby explaining the observed malic

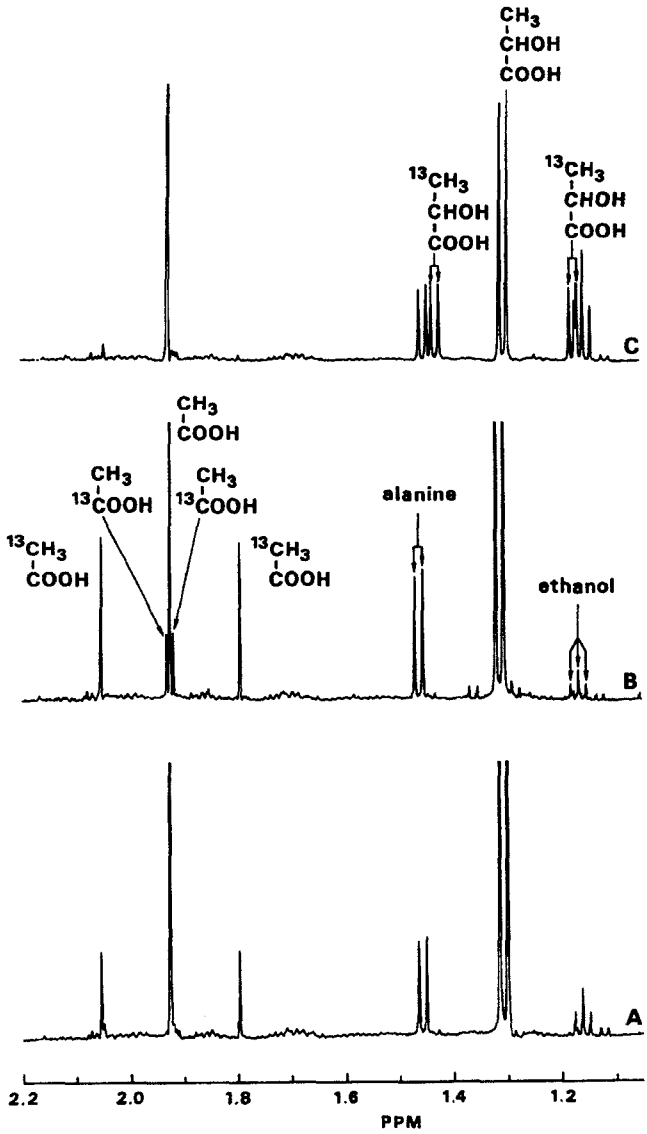

Fig. 7. ^{1}H NMR spectra of the products formed from the anaerobic metabolism of [1-^{13}C]glucose (A), [2-^{13}C]glucose (B), and [6-^{13}C]glucose (C) by non-growing cells of *O. oeni*. Once all the glucose had been used, the cell suspension was centrifuged and the supernatant was analysed by ^{1}H NMR at 500.13 MHz with H_2O presaturation and a repetition time of 9.5 s. The resonances due to the different isotopomers of acetate and lactate are highlighted.

acid-induced stimulation of growth.[75–77] When carbohydrates and malic acid are co-metabolized, the pattern of product formation is generally in agreement with the stoichiometry of both the malolactic reaction and the heterolactic fermentation of glucose.[78] However, in some strains of *O. oeni*, a severe sugar-induced inhibition of malolactic fermentation was observed. Miranda and co-authors[79] showed that the addition of glucose (or other carbohydrates such as galactose, trehalose, maltose and mannose) to whole cells caused an inhibition of malolactic fermentation up to 70%. The rate of malolactic fermentation was evaluated both by classical manometric techniques that measure the amount of carbon dioxide formed, and by *in vivo* ^{1}H NMR spectroscopy (Fig. 8). In experiments where multiple substrates are involved, manometric techniques are not satisfactory, since CO_2 is also produced from the metabolism of substrates other than malic acid (e.g., glucose, fructose, citric acid). The advantage of *in vivo* NMR is reinforced in experiments designed to study the effect of the gas phase on metabolism, because the gas phase in the NMR tube can easily be changed by bubbling the suitable gas using an air-lift system without disturbing signal acquisition.[80] The combination of several analytical techniques, which included *in vivo* ^{1}H NMR and *in vitro* ^{31}P NMR allowed the determination of the biochemical basis for the carbohydrate-induced inhibition of malolactic fermentation. This effect is caused by a direct inhibition of NADH, which accumulates during glucose metabolism, on the malolactic enzyme.[79] In addition to the fundamental interest underlying the elucidation of sugar-induced malolactic fermentation, these results are obviously relevant to the control of the vinification process.

3.4. Studies of citric acid metabolism

3.4.1. Pathway of citrate utilization

In citric acid-utilizing LAB, the first cytoplasmatic reaction of citrate metabolism is its cleavage to oxaloacetate and acetate by citrate lyase, followed by the decarboxylation of oxaloacetate to pyruvate (catalysed by oxaloacetate decarboxylase). The reactions described above determine the production of pyruvate from citrate, being the most common pathway of citric acid conversion.[81] This pathway was also detected in *O. oeni*, by ^{13}C NMR experiments in which citric acid labelled in positions 2 and 4 is supplied to cell suspensions. Citric acid is converted to acetate and oxaloacetate; the former is excreted from the cell, whereas the latter is decarboxylated, yielding pyruvate and carbon dioxide. Pyruvate is then metabolized, giving rise to a mixture of end-products, in proportions that depend on the culture conditions. A key role in the regulation of the metabolism of citric and pyruvic acids in wine bacteria is played by pH.[82,83] At low pH, acetoin is the main end-product of pyruvic acid metabolism, whereas at high pH (above pH 6.0), an equimolar

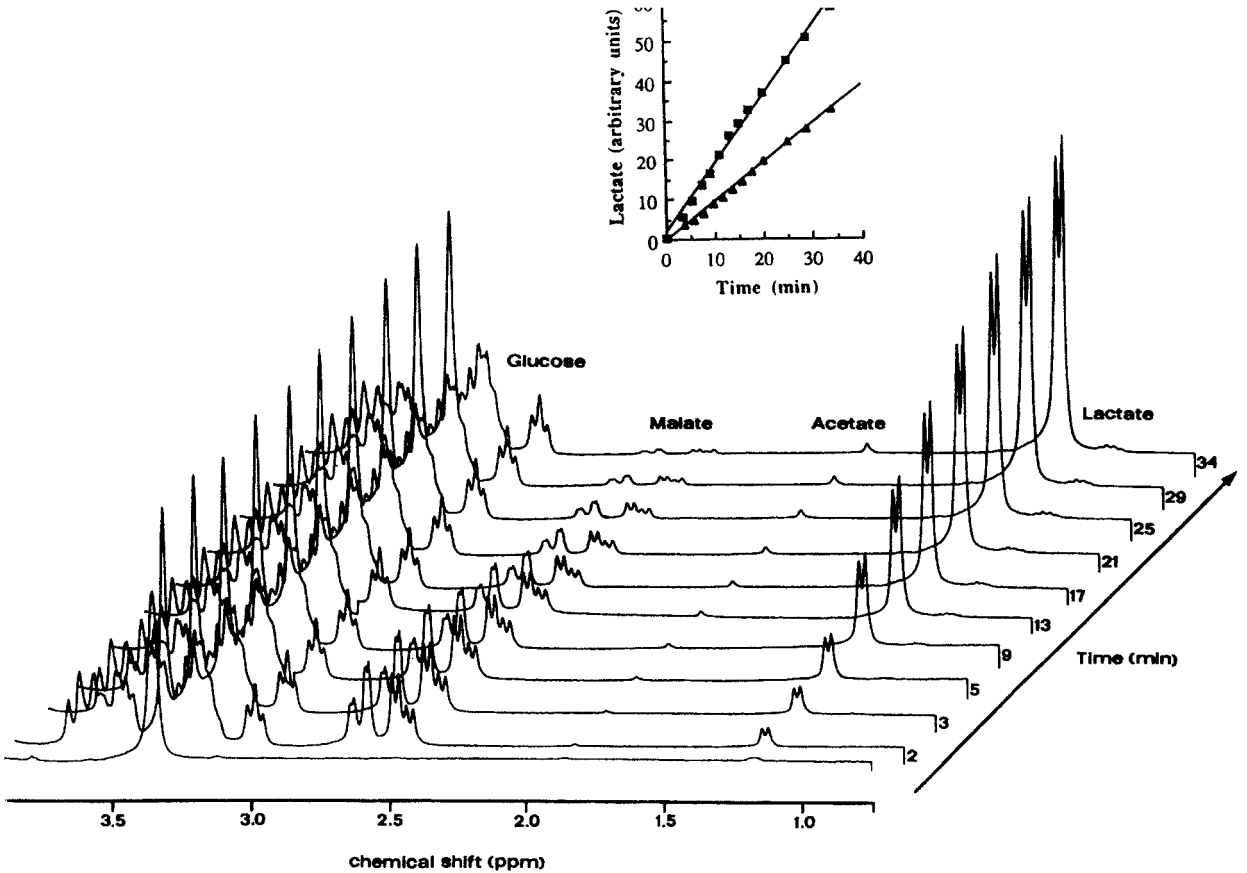

Fig. 8. Time course for the consumption of malate plus glucose by a cell suspension of *O. oeni* under anaerobic conditions monitored by *in vivo* ^{1}H NMR at 300.13 MHz. The experiments were performed in 0.1 mol l^{-1} glycine buffer (pH 3.5) supplemented with 45 mmol l^{-1} L-malic acid and 45 mmol l^{-1} glucose at 30°C. The inset shows a plot of the intensity of the resonance due to the methyl group of lactate as a function of time both in the presence (△) and in the absence (■) of glucose. (Reproduced from reference 79 with permission.)

mixture of lactic and acetic acids is produced from pyruvate. This pH-induced metabolic shift is caused by changes in the activity of enzymes involved in the breakdown of pyruvate, since the acetoin-forming enzymes have low pH optima.[70]

In non-growing cell suspensions of *O. oeni*, a significant amount of the citric acid supplied (10%) is channelled to the biosynthesis of aspartate. The intracellular accumulation of aspartate was confirmed in a ^{1}H–^{13}C correlation heteronuclear multiple quantum coherence (HMQC) spectrum of a cell extract obtained after the metabolism of citric acid, where it was evident that aspartate derived from citrate was the major intracellular metabolite.[70] This surprising result is in agreement with the observation that aspartate is no longer an essential amino acid for the growth of *O. oeni* provided that citrate is added to the medium.[84]

3.4.2. Citric acid/carbohydrate co-metabolism

The interactions between the metabolism of citrate and carbohydrates have been studied extensively in dairy bacteria.[85–87] These studies report growth stimulation, and alterations of substrate uptake rates and of the proportions of end-products caused by the additional presence of citrate. In homofermentative LAB, at least 80% of citrate and glucose is converted to lactate during the co-metabolism of citrate and glucose, as evaluated by ^{13}C NMR experiments where specifically enriched carbon-13 glucose and citric acid were supplied simultaneously.[69] These experiments allowed the origin of the carbon atoms in the end-products derived from both citric acid and glucose to be determined; a strong interrelationship between the catabolism of glucose and citric acid was found. Carbon from citrate was channelled towards the production of 2,3-butanediol and lactic acid,[88] whereas acetoin was the main end-product of citric acid metabolism alone.[70] On the other hand, citric acid induced a shift in the end-products of glucose metabolism; acetic acid accounted for 60% of the products derived from glucose,[88] whereas in the absence of citric acid the contribution of acetic acid is at most 38% and ethanol, glycerol and erythritol represent approximately 60% of the products derived from glucose.[72]

The accumulation of phosphorylated metabolites under different metabolic conditions, e.g. during metabolism of glucose alone and during co-metabolism of citric acid plus glucose, was evaluated by ^{31}P NMR in perchloric acid extracts. The intracellular concentration of glucose 6-phosphate decreased by a factor of 10 when citric acid was co-metabolized with glucose.[88] NMR data have shown that the metabolism of citric acid confers additional pathways for re-oxidation of NAD(P)H; under these conditions the metabolic flux from pyruvate is directed towards the production of 2,3-butanediol and lactic acid. This allows diversion of sugar carbon to reactions where ATP is synthesized, with consequent formation of acetic acid instead of ethanol. Formation of

additional ATP by substrate-level phosphorylation has important consequences for the survival and competitiveness of *O. oeni* in wine.

4. CONCLUDING REMARKS

NMR spectroscopy is a powerful technique not only for the characterization of wine components and detection of adulteration, but also for the elucidation of key metabolic traits of wine bacteria. The results show the decisive role of oxygen in the overall regulation of the metabolism of wine bacteria and consequently on the nature and proportions of end-products that contribute to the quality of wine. For instance, the production of the sweetener erythritol is strongly inhibited when oxygen is available, while glycerol is produced. On the other hand, the presence of oxygen is essential for the formation of the aroma compound diacetyl. Malolactic fermentation is inhibited by glucose, but this can be circumvented by the addition of citric acid. Furthermore, the final concentration of the aroma compound 2,3-butanediol is increased when both citric acid and glucose are provided as nutrients for malolactic bacteria. The nondestructive nature of NMR is one of its most attractive features, enabling the direct analysis of wine samples as well as studies of wine bacteria *in vivo*. We believe that the immense potential of this technique will be efficiently exploited in the near future to the benefit of wine quality.

ACKNOWLEDGEMENTS

We thank Dr A. Maretzek for technical assistance. Financial support from Fundação para a Ciência e Tecnologia, Project PRAXIS/PCNA/P/BIO/39/96 is acknowledged.

REFERENCES

1. H. F. Linskens and J. F. Jackson (eds), *Wine Analysis*, Modern Methods of Plant Analysis, New Series Vol. 6, Springer-Verlag, Berlin, 1988.
2. A. S. Curvelo-Garcia, *Controlo de Qualidade dos Vinhos: Química Enológica Métodos Analíticos*, Instituto do Vinho e da Vinha, Lisbon, 1988.
3. P. Lehtonen, *Am. J. Enol. Vitic.*, 1996, **47**, 127.
4. P. Marques-Vidal, P. Ducimetiere, A. Evans, J. P. Cambou and D. Arveiler, *Am. J. Epidemiol.*, 1996, **143**, 1089.
5. R. Abu-Amsha, K. D. Croft, J. M. Puddey, J. M. Proudfoot and L. J. Beilin, *Clin. Sci. (Colch.)*, 1996, **91**, 449.
6. B. D. Gehm, J. M. McAndrews, P. Y. Chien and J. L. Jameson, *Proc. Natl. Acad. Sci. USA*, 1997, **94**, 14138.
7. R. Baltenweck-Guyot, J.-M. Trendel, P. Albrecht and A. Schaeffer, *Phytochemistry*, 1996, **43**, 621.

8. G. K. Skouroumounis and P. Winterhalter, *J. Agric. Food Chem.*, 1994, **42**, 1068.
9. B. Baderschneider, M. Messerer and P. Winterhalter, *Vitis*, 1997, **36**, 159.
10. F. Mattivi, F. Reniero and S. Korhammer, *J. Agric. Food Chem.*, 1995, **43**, 1820.
11. P. W. Teguo, A. Decendit, S. Krisa, G. Deffieux, J. Vercauteren and J.-M. Mérillon, *J. Nat. Prod.*, 1996, **59**, 1189.
12. R. L. Baumes, C. C. Aubert, Z. Y. Günata, W. de Moor and C. L. Bayonove, *J. Essent. Oil Res.*, 1994, **6**, 587.
13. D. Strack and V. Wray, in *Methods in Plant Biochemistry*, Vol. 1, Plant Phenolics: Anthocyanins (ed. J. B. Harborne), p. 325, Academic Press, London, 1989.
14. T. Goto and T. Kondo, *Angew. Chem.*, 1991, **103**, 17.
15. H. Santos, D. L. Turner, J. C. Lima, P. Figueiredo, F. S. Pina and A. L. Maçanita, *Phytochemistry*, 1993, **33**, 1227.
16. C. Houbiers, J. C. Lima, A. L. Maçanita and H. Santos, *J. Phys. Chem.*, 1998, **102**, 3578.
17. J. Bakker and C. F. Timberlake, *J. Sci. Food Agric.*, 1985, **36**, 1315.
18. J. Bakker and C. F. Timberlake, *J. Agric. Food Chem.*, 1997, **45**, 35.
19. H. Fulcrand, P. Cameira dos Santos, P. Sarni-Manchado, V. Cheynier and J. Favre-Bonvin, *J. Chem. Soc., Perkin Trans.*, 1996, **1**, 735.
20. B. Saucier, C. Guerra, I. Pianet, M. Laguerres and Y. Glories, *Phytochemistry*, 1997, **46**, 229.
21. H. Pereira, P. C. Lemos, M. A. M. Reis, J. P. S. G. Crespo, M. J. T. Carrondo and H. Santos, *Water Res.*, 1996, **30**, 2128.
22. R. E. London, *Prog. NMR Spectrosc.*, 1988, **20**, 337.
23. G. J. Martin, M. L. Martin, F. Mabon and M. J. Michon, *J. Agric. Food Chem.*, 1983, **31**, 311.
24. EC Directive 2676/90, September 17, 1990.
25. G. G. Martin, in *Magnetic Resonance in Food Science* (ed. P. S. Belton, I. Delgadillo, A. M. Gil and G. A. Webb), p. 120, Royal Society of Chemistry, London, 1995.
26. G. J. Martin and M. L. Martin, in *Wine Analysis*, Modern Methods of Plant Analysis, New Series Vol. 6 (ed. H. F. Linskens and J. F. Jackson), p. 258, Springer-Verlag, Berlin, 1988.
27. G. J. Martin and M. L. Martin, *Annu. Rep. NMR Spectrosc.*, 1995, **31**, 81.
28. M. P. Day, B. L. Zhang and G. J. Martin, *J. Sci. Food Agric.*, 1995, **67**, 113.
29. G. G. Martin, Y. L. Martin, N. Naulet and H. J. D. Mcmanus, *J. Agric. Food Chem.*, 1996, **44**, 3206.
30. G. G. Martin, R. Wood and G. J. Martin, *J. Assoc. Oft. Anal. Chem. Int.*, 1996, **79**, 917.
31. D. Weber, A. Roßssman, S. Schwarz and H. L. Schmidt, *Z. Lebensm. Unters. Forsch.*, 1997, **205**, 158.
32. B. L. Yunianta, C. Zhang, G. J. Martin, C. Asselin and M. Schaeffer, *J. Int. Sci. Vigne Vin*, 1995, **29**, 89.
33. B. Holbach, H. Forstel, H. Otteneder and H. Hutzen, *Z. Lebensm. Unters. Forsch.*, 1994, **198**, 223.
34. A. Robmann and H.-L. Schmidt, *Z. Lebensm. Unters. Forsch.*, 1989, **188**, 434.
35. I. J. Colquhoun and M. Lees, in *Nuclear Magnetic Resonance Spectroscopy, Analytical Methods of Food Authentication* (ed. P. R. Ashurst and M. J. Dennis), p. 36, Blackie Academic and Professional, Glasgow, 1997.
36. J. K. Nicholson, P. J. Foxall, M. Spraul, R. D. Farrant and J. C. Lindon, *Anal. Chem.*, 1995, **67**, 793.
37. S. Maschke, N. Azaroual, J. M. Wieruszeski, G. Lippens, M. Imbenotte, D. Mathieu, G. Vermeersch and M. Lhermitte, *NMR Biomed.*, 1997, **10**, 277.
38. E. Holmes, P. J. Foxall, J. K. Nicholson, G. H. Neild, S. M. Brown, C. R. Beddel, B. C. Sweatman, E. Rahr, J. C. Lindon and M. Spraul, *Anal. Biochem.*, 1994, **220**, 284.
39. M. L. Anthony, V. S. Rose, J. K. Nicholson and J. C. Lindon, *J. Pharm. Biomed. Anal.* 1995, **13**, 205.
40. E. Holmes, P. J. Foxall, M. Spraul, R. D. Farrant, J. K. Nicholson and J. C. Lindon, *J. Pharm. Biomed. Anal.*, 1997, **15**, 1647.

41. P. J. D. Foxall, M. Spraul, R. D. Farrant, L. C. Lindon, G. H. Neild and J. K. Nicholson, *J. Pharm. Biomed. Anal.*, 1993, **11**, 267.
42. J. C. Lindon, J. K. Nicholson, U. G. Sidelmann and I. D. Wilson, *Drug Metab. Rev.*, 1997, **29**, 705.
43. J. C. Lindon, J. K. Nicholson and J. D. Wilson, *Adv. Chromatogr.*, 1996, **36**, 315.
44. J. P. Shockcor, S. E. Unger, I. D. Wilson, P. J. Foxall, J. K. Nicholson and J. C. Lindon, *Anal. Chem.*, 1996, **68**, 4431.
45. M. Spraul and M. Hofmann, in *Magnetic Resonance in Food Science* (ed. P. S. Belton, I. Delgadillo, A. M. Gil and G. A. Webb), p. 77, Royal Society of Chemistry, London, 1995.
46. H. Barjat, G. A. Morris, M. J. Newman and A. G. Swanson, *J. Magn. Reson., Ser. A*, 1996, **119**, 115.
47. J. T. W. E. Vogels, L. Terwel, A. C. Tas, F. Vandenberg, F. Dukel and F. Vandergreef, *J. Agric. Food Chem.*, 1996, **44**, 175.
48. P. S. Belton, I. Delgadillo, E. Holmes, A. Nicholls, J. K. Nicholson and M. Spraul, *J. Agric. Food Chem.*, 1996, **44**, 1483.
49. S. Belton, I. Delgadillo, A. M. Gil, P. Roma, F. Casuscelli, I. J. Colquhoun, M. J. Dennis and M. Spraul, *Magn. Reson. Chem.*, 1997, **35**, S52.
50. I. J. Colquhoun, *Spectrosc. Eur.*, 1998, **10**, 8.
51. U. Anders, F. Tittgemeier and G. Hailer, *Z. Lebensm. Unters. Forsch.*, 1976, **162**, 21.
52. M. Guillou and C. Tellier, *Anal. Chem.*, 1988, **60**, 2182.
53. A. Rapp, A. Markowetz, M. Spraul and E. Humpfer, *Z. Lebensm. Unters. Forsch.*, 1989, **188**, 138.
54. A. Rapp, A. Markowetz and H. Niebergall, *Z. Lebensm. Unters. Forsch.*, 1991, **192**, 1.
55. A. Rapp, M. Spraul and E. Humpfer, *Z. Lebensm. Unters. Forsch.*, 1986, **182**, 419.
56. A. Rapp, A. Markowetz, M. Spraul and E. Humpfer, *Deutsche Lebensm.-Runds.*, 1987, **83**, 375.
57. E. J. Waters, Z. Peng, K. F. Pocock, G. P. Jones, P. Clarke and P. J. Williams, *J. Agric. Food Chem.*, 1994, **42**, 1761.
58. O. Lutz, E. Veil, U. Brändle, H. Helber, E. Kammerer and A. Scheiter, *Z. Naturforsch.*, 1986, **41**, 1041.
59. O. Lutz, E. Humpfer and M. Spraul, *Naturwissenschaften*, 1991, **78**, 67.
60. A. D. Mortimer and B. A. Dawson, *J. Agric. Food Chem.*, 1991, **39**, 1781.
61. L. M. T. Dicks, F. Dellaglio and M. D. Collins, *Int. J. Syst. Bacteriol.*, 1995, **45**, 395.
62. C. R. Davis, D. Wiwobo, R. Eschenbruch, G. H. Fleet and T. H. Lee, *Am. J. Enol. Vitic.*, 1985, **36**, 290.
63. D. Wibowo, R. Eschenbruch, C. R. Davis, G. H. Fleet and T. H. Lee, *Am. J. Enol. Vitic.*, 1985, **36**, 302.
64. T. Henick-Kling, in *Wine Microbiology and Biotechnology* (ed. G. H. Fleet), p. 289. Harwood Academic Publishers, Chur, Switzerland, 1993.
65. C. R. Davis, D. Wibowo, G. H. Fleet and T. H. Lee, *Am. J. Enol. Vitic.*, 1988, **39**, 137.
66. R. E. Kunkee, *FEMS Microbiol. Rev.*, 1991, **88**, 55.
67. R. A. Speckman and E. B. Collins, *J. Bacteriol.*, 1968, **95**, 174.
68. W. M. Verhue and F. B. Tjan, *Appl. Environ. Microbiol.*, 1991, **57**, 3371.
69. A. Ramos, K. N. Jordan, T. M. Cogan and H. Santos, *Appl. Environ. Microbiol.*, 1994, **60**, 1739.
70. A. Ramos, J. S. Lolkema, W. N. Konings and H. Santos, *Appl. Environ. Microbiol.*, 1995, **61**, 3103.
71. O. Kandler, *Antonie Van Leeuwenhoek*, 1983, **49**, 209.
72. M. Veiga-da-Cunha, P. Firme, M. V. San Romão and H. Santos, *Appl. Environ. Microbiol.*, 1992, **58**, 2271.
73. M. Veiga-da-Cunha, H. Santos and E. van Schaftingen, *J. Bacteriol.*, 1993, **175**, 3941.
74. J. Ribéreau-Gayon, E. Peynaud, P. Ribéreau-Gayon and P. Sudraud, *Sciences et techniques du vin*, Vol. 2, p. 122, Dunod, Paris, 1975.

75. R. P. Tracey and T. J. van Rooyen, *J. Appl. Bacteriol.*, 1988, **65**, 113.
76. C. P. Champagne, N. Gardner and G. Doyon, *Appl. Environ. Microbiol.*, 1989, **55**, 2488.
77. M. P. Firme, M. C. Leitão and M. V. San Romão, *J. Appl. Bacteriol.*, 1994, **76**, 173.
78. P. Salou, M. J. Leroy, G. Goma and A. Pareilleux, *Appl. Microbiol. Biotechnol.*, 1991, **36**, 87.
79. M. Miranda, A. Ramos, M. Veiga-da-Cunha, M. C. Loureiro-Dias and H. Santos, *J. Bacteriol.*, 1997, **179**, 5347.
80. H. Santos and D. L. Turner, *J. Magn. Reson.*, 1986, **68**, 345.
81. J. Hugenholtz, *FEMS Microbiol. Rev.*, 1993, **12**, 165.
82. G. de Revel, A. Bertrand and A. Lonvaud-Funel, *J. Int. Sci. Vigne Vin*, 1989, **23**, 39.
83. A. Lonvaud-Funel, C. Zmirou and F. Weinzorm, *Sci. Aliments*, 1984, **4**, 81.
84. M. J. Amoroso, F. M. Saguir and M. C. Manca de Nadra, *J. Int. Sci. Vigne Vin*, 1993, **27**, 135.
85. T. M. Cogan, M. O'Dowd and D. Mellerick, *Appl. Environ. Microbiol.*, 1981, **41**, 1.
86. T. M. Cogan, *J. Appl. Bacteriol.*, 1987, **63**, 551.
87. P. Schmitt, C. Diviès and R. Cardona, *Appl. Microbiol. Biotechnol.*, 1992, **36**, 679.
88. A. Ramos and H. Santos, *Appl. Environ. Microbiol.*, 1996, **62**, 2577.

Proton Phase-sensitive Pulsed Field Gradient Double-quantum Spectroscopy

CLAUDIO DALVIT

Novartis Pharma AG, Basel, Switzerland
Present address: Pharmacia & Upjohn, Nerviano (Mi), Italy

JEAN-MARC BÖHLEN

Bruker AG, Fällanden, Switzerland

ANNUAL REPORTS ON NMR SPECTROSCOPY
VOLUME 37 ISBN 0-12-505337-1

An introduction to ^1H multidimensional pulsed field gradient (PFG) phase-sensitive double-quantum (DQ) spectroscopy and all related experiments is provided. The basic principles and different technical aspects of ^1H PFG DQ spectroscopy are discussed in detail. Application of the technique to real samples taken from daily laboratory life is reported. The complete suppression of solvent signals together with the high sensitivity of the experiment and the absence of artefacts in the DQ spectra make the ^1H PFG DQ experiments a powerful NMR tool for the analysis of chemical and biological molecules dissolved in non-deuterated solvents. In particular a combined strategy based on ^1H 2D PFG DQ and other multiple solvent suppression techniques is described for the application in liquid chromatography (LC)-NMR. This method is robust, reliable and easy to set up. Analysis of combinatorial chemistry samples, natural product extracts and biofluids profits significantly from this methodology.

1. INTRODUCTION

Over recent years proton NMR double-quantum (DQ) spectroscopy has found many useful applications ranging from NMR imaging to high-resolution NMR of biomolecules.[1–11] The one-dimensional refocused DQ experiment has been used extensively in NMR for the detection of lactate and other metabolites present in different tissues.[12–30] The 2D DQ experiment has been applied successfully in the assignment procedure of overlapped spectra of biomolecules.[31–39]

The 2D DQ experiment has some unique advantages when compared to other homonuclear 2D *J*-correlated experiments.

(1) The absence of diagonal peaks allows the identification of nearly degenerate coupled spins.
(2) The absence of diagonal peaks results also in spectra with reduced t_1 noise.
(3) The predominantly in-phase multiplet structure in the ω_1 dimension of the cross-peaks avoids problems associated with self-cancellation of antiphase multiplets that are encountered in the COSY spectra.
(4) The observation of remote peaks in DQ spectra provides a supplementary source of information for unambiguous assignment of spin systems.

Despite these advantages the DQ experiment has not encountered the same success as other 2D *J*-correlated experiments. This is mainly due to three different factors:

(1) The presentation of the DQ spectra along ω_1 makes the comparison with other two- or three-dimensional spectra more difficult.
(2) The presence of t_1 noise from solvent resonances can obscure some

important connectivities that are necessary for the identification of the spin systems.

(3) The fast relaxation of DQC together with the antiphase multiplet structure in ω_2 limits the application of the experiment to small and medium-size molecules. For large molecules, experiments with in-phase magnetization such as TOCSY (total correlation spectroscopy) are preferred.

The introduction of pulsed field gradient (PFG) technology in high-resolution NMR[40–42] has dramatically improved the performance of the different NMR experiments. Two-dimensional ^{1}H DQ[12,13,43] is one experiment that has significantly profited from this technology.

The aim of this chapter is to provide an introduction to ^{1}H multidimensional PFG phase-sensitive DQ spectroscopy and all related experiments. Owing to space limitations we shall restrict ourselves to covering applications in chemistry and biomolecular NMR. Practical aspects will be favoured over theoretical concepts. The theory of DQ spectroscopy has already been treated in considerable detail in several excellent review articles and books.[1,5,44–47] An integrated strategy combining the use of 2D ^{1}H PFG DQ experiments with different novel experiments for the identification of chemical mixtures (LC-NMR) and biofluids will be presented and discussed.

2. CREATION OF DQ COHERENCE

A nonvanishing off-diagonal element σ_{rs} of the density matrix represents coherence between the eigenstates $|r\rangle$ and $|s\rangle$. The difference in magnetic quantum numbers between the two spin states $\Delta M_{rs} = p_{rs}$ is defined as the coherence order. The matrix elements with $\Delta M_{rs} = \pm 2$ are called double-quantum coherence (DQC). Generation of DQC in a solution containing an ensemble of nuclei with spin $I = 1/2$ can be achieved via different physical processes.

2.1. Scalar coupling

The interaction between two spins I_1 and I_2 weakly scalar coupled is given by the Hamiltonian

$$\mathcal{H} = 2\pi J_{12} I_{1z} I_{2z} \tag{1}$$

where J_{12} is the scalar coupling between the two spins. The spin echo scheme of Fig. 1a is usually employed for exciting DQC.[48–50] The 180° pulse located in

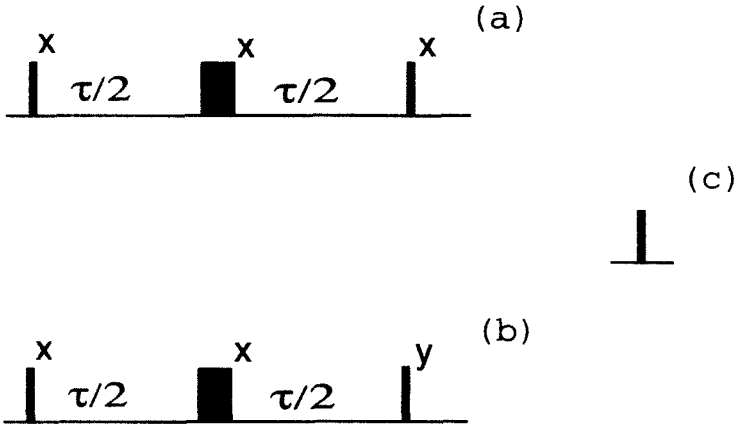

Fig. 1. Different schemes for generating DQC: (a) via scalar and dipolar couplings, (b) via DD-CSA cross-correlation, (c) via violation of the high-temperature approximation. The narrow and wide bars correspond to 90° and 180° pulses, respectively. This convention is used throughout this chapter. The delay τ is the excitation DQ period.

the middle of the excitation DQ period τ is used to refocus the evolution due to the chemical shift. The effect of the scheme of Fig. 1a for two spins I_1 and I_2 scalar coupled with J_{12}, according to the product operator formalism,[51–53] and leaving out the terms which do not give MQC is

$$I_{1z} \xrightarrow{(\pi/2)_x} -I_{1y} \xrightarrow{2\pi J_{12} I_{1z} I_{2z} \tau} 2I_{1x} I_{2z} \sin \pi J_{12} \tau \xrightarrow{(\pi/2)_x} -2I_{1x} I_{2y} \sin \pi J_{12} \tau \quad (2)$$

The Cartesian basis operators $E/2$, I_x, I_y and I_z expressed in terms of the single element basis operators I^α, I^β, I^+, and I^- are

$$\begin{aligned} I_x &= \tfrac{1}{2}(I^+ + I^-) \\ I_y &= \tfrac{1}{2i}(I^+ - I^-) \\ I_z &= \tfrac{1}{2}(I^\alpha - I^\beta) \\ \tfrac{1}{2}E &= \tfrac{1}{2}(I^\alpha + I^\beta) \end{aligned} \quad (3)$$

Using these definitions the right term of equation (2) becomes

$$-2I_{1x} I_{2y} = \tfrac{1}{2i}(I_1^+ I_2^- - I_1^- I_2^+ - I_1^+ I_2^+ + I_1^- I_2^-) \quad (4)$$

The first two terms represent zero-quantum coherence (ZQC) and the third and fourth terms represent +DQC ($p = +2$) and −DQC ($p = -2$), respectively.

2.2. Cross-correlation

With the advent of 2D NMR it became evident that other mechanisms could be responsible for the creation of DQC. The observation of the so-called DQ forbidden peaks in DQ spectra was the first experimental proof that relaxation represents another pathway for generation of DQC.[54–58] These relaxation-allowed coherences are possible only if the diagonal elements of the transverse relaxation matrix are different, in other words, if the parallel transitions of a spin have different relaxation.[54–60] Dipole–dipole (DD) and dipole–chemical shielding anisotropy (DD-CSA) cross-correlation rates are responsible for this differential relaxation. The net result of these mechanisms acting on in-phase transverse magnetization is the creation of antiphase magnetization.[54–64] This phenomenon is the analogue of the conversion of Zeeman order into longitudinal multispin order via cross-correlation.[65–72] These mechanisms, which were considered esoteric aspects of the relaxation phenomenon, nowadays find useful applications in structural studies.[73–80] For example, the measurement of the DD(^1H_N–^{15}N)/^1H_N CSA term[81] provides information on the magnitude of the hydrogen-bond length.[79,80]

Let us consider two spins I_1 and I_2 with $J_{12} = 0$. The two spins are close in space at a distance r_{12} and the spin I_1 has a chemical shift anisotropy $\Delta\sigma_1$. The evolution of the relevant terms in the scheme of Fig. 1b is described by

$$I_{1z} \xrightarrow{(\pi/2)_x} -I_{1y} \xrightarrow{\delta_{112}\tau} -2I_{1y}I_{2z} \xrightarrow{(\pi/2)_y} 2I_{1y}I_{2x} \tag{5}$$

The term δ_{112} is the CSA-DD cross-correlation rate deriving from the coupling of the CSA interaction of spin I_1 with the dipolar interaction between the two spins. The cross-correlation rate is given by

$$\delta_{112} \propto -2J_{112}(\omega_1) - \tfrac{8}{3}J_{112}(0) \tag{6}$$

where J are the CSA-DD cross-correlation spectral densities defined as[65,66]

$$J_{112}(\omega_1) = \tfrac{1}{20}(\mu_0/4\pi)\gamma_1^2\gamma_2\hbar B_0\Delta\sigma_1[\tau_c/(1+\omega_1^2\tau_c^2)]\tfrac{1}{2}(3\cos^2\phi_{112} - 1)\langle r_{12}^{-3}\rangle \tag{7}$$

ϕ_{112} is the angle between the unique axis of the CSA tensor σ_1 and the internuclear vector $\mathbf{r}_{12}$, τ_c is the correlation time and B_0 is the strength of the magnetic field. All the other symbols have their usual meanings. The right term in Eq. (5) represents again a mixture of ZQC and DQC. The antiphase magnetization created via relaxation at the end of the excitation period of Fig. 1b is in quadrature with the antiphase magnetization created via scalar coupling. Therefore in order to convert the antiphase magnetization to DQC, the phase of the second 90° pulse in Fig. 1b is shifted by 90° respect to the first 90° pulse.

2.3. Dipole–dipole coupling

The dipole–dipole coupling is usually averaged out for isotropic solutions. However, molecules with a nonzero magnetic susceptibility anisotropy placed in a strong magnetic field display a small degree of alignment.[82] Another method for aligning molecules with the magnetic field is the use of an aqueous, dilute, liquid crystalline phase.[83–86] In these cases the averaging is not complete and residual DD couplings are observed. The dipolar interaction between two spins I_1 and I_2 is given, in the high-field limit, by the formula[5]

$$H_D = -(\mu_0/4\pi)\gamma_1\gamma_2\hbar r_{12}^{-3}\langle(3\cos^2\theta - 1)/2\rangle[3I_{1z}I_{2z} - \mathbf{I}_1\cdot\mathbf{I}_2] \tag{8}$$

where θ is the angle between the internuclear vector and the static magnetic field, and r_{12} is the internuclear distance between the two spins. This Hamiltonian is similar to the scalar coupling Hamiltonian. Therefore the scheme of Fig. 1a can also be used to generate DQC via DD couplings.

2.4. Long-range dipole–dipole interactions

For concentrated samples such as solvents the long-range intermolecular DD interactions are not averaged to zero by the molecular diffusion. Fortunately, the sum of the long-range intermolecular DD interactions vanishes owing to the spatial isotropic spin distribution.[87] Indeed, the spatial average of the term $(3\cos^2\theta - 1)$ over all polar angles is

$$\langle 3\cos^2\theta - 1\rangle = \int_0^\pi \tfrac{1}{2}\sin\theta\,(3\cos^2\theta - 1)\,d\theta = 0 \tag{9}$$

However, this isotropy is broken when a PFG is applied that dephases the magnetization.[87] The effect of a PFG applied along the z-axis is to impart to the magnetization a phase that is a linear function of z. A magnetization helix is formed along this direction with wavelength $l = |2\pi/(\gamma G_z\delta)|$ where G_z and δ are the strength and duration of the gradient, respectively.[88] The result is that the long-range DD couplings are not averaged to zero. This phenomenon was first described by Deville *et al.*[89] in solid ^{3}He. Multiple echoes were observed after a sequence of two RF pulses (separated by a time τ) was applied. Recently, similar observations were made for H_2O in high magnetic fields.[90,91] These echoes were ascribed to the effect of the dipolar demagnetizing field produced by the bulk H_2O. Classical,[88,92,93] semi-classical[94–97] and quantum mechanical[87,98–101] demagnetization field theories have been developed for explaining the experimental observation of intermolecular multiple-quantum peaks.

2.5. Violation of the high-temperature approximation

The expression of the density matrix at thermal equilibrium for an ensemble of spins is

$$\rho_{eq} = \exp(-\mathcal{H}/kT)/\ \mathrm{Tr}[\exp(-\mathcal{H}/kT)] \tag{10}$$

where KT is the thermal energy and $\mathcal{H}$ is the Hamiltonian in the laboratory frame. At room temperature the energy separation between spin states is small compared to the thermal energy. Therefore, the equation is expanded in a Taylor series only up to the term linear in the Hamiltonian (the so-called high-temperature approximation). However, Warren and co-workers[87] pointed out that this expansion is not sufficient to describe the system for concentrated samples in strong magnetic fields. Higher terms have to be included in the expansion.[87,102] For example, an expansion of Eq. (10) up to the quadratic term is

$$\rho_{eq} = 2^{-N}\left[\left(1 - \frac{\Delta E}{kT}\sum_{i=1}^{N} I_{iz}\right) + \frac{1}{2}\left(\frac{\Delta E}{kT}\right)^2 \sum_{i=1}^{N}\sum_{j=1}^{N} I_{iz}I_{jz}\right] \tag{11}$$

ΔE, which is the energy separation between the spin states, is equal to $\hbar\omega$ where ω is the Larmor frequency. N represents the number of spins contained in the ensemble. It is evident that the simple application of a 90° pulse, as described in Fig. 1c, converts the quadratic term in Eq. (11) to

$$\frac{1}{2}\left(\frac{\Delta E}{kT}\right)^2 \sum_{i=1}^{N}\sum_{j=1}^{N} I_{iz}I_{jz} \xrightarrow{(\pi/2)_x} \frac{1}{2}\left(\frac{\Delta E}{kT}\right)^2 \sum_{i=1}^{N}\sum_{j=1}^{N} I_{iy}I_{jy} \tag{12}$$

which again is a mixture of ZQC and DQC:

$$I_{iy}I_{jy} = \tfrac{1}{4}(I_i^+ I_j^- + I_i^- I_j^+ - I_i^+ I_j^+ - I_i^- I_j^-) \tag{13}$$

2.6. Radiation damping

According to Warren and co-workers,[103,104] the radiation damping phenomenon, i.e. the coupling of the spins with the coil, can create DQC in a way similar to the bilinear scalar couplings. If radiation damping were small it would be refocused at the end of the spin-echo period of a DQ experiment. However, the use of high-Q probes, the long DQ excitation period, and probably deviation from the ideal 180° pulse, make the refocusing incomplete. This theory was then challenged by Abergel *et al.*,[105] who showed that the harmonic peaks observed in the COSY (correlation spectroscopy) and multiple-quantum spectra could not be explained with the quantized field theory of radiation damping.

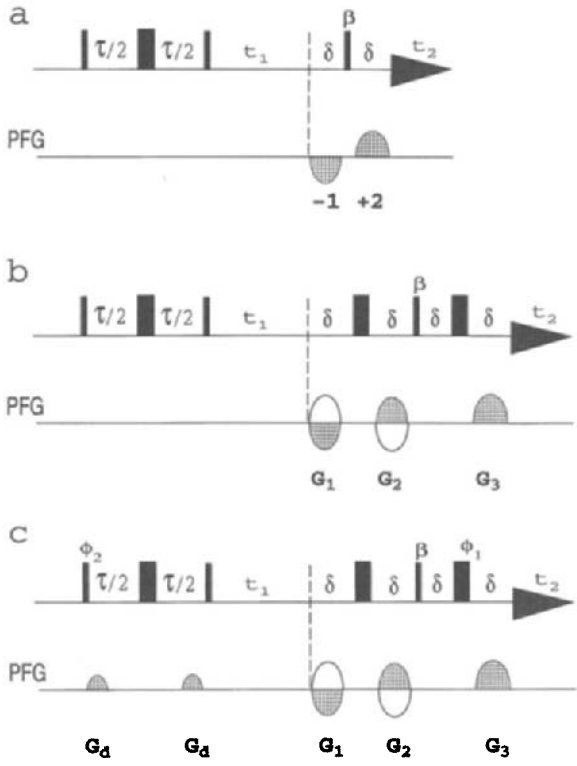

Fig. 2. Pulse sequences for recording ^{1}H PFG DQ spectra: (a) absolute value, (b) absorption mode, (c) improved absorption mode DQ. The angle β of the read-out pulse in (b) and (c) can be set to 90° (anti-echo)/90° (echo) or to 45° (or 60°) (anti-echo)/135° (or 120°) (echo). For the versions with β = 90°/90° the phases are $\phi_1 = 2(x), 2(-y), 2(-x), 2(y)$; $\phi_2 = (x, -x)$; and $\phi_{rec} = (x, -x, -x, x)$. For the version with β = 45°/135° or β = 60°/120° the phases are $\phi_1 = (x, -y, -x, y)$ for both echo and anti-echo pathways selections, $\phi_2 = x$; $\phi_{rec} = (x, -x)$ for the anti-echo pathway and $\phi_2 = -x$; and $\phi_{rec} = (-x, x)$ for the echo pathway. The τ and δ periods correspond to the DQ excitation period and to the length of the gradient plus a recovery time, respectively. The coherence selection gradients G_1, G_2 and G_3 are MAGs for efficient solvent suppression, but can be also z-PFGs. In (b,c) two data sets corresponding to the echo and anti-echo coherence pathway selections are recorded by reversing the sign of G_1 and G_2. The first two gradients in (c), labelled G_d, are weak PFGs, e.g. 0.5 G cm^{-1}, of the same intensity and sign applied at the beginning and end of the DQ excitation period.

3. SELECTION OF DQC WITH GRADIENTS

Coherence transfer pathway selection by magnetic field gradients is based on the different defocusing of the different coherences types in the presence of a gradient.[106–111]

The effect of a pulsed field gradient is a dephasing of the magnetization. This spatially dependent phase $\Phi(r, \delta)$ is given by

$$\Phi(r, \delta) = sp\gamma B_g(r)\delta \tag{14}$$

where s is a shape factor, B_g is the magnetic field produced by the gradient pulse (for a z-gradient $B_g = Gz$ where G is the gradient strength and the origin of the z-axis corresponds to the centre of the sample), δ is the length of the gradient, γ is the gyromagnetic ratio for each spin and p is the coherence order for each spin.

Figure 2a represents the simplest pulse sequence for recording an absolute-value DQ experiment.[40,41] The first gradient G_1 encodes a spatially dependent phase Φ_1 and the second a phase Φ_2 where

$$\Phi_1 = sp_1 B_{g1}\delta_1 \qquad \text{and} \qquad \Phi_2 = sp_2 B_{g2}\delta_2 \tag{15}$$

We have assumed that the two gradients have the same shape factor s.

The net phase at the end of the second PFG is

$$\Phi_1 + \Phi_2 = s(p_1 B_{g1}\delta_1 + p_2 B_{g2}\delta_2) \tag{16}$$

In order to select the desired coherence pathway, the condition $\Phi_1 + \Phi_2 = 0$ has to be fulfilled, i.e. the dephasing due to G_1 is undone by G_2. In our case with $p_1 = +2$ (+DQC) and $p_2 = -1$ we obtain the condition

$$\frac{B_{g1}\delta_1}{B_{g2}\delta_2} = \frac{G_1\delta_1}{G_2\delta_2} = \frac{1}{2} \tag{17}$$

Therefore, DQ can be selected either by making G_2 twice as strong as G_1 or by making G_2 and G_1 of equal strength but with G_2 twice as long as G_1 ($\delta_2 = 2\delta_1$).

Depending on the relative sign of the two PFGs, either coherence level +2 is selected during the evolution period, giving the N-type or echo spectrum, or level −2 is selected giving the P-type or anti-echo spectrum. The selection of just one coherence level during t_1 results in spectra where the peaks have a phase-twist lineshape, i.e. a mixture of absorption and dispersion. This lineshape is deleterious in high-resolution NMR because it is broad and because it has positive and negative dispersive tails. The tails can be reduced by the application of a strong weighting function followed by an absolute-value calculation. This process results in a reduction in signal-to-noise ratio in the spectrum and in the loss of information about the sign of the cross-peaks. This last point is detrimental, particularly in the DQ experiment where the knowledge of the sign of the cross-peaks is important for the differentiation of the direct and remote peaks.

Absorption-mode ^{1}H DQ spectra can be obtained with the pulse sequence of Fig. 2b,[112] where two data sets are recorded. A similar pulse sequence[113] was independently proposed for the ^{13}C INADEQUATE experiment. The gradient combination +1, −1, +4 (or −1, +1, −4) selects in the first experiment the coherence transfer echo pathway {+DQ}→{− SQ}, whereas the combination −1, +1, +4 (or +1, −1, −4) selects in the second experiment the anti-echo pathway {−DQ}→{−SQ}. P-type and N-type spectra are obtained from these experiments. By reversing the ω_1 axis of the N-type spectrum, the P-type spectrum is obtained except for the dispersive part that is opposite. Addition of the axis-reversed N-type and P-type spectra cancels the dispersive parts, resulting in cross-peaks with a double-absorption lineshape.[106,114] Experimentally this is achieved by manipulating the P- and N-type time domain data S_P and S_N, respectively. The cosine (S_{cos}) and sine (S_{sin}) modulated data needed for the hypercomplex (or states[115]) method are obtained by combining the P- and N-type data according to

$$S_{cos}(t_1,t_2) = (S_P + S_N)/2 = \cos(\Omega_{DQ} t_1) \exp(i\Omega_{SQ} t_2) \tag{18}$$

$$S_{sin}(t_1,t_2) = -i(S_P - S_N)/2 = \sin(\Omega_{DQ} t_1) \exp(i\Omega_{SQ} t_2) \tag{19}$$

Performing a Fourier transform with respect to t_1 and t_2 one obtains

$$S_{cos}(\omega_1, \omega_2) = (A_1^+ A_2 + A_1^- A_2)/2 \tag{20}$$

$$S_{sin}(\omega_1, \omega_2) = -i(A_1^+ A_2 - A_1^- A_2)/2 \tag{21}$$

where A_1^+ and A_1^- represent the absorption parts of the signals in the ω_1 dimension at the double-quantum frequencies $+\Omega_{DQ}$ and $-\Omega_{DQ}$, respectively and A_2 represents the absorption part of the signals in the ω_2 dimension.

Combining the equations (20) and (21) as a complex pair results in

$$S(\omega_1, \omega_2) = S_{cos}(\omega_1, \omega_2) + iS_{sin}(\omega_1, \omega_2) = A_1^+ A_2 \tag{22}$$

which provides frequency discrimination with a pure double-absorption lineshape.

A different version of the DQ experiment[116] uses gradients for coherence selection and time-proportional phase incrementation (TPPI)[117,118] for quadrature detection in ω_1. This experiment suffers a $\sqrt{2}$ sensitivity loss compared to the scheme of Fig. 2b. Furthermore, according to the authors of that work, after phase-sensitive ω_1 calculation, a magnitude calculation along ω_2 must be applied.

The PFGs in Fig. 2b are included in spin echo sequence elements in order to refocus the evolution under chemical shift occurring during the application of the PFGs. Additionally, the first gradient of Fig. 2a is replaced by two gradients

of opposite sign in Fig. 2b. This allows suppression of artefacts produced by imperfections of the 180° pulse located in the evolution period[119] without need for EXORCYCLE[120] phase cycling. Furthermore, in our experience DQ spectra recorded with two PFGs in t_1 contain less residual solvent signal.

A typical DQ spectrum of the protein lysozyme in H_2O obtained with the pulse sequence of Fig. 2b is shown in Fig. 3. The lower spectrum contains the so-called fingerprint region and the upper spectrum contains the remote peaks of the glycine residues.

The peaks that are present in a DQ spectrum are classified into three types:[2,3,5–6]

(i) The direct peaks originate from DQC actively involving a given spin and transferred to single-quantum coherence (SQC) of the same spin.
(ii) The remote peaks result from DQC between two spins and transferred to SQC on a third passive spin.
(iii) The combination peaks arise from q-spin 2-quantum coherence in systems with more than three spins. These DQCs involve q spins ($q = 2 + 2k, k = 1, 2,...$) and can be observed on a spin only if this spin is coupled to all other $q - 1$ spins.

Let us consider a MAX spin system. Simulated DQ spectra of this three-spin system with all the spins mutually coupled ($J_{AM} = J_{AX} = J_{MX} = 10$ Hz) and with one coupling set to zero ($J_{AX} = 0$) are shown in Fig. 4 (left) and Fig. 4 (right), respectively. The Cartesian operator expressions for four different cross-peaks are described in Table 1. When all $J \neq 0$, all three spins contribute to each cross-peak. But when $J_{AX} = 0$, two spins contribute to each direct peak and only one spin contributes to the remote peak. Six direct peaks and three remote peaks are observed in the spectrum with all $J \neq 0$, and four direct peaks and one remote peak are observed in the spectrum with $J_{AX} = 0$. The direct peaks appear as ω_1-pairs of peaks symmetrically disposed around the DQ-diagonal. For example, the signals labelled a and b in Fig. 4 (left) constitute such a pair. The multiplets of the remote peaks are doubly antiphase and dispersive along ω_2 (see Table 1). This characteristic lineshape,[34,121] together with their asymmetric disposition around the DQ-diagonal, allows their identification. For example, the peak e in Fig. 4 (left) is a remote peak.

4. FLIP ANGLE DEPENDENCE

The angle β of the read-out pulse of Fig. 2b and 2c is usually 90°. However, it can be set to other values for editing and sensitivity improvement.[2,3] For example, for a two-spin system maximum sensitivity is obtained with $\beta = 60°$ for the anti-echo and $\beta = 120°$ for the echo selections. We will refer to this experiment as the 60°/120° PFG DQ.

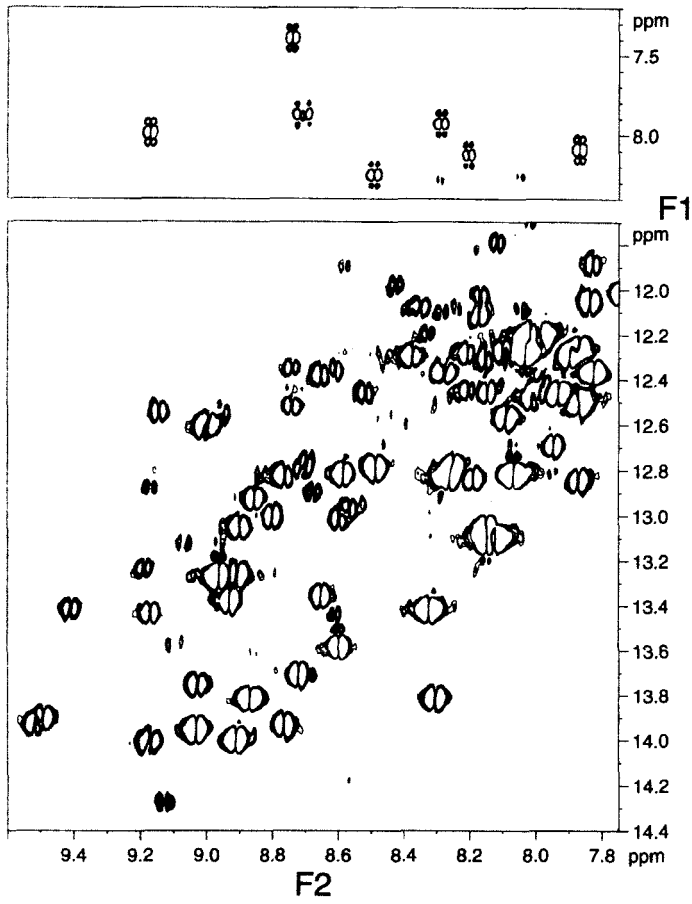

Fig. 3. Two selected regions of the DQ spectrum recorded with the scheme of Fig. 2b with $\beta = 90°$ for a solution of chicken egg-white lysozyme dissolved in H_2O (7% D_2O). The lower section contains the $\{DQ\}^{NH\alpha H}$ direct peaks and the upper section contains the $\{DQ\}^{\alpha H\alpha H'}$ remote peaks of the glycine residues. A total of 16 scans were recorded for each of the 256 t_1 complex points.

Let us consider a linear three-spin system composed of I_N, I_α and I_β spins of an amino acid moiety with the scalar couplings $J_{N\alpha}, J_{\alpha\beta} \neq 0$ and $J_{N\beta} = 0$, i.e. the same type of spin system described in Fig. 4 (right). We limit the analysis to the $\{DQ\}_{N\alpha}$ and $I_\alpha^z\{DQ\}_{N\beta}$ terms present during t_1. The conversion of these {DQ} terms to observable magnetization I_N^- (direct peak) and I_α^- (remote peak) in function of the angle β is given by

$$I_N^+ I_\alpha^+ \xrightarrow{\beta I^x} -i/4\,[I_N^- I_\alpha^\alpha - I_N^- I_\alpha^\beta] \sin\beta\,(\cos\beta - 1) \tag{23}$$

$$I_N^- I_\alpha^- \xrightarrow{\beta I^x} -i/4\,[I_N^- I_\alpha^\alpha - I_N^- I_\alpha^\beta] \sin\beta\,(\cos\beta + 1) \tag{24}$$

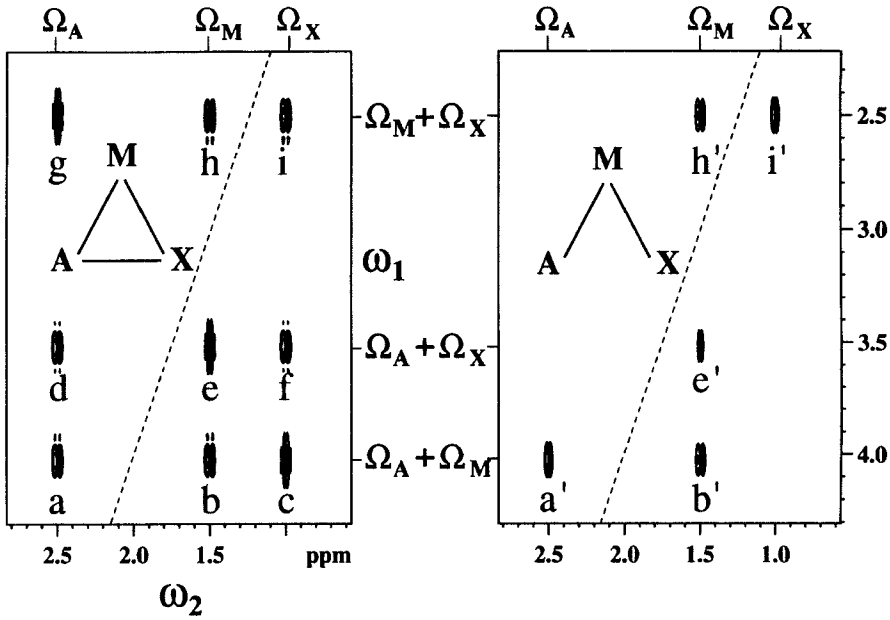

Fig. 4. Simulated 2D DQ spectra of two MAX spin systems with $\Omega_A = 2.5$, $\Omega_M = 1.5$ and $\Omega_X = 1.0$ ppm, and with $J_{AM} = J_{AX} = J_{MX} = 10$ Hz (left) and $J_{AM} = J_{MX} = 10$ Hz, $J_{AX} = 0$ (right). The direct DQ correlation peaks are labelled a, b, d, f, h and i for the system with all $J \neq 0$ (left) and a', b', h' and i' for the system with $J_{AX} = 0$ (right). The remote DQ correlation peaks are labelled c, e and g (left), and e' (right). The resolution was 3.5 Hz/pt for the acquisition and 0.75 Hz/pt for processing in ω_2, and 26 Hz/pt for the acquisition and 13 Hz/pt for processing in ω_1, corresponding to an experimental situation. The dashed line represents the double-quantum diagonal.

$$I_\alpha^z I_N^+ I_\beta^+ \xrightarrow{\beta I^x} \text{i/8}\,[I_\alpha^- I_N^\alpha I_\beta^\alpha - I_\alpha^- [I_N^\alpha I_\beta^\beta - I_\alpha^-] I_N^\beta I_\beta^\alpha + I_\alpha^- I_N^\beta I_\beta^\beta] \sin^3\beta \quad (25)$$

$$I_\alpha^z I_N^- I_\beta^- \xrightarrow{\beta I^x} \text{i/8}\,[I_\alpha^- I_N^\alpha I_\beta^\alpha - I_\alpha^- [I_N^\alpha I_\beta^\beta - I_\alpha^-] I_N^\beta I_\beta^\alpha + I_\alpha^- I_N^\beta I_\beta^\beta] \sin^3\beta \quad (26)$$

Plots of coherence transfer amplitude of DQC into SQ observable magnetization in the ^{1}H PFG anti-echo/echo DQ experiment based on Eqs. (23–26) are shown in Fig. 5a and 5b. The relative signal intensities in the different versions (dashed vertical lines in Fig. 5) of the experiment (normalized to the 90°/90° version) for the direct peak, for the remote peak and for the direct-peak/remote-peak ratios are reported in Table 2.

Figure 6 shows experimental results for the direct peak at $\omega_1 = \omega_N + \omega_\alpha$ and $\omega_2 = \omega_N$ (Fig. 6a) and for the remote peak at $\omega_1 = \omega_N + \omega_\beta$ and $\omega_2 = \omega_\alpha$ (Fig. 6b) of the residue valine-5 in the cyclic undecapeptide cyclosporin (CsA).

Table 1. Cartesian operator expressions for direct and remote peaks of the MAX spin-systems of Fig. 4 at the beginning of acquisition

Peak a

$$2I_X^A I_Z^M \cos(\Omega_A + \Omega_M)t_1[\sin \pi J_{AM}\tau \cos \pi J_{AX}\tau \cos \pi(J_{AX} + J_{MX})t_1 + \sin \pi J_{AM}\tau \cos \pi J_{MX}\tau \cos \pi(J_{AX} + J_{MX})t_1 + \sin \pi J_{AX}\tau \sin \pi J_{MX}\tau \sin \pi(J_{AX} + J_{MX})t_1]$$

Peak a'

$$2I_X^A I_Z^M \cos(\Omega_A + \Omega_M)t_1[\sin \pi J_{AM}\tau \cos \pi J_{MX}t_1 + \sin \pi J_{AM}\tau \cos \pi J_{MX}\tau \cos \pi J_{MX}t_1]$$

Peak e

$$4I_Y^M I_Z^A I_Z^X \cos(\Omega_A + \Omega_X)t_1[\sin \pi J_{AM}\tau \sin \pi J_{MX}\tau \cos \pi(J_{AM} + J_{MX})t_1 - \sin \pi J_{AX}\tau \cos \pi J_{AM}\tau \sin \pi(J_{AM} + J_{MX})t_1 - \sin \pi J_{AX}\tau \cos \pi J_{MX}\tau \sin \pi(J_{AM} + J_{MX})t_1]$$

Peak e'

$$4I_Y^M I_Z^A I_Z^X \cos(\Omega_A + \Omega_X)t_1[\sin \pi J_{AM}\tau \sin \pi J_{MX}\tau \cos \pi(J_{AM} + J_{MX})t_1]$$

The expressions of the other peaks are obtained by simply interchanging the indices.

The peaks have been extracted from six 2D ^{1}H PFG DQ experiments recorded with different angles for the read-out pulse. In agreement with the theory, maximum signals for the direct peak and for the remote peak are observed in the $\beta = 60°/120°$ and $\beta = 90°/90°$ DQ experiments, respectively.

The version with $\beta = 60°/120°$ should be recorded when maximum sensitivity for the direct peaks is desired. This is important in experiments where weak signals have to be detected. Application of this experiment to a 200 μmol l^{-1} solution of the 1-40 β-amyloid peptide is shown in Fig. 7. In spite of the sample's low concentration, the intensity of the peaks in the DQ spectrum is high, as seen for the representative cross-peak of M35. According to this spectrum it is evident that samples at concentration of the order of 50 μmol l^{-1} or less could be analysed with this method. The $\beta = 30°/150°$ or $\beta = 45°/135°$ versions should be used if attenuation of the remote peaks is desired. This may be useful for simplifying crowded spectral regions. Furthermore, the reduced number of cross-peaks makes these spectra suitable for automated analysis.[122,123] Finally,

Fig. 5. (a) Plot of the coherence transfer amplitude of DQC to observable SQC as function of the angles of the read-out pulse used in the PFG DQ experiments according to Eqs. (23–26). The first value of the angle is for the anti-echo pathway selection ($I^-I^- \rightarrow I^-$) and the second value is for the echo pathway selection ($I^+I^+ \rightarrow I^-$). The vertical lines correspond to the different flip-angle versions of the ^{1}H PFG DQ experiment. (b) Plot of the coherence transfer amplitude direct peaks/remote peaks as function of the angles of the read-out pulse used in the PFG DQ experiments. (Reproduced with permission from Dalvit and Böhlen.[148] © John Wiley & Sons Ltd.)

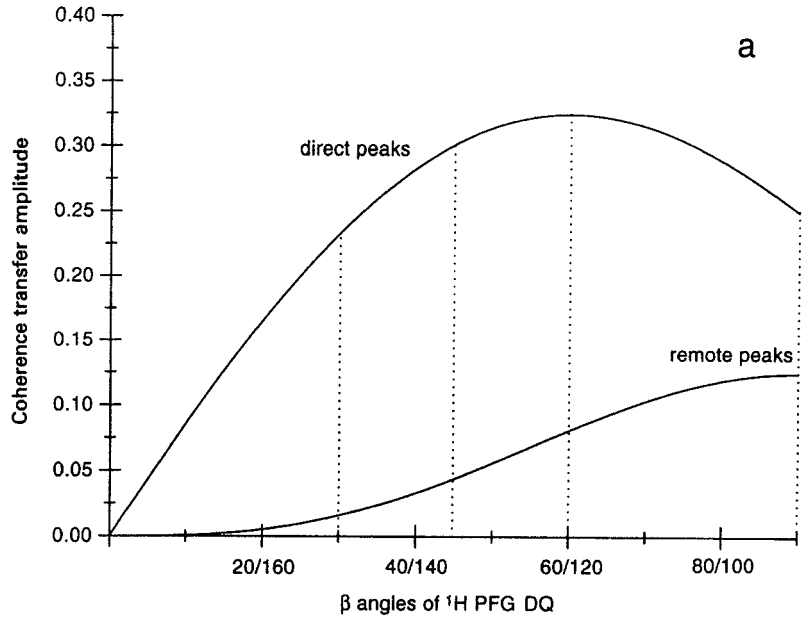
a
0.40
0.35
0.30
0.25
0.20
0.15
0.10
0.05
0.00
Coherence transfer amplitude
direct peaks
remote peaks
20/160
40/140
60/120
80/100
β angles of ^{1}H PFG DQ

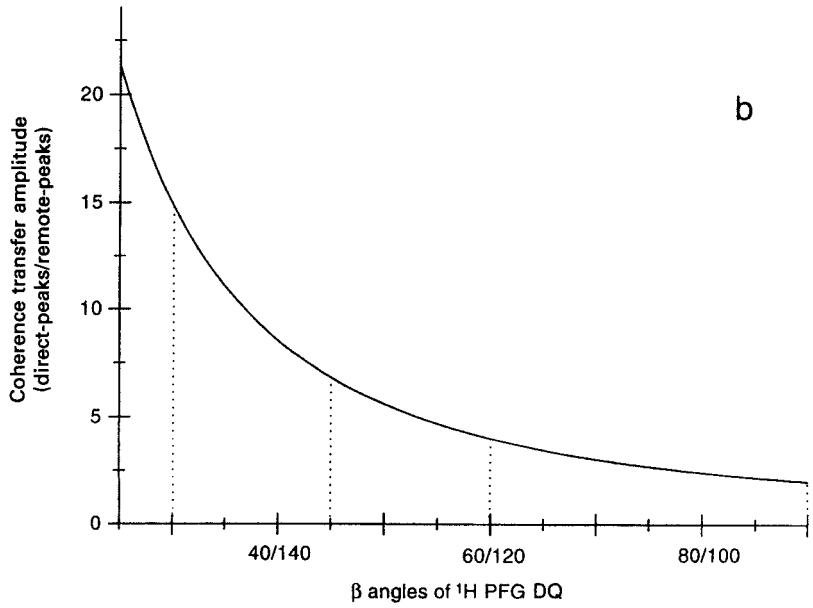
b
20
15
10
5
0
Coherence transfer amplitude
(direct-peaks/remote-peaks)
40/140
60/120
80/100
β angles of ^{1}H PFG DQ

Table 2. Relative sensitivity of the ^1H PFG DQ experiment as function of the read-out pulse

PFG DQ experiment	Direct peak $\{DQ\}_{NH\alpha H} \rightarrow \{SQ\}_{NH}$	Remote peak $\{DQ\}_{NH\beta H} \rightarrow \{SQ\}_{\alpha H}$	Ratio Direct peak / Remote peak
90°/90°	1	0.5	2
30°/150°	0.93	0.06	14.9
45°/135°	1.21	0.18	6.8
60°/120°	1.3	0.32	4

the $\beta = 90°/90°$ version gives maximum intensity for the remote peaks. This is useful, for example, in the identification of different types of spin systems and in the identification of magnetic equivalence. It should be pointed out that for more complex spin systems the use of a PFG DQ experiment with $\beta \neq 90°$ results in the presence of some dispersive components. This is because for certain cross-peaks the N-type and P-type spectra have different intensities for $\beta \neq 90°$ and therefore the dispersive tails are not cancelled completely in the combined spectrum. However, these are small and weak weighting functions can still be applied. If necessary the spectra can always be processed in absolute value afterwards.

5. SOLVENT SUPPRESSION

The PFG DQ experiment, when recorded with certain modifications discussed below, achieves remarkable solvent suppression. Therefore it represents a powerful tool for the analysis of compounds dissolved in non-deuterated solvents.

5.1. Singlet resonances

PFG DQ experiments recorded for samples dissolved in H_2O result in spectra that contain a large residual solvent signal. H_2O is a singlet and consequently cannot create DQC via scalar couplings. However, as discussed in Sections 2.4 and 2.6, long-range DD interactions and radiation damping contribute to the observation of the undesired H_2O signal. Knowledge of these effects has allowed the design of the modified pulse sequence of Fig. 2c.[124,125] The changes have the purpose of inhibiting the creation and detection of H_2O DQC. The first modification is the utilization of two weak PFGs of equal strength and intensity applied at the beginning and end of the DQ excitation period. These have the function of keeping H_2O magnetization dephased during the entire

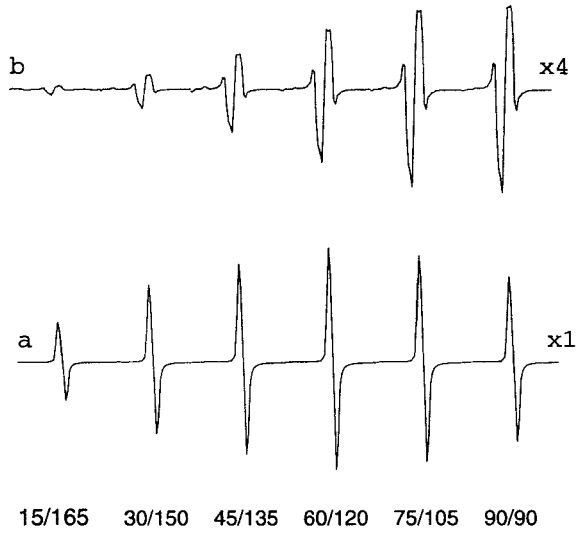

Fig. 6. Experimental behaviour of the intensity of the direct peak at $\omega_1 = \omega_N + \omega_\alpha$ (12.13 ppm), and $\omega_2 = \omega_N$ (7.47 ppm) (a) and of the remote peak at $\omega_1 = \omega_N + \omega_\beta$ (9.90 ppm), $\omega_2 = \omega_\alpha$ (4.65 ppm) (b) for the residue valine-5 as function of the angles of the read-out pulse of the ^{1}H PFG DQ experiment. The spectra in (b) have been plotted at four times the level of the spectra in (a). The sample is the cyclic undecapeptide cyclosporin (CsA) dissolved in $CDCl_3$. The two peaks have been extracted from six 2D ^{1}H PFG DQ spectra recorded with the pulse sequence of Fig. 2b and with different angles for the detection pulse, as indicated in the figure. Four scans were acquired for each of the 200 t_1 complex points. The data were multiplied in both dimensions with a cosine window function[248] prior to 2D Fourier transformation. The direct peak has an absorptive single anti-phase lineshape and the remote peak has dispersive doubly anti-phase lineshape along ω_2. The strongest signals for the direct peak and for the remote peak are observed in the 60°/120° and 90°/90° PFG DQ experiments, respectively, in agreement with the theory. (Reproduced with permission from Dalvit and Böhlen.[148] © John Wiley & Sons Ltd.)

length of the spin-echo period and thus suppressing the radiation-damping effect. Two PFGs have been applied immediately before and after the 180° pulse in DQ imaging[13] for suppressing artefacts originating from imperfections of the 180° pulse. However, during the rest of the spin echo period, water magnetization is not defocused and thus radiation damping is effective.[125] The second modification is the use of coherence selection gradients tilted at the magic angle[87,112,126,127] (MAG), i.e. $\theta = 54.7°$ where θ is the angle between the gradient direction and the static magnetic field direction. A nonuniform spin spatial distribution is created along this gradient direction. However, for this angle the DD couplings are equal to 0 ($3\cos^2\theta - 1 = 0$) and therefore will not contribute to the conversion of H_2O antiphase magnetization present at the acquisition start to in-phase magnetization and thus to observable signal.

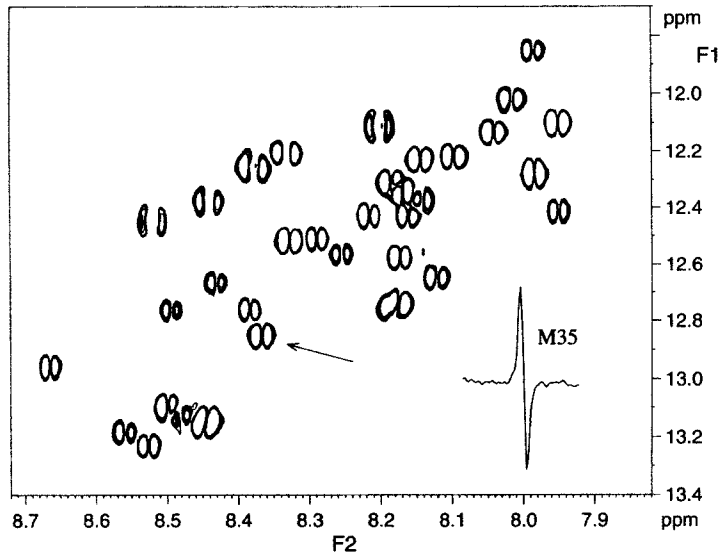

Fig. 7. Fingerprint region of the DQ spectrum of the 1-40 β-amyloid peptide in H_2O (7% D_2O) recorded with the pulse sequence of Fig. 2 with $\beta = 60°/120°$. The peptide concentration was 200 μmol l^{-1} and the pH of the solution was 2.9. The spectrum was recorded at T_e = 297 K with a Bruker Avance-500 spectrometer. Thirty-two scans were recorded for each of the 512 t_1 increments. The repetition time was 1.6 s, τ was 30 ms and the total measuring time was about 7 h. The ω_1 and ω_2 spectral widths were 16 and 8.8 ppm, respectively. The strength of the first two 1.25 ms long sine-shaped PFGs was +0.35 G cm^{-1}. The strength of the three 0.6 ms long coherence selection z-PFGs was ±5, ∓5, −20 G cm^{-1}, respectively. The gradient recovery time was 100 μs. The data were multiplied in both dimensions with a cosine window function prior to 2D Fourier transformation. The 1D cross-section taken at the cross-peak of M35, indicated by the arrow, is displayed in order to show the S/N ratio. (Reproduced with permission from Dalvit and Böhlen.[148] © John Wiley & Sons Ltd.)

The improvements in solvent suppression obtained by the introduction of these changes in the DQ experiment can be appreciated in Fig. 8. The spectrum recorded with five z-PFGs(b) contains significantly less H_2O signal compared to the spectrum recorded with only the three coherence selection z-PFGs(a). Furthermore, the spectra recorded with three MAGs and two weak z-PFGs have slightly better solvent suppression compared to the spectra recorded simply with three MAGs. The residual H_2O signal in (c) and (d) is probably due to differential nonlinearity of the x, y and z gradients,[128] which results in deviation from the magic angle condition for some parts of the sample with consequent leakage of the H_2O signal. Owing to the fact that the amount of antiphase magnetization present at the beginning of t_2 is larger in the DQ experiment recorded without the first two weak z-PFGs, more H_2O magnetization will become observable via this mechanism.

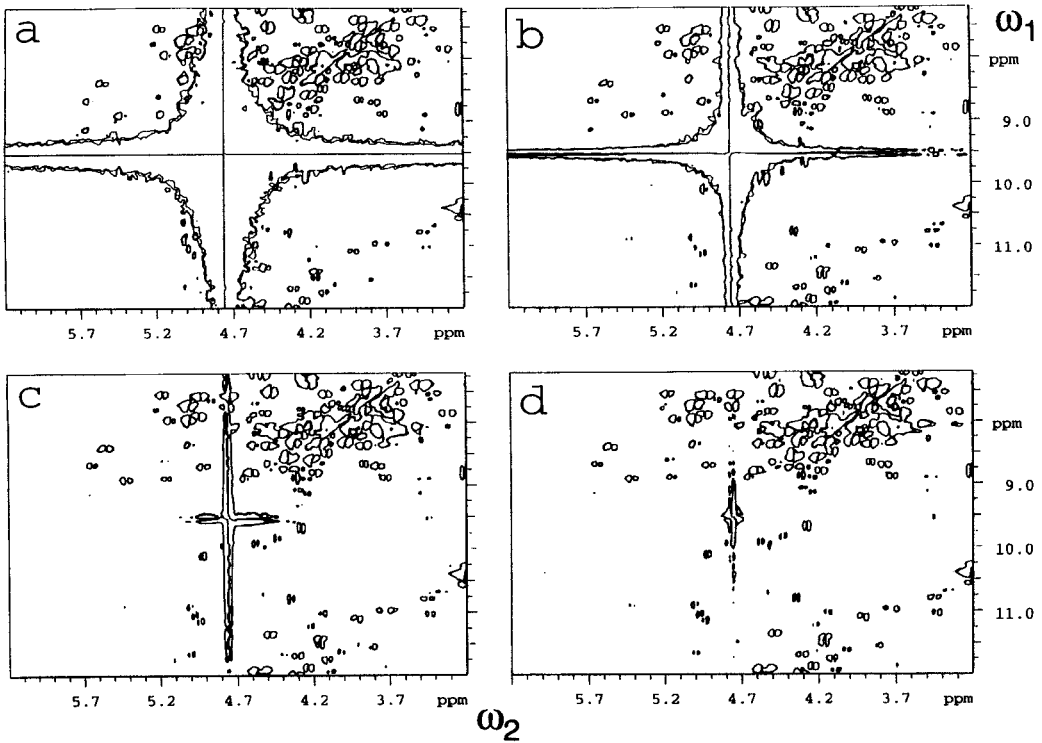

Fig. 8. Two-dimensional DQ spectra recorded with the basic pulse sequence of Fig. 2b and 2c and with $\beta = 90°$ for a solution of the protein chicken egg-white lysozyme dissolved in H_2O (7% D_2O). A small region centred at $\omega_2 = \omega_{H_2O}$ and $\omega_1 = 2\omega_{H_2O}$ is displayed. Eight scans were recorded for each of the 256 complex t_1 points. The ω_1 and ω_2 spectral widths were 12 and 15 ppm, respectively. The repetition time and τ were 1.5 s and 30 ms, respectively. The length of the sine-shaped gradients was 1.5 ms and the recovery time was 200 μs. The spectra were recorded without (a,c) and with (b,d) the first two weak z-PFGs. The three coherence selection gradients were z-PFGs in (a,b) and MAGs in (c,d). The total strengths of the MAGs in (c,d) are equal to the strengths of the z-PFGs in (a,b). No treatment of the data was done for H_2O signal reduction. The weak H_2O residual signal in (d) allows the observation of several weak remote peaks at $\omega_2 = \omega^{\alpha}H$ and $\omega_1 = \omega^{N}H + \omega^{\beta}H$ that are degenerate with the H_2O signal. (Reproduced with permission from Dalvit and Böhlen.[125])

Calibration of the magic angle gradient condition is achieved by recording the one-dimensional version of the 2D DQ experiment. The x and y components of the gradients are kept constant whereas the strength of the z gradient component is varied stepwise, or conversely the x and y components are varied and the z component is kept constant. This is shown experimentally in Fig. 9 for a sample of blood plasma from a male Sprague–Dawley rat. The H_2O and the β-glucose H_1 signals are plotted against increasing values of θ (angle of the gradient) crossing the magic angle value. The H_2O signal diminishes and that of glucose, located at 0.1 ppm from H_2O, remains unchanged, when approaching the magic angle orientation of the gradient. For this angle the H_2O signal is half the intensity of the glucose signal. A simple 1° decrease and increase of the angle θ from the magic angle results in respectively 7 times and 5 times increase of the residual H_2O signal. This experimental angle dependence is in qualitative agreement with the theory, which indicates that more solvent will be visible by moving towards the z-axis than towards the x–y plane. The trigonometric function $(3\cos^2\theta - 1)$ is maximum for $\theta = 0$, i.e. for z-gradients.

In our experiments we used three orthogonal x, y and z gradients that had the same strength (i.e. $G_x = G_y = G_z$). However, magic angle gradients can also be obtained simply by using two gradient coils, namely the x (or y) and z gradient coils with $G_x = \sqrt{2}\,G_z$; $G_y = 0$ (or $G_y = \sqrt{2}\,G_z$; $G_x = 0$). A third possibility is the use of a single gradient coil tilted at the magic angle.[127] The last two possibilities may be useful for probe-heads that have limited available space, such as cryogenic probes, or high-temperature probes or simply 8 mm or 10 mm probes.

Another phenomenon that is responsible for the spurious H_2O signal observed in the DQ experiments recorded with $\beta \neq 90°$ is radiation damping acting during the acquisition period. The current induced in the receiver coil by the transverse solvent magnetization produces a magnetic field in the x–y plane with intensity proportional to the transverse magnetization.[129–139] This field is given by

$$\mathbf{B}_r(t) = \mathrm{i}2\pi\eta Q\mathbf{m} \tag{27}$$

where $\mathbf{m} = \mathbf{m}_x + \mathrm{i}\mathbf{m}_y$ is the solvent transverse magnetization, Q is the quality factor of the circuit and η is the filling factor. This field exerts a torque on the magnetization with the result of a rapid return of the magnetization to the equilibrium state.

Figure 10a shows the behaviour of the residual H_2O signal as a function of the β angle of the read-out pulse of the PFG DQ experiment.[124] In the range $90° < \beta < 270°$ part of the H_2O magnetization is aligned along the $-z$-axis at the beginning of the acquisition period. The last PFG of the pulse sequence of Fig. 2b and 2c destroys all the H_2O transverse magnetization. However, during the acquisition period the H_2O $-z$ magnetization acquires a transverse com-

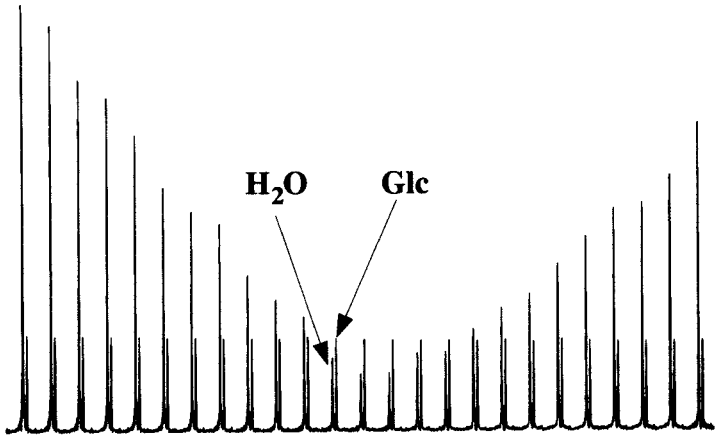

Fig. 9. Calibration of the magic angle gradient condition. The experiments were recorded at T_e = 296 K with a Bruker Avance-600 spectrometer for a sample of blood plasma from a male Sprague–Dawley rat. The spectra were acquired with the 1D version of the pulse sequence of Fig. 2b with $\beta = 90°$, t_1 = 10 ms (corresponding to an intermediate value of the evolution period of a 2D experiment), τ = 30 ms and with an acquisition time of 250 ms. The length of the three gradients was 1.5 ms and the recovery delay was set to 200 μs. A small portion of the blood plasma spectrum showing the residual water signal and the β-glucose H_1 signal, located at 0.1 ppm upfield from H_2O, is displayed in magnitude mode. The z components of the three coherence selection gradients were kept fixed at +11.9%, −11.9% and +47.6% throughout the measurements. The strengths of their x and y components were varied simultaneously from +15.85% to +17.07%, from −15.85% to −17.07% and from +63.4% to +68.2%. The increment for each step was 0.05, −0.05 and 0.2%, respectively. According to our gradient calibration, the changes on x and y components correspond to a total variation of θ by ±1° around the magic angle. One scan was recorded for each measurement. Note the improvement of the water suppression when approaching the right setting and the unchanged glucose signal intensity. (Reproduced with permission from Dalvit and Böhlen.[148] © John Wiley & Sons Ltd.)

ponent. According to Eq. (27) the H_2O transverse magnetization then triggers the radiation damping mechanism, with consequent fast H_2O decay and large detected H_2O signal. The use of MAGs does not suppress this mechanism, but as shown in Fig. 10, it results in a narrower band where the radiation damping is efficient. The transverse H_2O magnetization present during t_2 originates solely from the H_2O $-z$-axis component present at the beginning of t_2 in the experiments recorded with MAGs. In addition to this mechanism, the conversion of antiphase H_2O SQC that was DQC during t_1 to in-phase SQC also contributes to the H_2O signal in the DQ experiments recorded with only z-PFGs. The larger amount of transverse magnetization in this experiment results in a more pronounced radiation damping effect. When the radiation damping mechanism becomes predominant, there are no differences between the two experiments. The same 2D experiments recorded simply reversing by

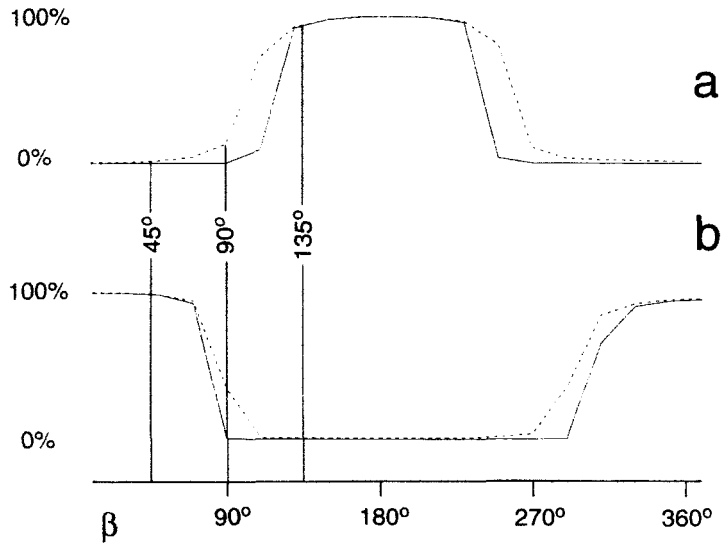

Fig. 10. Behaviour of the residual H_2O signal as function of the β angle of the read-out pulse of the DQ experiment. The sample is a solution of chicken egg-white lysozyme dissolved in H_2O (7% D_2O). The spectra were acquired at T_e = 300 K with a Bruker Avance-600 spectrometer. The spectra have been recorded with the scheme of Fig. 2b. The delay t_1 was kept fixed at 3 μs and the β angle was incremented in steps of 10° from 10° to 370°. A t_2 Fourier transformation was carried out and an absolute value presentation was displayed. The spectra shown correspond to the column at the H_2O chemical shift extracted from this interferogram. The spectra in (a) and (b) were recorded respectively with phase x and $-x$ for the first 90° pulse. The spectra were acquired with only z-PFGs (dashed line) and with MAGs (full line). The gradients selected the anti-echo pathway. The gradient recovery time was 200 μs and the DQ excitation period τ was 30 ms. One scan was recorded for each β increment. The repetition time and the acquisition time were 15 s and 0.5 s, respectively. The value 0% and 100% refer to the minimum and maximum observed H_2O signal. The vertical lines correspond to the β angles of the detection pulse that are used in different versions of the DQ experiment. (Reproduced with permission from Dalvit and Böhlen.[124])

180° the phase of the first 90° pulse of the scheme of Fig. 2b is shown in Fig. 10b. In this case the H_2O magnetization at the beginning of t_2 has $-z$-component for $270° < \beta < 90°$. The resulting spectra correspond to the spectra of Fig. 10a shifted by 180°.

Based on these observations it was easy to modify the pulse sequence for the echo part of the 60°/120° and 45°/135° PFG DQ experiments. In addition to the opposite sign of the first two PFGs and different β angle for the detection pulse, the echo version differs from the anti-echo version in a 180° phase shift of the first 90° pulse and of the receiver.[124] The shift in the receiver phase is applied simply to avoid phase corrections after Fourier transformation. For long t_1 periods (>20–30 ms), radiation damping may bring H_2O from the $-z$ axis to

the $+z$ axis during t_1 in the echo version. If necessary, this phenomenon can be suppressed by incorporating in the pulse sequence of Fig. 2c two weak bipolar PFGs applied for the entire length of t_1.[140]

The 1D version of the PFG DQ experiment is recorded with the pulse sequence of Fig. 2c by setting t_1 to 3 μs and by selecting with the gradients one of the two possible coherence pathways, preferably the echo pathway because it contains less residual H_2O signal. As discussed above, maximum sensitivity is obtained when β is set to 120°.

DMSO (CH_3SOCH_3), acetone (CH_3COCH_3), acetonitrile (CH_3CN) and methanol (CH_3OH) in H_2O are singlets and therefore, like H_2O, cannot create DQ via scalar couplings. The use of MAGs for solvent suppression is not limited to samples in H_2O but can also be extended to the suppression of these solvents and mixtures of them.[141] Application of this technique in the identification of drugs in blood plasma is shown in Fig. 11. The first serial file of a 2D MAG DQ experiment recorded for a sample of blood plasma in a mixture of H_2O, CH_3OH and CH_3CN is displayed in Fig. 11 (lower trace). The strong solvents resonances and their ^{13}C-satellite signals present in the reference spectrum (Fig. 11 upper trace) are completely suppressed in the MAG DQ spectrum. The resonances of the drugs α-yohimbine and Lamisil present in this plasma sample are visible in the MAG DQ spectrum. The olefinic resonances of Lamisil are at the limit of detection in the 1D DQ spectrum, but are clearly visible in the 2D DQ spectrum (Fig. 11 contour plot). The complete solvent suppression allows the observation of resonances that have exactly the same chemical shifts as the solvents.

Another application of the experiment of Fig. 2c is in the detection and measurement of homonuclear dipolar couplings in biological molecules dissolved in an aqueous, dilute, liquid crystalline phase.

5.2. Solvent–solute DQC

DQ spectra recorded with the pulse sequence of Fig. 2b using three z-PFG for coherence selection contain weak signals located on a diagonal at $\omega_2 = \omega_{\text{solute}}$ and $\omega_1 = \omega_{\text{solute}} + \omega_{H_2O}$.[141] This is shown experimentally in Fig. 12a, where a small region of the DQ spectrum recorded for the protein lysozyme dissolved in H_2O is displayed. Some of these signals originate from protons that reside in the interior of the protein but nevertheless are involved in intermolecular DQC with the solvent. The H_2O–protein DQ signals are suppressed in the DQ spectrum recorded with the same pulse sequence of Fig. 2b but with MAGs for coherence selection (Fig. 12b) or simply with the pulse sequence of Fig. 2c and only z-PFGs (Fig. 12c). Thus, the function of the two weak z-PFGs applied at the beginning and end of the excitation DQ period is not only to reduce the solvent–solvent DQ signals but also to reduce significantly the solvent–solute DQ signals. In the absence of the two weak PFGs, radiation damping exerts a

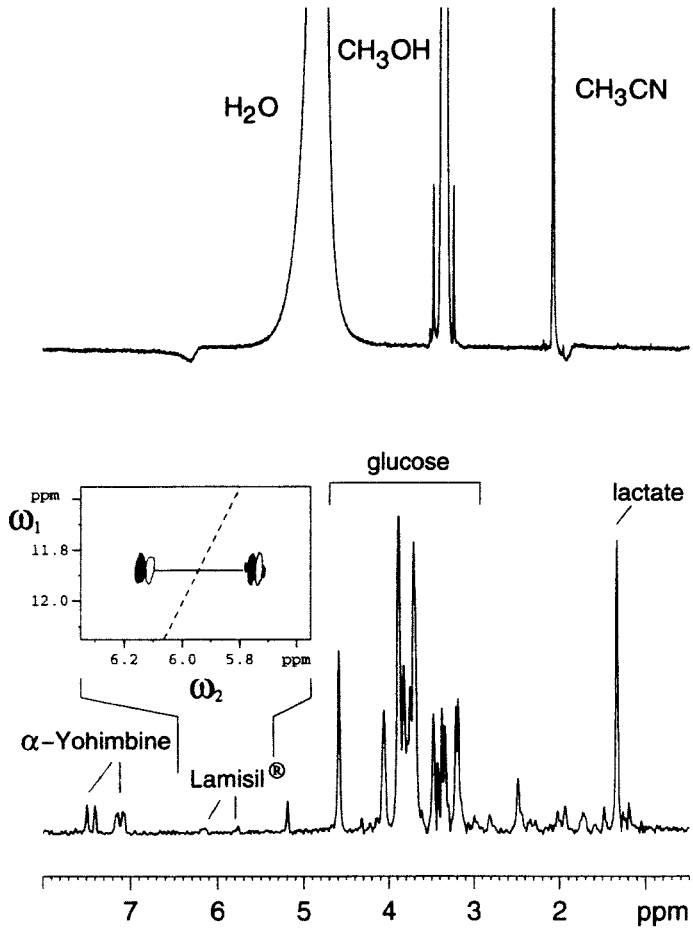

Fig. 11. (a) One-dimensional reference spectrum (upper trace), 1D MAG DQ (lower trace) and an expanded region of the 2D MAG DQ spectrum (contour plot). The sample is a rat plasma solution in H_2O, CH_3OH and CH_3CN containing the drugs α-yohimbine and Lamisil®. The data were simply multiplied with a cosine window function prior to Fourier transformation. No treatment of the data was carried out for solvent suppression. The complete suppression of the solvent resonances and of their ^{13}C satellite signals in the MAG DQ spectrum allows the identification of the resonances of the drugs present in this sample. The olefinic resonance of Lamisil®, although at the limit of detection in 1D MAG DQ spectrum, are clearly visible in the 2D spectrum.

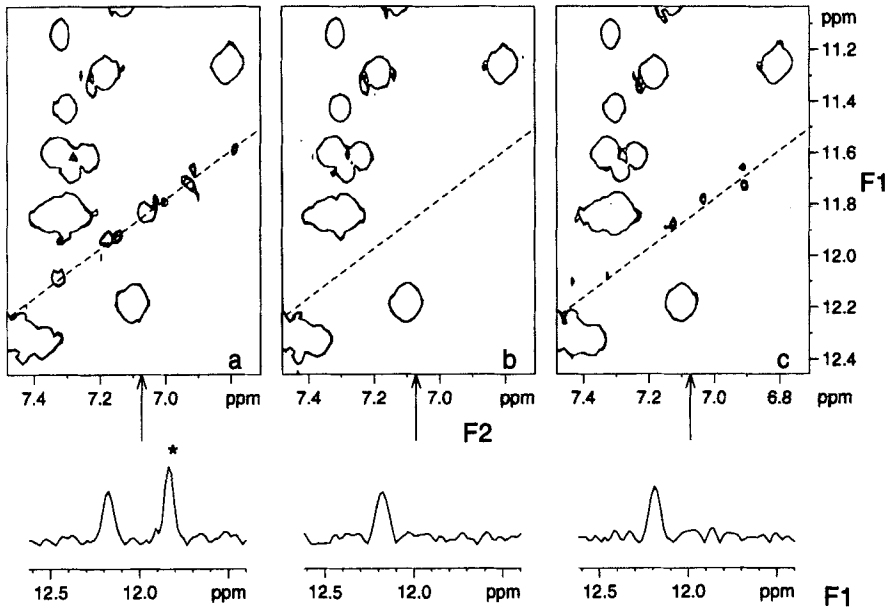

Fig. 12. A small region of the DQ spectrum recorded for an aqueous solution of the protein chicken egg-white lysozyme. The spectra in (a) and (b) were recorded with the scheme of Fig. 2b with z-PFGs and MAGs, respectively. The spectrum in (c) was recorded with the scheme of Fig. 2c and only z-PFGs. Sixteen scans were recorded for each of the 512 t_1 increments. The τ period was 30 ms and the repetition time was 2.17 s. The transmitter was set 280 Hz upfield from the H_2O signal. Similar results were obtained with the transmitter set at the H_2O frequency (data not shown). The absolute value presentation is displayed owing to the mixed phase of the solvent–solute intermolecular DQ signals. These weak peaks lie on the dotted diagonal in (a) at $\omega_1 = \omega_{H_2O} + \omega_{protein}$ and $\omega_2 = \omega_{protein}$. These signals are absent in (b) and are strongly attenuated in (c). The 1D spectra are columns extracted from the three 2D spectra at the ω_2 frequency indicated by the arrow. The solvent–solute DQ peak labelled with an asterisk in (a) is absent in (b) and (c).

rotary force on the H_2O magnetization and at the end of the excitation DQ period the solvent magnetization has a z component. The application of the second 90° pulse converts this component to transverse magnetization, which is modulated during t_1. In the presence of the two weak z-PFGs, all H_2O magnetization is aligned along the z-axis during t_1. The intensity of the solvent–solute DQ signals in the DQ experiments is directly proportional to the amount of transverse solvent magnetization present during t_1. For example, DQ experiments recorded with the pulse sequence of Fig. 2c with z-PFGs and with the second 90° pulse with phase y results in spectra with stronger solvent–solute DQ peaks (data not shown). According to the theory developed by Warren and co-workers,[87] this intermolecular DQ coherence originates

from the long-range solvent–solute DD couplings that are not averaged out in the presence of z-gradients. It should be pointed out that these signals are different from the DQ H_2O–macromolecule signals recently detected in rat tail tendon,[142] i.e. a highly anisotropic milieu.

5.3. Multiplet resonances

The use of MAGs for solvent suppression in DQ experiments is restricted only to solvents that are singlets. However, other solvent systems including ethanol, tetrahydrofuran, ethyl acetate and many others give rise to spectra with resonances having multiplet structure. The creation of DQC between these spins via scalar couplings results in DQ spectra with very strong DQ solvent peaks. These signals obscure the weak DQ solute signals and therefore have to be suppressed by other methods.

A scheme that achieves this purpose is shown in Fig. 13. During the excitation DQ period, two excitation sculpting sequences[143] with the modification for multiple solvent suppression[144] (see Section 8) are applied. The selective pulses of the excitation sculpting sequence are soft 180° shifted laminar pulses (SLP)[145,146] with excitation at the different solvent's multiplet resonances. These pulses are very selective in order to restrict the band of excitation. The solvent magnetization is completely dephased by these schemes and is not refocused by the coherence selection gradients. Application of this DQ experiment to a sample of the peptide Sandostatin dissolved in THF is shown in Fig. 14. The almost complete suppression of the strong solvent DQ signals permits the analysis of the solute. DQ connectivities of the peptide resonating at or near the ω_2 solvent signal frequencies can also be detected. However, these connectivities will be partially attenuated. DQC between two spins is created starting from both spins. If one of the two spins resonates at the solvent frequency, only the other spin contributes to the generation of DQC during the DQ excitation period. The net result is that the DQ connectivity involving these spins is attenuated by 50%.

5.4. Creation of DQC through carbon isotopic effect

The two methyl groups of DMSO and acetone are magnetically equivalent ($J = 0$) and therefore do not create DQC via scalar coupling. However, this overlooks the fact that in natural abundance 1.1% of the carbon positions are occupied by ^{13}C. In the molecules of DMSO with one ^{13}C atom ($^{13}CH_3{-}SO{-}{}^{12}CH_3'$), the methyl groups are scalar coupled ($^4J_{HH'} \cong 0.5$ Hz)[147] and therefore it is possible to generate DQC between them. Figure 15a shows

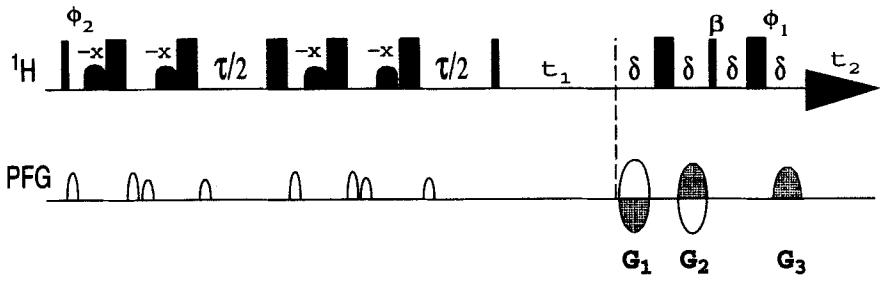

Fig. 13. Pulse sequence of the 2D ^{1}H PFG phase-sensitive DQ experiment with multiple suppression of solvent DQC created via scalar coupling. The selective ^{1}H pulses are soft 180° SLPs with excitation at the different solvent multiplet resonances. If necessary a ^{13}C filter can be applied as discussed later (see text). The gradients G_1 to G_3 are the coherence selection gradients of the DQ experiment. The angle β of the read-out pulse in (b) and (c) can be set to 90° (anti-echo)/90° (echo) or to 45° (or 60°) (anti-echo)/135° (or 120°) (echo). For the versions with $\beta = 90°/90°$ the phases are $\phi_1 = 2(x), 2(-y), 2(-x), 2(y)$; $\phi_2 = (x, -x)$; and $\phi_{rec} = (x, -x, -x, x)$. In the version with $\beta = 45°/135°$ or $\beta = 60°/120°$ the phases are $\phi_1 = (x, -y, -x, y)$ for both pathways selections; $\phi_2 = x$, $\phi_{rec} = (x, -x)$ for the anti-echo pathway selection; and $\phi_2 = -x$, $\phi_{rec} = (-x, x)$ for the echo pathway selection.

the experimental multiplet structure of DMSO recorded with the pulse sequence of Fig. 2c. This multiplet structure is verified in the simulation (without gradients) shown in Fig. 15b. The DMSO multiplet is centred at the proton {SQ} frequency ($\Omega_H = \Omega_{H'} = 2.5$ ppm) and {DQ} frequency ($\Omega_H + \Omega_{H'} = 2\,\Omega_H = 5$ ppm), in ω_2 and ω_1, respectively. The antiphase structure in ω_2 arises through the active coupling $^4J_{HH'}$. This multiplet is further split according to the passive heteronuclear couplings $^1J_{HC}$ and $^3J_{H'C}$ in both dimensions. The different components of the multiplet are centred at the positions

$$(\omega_1'; \omega_2') = (2\Omega_H + (J_{HC} + J_{H'C})/2; \Omega_H + J_{HC}/2)$$

$$(\omega_1''; \omega_2'') = (2\Omega_H + (J_{HC} + J_{H'C})/2; \Omega_H + J_{H'C}/2)$$

$$(\omega_1'''; \omega_2''') = (2\Omega_H - (J_{HC} + J_{H'C})/2; \Omega_H - J_{HC}/2)$$

$$(\omega_1''''; \omega_2'''') = (2\Omega_H - (J_{HC} + J_{H'C})/2; \Omega_H - J_{H'C}/2)$$

In our experiment, the delay for the creation of DQC was not tuned to the small coupling $^4J_{HH'}$. Nevertheless, owing to the high concentration of the solvent, the intensities of the DMSO DQ signals were of the same order of magnitude as those of the molecule of interest. It is possible to halve the intensity of these peaks by employing the ^{13}C filter as discussed in Section 9.

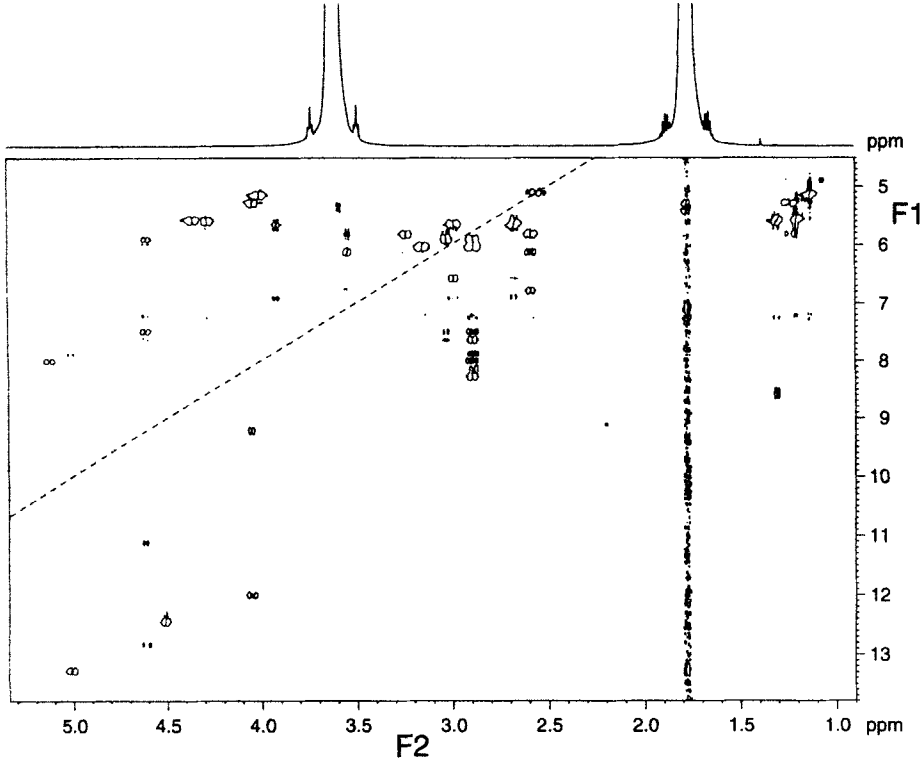

Fig. 14. DQ spectrum recorded with the scheme of Fig. 13 for a 1 mg solution of the peptide Sandostatin® dissolved in THF-*h*8. Eight scans were recorded for each of the 256 t_1 complex points. The lengths of the double-selective 180° rectangular SLPs and of the gradients were 2.5 and 1.2 ms, respectively. The dashed line is the DQ diagonal. The upper trace contains the 1D reference spectrum of the solution.

6. SENSITIVITY CONSIDERATIONS

Sensitivity comparison between different experiments is a complex matter and is subject to controversy. The particular choice of several experimental parameters can influence differently the performance of the experiments to be compared. In the comparison presented here, we have tried as far as possible to use the same experimental conditions.[148]

6.1. Comparison with ^{1}H 2D DQ

The use of coherence selection gradients in the 2D 90°/90° PFG DQ experiment results in a $\sqrt{2}$ theoretical loss in sensitivity compared to the respective

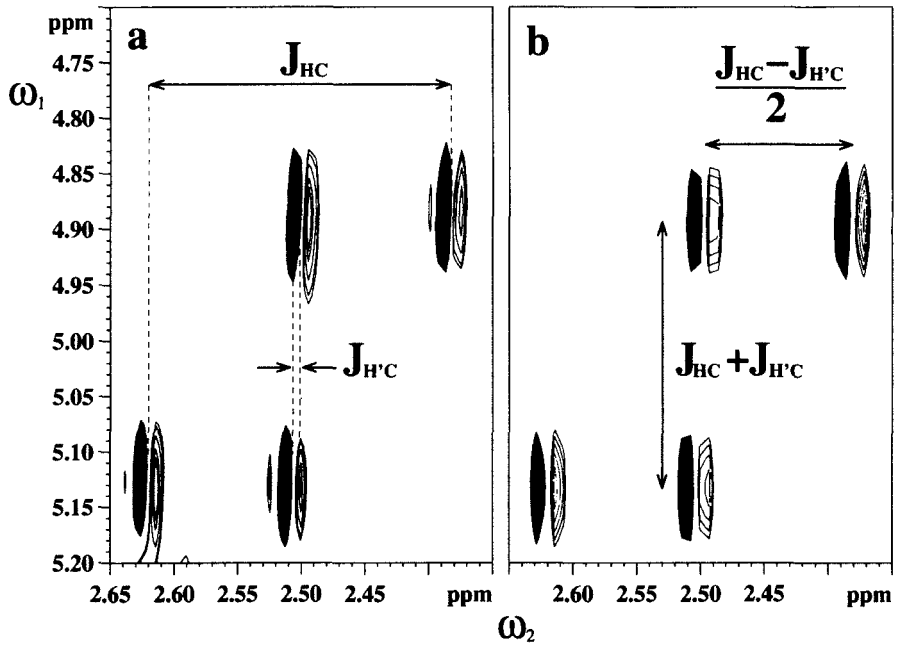

Fig. 15. Multiplet structure of DMSO at ^{13}C natural abundance obtained experimentally (a) and by simulation (b) in the 2D DQ ^{1}H spectrum recorded with a DQ excitation period of 30 ms. No relaxation was taken into account for the simulation. Both spectra were acquired with resolutions of 4.1 and 24.4 Hz per sampling point and processed with resolutions of 4.1 and 6.1 Hz per sampling point, in ω_2 and ω_1, respectively. For the experimental spectrum, Gaussian (LB = −16, GB = 0.37) and cosine^2 window functions were applied in ω_2 and ω_1, respectively. In the simulated spectrum, Gaussian window functions were adjusted in both dimensions in order to fit the experimental multiplet lineshape (LB = −20, GB = 0.32 in ω_2 and LB = −0.07, GB = 0.0005 in ω_1). The spin system was defined as two groups of methyl protons H and H′ ($\Omega_H = \Omega_{H'} = 2.5$ ppm) strongly coupled ($^4J_{HH'} = 0.5$ Hz) and a ^{13}C ($\Omega_C = 39.5$ ppm) weakly coupled with the methyl protons H ($^1J_{HC} = 137$ Hz) and with the methyl protons H′ ($^3J_{H'C} = 4$ Hz). The residual signals in the lower left part of the experimental spectrum are DQ signals from the analyte dissolved in DMSO.

non-gradient DQ experiment.[149] This is because in each data set the PFGs select only one of the two coherence pathways that can contribute to the observed signal. However, the signal loss of the 60°/120° PFG DQ experiment with respect to the TPPI DQ experiment is reduced to 1.088. This implies only an 18% increase in the measuring time of the PFG DQ experiment in order to achieve the same S/N ratio obtained with the non-gradient DQ version.

However, experimental factors contribute to the superior performance of the PFG version. Phase cycling, which is a method based on difference spectroscopy, is used in the non-gradient DQ experiment to select the proper

coherence pathway. Owing to various instabilities, the resulting spectra contain some residual t_1 noise originating from improper cancellation of the undesired magnetization. This problem is not present in the PFG DQ version because the gradients select in every transient only the desired coherence pathway. Therefore the limits of signal detection in the PFG DQ experiment are determined solely by the thermal noise and not by the t_1 noise. Furthermore, for samples dissolved in H_2O other factors contribute to the better performance of the PFG DQ experiment. The use of H_2O presaturation in the standard DQ experiment has several negative effects. First the saturation of H_2O and the large residual t_1 noise of H_2O do not allow the detection of the $\{DQ\}^{NH\alpha H}$ direct peaks and of the $\{DQ\}^{NH\beta H}$ remote peaks resonating at or close to the H_2O signal. The observation of these resonances is particularly important in DQ spectra of biomolecules for tracing the different amino acid spin systems. Other negative effects are presented in Fig. 16, with two examples extracted from 2D PFG DQ (a,c) and 2D DQ with H_2O presaturation (b,d) experiments acquired for the protein lysozyme dissolved in H_2O (7% D_2O). The spectra have been recorded using the same experimental parameters and are displayed at the same level. The signal improvement for some resonances in the PFG DQ spectra is striking. The radio-frequency field applied at the H_2O frequency produces an evolution of the populations of the two energy levels towards equalization and therefore the longitudinal H_2O magnetization decays to zero. The main disadvantages of using H_2O irradiation are that the longitudinal magnetization of the resonances close to the H_2O signal also decay to zero and that saturation transfer may partially saturate fast exchangeable NH resonances.[11] The $\{DQ\}^{NH\alpha H}$ coherence is created starting from both ^{N}H and $^{\alpha}H$ spins. Therefore saturation of one or both of these spins will result in a reduced amount of $\{DQ\}^{NH\alpha H}$ coherence (see Section 5.3). This is the case, for example, for the resonances of I88 and T118 in Fig. 16. The $^{\alpha}H$ signals of these residues resonate at the H_2O chemical shift. Saturation transfer results in signal attenuation also via an indirect process. The H_2O irradiation achieves efficient saturation of the OH protons of Tyr, Ser and Thr. During the long irradiation period, which is typically of 1 to 2 s, the magnetization of the OH spins migrates via the efficient flip-flop transitions to other protons close in space. The final result is again a signal reduction of these spins. This is in part the case for the resonance of S50 in Fig. 16. The ^{N}H and $^{\alpha}H$ spins of S50 have reduced intensity at the beginning of the DQ excitation period owing to the intraresidual NOE originating from the OH spin.

6.2. Comparison with ^1H 2D COSY

The COSY experiment[150] is in theory twice as sensitive as the DQ experiment. However, as explained clearly by Cavanagh *et al.*,[11] the performance of the COSY experiment is strongly dependent on some practical parameters. First,

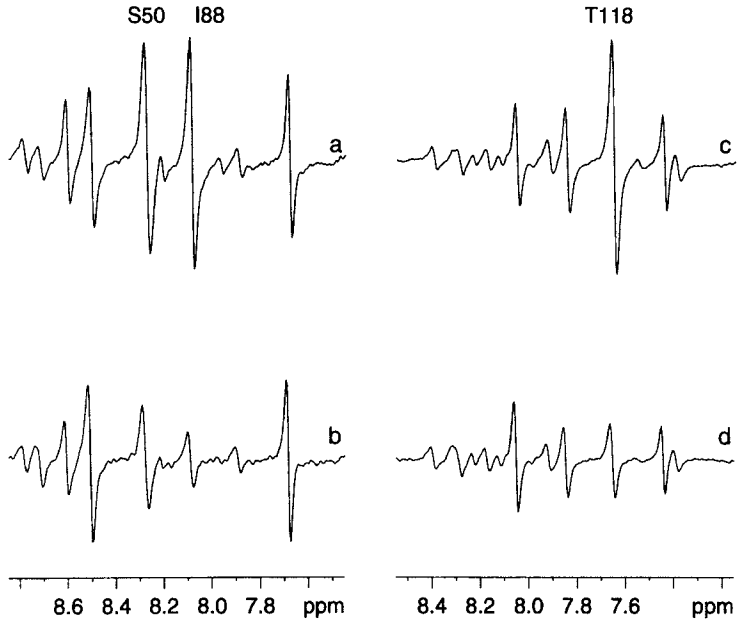

Fig. 16. Two rows extracted from 45°/135° PFG DQ (a,c) and DQ with H_2O presaturation (b,d) spectra recorded for a solution of chicken egg-white lysozyme dissolved in H_2O (7% D_2O) and at pH 3.8. The spectra have been plotted at the same level. The signals present in these rows originate from $\{DQ\}^{NH\alpha H}$. Only the amide region is displayed. The spectra were acquired and processed with the same experimental parameters. The experiments were recorded at T_e = 297 K with a Bruker Avance-500 spectrometer. Sixteen scans were acquired for each of the 300 t_1 increments. The repetition time and the τ delay were 1.65 s and 30 ms, respectively. The length of the H_2O presaturation period was 1.4 s and the strength of the RF field was 50 Hz. The gradient recovery time was 100 μs. The data were multiplied with a cosine window function in both dimensions prior to Fourier transformation. The NH of I88, S50 and T118 (assignment taken from reference 245) are labelled. The sensitivity improvement in the PFG DQ vs DQ with presaturation experiment for S50, I88 and T118 is 2.0, 4.2, 3.1, respectively. (Reproduced with permission from Dalvit and Böhlen.[148] © John Wiley & Sons Ltd.)

the digital resolution in t_1 is critical in the COSY for determining the relative cross-peak intensity. The COSY multiplets are antiphase in both dimensions. Low digital resolution in ω_1 results in partial cancellation of the positive and negative lobes of the cross-peaks, with consequent reduction of the signal intensity. This effect is more pronounced for the cross-peaks with small active coupling constants. Second, the COSY experiment is a so-called t_1 sine-modulated experiment owing to its sin $\pi J t_1$ dependence. As a result, a large number of t_1 increments is required if cross-peaks are to be observed. In contrast, DQ experiments are cosine-modulated experiments and conse-

quently the maximum signal is observed in the first t_1 increments. DQ experiments can be recorded rapidly by acquiring only a small number of t_1 increments. Linear prediction can then be applied in the t_1 dimension for improving the frequency resolution.[151] Furthermore, the presence of the strong dispersive diagonal peaks in the COSY experiment introduces t_1 noise in the spectra and does not allow the observation of connectivities between spins with almost degenerate chemical shift. These problems are not encountered in the DQ experiments.

Figure 17 shows two rows extracted from ^{1}H PFG DQ and ^{1}H COSY with H_2O presaturation experiments recorded for a biological plasma sample. These rows contain the signals of the amino acids Ala and Tyr, which are found in biological plasma. The two 2D PFG DQ spectra were recorded with read-out pulses $\beta = 45°/135°$ and 90°/90° (two spectra on the left). The COSY spectrum was acquired with the same measuring time and processed with two different window functions (two spectra on the right). The peaks with the highest S/N ratio are observed in the DQ spectra.

6.3. Comparison with ^{1}H 2D TOCSY

A t_1 cosine-modulated experiment that provides information about the spin system networks is the TOCSY experiment.[152,153] The version of this experiment with the WATERGATE scheme[154,155] is usually employed for the analysis of samples dissolved in H_2O.

The intensity of a TOCSY cross-peak depends on all the couplings within a spin system. TOCSY experiments with short isotropic mixing periods are recorded in order to ensure magnetization transfer through a single scalar coupling interaction and therefore give information similar to the COSY and DQ experiments. However, the presence of zero-quantum artefacts in these spectra, especially for small and medium-size molecules, distorts severely the cross-peaks. The use of z-filters[156,157] or of a spin-lock pulse combined with a gradient[158] at the end of the TOCSY experiment partially reduces this effect. Assignments based on the TOCSY cross-peak intensities are not infallible, especially for complex spin system networks. For long mixing periods the ROE transfer, which is of opposite sign to the TOCSY transfer, attenuates the TOCSY cross-peaks between spins that are close in space. The use of 'clean' isotropic mixing sequences[159] suppresses this effect in TOCSY experiments of large molecules. Its use cannot be extended to small molecules because the NOEs and ROEs in small molecules have the same sign.

Figure 18 shows three cross-peaks extracted from two ^{1}H 2D PFG DQ spectra recorded with read-out pulses $\beta = 45°/135°$ and 90°/90° (left) and three 2D WATERGATE TOCSY (right) spectra recorded for a biological plasma sample. The DQ cross-peaks for the small molecules Ala and Tyr are clearly more intense than the respective TOCSY cross-peaks. However, for large

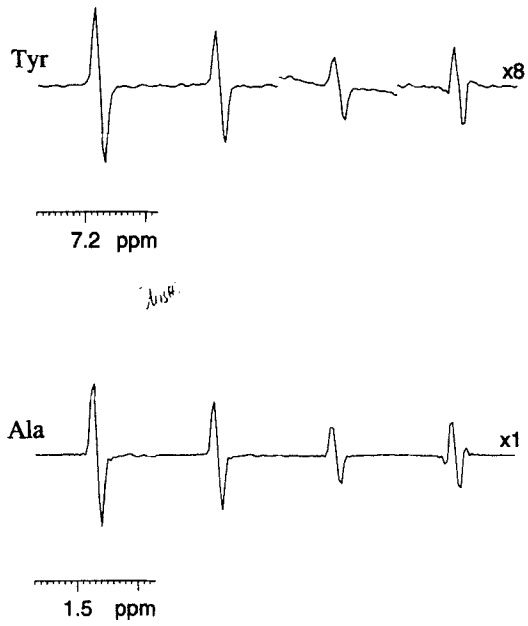

Fig. 17. Two rows extracted from 2D spectra recorded for a sample of rat blood plasma. The cross-peaks are for the amino acids Ala and Tyr. The cross-sections from left to right are from 2D 45°/135° PFG DQ, 90°/90° PFG DQ, and two differently processed COSY spectra with presaturation, respectively. The spectra are plotted at the same level. The scale tick spacing corresponds to 0.01 ppm. The experiments were recorded at T_e = 297 K with a Bruker Avance-500 spectrometer. Sixteen scans with a repetition time of 1.65 s were recorded for each of the 512 t_1 increments. The length of the H_2O presaturation period was 1.4 s and the strength of the RF field was 50 Hz in the COSY experiment. The excitation DQ period τ and the gradient recovery time were 32 ms and 100 μs, respectively. The three spectra on the left were processed with cosine window functions applied in both dimensions. The COSY spectrum on the right was processed in both dimensions with 3° shifted sine-bell window functions. The use of this strong window function best matches the detected COSY signal. The relative intensity of the cross-peaks, normalized to the cross-peak intensities in the 90°/90° PFG DQ spectrum, for both Ala and Tyr are, from left to right, 1.3, 1.0, 0.5, 0.6, respectively. (Reproduced with permission from Dalvit and Böhlen.[148] © John Wiley & Sons Ltd.)

molecules such as the VLDL particles in plasma the TOCSY cross-peaks are more intense than the DQ cross-peaks. The TOCSY cross-peaks are in-phase in both dimensions, whereas the DQ cross-peaks, as seen in Section 3, are predominantly in-phase in ω_1 and antiphase in ω_2. The large half-height width of the VLDL CH_3 resonance (30 Hz) attenuates the intensity of the DQ cross-peak due to the partial cancellation of the positive and negative lobes along ω_2. The spectra in the right column of Fig. 18 will be discussed in Section 9.

6.4. Comparison with double-quantum filter COSY

Another experiment that achieves excellent H_2O suppression by employing magic angle gradients is the PFG double-quantum filter (DQF) COSY.[126,160] Sensitivity and quality of the water suppression of the PFG DQ experiment have been compared to those of PFG DQF COSY.[161,162] A double-quantum-filtered COSY was performed under conditions comparable to those used for the DQ experiment. The MAG DQF COSY pulse sequence[161] was $(\pi/2)$–t_1–$(\pi/2)$–δ–(π)–MAG_1–$(\pi/2)$–δ–(π)–MAG_2, where $MAG_2 = 2\,MAG_1$ and MAG_2 has also the same strength and length as the last MAG of the DQ experiment. A significant improvement in the H_2O suppression, by a factor of 32, was observed in the DQ experiment vs the DQF COSY experiment (Fig. 19). This improvement might be of importance for the observation of very diluted species, where the dynamic range of the receiver needs to be utilized in an optimal way.

As mentioned earlier, another important aspect is the sensitivity of the method. Figure 19 shows slices extracted from the two experiments recorded for biological plasma in order to compare the correlation peaks of lactate CH, the citrate CH_2 and the threonine β-CH signals. The striking superior sensitivity of the DQ experiment can be explained with simple considerations. The ^1H DQF COSY experiment has a two-fold decrease in sensitivity compared to the COSY experiment. Furthermore, the use of PFGs in DQF COSY experiments results in an additional two-fold signal loss. The other sensitivity considerations explained for the COSY experiment apply also for the DQF COSY experiment.

7. REFOCUSED ^1H PFG DQ

The antiphase multiplet structure of DQ peaks along ω_2 limits the application of the technique to small and medium-size molecules. However, it is possible to record in-phase DQ spectra by refocusing the coupling constant[163–165] as shown, for example, with the pulse sequence of Fig. 20a. In this experiment, antiphase magnetization present at the beginning of τ' is partially refocused to in-phase magnetization at the end of τ' and detected after a z-filter. The remaining antiphase magnetization present at the end of τ' is transformed by the penultimate 90° pulse to a mixture of ZQC and DQC. The gradient in the z-filter[166] destroys the DQC, whereas the contribution of ZQC to the detected signal is reduced by varying in a defined way from scan to scan the length of the z-filter delay.

In spite of the favourable in-phase multiplet structure of the peaks, the refocused DQ experiment suffers from other limiting factors. At the end of the refocusing period τ', not all the antiphase magnetization is refocused into in-phase magnetization. In addition, there are magnetization losses due to the

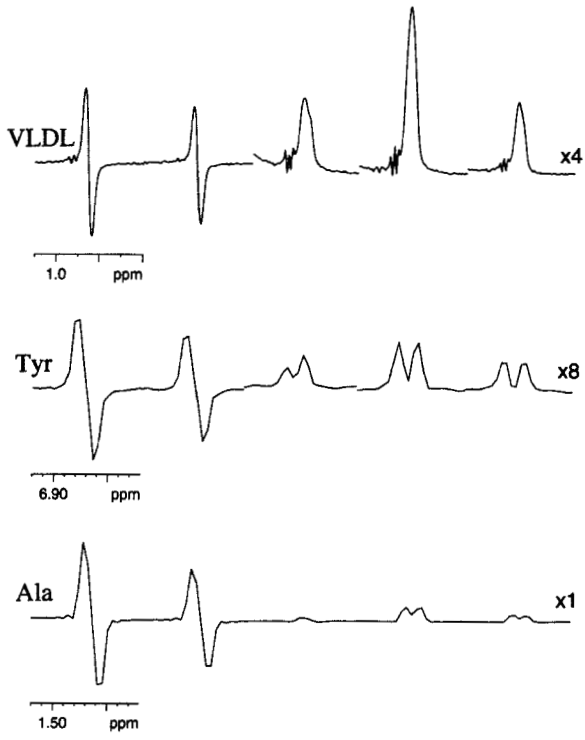

Fig. 18. Three rows extracted from 2D spectra recorded for a sample of biological plasma. The cross-peaks are for the amino acids, Ala and Tyr and for VLDL particles. The cross-sections from left to right are from 2D 45°/135° PFG DQ, 90°/90° PFG DQ, WATERGATE TOCSY with $\tau = 15$ ms, WATERGATE TOCSY with $\tau = 31$ ms and WATERGATE stimulated-echo TOCSY with $\tau = 31$ ms. The τ period represents the length of the spin-locking period. The spectra are plotted at the same level. The scale tick spacing corresponds to 0.01 ppm in the lower spectra and 0.1 ppm in the upper spectrum. The experiments were recorded at $T_e = 297$ K with a Bruker Avance-500 spectrometer. Sixteen scans with a repetition time of 1.65 s were recorded for each of the 400 t_1 increments. The other acquisition parameters are the same as described in Fig. 17. In the stimulated-echo TOCSY experiment the delay between the start of the two bipolar gradients comprising the stimulated echo scheme was 31 ms. The length of the two sine-shaped bipolar gradients was 1.25 ms. Their strength was set to the low value of $|0.35|$ G cm^{-1} in order to avoid signal attenuation due to spatial diffusion and thus allow a direct comparison with the other experiments. The relative cross-peak intensities, normalized to the cross-peak intensities of the 90°/90° PFG DQ spectrum, are from left to right for Ala 1.4, 1.0, 0.1, 0.3, 0.2, for Tyr 1.3, 1.0, 0.6, 1.0, 0.5 and for VLDL 1.3, 1.0, 1.0, 3.1, 1.3. (Reproduced with permission from Dalvit and Böhlen.[148]

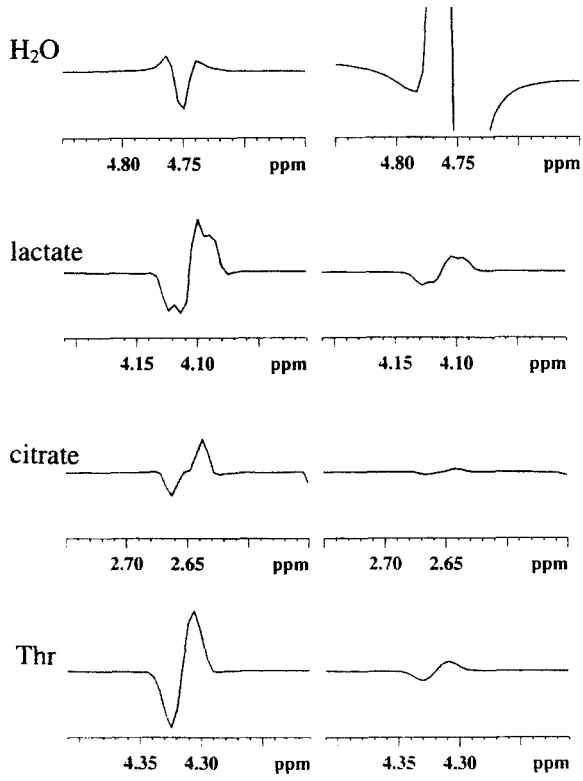

Fig. 19. Slices from 2D MAG experiments recorded at T_e = 297 K for a sample of biological plasma, using same acquisition and processing parameters. The spectra were recorded with a Bruker Avance-600 spectrometer. The slices are from MAG DQ spectrum (left) and MAG DQF COSY spectrum (right). For the DQF COSY experiment (see text), the last gradient has the same strength and length as the last PFG of the DQ experiment. The slices, plotted at the same level, show the H_2O, lactate CH, the citrate CH_2 and the threonine β-CH signals. The signal-to-noise ratio is 3.5, 9.0 and 5.4 times higher, for lactate, citrate and Thr, respectively, in the DQ than in the DQF COSY. In contrast, the water peak is 32 times smaller in the MAG DQ experiment compared to the MAG DQF COSY.

spin–spin relaxation (T_2) occurring during the additional refocusing period. The experiment is hence applicable only to concentrated samples. Another variant of the refocused PFG DQ experiment, as shown in Fig. 20b, can be used if the spectral analysis is limited only to a certain spectral region, for example the amide region. A semi-selective shaped pulse homodecoupling[167] is applied in the αH spectral region during t_2. The use of the z-filter is not necessary in this experiment because the decoupling sequence destroys the antiphase multiplet components. The amide resonances in this experiment are decoupled

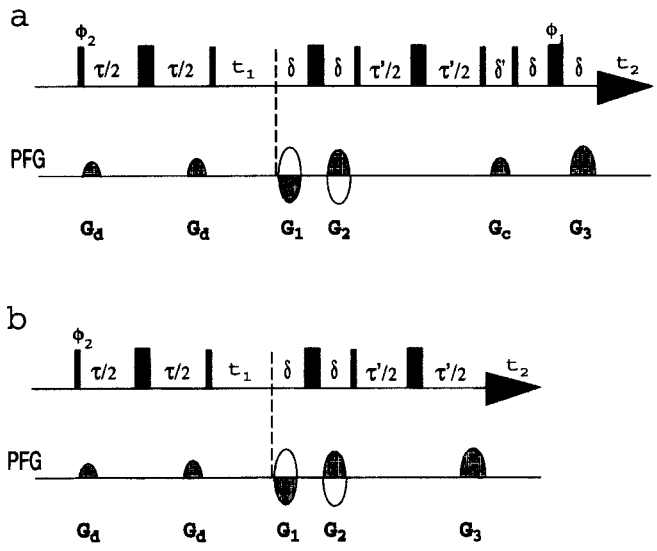

Fig. 20. Pulse sequences for recording (a) ^{1}H phase-sensitive PFG refocused DQ experiment (b) ^{1}H phase-sensitive PFG refocused DQ with homonuclear band-selective shaped pulse decoupling. The phases are $\phi_1 = 2(x)$, $2(-y)$, $2(-x)$, $2(y)$; $\phi_2 = (x, -x)$; and $\phi_{rec} = (x, -x, -x, x)$. The gradient G_c is a *crusher*. The period τ' is the refocusing period. The period δ' of the z-filter is varied in a defined way for reduction of the ZQC contribution. All other symbols have the same meaning as previously. In (b) homonuclear semi-selective shaped pulse decoupling is applied during t_2.

from the α protons and their signal heights should increase with respect to the version without decoupling. However, in reality, the presence of a large H_2O signal in these experiments results in an increased noise level.

8. INTEGRATED STRATEGY FOR ANALYSIS OF SAMPLES IN LC- NMR

The direct coupling of chromatographic separations to NMR spectroscopy (LC-NMR) is becoming a powerful method for the characterization of individual components present in biofluids, natural product extracts and combinatorial chemistry mixtures.[168,169] A problem that delayed useful application of the technique was the requirement for use of prohibitively expensive deuterated solvents. Nowadays, thanks to the development of new solvent suppression schemes and thanks to the technological developments, the use of deuterated solvents is no longer necessary. One of the common solvent mixtures used in reversed-phase high-performance liquid chromatography

(HPLC) is acetonitrile and H_2O. D_2O is used in LC-NMR rather than H_2O in order to make the multiple solvent suppression of the acetonitrile and of the residual H_2O signals more efficient. However, the use of D_2O has the drawback that the exchangeable resonances are not visible in the spectrum. Furthermore, even if D_2O is not as expensive as other deuterated solvents, massive use of it in large-scale analysis results in significant costs.

We propose in the following a concerted strategy that can be used in LC-NMR and that does not require the use of D_2O.

8.1. One-dimensional experiments

First a one-dimensional proton spectrum is acquired using the multiple solvent pulse sequence depicted in Fig. 21a. This sequence is a modified version[144] of the excitation sculpting sequence (also known as DPFGSE[170,171] solvent suppression) proposed by Hwang and Shaka.[143] The two selective 180° pulses are SLPs with excitation at the frequencies of the different solvents. The ^{13}C-satellite signal suppression is achieved by applying ^{13}C decoupling during the ^1H soft 180° pulses.[144,172] An alternative to this scheme is the use of two hard ^{13}C pulses applied at two different delays from the first 90° hard pulse. The length of these delays and of the ^{13}C pulses are varied in an interactive way until minimum intensity for the ^{13}C satellite signals is observed. The set-up of these schemes is easy and straightforward. However, the experiment with ^{13}C decoupling is simpler and does not require the interactive optimization necessary with the other method. An inevitable drawback is the bleaching of a small spectral region centred at the solvent frequencies. This bandwidth depends on the selectivity and on the type of soft 180° SLP pulses employed.

Figure 22 shows the simulated suppression profiles obtained for 5 ms 180° square, sinc, sine and Gaussian pulses. For the Gaussian pulse,[173] different truncation levels have been used, namely 1%, 40% and 80% of the maximum amplitude. In terms of selectivity of the suppression domain, the square pulse has the best properties (200 Hz at half-height), but a suppression of about 20% is also observed on the first sidelobes. The popular Gaussian pulse truncated at 1%, which gives almost no suppression outside of the excitation spectral region, has the widest profile of the used shapes. This can be explained in a qualitative way by the fact that this shape has the smallest relative integrated amplitude (only 41% of that of the square pulse) or the narrowest width at half-height. Minimization of the sidelobes is obtained with shapes that have slow ascending and descending edges, but this causes a broadening of the suppression profile. A good compromise is obtained between selectivity of the suppression (240 Hz) and attenuation of the sidelobes (~6% suppression on the first sidelobe) with the Gaussian pulse truncated at 40% (integrated amplitude is 76% of that of the square pulse).

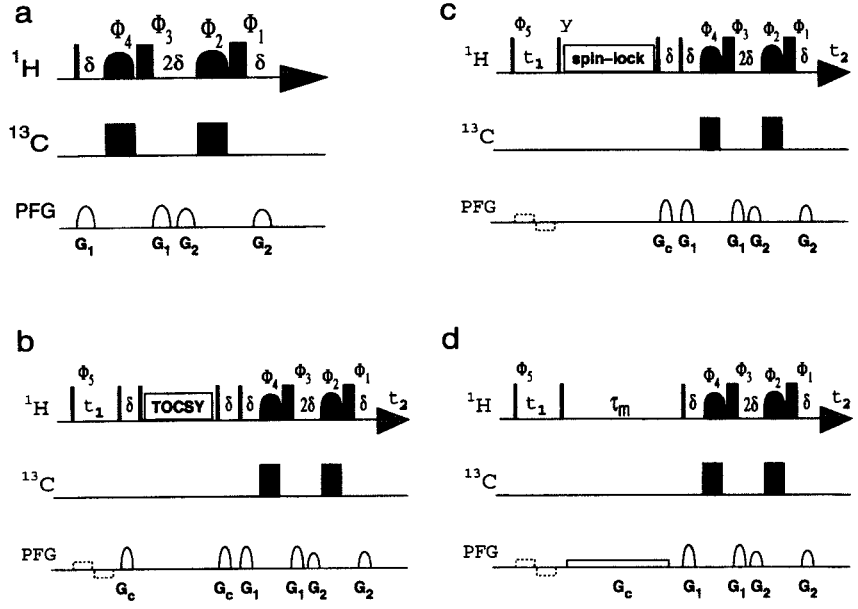

Fig. 21. Pulse sequences for recording 1D (a) and 2D (b–d) spectra with multiple solvent suppression. The selective ^{1}H pulses are soft 180° SLP with excitation at the different solvent resonances. These pulses are either soft rectangular or strongly truncated Gaussian pulses. The suppression of the solvent ^{13}C-satellite signals is achieved with ^{13}C decoupling applied during the entire length of the ^{1}H soft 180° pulses. The other method for ^{13}C-satellites signal suppression is described in the text. The phases are (a–d) $\phi_1 = (x, y, -x, -y)$; $\phi_2 = (-x, -y, x, y)$; $\phi_3 = 4(x), 4(y), 4(-x), 4(-y)$; $\phi_4 = 4(-x), 4(-y), 4(x), 4(y)$; (a) $\phi_{rec} = 2(x, -x), 2(-x, x)$. The phases of the first pulse and of the receiver in (b–d) are $\phi_5 = 16(x), 16(-x)$ $\phi_{rec} = 2[2(x, -x), 2(-x, x)], 2[2(-x, x), 2(x, -x)]$. The phase cycle can be reduced to eight steps.[188] The spin-lock in (c) is achieved with a train of 180° pulses with phase alternately x and $-x$.[249,250] All other pulses have phase x unless indicated. The gradient G_C are *crushers* for destroying transverse magnetization. The gradient G_c in (d) is a weak PFG applied for almost the entire length of the mixing time τ_m.[140,244,251] The weak bipolar gradients applied during t_1,[140] shown with dashed lines, are optional. These gradients are used for optimal detection of solvent–solute interactions. The two-dimensional experiments are recorded with TPPI method for quadrature detection in ω_1.

In the suppression of several solvent resonances it is important to choose the selective SLP 180° pulses with the narrowest excitation bandwidth. Of all the soft 180° pulses analysed in Fig. 22, those that achieve the best performance are the rectangular and the strongly truncated Gaussian pulses. The multiple solvent suppression achieved with the scheme of Fig. 21a is remarkable and the disadvantage of a small bleached region centred at the solvent frequencies can be accepted. In our experience the use of soft square 180° SLPs of length between 3 and 7 ms achieves good selectivity. If necessary, even longer SLPs

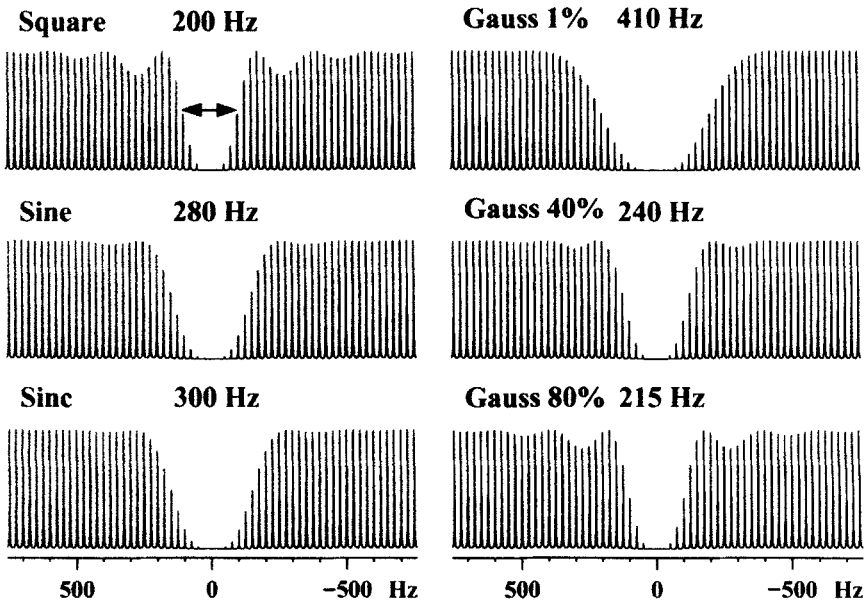

Fig. 22. Simulated suppression profiles of the excitation sculpting experiment using different selective 180° pulses of 5 ms duration: square (field strength $\gamma B_1/2\pi = 100$ Hz); sine (157.2 Hz); sinc with one lobe (169.8 Hz); Gaussian truncated at 1% (243.2 Hz), at 40% (131.1 Hz) and at 80% (107.5 Hz). The hard pulses had 25 kHz strength (corresponding to a 90° pulse of 10 μs), G_1 and G_2 had a duration of 1 ms and strengths of 10 and 3 G cm^{-1}, respectively, and the gradient recovery time was 100 μs. The 1.5 kHz wide profiles were obtained by shifting the transmitter frequency in 25 Hz steps. The values in Hz on the profiles indicate the full width at half height of the suppression domains. (Reproduced with permission from Dalvit *et al.*,[188] John Wiley & Sons Ltd).

can be used, but then the multiplet resonances will contain some dispersive component. This contribution can be suppressed by applying a short spin-lock (1–2 ms) with phase y after the last PFG and before acquisition. The resonances falling in the bleached regions are nevertheless then identified in the 2D spectra or, if triple-axis gradients are available and the resonances are not singlets in a 1D PFG DQ spectrum.

Application of the scheme of Fig. 21a to a 380 μmol l^{-1} solution (205 nmol l^{-1} in 540 μl) of the molecule reserpine (**1**) in 50% CH_3CN and 50% H_2O is shown in Fig. 23. The spectra in (b) and (c) were recorded with the two different ^{13}C filters. The expanded regions in (b) and (c) contain the exchangeable NH resonance. The asterisks indicate the residual solvent resonances.

Other pulse sequences based on gradients and selective pulses for multiple solvent suppression have appeared in the literature. The use of SLP in

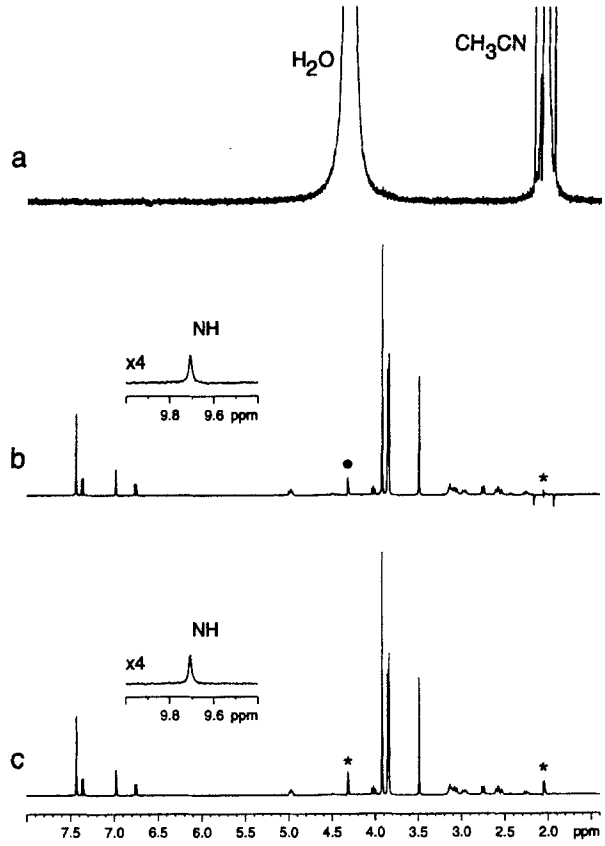

Fig. 23. (a) Reference spectrum of a 380 μmol l^{-1} solution of reserpine in 50% H_2O and 50% CH_3CN (125 μg of (**1**) in 540 μl of solvents). (a) One-dimensional reference spectrum, (b,c) one-dimensional spectra obtained with the scheme of Fig. 21a. The ^{13}C-satellite suppression was achieved with the use of two hard ^{13}C pulses (b) and with ^{13}C decoupling (c). Thirty-two scans were recorded with a repetition time of 3.3 s. No treatment of the data was carried out for the solvent signal reduction. The asterisks indicate the residual solvent signals. The expanded region shows the NH exchangeable proton resonance.

combination with gradients for multiple solvent suppression was described previously in optimized[172] WET[174] and in modified[175] WATERGATE[154,155] pulse sequences. In our experience the scheme of Fig. 21a achieves better multiple solvent suppression than the modified WATERGATE and requires fewer adjustments in the optimization procedure. The WET scheme uses four selective pulses with different tip angle followed by gradients. The soft pulses are more selective than those in the scheme of Fig. 21a and therefore the bleached regions are narrower. However, application of the optimized WET sequence has been reported for CH_3CN:D_2O solvent mixtures.[172] A com-

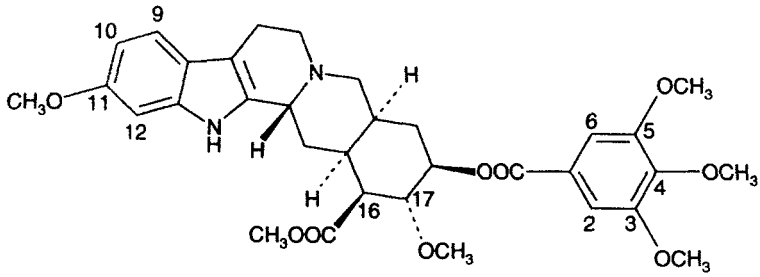

(1)

parison of the performance of the two methods applied to a low-concentration sample dissolved in a non deuterated binary solvent mixture has not yet been carried out. Parella *et al.*[176] proposed a different scheme, also based on the excitation sculpting sequence. The selective 180° pulses are applied sequentially in their scheme.[177] For example, the suppression of two solvent signals is achieved with the use of four selective 180° pulses. The sequence allows independent optimization of the selective pulses and consequently achieves probably superior multiple solvent suppression compared to the experiment of Fig. 21a. Its use is particularly advantageous in systems where the difference in chemical shift between the solvent resonances is not large. A drawback of this sequence is its length.

8.2. Two-dimensional experiments

In our combined strategy, a 2D PFG DQ experiment is then acquired with the scheme of Fig. 2c. DQ experiments can be recorded rapidly by acquiring only a small number of t_1 increments. If necessary linear prediction can then be applied in the t_1 dimension for improving the frequency resolution. A typical DQ spectrum of the reserpine sample obtained with the scheme of Fig. 2c is shown in Fig. 24. The 1D spectrum of Fig. 23 and the 2D DQ spectrum are then analysed together for the identification of the compound. Some resonances are not visible in the 1D spectrum owing to their degeneracy with the CH_3CN signal. However, these resonances and their spin systems can easily be identified in the 2D DQ spectrum and in the 1D DQ spectrum (Fig. 24). The DQ experiment is very efficient for establishing scalar connectivities by way of small long-range couplings.[178] Two examples with DQ connectivities between protons separated by four bonds are shown in Fig. 25(a,b). Although the ^4J coupling between the two aromatic protons C12-H and C10-H is sufficiently large (2 Hz), the ^4J coupling between C(5,3)O-CH_3–C2,6-H_2 is very small and cannot be observed in the 1D spectrum even by applying resolution enhancement. If necessary, a 2D TOCSY[152,153] and/or a 2D ROESY[179,180] or NOESY[181] experiment with the pulse sequences of Fig. 21b–d[144] can also be recorded. The

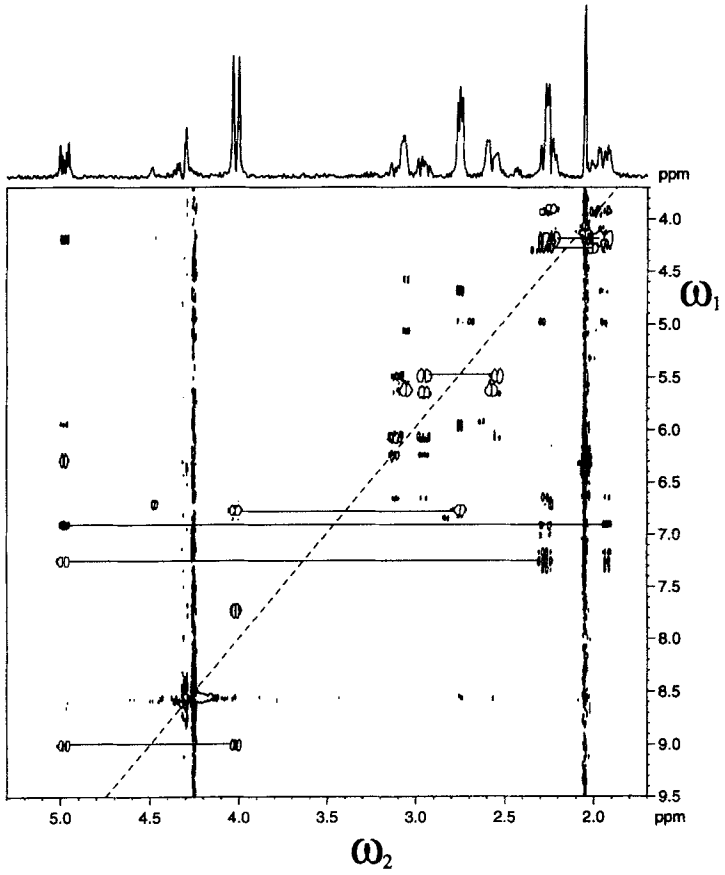

Fig. 24. Two-dimensional ^{1}H PFG DQ spectrum for the sample of reserpine recorded with the pulse sequence of Fig. 2c and with $\beta = 90°/90°$. Eight scans were recorded for each of the 200 complex t_1 points. The dashed line represents the DQ diagonal and the horizontal lines represent some of the connectivities between direct peaks. The upper trace contains the 1D MAG DQ spectrum of the same compound.

reserpine ^{1}H spectrum contains five singlets in the spectral region 4–3.5 ppm originating from the OCH_3 moieties. Two-dimensional DQ and TOCSY experiments alone do not allow complete assignment of all the OCH_3 resonances. In this specific case assignments of these resonances can be obtained, by homonuclear experiments, only with the 2D ROESY or NOESY experiments of Fig. 21c and 21d. Cross-peaks between the OCH_3 and the aromatic resonances displayed in Fig. 25c allow the specific resonance assignments.

Alternatives to the PFG DQ experiment are the absolute value and mostly absorption mode PFG COSY experiments of Fig. 26a and 26b, respectively, or

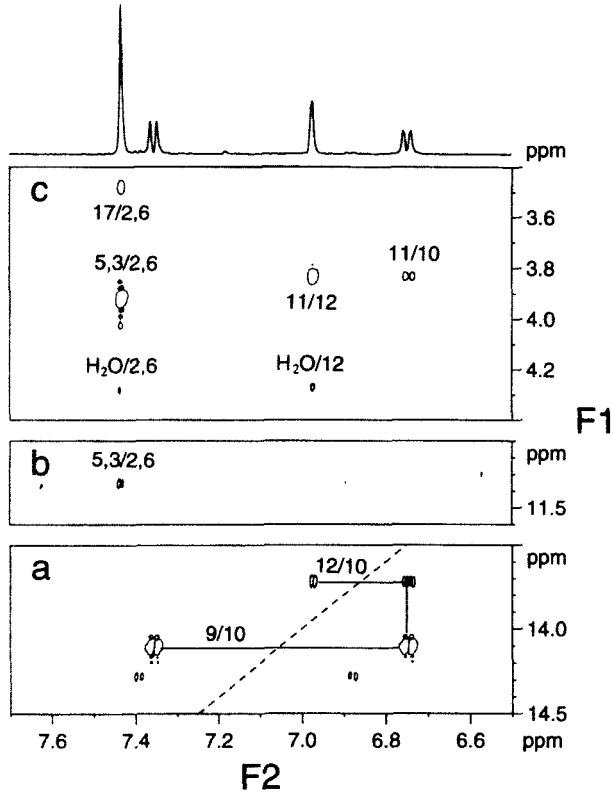

Fig. 25. Two expanded regions (a,b) of the ^{1}H PFG DQ spectrum and one expanded region (c) of the 2D ROESY spectrum recorded with the pulse sequence of Fig. 21c. The sample is a 380 μmol l^{-1} solution of reserpine in 50% H_2O and 50% CH_3CN. The experimental conditions for the DQ spectrum are the same as in Fig. 24. For the ROESY, 32 scans were recorded for each of the 512 t_1 increments. The lengths of the spin-lock period and of the double-selective 180° rectangular SLP pulse were 370 and 3 ms, respectively. The upper trace contains the 1D reference spectrum. The dashed line and the horizontal lines represent the DQ diagonal and the direct connectivities, respectively. Cross-peaks important for the resonance assignments are labelled. The weak aromatic cross-peaks in (a) originate from reserpine's oxidation product. This component is present at 5% concentration compared to the major component. In spite of its low concentration (~19 μmol l^{-1}), DQ connectivities originating from this molecule are clearly detected in (a).

the mostly absorption mode COSY experiment of Fig. 26c. The delay δ' is usually equal to the length of the PFG plus a gradient recovery time. However, it can be set to longer values for recording a so-called ω_1 scaled COSY experiment[182,183] or for detecting small coupling constants.[184] The excitation sculpting scheme of the PFG COSY differs from the scheme shown in Fig. 21a–d and Fig. 26c in the last two PFGs. The two PFGs are not equivalent in

Fig. 26a,b. The gradient G_1, and the last two gradients G_3 and G_4 of the excitation sculpting sequence are used for coherence selection. In order to select the desired coherence pathway the condition $G_4 - G_3 = \pm 2G_1$ in Fig. 26b and $G_4 - G_3 = G_1$ or $G_4 - G_3 = -G_1$ in Fig. 26a have to be satisfied. The same principle was used in the 1D and 2D PHOGSY experiments[185,186] and in 1D off-resonance selective ROESY.[187] Application of the pulse sequence of Fig. 26a to (**1**) is shown in Fig. 27. Remarkable solvent suppression is again achieved. The sensitivity of these experiments is low, however, compared to the PFG DQ experiment. The technical aspects of the excitation sculpting sequence with modification for multiple solvent suppression have been analyzed in detail in a recent publication.[188]

The robustness and easy set-up of all these experiments make them quite suitable for automation. This represents an important aspect in coupled separation–NMR techniques.

9. DIFFUSION WEIGHTED DQ

NMR studies of diffusional processes in solution have recently undergone a revival.[189] This has been made possible by the introduction in high-resolution NMR of actively shielded gradient coils and by the development of 2D and 3D diffusion-ordered spectroscopy (DOSY) experiments.[189–194]

The two PFGs inserted in the excitation DQ period of the ^{1}H PFG DQ experiments for the suppression of DQC via the radiation damping phenomenon[125] can also be used to measure the diffusion coefficient of a molecule.[195,196] The DQ excitation sandwich, as drawn in Fig. 2c, corresponds to a pulsed field gradient spin echo (PFG-SE) scheme.[197] In the diffusion experiments we use the definition G_d (gradient diffusion) for the two PFGs. In the presence of weak G_d all the magnetization is refocused at the end of the DQ period. However, if strong G_d are used, some of the magnetization will not be refocused owing to spatial diffusion. A series of 2D ^{1}H PFG DQ experiments is recorded with the pulse sequence of Fig. 2c and with increasing strength of the two G_d. The intensities of the DQ signals are then measured and analysed according to the Stejskal–Tanner equation.[197] For rectangular G_d, the signal attenuation is given by

$$\ln A(G)/A(0) = -\gamma^2 G^2 D\delta^2 (\Delta - \delta/3) \tag{28}$$

and for G_d with a sine-shape[198]

$$\ln A(G)/A(0) = -\gamma^2 G^2 D\delta^2 (4\Delta - \delta)/\pi^2 \tag{29}$$

where $A(G)$ is the measured signal intensity, $A(0)$ is the signal intensity in the absence of the two gradients, D is the diffusion constant, γ is the gyromagnetic

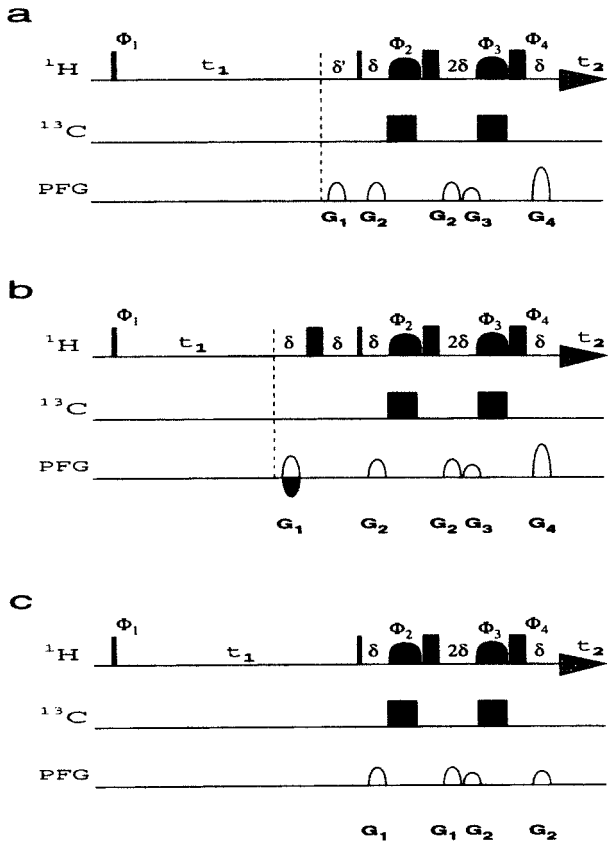

Fig. 26. Pulse sequences with multiple solvent suppression for the (a) absolute value and (b) mostly absorptive PFG COSY experiments and (c) for the mostly absorptive COSY experiment. The selective ^{1}H pulses are soft 180° SLPs with excitation at the different solvent resonances. These pulses are either soft rectangular or strongly truncated Gaussian pulses. The suppression of the solvent ^{13}C-satellite signals is achieved with ^{13}C decoupling applied during the entire length of the ^{1}H soft 180° pulses. The coherence selection gradients in (a) and (b) are G_1, G_3 and G_4 (see text). In (b) two data sets that correspond to the echo and anti-echo coherence pathway selections are recorded by reversing the sign of G_1.[252] The data are then added as described in the text. The phases are $\phi_1 = 4(x), 4(-x)$; $\phi_2 = -x$; $\phi_3 = (-x, y, x, -y)$; $\phi_4 = (x, -y, -x, y)$; and $\phi_{rec} = 2(x, -x), 2(-x, x)$. All other pulses have phase x. In (c) quadrature detection in ω_1 is achieved with TPPI method.

ratio, G and δ are the amplitude and duration of the two G_d, respectively, and Δ is the time between the rising edge of the two G_d. Typically $\tau = 30$–40 ms is used in DQ experiments, and with gradient strength up to 50 G cm^{-1} it is possible to determine the diffusion coefficients D for small and medium-sized molecules. Figure 28 shows four cross-peaks extracted from eight 2D diffusion

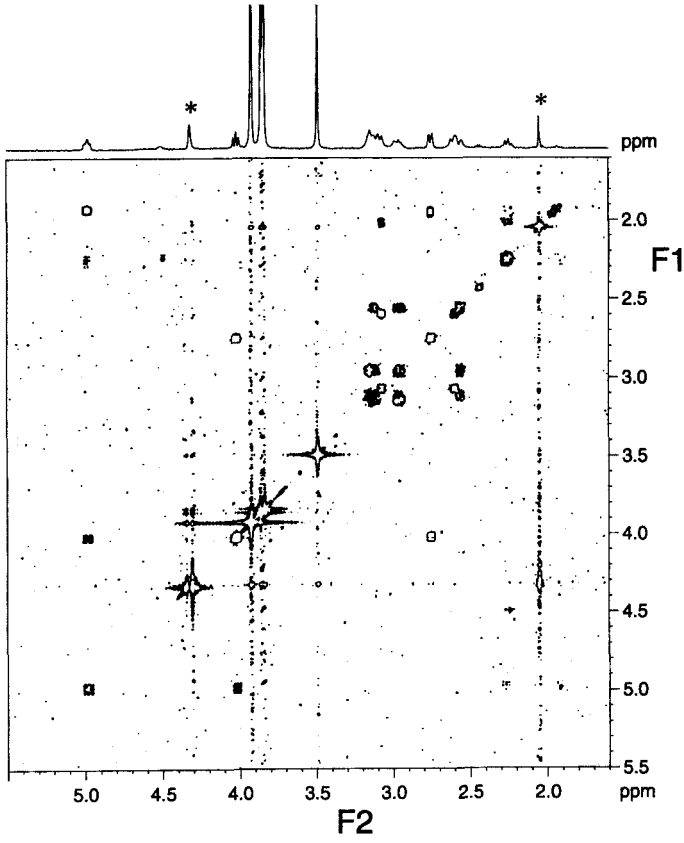

Fig. 27. Two-dimensional ^{1}H PFG absolute value COSY spectrum for the sample of reserpine recorded with the pulse sequence of Fig. 26a. Eight scans were recorded for each of the 1024 t_1 points. The lengths of the sine-shaped gradients and of the double-selective square 180° SLP pulses were 1 and 3 ms, respectively. The z-gradients G_1 to G_4 had strengths 12, 13.8, 7.8 and 19.8 G cm^{-1}, respectively. The upper trace contains the one-dimensional spectrum of the same compound. The asterisks indicate the residual solvent signals. The spectrum is plotted at the thermal noise. The t_1 noise observed in the spectrum originates from the O—CH_3 singlet resonances and from the residual solvent signals.

weighted DQ (DWDQ) spectra of a sample of blood plasma in H_2O recorded with the pulse sequence of Fig. 2c and with increasing strength for the two G_d. A magnitude calculation of the spectra along ω_2 is preferred for facilitating the analysis of the cross-peak intensities. Significant signal attenuation of the resonances of small molecules is obtained in the experiments recorded with strong G_d. In contrast, the attenuation of the CH_3 resonances of the fatty acids in very low-density lipoproteins (VLDL) and low-density lipoproteins (LDL) at the maximum G_d strength used (40.5 G cm^{-1}) is only 17%. A plot of the

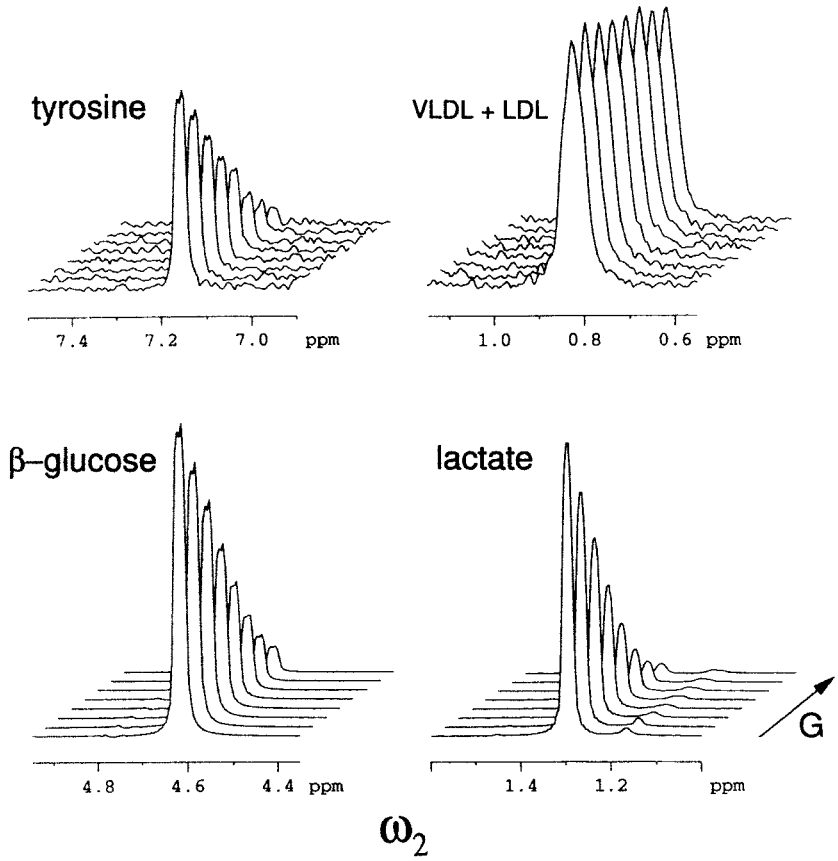

Fig. 28. Behaviour of the signal intensity of four representative DQ cross-peaks as a function of the strength of the two z-G_d of the scheme of Fig. 2c. A total of eight 2D PFG DQ spectra were recorded for a sample of biological plasma with increasing strength of the sine-shaped z-G_d. The spectra were acquired at $T_e = 297$ K with a Bruker Avance-500 spectrometer. Sixteen scans were recorded for each of the 320 t_1 increments (160 t_1 values for both the echo and anti-echo parts) with a repetition time of 1.7 s. The τ period and the acquisition time were 40 and 220 ms, respectively. The lengths of the two z-G_d and of the three coherence selection z-PFGs were 5 and 1.25 ms, respectively. The strength of the two sine-shaped z-G_d in the eight experiments starting from the lowest value was 0.35, 10.5, 15.5, 20.5, 25.5, 30.5, 35.5, 40.5 G cm^{-1}, respectively. The strength of G_1, G_2 and G_3 was ± 5, ∓ 5, and -20 G cm^{-1}, respectively. The data were multiplied with a cosine window function prior to Fourier transformation. Four rows were extracted from the 2D spectra and only one of the two connectivities is shown. (Reproduced with permission from Dalvit and Böhlen,[196] John Wiley & Sons Ltd).

Table 3. Diffusion coefficients D for molecules contained in rat plasma measured with the pulse sequence of Fig. 2c at 297 K.

	D (10^{-6} cm^2 s^{-1})
β-Glucose	6.3
Citrate	5.3
VLDL + LDL[a]	0.5
Lactate	8.7
Alanine	8.7
Valine	6.7
Alanine[b]	8.6
Valine[b]	7.3

(Reproduced with permission from Dalvit and Böehlen,[195] John Wiley & Sons Ltd).

[a]R value for VLDL + LDL was 0.990 and for the others was >0.999.

[b]Measured in H_2O.

signal intensity against G^2 and the linear-regression fits for six representative molecules contained in the plasma are shown in Fig. 29. The apparent diffusion coefficients D calculated from the slopes of the fitting lines using Eq. (29) are shown in Table 3. Lactate and alanine, which have very similar molecular masses, have almost the same diffusion coefficient. Despite the relatively narrow linewidths of the VLDL and LDL CH_3 fatty acid resonances, the large lipoprotein particles (ranging from 90 to 2500 Å)[199,200] have a very small D value. The CH_3 resonances are narrow owing to the high internal mobility of this moiety within the particles. Knowledge of the diffusion coefficients can also give valuable information concerning the possible weak interactions of a metabolite or drug with the proteins contained in the biofluids. This is shown in Table 3, which also reports the diffusion coefficients measured with the pulse sequence of Fig. 2c for the two amino acids valine and alanine in H_2O. The D coefficient for free alanine is the same in the two solutions, indicating that this residue does not interact with the proteins present in the plasma. In contrast, a 10% reduction of D is observed for free valine in plasma compared to H_2O, suggesting possible weak interactions of this amino acid with the plasma proteins. However, if the drug or metabolite interacts strongly with the large plasma proteins, it will not be visible by NMR. The excellent solvent suppression and the absence of t_1 noise in the spectra recorded with the scheme of Fig. 2c are important factors for the precise measurement of the resonance intensities, particularly in those experiments recorded with weak G_d. This can be seen in Fig. 28 where the complete H_2O suppression allows a reliable intensity measurement of the cross-peak of β-glucose which is at only 0.1 ppm from H_2O.

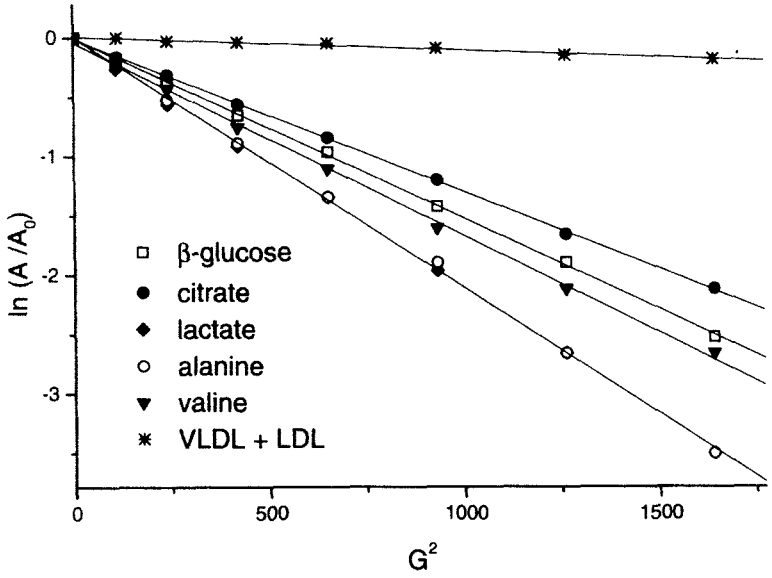

Fig. 29. Plot of the natural logarithm of intensity of six cross-peaks extracted from eight 2D DWDQ spectra versus G^2 where G is expressed in G cm^{-1}. The sample is the same as described in Fig. 28. The lines represent the linear fits. (Reproduced with permission from Dalvit and Böhlen.[196] © John Wiley & Sons Ltd.)

Another experiment that is used for the determination of the diffusion coefficient of a molecule is the so-called PFG stimulated-echo[201] TOCSY experiment.[202–206] A stimulated-echo scheme is applied before the TOCSY step. The cross-peaks of the right column of Fig. 18 are extracted from a stimulated-echo TOCSY spectrum recorded with the same isotropic mixing period of the TOCSY spectrum second from right. The gradients in the stimulated-echo select only one of the two possible coherence pathways, resulting in a two-fold signal loss. This is clearly seen in Fig. 18 for Ala and Tyr. For large molecules (VLDL in Fig. 18) the extra delays of the stimulated-echo scheme result in additional signal losses via T_1 and T_2 relaxation.

The diffusion weighting in the DWDQ experiments is achieved within the DQ preparation period τ without the need for extra pulses or delays that are required in other diffusion weighted 2D experiments. The diffusion weighted DQ experiment compares favourably with other 2D experiments developed for diffusion measurements. For small and medium-size molecules it represents the most sensitive experiment, whereas for large molecules the 2D stimulated-echo NOESY[207] and TOCSY[202–206] experiments are superior. A DOSY-[190–194] type analysis of the 2D DWDQ can also be performed. This results in 3D spectra where one of the axes corresponds to the diffusion coefficient D dimension.

Another type of diffusion weighted DQ experiment uses a PFG-SE scheme in the DQ evolution period. The experiment, originally developed for liquid crystals,[208,209] has subsequently been applied in diffusion studies of small molecules.[15,210] The signal attenuation due to diffusion in this experiment is given by the right-hand side of Eqs. (28) and (29) multiplied by a factor of 4. Therefore, weaker G_d can be used and smaller diffusion coefficients can be measured. In spite of these important advantages, the experiment has some drawbacks. First, this method does not allow one to obtain pure absorption ^{1}H 2D DQ spectra. Second, the presence of the additional delay together with the fast DQ relaxation results in significant signal losses when applied to large molecules.

10. X-FILTER DQ

Isotope-edited NMR experiments have been shown to be very useful for studying the inter- and intramolecular interactions in macromolecular complexes.[211–228] This methodology is becoming increasingly important in the rational drug design process. Knowledge of the conformation of a ligand bound to a receptor can guide the chemist to the design of an inhibitor with improved binding affinity. In the X-filter experiments one of the two components forming the complex is labelled with ^{13}C and/or ^{15}N isotopes. The X-filter then selects the magnetization that originated solely from one of the two components. The resulting ^{1}H spectra contain a reduced number of resonances and therefore are amenable to detailed spectral analysis. A common approach for protein–ligand complexes involves uniform labelling of the protein. This is because the labelling of the ligand can sometimes be chemically very difficult and/or prohibitively expensive. Several methods have been proposed for obtaining X-filter spectra. DQ can also be used for this purpose. The pulse sequences for the ^{13}C-filter 2D DQ experiments are shown in Fig. 30.[229] One or two or even three 90° ^{13}C pulses are applied during the excitation DQ period. The delays between the different ^{13}C pulses are tuned to the different values of the heteronuclear $^1J_{CH}$ coupling constants. For the simultaneous ^{15}N filter a ^{15}N 90° pulse is also applied at a delay of ~5.4 ms $(1/(2^1J_{NH}))$ from the first ^{1}H pulse. It is sufficient to use only one ^{15}N pulse because all the $^1J_{NH}$ couplings have similar values.

The function of these pulse sequences can be explained by considering the spin-system I–K where I and K represent two protons scalar coupled with a coupling J^{IK}. The behaviour of the relevant terms is analysed, using the product operator formalism, in the presence and absence of the heteronuclear spins S and S'. These spins are coupled to spin I and spin K with heteronuclear scalar couplings $^1J_{IS}$ and $^1J_{KS'}$, respectively. We further assume that the heterospins S and S' are scalar coupled with a coupling $^1J_{SS'}$.

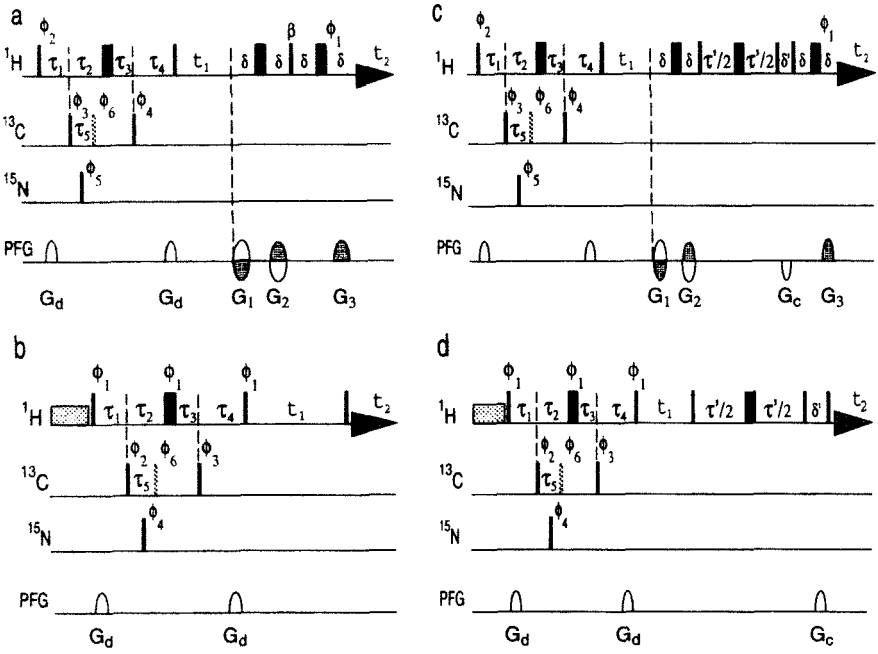

Fig. 30. Pulse sequences for the 2D ^{13}C and ^{15}N filter DQ experiment with coherence selection gradients (a) and with phase cycling (b). Pulse sequences for the 2D ^{13}C and ^{15}N filter refocused DQ with coherence selection gradients (c) and with phase cycling (d). Narrow and wide bars correspond to 90° and 180° hard pulses, respectively. The experiments in (b) and (d) are recorded with H_2O presaturation.The experiment in (a) can be recorded with either $\beta = 90°/90°$, with $\beta = 45°/135°$ or with $\beta = 60°/120°$. The phases are $\phi_1 = 8(x), 8(-y), 8(-x), 8(y)$; $\phi_2 = 4(x), 4(-x)$; $\phi_3 = (x, -x)$; $\phi_4 = 2(x), 2(-x)$; $\phi_5 = 32(x), 32(-x)$; $\phi_{rec} = 4(x), 8(-x), 4(x)$ for the experiment in (a) recorded with $\beta = 90°/90°$ and for the experiment in (c). The phases are $\phi_1 = 4(x), 4(-y), 4(-x), 4(y)$; $\phi_3 = (x,-x)$; $\phi_4 = 2(x), 2(-x)$; $\phi_5 = 16(x), 16(-x)$ for the experiment in (a) with $\beta = 45°/135°$ or (60°/120°). The phases of the first ^1H 90° pulse and the receiver are in (a) $\phi_2 = x$; $\phi_{rec} = 4(x), 4(-x)$ for $\beta = 45°$ (or 60°) and $\phi_2 = -x$; $\phi_{rec} = 4(-x), 4(x)$ for $\beta = 135°$ (or 120°). The phases in (b,d) are $\phi_1 = 2(x), 2(y), 2(-x), 2(-y)$; $\phi_2 = (x, -x)$; $\phi_3 = 8(x), 8(-x)$; $\phi_4 = 16(x), 16(-x)$; $\phi_{rec} = 2(x), 2(-x)$. Furthermore, half or an entire cycle of CYCLOPS[253] can be applied in (b,d) by incrementing all ^1H pulse phases and the receiver in steps of $\pi/2$. The length $|\tau_1 + \tau_2|$, which is equal to $|\tau_3 + \tau_4|$, corresponds to half the DQ excitation period. The delay τ_1 is set to $1/(2J_{CH})$ and τ_4 is set to $1/(2J'_{CH})$ where $J_{CH} \neq J'_{CH}$. The time between the first 90° ^1H pulse and the 90° ^{15}N pulse is equal to 5.4 ms ($1/(2J_{NH})$). The use of an additional third ^{13}C 90° pulse applied at a delay τ_5 from the first ^{13}C 90° pulse. This pulse is phase cycled in the same way as the other two ^{13}C 90° pulses. The first two gradients, applied at the beginning and end of the DQ excitation period are short and weak PFGs of equal sign and strength. The three gradients G_1, G_2, G_3 are coherence selection gradients. Their strengths must obey the ratios +1:−1:−4 or −1:+1:+4 for the anti-echo pathway selection and −1:+1:−4 or +1:−1:+4 for the echo pathway selection. For excellent H_2O suppression these PFGs should be MAGs. The delay δ corresponds to the length of the PFG plus the gradient recovery time. Quadrature detection in t_1 in (b,d) is achieved with the TPPI method where all the ^1H pulses preceding the evolution period are incremented in step of 45° in concert with t_1. For suppression of only ^{13}C-bound ^1H magnetization it is sufficient to remove the ^{15}N 90° pulse.

The amount of DQC between spins I and K present at the beginning of the evolution period and originating from spin I is proportional to

$$\{DQ\}_{IK} \propto (\cos \pi J_{IS} \tau_1)^2 \sin \pi J_{IK} (\tau_1 + \tau_2 + \tau_3 + \tau_4)$$

(pulse sequence with only the first 90° ^{13}C pulse) (30)

$$\{DQ\}_{IK} \propto [\cos \pi J_{IS} \tau_1 \cos \pi J_{IS} \tau_4 \cos \pi J_{IS} (\tau_2 - \tau_3)] \sin \pi J_{IK} (\tau_1 + \tau_2 + \tau_3 + \tau_4)$$

(pulse sequence with two 90° ^{13}C pulses) (31)

In deriving Eq. (31) the effect of the phase cycle of the 90° ^{13}C-pulses has been considered. In the absence of the spins S and S' the amount of $\{DQ\}_{IK}$ is simply proportional to

$$\{DQ\}_{IK} \propto \sin \pi J_{IK} (\tau_1 + \tau_2 + \tau_3 + \tau_4) \quad (32)$$

The suppression of unwanted DQC in Eq. (30) is proportional to $(\cos \pi J_{IS} \tau_1)^2$. This implies that the choice of a τ_1 value that does not perfectly match $1/(2J_{IS})$ can still provide good ^{1}H DQ suppression of protons attached to ^{13}C nuclei. Therefore the experiment is recorded with a value for τ_1 that is tuned to a compromise J value.

In the version of the experiment with two 90° ^{13}C-pulses, Eq. (31), it is possible to optimize the suppression of unwanted DQC simply by using two different values for τ_1 and τ_4. For proteins these two values are tuned for the aliphatic and aromatic $^1J_{CH}$ heteronuclear coupling constants, respectively. Furthermore, the term $\cos \pi J_{IS}(\tau_2 - \tau_3)$, where $|\tau_2 - \tau_3| = |\tau_1 - \tau_4|$, is less than 1 ($\tau_1 \neq \tau_4$) resulting in a further suppression of the unwanted magnetization.

In systems with very different $^1J_{CH}$ heteronuclear couplings, such as ^{13}C-labelled RNA and DNA molecules, it is possible to improve the suppression of the ^{13}C–^{1}H signals by inserting in the pulse sequences, as shown in Fig. 30a, an additional third ^{13}C 90° pulse after a delay τ_5 from the first ^{13}C 90° pulse and at a delay τ_6 before the 180° ^{1}H pulse. The term $\tau_5 + \tau_6$ corresponds to the τ_2 value. In this experiment the delay τ_5 can be tuned to a third $^1J_{CH}$ value.

Application of the experiment to a mixture of ^{13}C-labelled glucose and unlabelled phenylalanine in D_2O is shown in Fig. 31. The values of the $^1J_{CH}$ couplings for glucose range from 170 Hz to 140 Hz. Only the resonances of the unlabelled amino acid are visible in the ^{13}C-filter DQ spectrum. Excellent suppression of the glucose signals is achieved in spite of the different values for $^1J_{CH}$ present in this molecule. The weak glucose signals seen in this spectrum originate mainly from the residual unlabelled glucose molecules (^{13}C labelling measured in the upper trace of Fig. 31 is 97%).

A more relevant system for the application of the technique is represented by a protein–ligand complex. The ^{13}C and ^{15}N doubly labelled protein is the

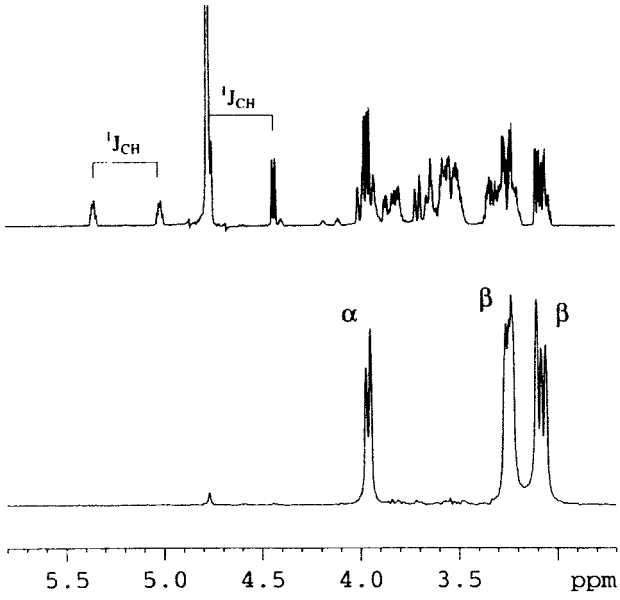

Fig. 31. One-dimensional ^1H reference spectrum of a mixture of ^{13}C-labelled glucose and [^{12}C]phenylalanine dissolved in D_2O (upper trace) and the first serial file of a ^{13}C filter 2D PFG DQ experiment (lower trace) recorded with the pulse sequence of Fig. 30a. The angle β was 135° and only the first ^{13}C 90° pulse was applied. An absolute value presentation is shown for the DQ spectrum. The spectra were recorded at T_e = 297 K on a Bruker Avance-500 spectrometer. A triple-resonance probe equipped with an actively shielded z-gradient coil connected to a Bruker 10A amplifier was used. The delays τ_1 and $|\tau_1 + \tau_2|$ were 2.9 ms and 15 ms, respectively. The strength of the five 1.25 ms long sine-shaped z-PFGs was +0.35, +0.35, −5, +5, −20 G cm^{-1}, respectively. A total of 16 scans with a repetition time of 1.4 s were recorded. Lines showing the $^1J_{CH}$ splitting of the anomeric protons are drawn in the reference spectrum. The resonances of the unlabelled phenylalanine spin system are labelled in the DQ spectrum. (Reproduced with permission from Dalvit *et al.*[229])

inserted domain (I-domain) of the leukocyte function-associated antigen (LFA-1) consisting of 188 amino acids and with molecular mass 21 399 (when non-labelled). The unlabelled ligand is a natural product and the complex is 1:1. Intermolecular NOEs between ligand and protein, and same self-diffusion coefficient observed for the ligand and for the protein are strong indications that this ligand is tightly bound to the protein. An expanded region of the 2D ^{13}C-filter DQ spectrum recorded for this complex is shown in Fig. 32. This experiment has allowed complete unequivocal spectral assignment of the bound ligand. It should be pointed out that the T_2 of the protein ^1H resonances are shorter than the T_2 of the ligand resonances owing to the presence in the protein of the strong one-bond ^{13}C–^1H dipolar interaction. The magnitude of this interaction is equivalent to the dipolar interaction between two protons

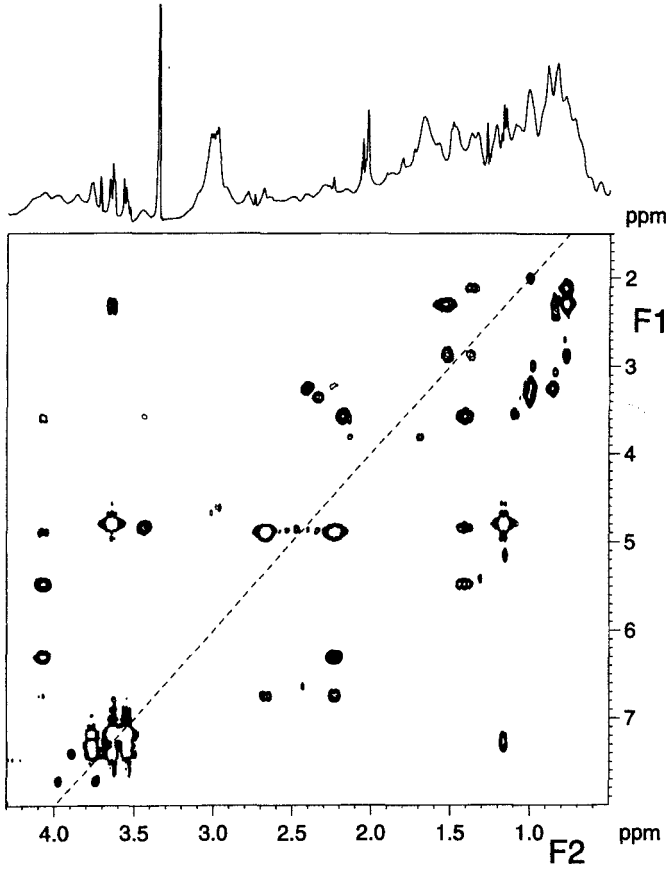

Fig. 32. An expanded region of the ^{13}C-filter DQ spectrum recorded for a 500 μmol l^{-1} solution of the ^{13}C and ^{15}N uniformly labelled inserted domain (I-domain) of the leukocyte function-associated antigen (LFA-1) complexed with an unlabelled ligand. The sample was in H_2O and the experiments were recorded at T_e = 296 K with a Bruker 500 MHz Avance spectrometer equipped with a 5 mm CRYOPROBE DUI 500 SB – H/C and z gradients. The spectrum was acquired with the pulse sequence of Fig. 30a with three ^{13}C 90° pulses. The length $|\tau_1 + \tau_2|$ was only 10 ms in order to reach a compromise between sufficient DQ creation and signal loss limitation due to rapid T_2 relaxation. A total of 32 scans for each of the 320 t_1 increments were recorded. The repetition time was 1.2 s, corresponding to a total measurement time of 3 hours and 25 minutes. The dashed line corresponds to the DQ diagonal. The spectrum is displayed in absolute value for facilitating visualization of the complex cross-peaks. The upper trace contains the 1D reference spectrum.

separated by a distance of only 1.7 Å. Consequently, magnetization losses via T_2 during the excitation DQ period are more pronounced for the protein resonances. This helps in the additional suppression of the protein DQ signals.

The scheme of Fig. 30 can also be used, as discussed above, to measure the diffusion coefficient of an unlabelled molecule by simply changing the strength of the first two PFGs. A useful application of the X-filter diffusion weighted DQ experiment is in the identification, in a mixture of unlabelled compounds in solution with a labelled protein, of those molecules that interact with the protein.[229]

11. EXTENSION OF ^{1}H PFG 2D DQ TO THREE DIMENSIONS

The DQ experiment can also be coupled with other experiments. This was shown for the 2D DQ NOESY,[230] 2D DQ TOCSY,[231] 2D DQ ROESY[232] and 2D DQ-relay.[233,234] Extension of these experiments to three dimensions[39,124,235–236] has the advantage of removing the large cross-peak overlap and degeneracy. Two different types of 3D PFG DQ experiments[235,236] exist that differ in the order of the DQ scheme.

11.1. ^{1}H 3D PFG DQ NOESY (or TOCSY)

The pulse sequence of the ^{1}H 3D PFG DQ NOESY and DQ TOCSY are depicted in Fig. 33a and Fig. 33b, respectively.[235] The refocused in-phase magnetization present before the NOESY and TOCSY steps is labelled during t_2 according to the {SQ} frequencies of the two spins that formed DQC during t_1. The two-dimensional versions of these experiments are obtained simply by setting t_2 to 0. Two data sets are recorded for these experiments, with reversed sign of the first two coherence selection gradients. For the 3D experiments, in addition, quadrature detection in t_2 is achieved with the TPPI method. If the spectrometer is equipped with actively shielded x,y,z-gradient coils, excellent H_2O suppression is achieved using MAGs for the coherence selection gradients. This is important for the observation of $^{\alpha}$H cross-peaks resonating in ω_3 at or near the H_2O frequency. Typical $\omega_2\omega_3$ planes extracted from these experiments recorded for the protein lysozyme are shown in Fig. 34. Although several peaks have the same DQ frequency in ω_1, they are separated on the basis of their {SQ} frequencies in ω_2. Two different types of peaks are observed in these planes: (i) the cross-peaks with different Larmor frequencies in all three dimensions, and (ii) the cross-diagonal peaks with same ω_2 and ω_3 frequencies. The cross-diagonal peaks with $\omega_1 = \omega_3$, the back-transfer peaks and the diagonal peaks with $\omega_1 = \omega_2 = \omega_3$ that are typical of the homonuclear 3D NOESY-TOCSY spectra[237–239] are absent in these 3D spectra. The labelled cross-peaks in Fig. 34a above and below the cross-diagonal represent the sequential $^{\alpha}H_i{}^{N}H_{i+1}$ and $^{N}H_i{}^{\alpha}H_{i-1}$ NOEs, respectively.

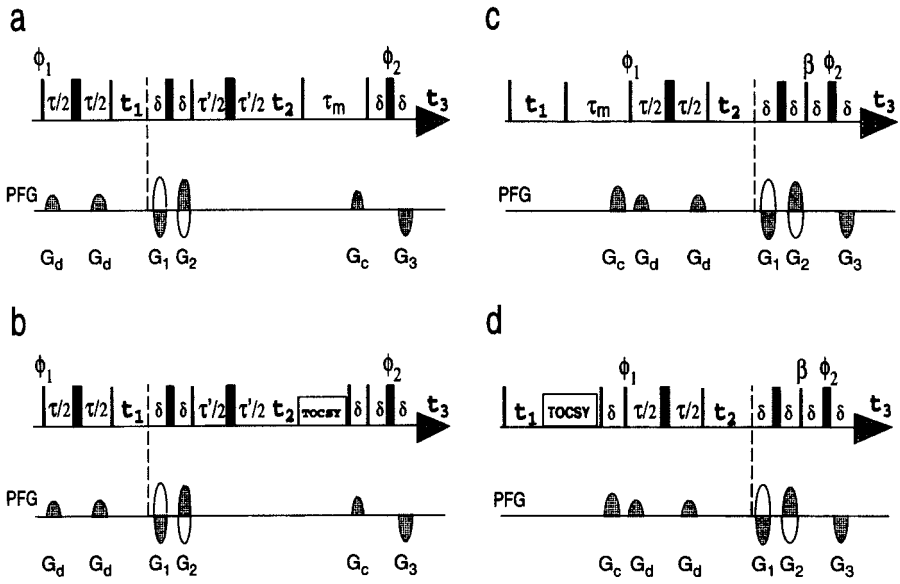

Fig. 33. Pulse sequences for the 3D homonuclear PFG DQ NOESY (a), DQ TOCSY (b), NOESY DQ (c), TOCSY DQ (d) experiments. The narrow and large bars represent 90° and 180° pulses, respectively. The phases in (a,b) are $\phi_1 = (x, -x)$; $\phi_2 = 2(x), 2(-y), 2(-x), 2(y)$; $\phi_{rec} = [x, 2(-x), x]$. The phases in (c,d) are $\phi_1 = -x$ (c), $\phi_1 = x$ (d), $\phi_2 = (x, -y, -x, y)$ (c,d), $\phi_{rec} = (x, -x)$ (c,d) for the echo part and $\phi_1 = x$ (c), $\phi_1 = (-x)$ (d), $\phi_2 = (x, -y, -x, y)$ (c,d), $\phi_{rec} = (-x, x)$ (c,d) for the anti-echo part. In addition, the first 90° pulse in (c) is phase cycled $\pm x$ together with the receiver. The G_c in (c) is applied at the end of τ_m. An alternative to this short G_c is the use of a weak and long gradient applied for the entire length of τ_m. This has the function of inhibiting the radiation damping mechanism during τ_m. In this case, however, the phase ϕ_1 has to be the same as that used in (d) and the phase of the first 90° pulse has to be always x. The τ, τ' and τ_m periods correspond to the excitation double-quantum period, the refocusing period and the mixing time, respectively. The time δ is equal to the length of the PFG plus a gradient recovery time. The gradients G_1 to G_3 are the coherence selection gradients and are MAGs, if triple-axis gradient hardware is available, for improved solvent suppression. Their relative strengths are the same as described for the DQ experiment. Two data sets that correspond to the echo and anti-echo coherence pathway selections are recorded by reversing the sign of G_1 and G_2. The flip angle β of the read-out pulse in (c,d) is set to 60° (or 45°) for the anti-echo pathway selection and to 120° (or 135°) for the echo pathway selection in order to maximize the coherence transfer amplitude. The two data sets are then properly added.

Sensitivity problems of these experiments are experienced in the assignment of helical segments. Residues located in α helices have a small $J^{NH\alpha H}$ coupling constant. A long τ period is required in order to excite a significant amount of $\{DQ\}^{NH\alpha H}$ coherence for these residues, but this is not possible if the resonances have a short T_2 relaxation.

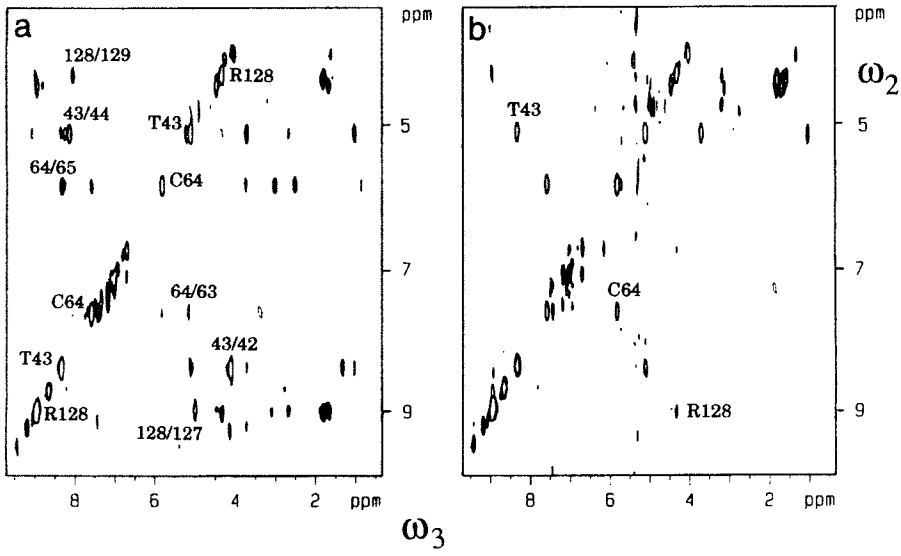

Fig. 34. A $\omega_2\omega_3$ plane extracted from the 3D PFG DQ NOESY (a) and from the 3D PFG DQ TOCSY (b) spectra recorded for a solution of chicken egg-white lysozyme in H_2O (7% D_2O) at pH 3.8 with the pulse sequences of Fig. 33a and 33b, respectively. The plane was taken at the $\{DQ\}^{NH\alpha H}$ frequency of 13.4 ppm in ω_1. The data matrix consisted of $128 \times 128 \times 512$ points, and eight scans were recorded for each increment. The τ_m and the TOCSY step were 150 and 40 ms long, respectively. The τ, τ' and the gradient recovery time were 30 ms, 30 ms and 100 μs, respectively. The data were multiplied in all three dimensions with a cosine window function prior to 3D Fourier transformation. (Reproduced with permission from Dalvit.[235])

11.2. ^{1}H 3D PFG NOESY (or TOCSY) DQ

The pulse sequence of the ^{1}H 3D PFG NOESY (or TOCSY) DQ experiments are depicted in Fig. 33c and 33d, respectively.[124,236] The first steps in these pulse sequences are the NOESY or TOCSY schemes. The in-phase single-quantum coherence is then converted, with the DQ excitation step, to DQC and labelled during t_2 with its characteristic frequency. The pulse with flip-angle β at the end of the evolution period t_2 converts this DQC to antiphase magnetization, which is immediately detected after the last PFG. The refocusing period is missing in these schemes. The peaks of the resulting 3D spectrum are in phase in ω_1 and ω_2 and anti-phase in ω_3. A 90° shift in the phase of the peaks along ω_3 results in peaks that are mostly positive with small negative lobs on both sides.[240]

Two typical $\omega_1\omega_3$ planes taken at two different ω_2 $\{DQ\}^{NH\alpha H}$ frequencies are shown in Fig. 35. The planes in (a,c) and (b,d) have been extracted from the 3D PFG NOESY DQ and from the 3D PFG TOCSY DQ spectra, respectively.

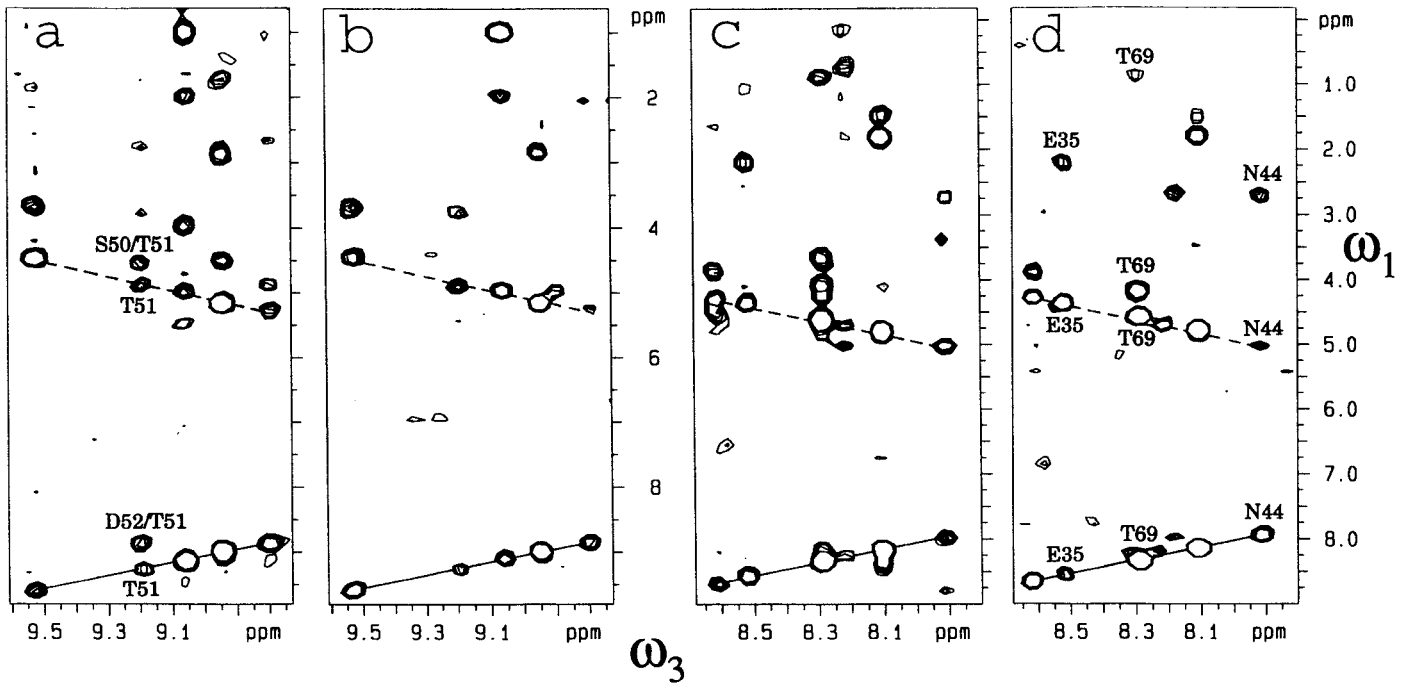

Fig. 35. Two $\omega_1\omega_3$ planes extracted from the 3D PFG NOESY DQ spectrum (a,c) and from the 3D PFG TOCSY DQ spectrum (b,d). Only the positive contour levels are displayed. The planes in (a,b) and (c,d) are taken at $\{DQ\}^{NH\alpha H}$ frequencies of 14.2 and 12.9 ppm in ω_2, respectively. The spectra were acquired with the pulse sequences of Fig. 33c, 33d for a solution of chicken egg-white lysozyme, pH 3.8 in H_2O (7% D_2O). The experiments were recorded at 297 K with a Bruker Avance-500 spectrometer. A triple resonance inverse probe equipped with an actively shielded z-gradient coil connected to a Bruker 10A amplifier was used. The data matrix consisted of $128 \times 128 \times 512$ points and four scans were recorded for each t_1 and t_2 increment. The lengths of τ_m (a,c) and of the TOCSY step (b,d) were 150 and 40 ms, respectively. The excitation double-quantum period was 30 ms. The cross-diagonal is indicated with a continuous line and the anti-cross-diagonal is indicated with a dashed line. The peaks located outside these two diagonals are the true cross-peaks. The NOE sequential connectivities for the NH of Thr-51 in (a) and some of the TOCSY connectivities in (d) are labelled. (Reproduced with permission from Dalvit.[236])

Only the amide region of the spectra is shown along ω_3. The appearance of these 2D planes is different from the planes in Fig. 34. In this displayed spectral region different types of peaks are observed that originate from different magnetization pathways. The peaks centred on the diagonal at $\omega_1 = \omega_3 = \omega^{NH}$ are the so-called cross-diagonal peaks. The peaks located at $\omega_1 = \omega^{\alpha H}$ and $\omega_3 = \omega^{NH}$ lie on an antidiagonal with respect to the cross-diagonal peaks. These peaks originate from the conversion process of SQC to DQC and from the reverse conversion process of DQC to SQC. This is better explained by describing the behaviour of the relevant terms during the three evolution periods:

$$\{SQ\}^{NH}\,[t_1] \longrightarrow \{DQ\}^{NH\alpha H}\,[t_2] \begin{cases} \longrightarrow \{SQ\}^{NH}\,[t_3] \text{ (cross-diagonal peaks)} \\ \longrightarrow \{SQ\}^{\alpha H}\,[t_3] \text{ (anti-cross-diagonal peaks)} \end{cases} \tag{33}$$

$$\{SQ\}^{\alpha H}\,[t_1] \longrightarrow \{DQ\}^{NH\alpha H}\,[t_2] \begin{cases} \longrightarrow \{SQ\}^{\alpha H}\,[t_3] \text{ (cross-diagonal peaks)} \\ \longrightarrow \{SQ\}^{NH}\,[t_3] \text{ (anti-cross-diagonal peaks)} \end{cases}$$

The anti-cross-diagonal peaks are not present in the 3D PFG DQ NOESY and DQ TOCSY spectra because DQC is created here first. The behaviour of the relevant terms in these experiments is

$$\{DQ\}^{NH\alpha H}\,[t_1] \begin{cases} \longrightarrow \{SQ\}^{\alpha H}\,[t_2] \longrightarrow \{SQ\}^{\alpha H}\,[t_3] \text{ (cross-diagonal peaks)} \\ \longrightarrow \{SQ\}^{NH}\,[t_2] \longrightarrow \{SQ\}^{NH}\,[t_3] \text{ (cross-diagonal peaks)} \end{cases} \tag{34}$$

The peaks located outside the two diagonals in Fig. 35 are the cross-peaks that have $\omega_1 \neq \omega_2 \neq \omega_3$. These peaks originate from the NOESY or TOCSY transfers.

Analysis of the 3D planes of the TOCSY DQ spectra is straightforward. Some attention should be paid to the analysis of the 3D planes of the NOESY DQ spectra owing to the concomitant occurrence of the same process responsible for the anti-cross-diagonal peaks. This process, which helps in the TOCSY version to relay the magnetization from the side-chain protons to the ^{N}H protons via the $^{\alpha}H$ protons, can give rise to erroneous interpretations in the NOESY version. This can be explained with an example. Let us assume that a $^{N}H_{i+1}$ proton is close in space to a $^{\alpha}H_i$ proton, but not to the $^{N}H_i$ proton. In

the plane taken at the ω_2 $\{DQ\}^{NH_i\alpha H_i}$ frequency, in addition to the true NOE cross-peak between $^NH_{i+1}$ and $^\alpha H_i$ protons, a cross-peak between the $^NH_{i+1}$ and the ^NH_i resonances is also observed. This process can be used constructively for the sequential assignments of residues located in β sheets as shown for Thr-51 in Fig. 35a. In addition to the typical sequential NOE $^\alpha H_{i-1}{}^N H_i$ (S50/T51), the sequential connectivity $^NH_{i+1}{}^NH_i$ (D52/T51) is also observed.

If only the $\{DQ\}^{NH\alpha H}$ connectivities are studied along the t_2 (t_1 for the other 3D experiments) it is sufficient to carry out extensive folding along this dimension. Another possibility is the replacement of the hard 180° pulse flanked by the first two coherence selection gradients with an SLP semi-selective REBURP pulse[241] or other semi-selective pulses[242] applied simultaneously in the NH and αH spectral regions. Furthermore, the 3D TOCSY (or NOESY) DQ experiments could be recorded with αH semi-selective homodecoupling during acquisition. In this case, however, the NH antiphase single-quantum coherence has to be converted to in-phase magnetization before its detection.

12. e-PHOGSY-DQ

A final combination of the DQ experiment is with the e-PHOGSY experiment (Fig. 36a).[243,244] This experiment allows the observation of NOE and chemical exchange between H_2O and biomolecules. The selectively excited H_2O magnetization is partially transferred via chemical exchange or via cross-relaxation to protons of the protein during τ_m. This magnetization is then converted with the DQ excitation period to DQC and labelled with its characteristic frequency in ω_1. This coherence is then converted back to anti-phase single-quantum coherence and detected. No presaturation or WATERGATE schemes for H_2O suppression are needed in this experiment, allowing observation of resonances close to the H_2O signal. The three coherence selection gradients should be MAGs if triple-axis gradients are available. An application of this pulse sequence for the identification of the aromatic spin systems of the three tyrosines of chicken egg-white lysozyme is shown in Fig. 36. The C3,5H protons of the tyrosines show usually a strong NOE with H_2O. This NOE originates from a relay process via the tyrosine OH proton. The hydroxyl proton, if not involved in a hydrogen-bond in the interior of the protein, exchanges rapidly with the solvent. The aromatic spectral region extracted from a DQ spectrum recorded with the pulse sequence of Fig. 2c is shown in Fig. 36b. The corresponding spectral region extracted from the spectrum recorded with the pulse sequence of Fig. 36a is shown in Fig. 36c. The DQ connectivities for the three tyrosines, namely Tyr-20, Tyr-23, Tyr-53 (assignments taken from reference 245) are the only strong connectivities observed in (c), allowing their spin system assignments. Based on this same principle, the e-PHOGSY DQ can be used in the identification of serine and threonine spin systems.

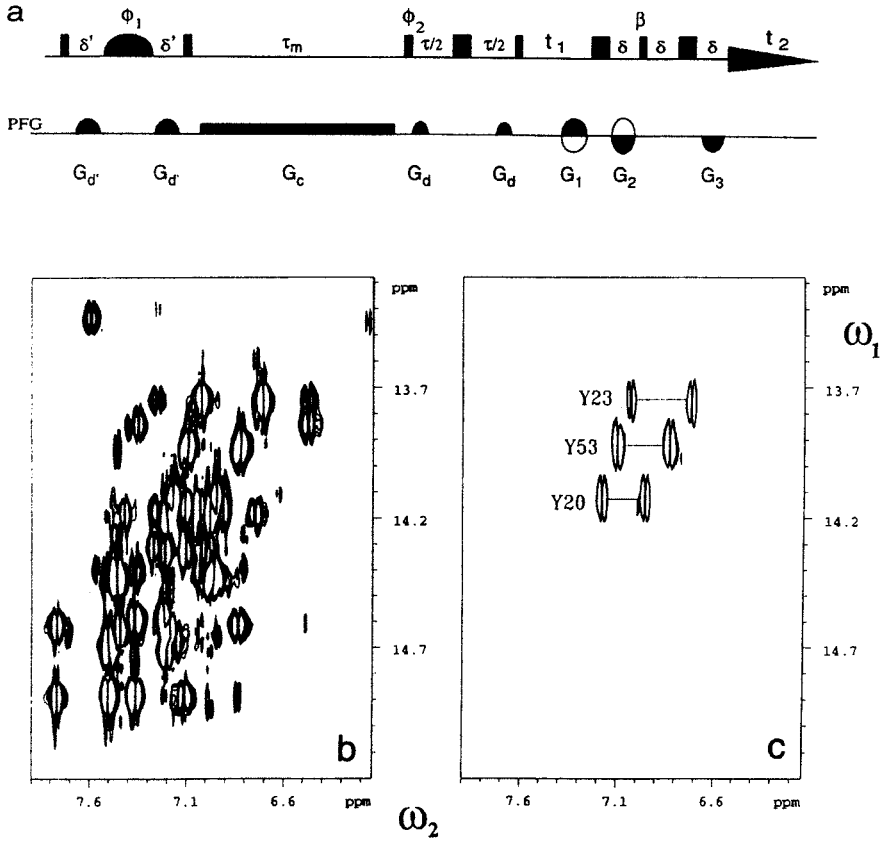

Fig. 36. (a) Pulse sequence of the ^{1}H PFG e-PHOGSY DQ experiment. The H_2O selective 180° pulse is located between two gradients of equal sign and amplitude. The gradients G_1 to G_3 are the DQC selection gradients and these are MAGs if triple-axis gradients are available. The G_c is a weak PFG applied for the entire length of τ_m. The delay δ' is usually equal to the length of $G_{d'}$ plus the gradient recovery time. However, it can be set to longer values. The phases are $\phi_1 = (x, -y\ -x, y)$; $\phi_2 = 4(x), 4(-x)$; and $\phi_{rec} = 2\ (x, -x), 2(-x, x)$. Aromatic region extracted from the DQ spectra recorded with the pulse sequence of Fig. 2c (b) and with the pulse sequence of Fig. 36a and with $\beta = 90°$(c). The sample is a solution of chicken egg-white lysozyme in H_2O (7% D_2O). Totals of 16 and 160 scans were recorded for each t_1 increment in (b) and (c), respectively. The excitation DQ period τ_2 was 15 ms in (b) and 12 ms in (c). Totals of 512 and 208 t_1 values were recorded for (b) and (c), respectively. The length of the H_2O-selective 180° pulse was 50 ms and τ_m was 120 ms long in (c). (Adapted with permission from Dalvit.[244])

13. CONCLUDING REMARKS

We have described the basic principles of pulsed-field-gradient ^{1}H absorption-mode DQ spectroscopy and of related experiments. The complete suppression of the solvent signals together with the absence of artefacts makes the ^{1}H PFG DQ experiment a very powerful NMR tool. In our experience the ^{1}H PFG DQ represents the most sensitive 2D NMR experiment for the analysis of small and medium-size molecules dissolved in non-deuterated solvents. We hope to have convinced readers of this with some applications of the technique to real samples taken from daily laboratory experience. It can be envisaged that the experiment when recorded with the newly developed cryogenic probes as the example of Fig. 32 could become an attractive tool for the identification and quantitation of metabolites and drugs in biofluids. Computed automated methods similar to those developed for the ^{13}C 2D INADEQUATE spectra[246,247] could also be used in the analysis of the ^{1}H 2D PFG DQ spectra for improving the detection limits and for facilitating the resonance assignment.

Finally, a combined strategy based on 2D PFG DQ and multiple solvent suppression techniques has been described for the applications in LC-NMR. This method is robust, reliable, easy to set up and, importantly, does not require the use of expensive deuterated solvents. Analysis of combinatorial chemistry samples, natural product extracts and biofluids will certainly profit from this methodology.

ACKNOWLEDGEMENTS

The authors thank Dr Ramsay Richmond for helpful discussions and Dr Teodor Parella for preprints of references 176 and 177. We also thank Bruker AG Switzerland for the opportunity to measure and publish the CRYOPROBE spectrum of Fig. 32.

Dedicated to the memory of Ezio Dalvit.

REFERENCES

1. G. Bodenhausen, *Prog. NMR Spectrosc.*, 1981, **14**, 137.
2. L. Braunschweiler, G. Bodenhausen and R. R. Ernst, *Mol. Phys.*, 1983, **48**, 535.
3. T. H. Mareci and R. Freeman, *J. Magn. Reson.*, 1983, **51**, 531.
4. K. Wüthrich, *NMR of Proteins and Nucleic Acids*, Wiley, New York, 1986.
5. R. R. Ernst, G. Bodenhausen and A. Wokaun, *Principles of Nuclear Magnetic Resonance in One and Two Dimensions*, Clarendon Press, Oxford, 1987.
6. M. Rance, W. J. Chazin, C. Dalvit and P. Wright, *Methods in Enzymology* (ed. N. J. Oppenheimer and T. L. James), Vol. 176, p. 114, Academic Press, San Diego, 1989.
7. Norwood, *Prog. NMR Spectrosc.*, 1992, **24**, 295.

8. W. E. Hull, in *Two-Dimensional NMR Spectroscopy Applications for Chemists and Biochemists* (ed. W. R. Croasmun and R. M. K. Carlson), p. 64, VCH, New York, 1994.
9. F. J. M. Van De Ven, *Multidimensional NMR in Liquids: Basic Principles and Experimental Methods*, VCH, 1995.
10. D. Canet, Nuclear Magnetic Resonance Concepts and Methods, John Wiley & Sons Ltd., Chichester, 1996.
11. J. Cavanagh, W. J. Fairbrother, A. G. Palmer III and N. J. Skelton, *Protein NMR Spectroscopy*, Academic Press, San Diego, 1996.
12. C. H. Sotak, D. M. Freeman and R. E. Hurd, *J. Magn. Reson.*, 1988, **78**, 355.
13. R. E. Hurd and D. M. Freeman, *Proc. Natl. Acad. Sci. USA*, 1989, **86**, 4402.
14. L. A. Trimble, J. F. Shen, A. H. Wilman and P. S. Allen, *J. Magn. Reson.*, 1990, **86**, 191.
15. C. H. Sotak, *J. Magn. Reson.*, 1990, **90**, 198.
16. D. M. Freeman, C. H. Sotak, H. H. Muller, S. W. Young and R. E. Hurd, *Magn. Reson. Med.*, 1990, **14**, 321.
17. S. Crozier, I. M. Brereton, S. E. Rose, J. Field, G. F. Shannon and D. M. Doddrell, *Magn. Reson. Med.*, 1990, **16**, 496.
18. C. H. Sotak, *NMR Biomed.*, 1991, **4**, 70.
19. D. Freeman and R. Hurd, *NMR Basic Princ. Prog.*, 1992, **27**, 199.
20. J. E. Van Dijk, A. F. Mehlkopf and W. M. M. J. Bovée, *NMR Biomed.*, 1992, **5**, 75.
21. P. Zhao, A. D. Sherry, C. R. Malloy and E. E. Babcock, *FEBS Lett.*, 1992, **303**, 247.
22. A. A. de Graaf, P. R. Luyten, J. A. den Hollander, W. Heindel and W. M. M. J. Bovée, *Magn. Reson. Med.*, 1993, **30**, 231.
23. A. H. Wilman and P. S. Allen, *J. Magn. Reson. B*, 1993, **101**, 165.
24. J.-M. Böhlen, M. Izquierdo and M. Decorps, *J. Magn. Reson. A*, 1994, **110**, 106.
25. Q. He, D. C. Shungu, P. C. M. van Zijl, Z. M. Bhujwalla and J. D. Glickson, *J. Magn. Reson. B*, 1995, **106**, 203.
26. G. Bloch, L. Jouvensal and P. G. Carlier, *Magn. Reson. Med.*, 1995, **34**, 353.
27. Q. He, Z. M. Bhujwalla, R. J. Maxwell, J. R. Griffiths and J. D. Glickson, *Magn. Reson. Med.*, 1995, **33**, 414.
28. L. Jouvensal, P. G. Carlier and G. Bloch, *Magn. Reson. Med.*, 1996, **36**, 487.
29. A. H. Wilman and P. S. Allen, *J. Magn. Reson. B*, 1995, **109**, 169.
30. Q. He, Z. M. Bhujwalla and J. D. Glickson, *J. Magn. Reson. B*, 1996, **112**, 18.
31. G. Wagner and E. R. P. Zuiderweg, *Biochem. Biophys. Res. Commun.*, 1983, **113**, 854.
32. J. Boyd, C. M. Dobson and C. Redfield, *J. Magn. Reson.*, 1983, **55**, 170.
33. J. Boyd, C. M. Dobson and C. Redfield, *FEBS Lett.*, 1985, **186**, 35.
34. G. Otting and K. Wüthrich, *J. Magn. Reson.*, 1986, **66**, 359.
35. M. Rance and P. E. Wright, *J. Magn. Reson.*, 1986, **66**, 372.
36. W. Chazin, M. Rance and P. E. Wright, *FEBS Lett.*, 1987, **222**, 109.
37. S. Nicula and G. Bodenhausen, *J. Magn. Reson. A*, 1993, **101**, 209.
38. K. D. Bishop, P. N. Borer and I. Pelczer, *J. Magn. Reson. B*, 1996, **110**, 9.
39. P. N. Borer, L. Pappalardo, D. J. Kerwood and I. Pelczer, *Adv. Biophys. Chem.*, 1997, **6**, 173.
40. A. A. Maudsley, A. Wokaun and R. R. Ernst, *Chem. Phys. Lett.*, 1978, **55**, 9.
41. A. Bax, P. G. DeJong, A. F. Mehlkopf and J. Smidt, *Chem. Phys. Lett.*, 1980, **69**, 567.
42. R. E. Hurd, *J. Magn. Reson.*, 1990, **87**, 422.
43. I. M. Brereton, S. Crozier, J. Field and D. M. Doddrell, *J. Magn. Reson.*, 1991, **93**, 54.
44. D. P. Weitekamp, *Adv. Magn. Reson.*, 1983, **11**, 111.
45. O. W. Sørensen, Ph.D. Dissertation No. 7658, ETH Zürich, 1984.
46. M. Munowitz and A. Pines, in *Advances in Chemical Physics* (ed. I. Prigogine and S. A. Rice), Vol. 66, p. 1, Wiley, New York, 1987.
47. M. Goldman, *Quantum Description of High Resolution NMR in Liquid*, Oxford University Press, Oxford, 1991.

48. A. Bax, R. Freeman and S. P. Kempsell, *J. Am. Chem. Soc.*, 1980, **102**, 4849.
49. A. Bax, R. Freeman, T. Frenkiel and M. H. Levitt, *J. Magn. Reson.*, 1981, **43**, 478.
50. T. H. Mareci and R. Freeman, *J. Magn. Reson.*, 1982, **48**, 158.
51. O. W. Sørensen, G. W. Eich, M. H. Levitt, G. Bodenhausen and R. R. Ernst, *Prog. NMR Spectrosc.*, 1983, **16**, 163.
52. K. J. Packer and K. M. Wright, *Mol. Phys.*, 1983, **50**, 797.
53. F. J. M. Van de Ven and C. W. Hilbers, *J. Magn. Reson.*, 1983, **54**, 512.
54. N. Müller, G. Bodenhausen, K. Wüthrich and R. R. Ernst, *J. Magn. Reson.*, 1985, **65**, 531.
55. M. Rance and P. E. Wright, *Chem. Phys. Lett.*, 1986, **124**, 572.
56. N. Müller, G. Bodenhausen and R. R. Ernst, *J. Magn. Reson.*, 1987, **75**, 297.
57. L. E. Kay and J. H. Prestegard, *J. Am. Chem. Soc.*, 1987, **109**, 3829.
58. S. Wimperis and G. Bodenhausen, *Mol. Phys.*, 1989, **66**, 897.
59. S. Wimperis and G. Bodenhausen, *Chem. Phys. Lett.*, 1987, **140**, 41.
60. I. Bertini, C. Luchinat, M. Piccioli and D. Tarchi, *Concepts Magn. Reson.*, 1994, **6**, 307.
61. R. Brüschweiler and R. R. Ernst, *J. Chem. Phys.*, 1992, **96**, 1758.
62. C. Dalvit, *J. Magn. Reson.*, 1992, **97**, 645 and correction in *J. Magn. Reson. A*, 1993, **104**, 242.
63. T. E. Bull, *Prog. NMR Spectrosc.*, 1992, **24**, 377.
64. H. Desvaux, *J. Magn. Reson.*, 1997, **127**, 1.
65. L. G. Werbelow and D. M. Grant, *Adv. Magn. Reson.*, 1977, **9**, 189.
66. R. L. Vold and R. R. Vold, *Prog. NMR Spectrosc.*, 1978, **12**, 79.
67. J. M. Böhlen, S. Wimperis and G. Bodenhausen, *J. Magn. Reson.*, 1988, **77**, 589.
68. D. Canet, *Prog. NMR Spectrosc.*, 1989, **21**, 237.
69. J. Kowalewski, *Annu. Rep. NMR Spectrosc.*, 1990, **11**, 307.
70. C. Dalvit and G. Bodenhausen, *Adv. Magn. Reson.*, 1990, **14**, 1.
71. M. H. Levitt and L. Di Bari, *Bull. Magn. Reson.*, 1994, **16**, 94.
72. A. Kumar and P. K. Madhu, *Concepts Magn. Reson.*, 1996, **8**, 139.
73. L. Maler, L. Di Bari and J. Kowalewski, *J. Phys. Chem.*, 1994, **98**, 6244.
74. G. Batta and J. Gervay, *J. Am. Chem. Soc.*, 1995, **117**, 368.
75. G. Batta, K. E. Kövér, J. Gervay, M. Hornyák and G. M. Roberts, *J. Am. Chem. Soc.*, 1997, **119**, 1336.
76. D. Yang, R. Konrat and L. E. Kay, *J. Am. Chem. Soc.*, 1997, **119**, 11938.
77. M. W. F. Fischer, L. Zeng, Y. Pang, W. Hu, A. Majumdar and E. R. P. Zuiderweg, *J. Am. Chem. Soc.*, 1997, **119**, 12629.
78. B. Reif, M. Hennig and C. Griesinger, *Science*, 1997, **276**, 1230.
79. N. Tjandra and A. Bax, *J. Am. Chem. Soc.*, 1997, **119**, 8076.
80. M. Tessari, H. Vis, R. Boelens, R. Kaptein and G. W. Vuister, *J. Am. Chem. Soc.*, 1997, **119**, 8985.
81. M. Gueron, J. L. Leroy and R. H. Griffey, *J. Am. Chem. Soc.*, 1983, **105**, 7262.
82. J. R. Tolman, J. M. Flanagan, M. A. Kennedy and J. H. Prestegard, *Proc. Natl. Acad. Sci. USA*, 1995, **92**, 9279.
83. A. Saupe and G. Englert, *Phys. Rev. Lett.*, 1963, **11**, 462.
84. J. W. Emsley and J. C. Lindon, *NMR Spectroscopy Using Liquid Crystal Solvents*, Pergamon, New York, 1975.
85. P. Diehl, in *Nuclear Magnetic Resonance of Liquid Crystals* (ed. J. W. Emsley), Reidel, Dordrecht, 1985, p. 147.
86. N. Tjandra and A. Bax, *Science*, 1997, **278**, 1111.
87. W. S. Warren, W. Richter, A. H. Andreotti and B. T. Farmer II, *Science*, 1993, **262**, 2005.
88. M. Levitt, *Concepts Magn. Reson.*, 1996, **8**, 77.
89. G. Deville, M. Bernier and J. M. Delrieux, *Phys. Rev. B*, 1979, **19**, 5666.
90. R. Bowtell, R. M. Bowley and P. Glover, *J. Magn. Reson.*, 1990, **88**, 643.
91. R. Bowtell, *J. Magn. Reson.*, 1992, **100**, 1.

92. D. Einzel, G. Eska, Y. Hirayoshi, T. Kopp and P. Wölfle, *Phys. Rev. Lett.*, 1984, **53**, 2312.
93. H. T. Edzes, *J. Magn. Reson.*, 1990, **86**, 293.
94. A. Vlassenbroek, J. Jeener and P. Broekaert, *J. Magn. Reson. A*, 1996, **118**, 234.
95. J. Jeener, A. Vlassenbroek and P. Broekaert, *J. Chem. Phys.*, 1995, **103**, 1309.
96. C. J. Bowden, T. Heseltine and M. J. Prandolini, *Chem. Phys. Lett.*, 1995, **233**, 639.
97. P. Broekaert, A. Vlassenbroek, J. Jeener, G. Lippens and J.-M. Wieruszeski, *J. Magn. Reson. A*, 1996, **120**, 97.
98. Q. He, W. Richter, S. Vathyam and W. S. Warren, *J. Chem. Phys.*, 1993, **98**, 6779.
99. W. Richter, S. Lee, W. S. Warren and Q. He, *Science*, 1995, **267**, 654.
100. S. Lee, W. Richter, S. Vathyam and W. S. Warren, *J. Chem. Phys.*, 1996, **105**, 874.
101. S. Vathyam, S. Lee and W. S. Warren, *Science*, 1996, **272**, 92.
102. P. Kumar, *Chem. Phys. Lett.*, 1996, **259**, 611.
103. M. McCoy and W. S. Warren, *J. Chem. Phys.*, 1990, **93**, 858.
104. W. S. Warren, Q. He, M. McCoy and F. C. Spano, *J. Chem. Phys.*, 1992, **96**, 1659.
105. D. Abergel, M. A. Delsuc and J. Y. Lallemand, *J. Chem. Phys.*, 1992, **96**, 1657.
106. J. Keeler, R. T. Clowes, A. L. Davis and E. D. Laue, in *Methods in Enzymology* (ed. N. J. Oppenheimer and T. L. James), Vol. 239, p. 145, Academic Press, San Diego, 1994.
107. D. Canet and M. Decorps, in *Dynamics of Solutions and Fluid Mixture by NMR* (ed. J. J. Delpuech), p. 310, Wiley, New York, 1995.
108. W. S. Price, *Annu. Rep. NMR Spectrosc.*, 1996, **32**, 51.
109. T. Parella, *Magn. Reson. Chem.*, 1996, **34**, 329.
110. S. Berger, *Prog. NMR Spectrosc.*, 1997, **30**, 137.
111. T. Parella, *Magn. Reson. Chem.*, 1998, **36**, 467.
112. C. Dalvit and J. M. Böhlen, *J. Magn. Reson. B*, 1996, **111**, 76.
113. N. C. Nielsen, H. Thøgersen and O. W. Sørensen, *J. Am. Chem. Soc.*, 1995, **117**, 11365.
114. J. Keeler and D. Neuhaus, *J. Magn. Reson.*, 1985, **63**, 454.
115. D. J. States, R. A. Haberkorn and D. J. Ruben, *J. Magn. Reson.*, 1982, **48**, 286.
116. J. Balbach and H. Kessler, *J. Magn. Reson. B*, 1994, **105**, 83.
117. G. Drobny, A. Pines, S. Sinton, D. P. Weitekamp and D. Wemmer, *Symp. Faraday Soc.*, 1979, **13**, 49.
118. D. Marion and K. Wüthrich, *Biochem. Biophys. Res. Commun.*, 1983, **113**, 967.
119. A. Bax and S. S. Pochapsky, *J. Magn. Reson.*, 1992, **99**, 638.
120. G. Bodenhausen, R. Freeman and D. L. Turner, *J. Magn. Reson.*, 1977, **27**, 511.
121. C. Dalvit, M. Rance and P. E. Wright, *J. Magn. Reson.*, 1986, **69**, 356.
122. H. Oschkinat and G. Bodenhausen, *J. Magn. Reson.*, 1987, **73**, 565.
123. M. Novic, H. Oschkinat, P. Pfaendler and G. Bodenhausen, *J. Magn. Reson.*, 1987, **73**, 493.
124. C. Dalvit and J. M. Böhlen, *J. Magn. Reson. B*, 1996, **113**, 195.
125. C. Dalvit and J. M. Böhlen, *J. Magn. Reson.*, 1997, **126**, 149.
126. P. C. M. Van Zijl, M. O. Johnson, S. Mori and R. E. Hurd, *J. Magn. Reson. A*, 1995, **113**, 265.
127. R. Bowtell and A. Peters, *J. Magn. Reson. A*, 1995, **115**, 55.
128. R. E. Hurd, A. Deese, M. O. Johnson, S. Sukumar and P. C. M. Van Zijl, *J. Magn. Reson. A*, 1996, **119**, 285.
129. N. Bloembergen and P. V. Pound, *Phys. Rev.*, 1954, **95**, 9.
130. A. Abragam, *The Principles of Nuclear Magnetism*, Oxford University Press, London, 1961.
131. W. S. Warren, S. L. Hammes and J. L. Bates, *J. Chem. Phys.*, 1989, **91**, 5895.
132. A. Vlassenbroek, J. Jeener and P. Broekhaert, *J. Chem. Phys.*, 1995, **233**, 639.
133. A. L. Joseph, D. Abergel and J.-Y. Lallemand, *J. Biomol. NMR*, 1995, **5**, 212.
134. P. Broekaert and J. Jeener, *J. Magn. Reson. A*, 1995, **113**, 274.
135. W. E. Mass, F. H. Laukien and D. G. Cory, *J. Magn. Reson. A*, 1995, **113**, 274.
136. S. Zhang and D. G. Gorenstein, *J. Magn. Reson. A*, 1996, **118**, 291.

137. G. E. Ball, G. J. Bowden, T. H. Heseltine, M. J. Prandolini and W. Bermel, *Chem. Phys. Lett.*, 1996, **261**, 421.
138. X.-A. Mao and C. H. Ye, *Concepts Magn. Reson.*, 1997, **9**, 173.
139. J.-H. Chen and X.-A. Mao, *J. Chem Phys.*, 1997, **107**, 7120.
140. V. Sklenár, *J. Magn. Reson. A*, 1995, **114**, 132.
141. C. Dalvit and J. M. Böhlen, *Magn Reson. Chem.*, 1996, **34**, 829.
142. L. Tsoref, H. Shinar and G. Navon, *Magn. Reson. Med.*, 1998, **39**, 11.
143. T.-L. Hwang and A. J. Shaka, *J. Magn. Reson. A*, 1995, **112**, 275.
144. C. Dalvit, *J. Biomol. NMR*, 1998, **11**, 437.
145. J. Boyd and N. Soffe, *J. Magn. Reson.*, 1989, **85**, 406.
146. S. L. Patt, *J. Magn. Reson.*, 1992, **96**, 94.
147. E. Liepinsh and G. Otting, *Nature Biotechnol.*, 1997, **15**, 967.
148. C. Dalvit and J. M. Böhlen, *Magn Reson. Chem.*, 1998, **36**, 670.
149. G. Kontaxis, J. Stonehouse, E. D. Laue and J. Keeler, *J. Magn. Reson. A*, 1994, **111**, 70.
150. W. P. Aue, E. Bartholdi and R. R. Ernst, *J. Chem. Phys.*, 1976, **64**, 2229.
151. J. C. Hoch and A. S. Stern, *NMR Data Processing*, Wiley-Liss, New York, 1996.
152. L. Braunschweiler and R. R. Ernst, *J. Magn. Reson.*, 1983, **53**, 521.
153. A. Bax and D. G. Davis, *J. Magn. Reson.*, 1985, **65**, 355.
154. M. Piotto, V. Saudek and V. Sklenar, *J. Biomol. NMR*, 1992, **2**, 661.
155. V. Sklenár, M. Piotto, R. Leppik and V. Saudek, *J. Magn. Reson. A*, 1993, **102**, 241.
156. M. Rance, *J. Magn. Reson.*, 1987, **74**, 557.
157. R. Bazzo and I. D. Campbell, *J. Magn. Reson.*, 1988, **76**, 358.
158. A. L. Davis, G. Estcourt, J. Keeler, E. D. Laue and J. J. Titman, *J. Magn. Reson. A*, 1993, **105**, 167.
159. C. Griesinger, G. Otting, K. Wüthrich and R. R. Ernst, *J. Am. Chem. Soc.*, 1988, **110**, 7870.
160. D. L. Mattiello, W. S. Warren, L. Müller and B. T. Farmer II, *J. Am. Chem. Soc.*, 1996, **118**, 3253.
161. A. L. Davis, E. D. Laue, J. Keeler, D. Moskau and J. Lohman, *J. Magn. Reson.*, 1991, **94**, 637.
162. B. Ancian, I. Bourgeois, J.-F. Dauphin and A. A. Shaw, *J. Magn. Reson.*, 1997, **125**, 348.
163. O. W. Sørensen, M. H. Levitt and R. R. Ernst, *J. Magn. Reson.*, 1983, **55**, 104.
164. M. Rance, O. W. Sørensen, W. Leupin, H. Kogler, K. Wüthrich and R. R. Ernst, *J. Magn. Reson.*, 1985, **61**, 67.
165. S. Wimperis, *J. Magn. Reson.*, 1990, **87**, 174.
166. O. W. Sørensen, M. Rance and R. R. Ernst, *J. Magn. Reson.*, 1984, **56**, 527.
167. A. Hammarström and G. Otting, *J. Am. Chem. Soc.*, 1994, **116**, 8847.
168. K. Albert, *J. Chromatogr. A*, 1995, **703**, 123.
169. J. C. Lindon, J. K. Nicholson and I. D. Wilson, *Prog. NMR Spectrosc.*, 1996, **29**, 1.
170. K. Stott, J. Stonehouse, J. Keeler, T. L. Hwang and A. J. Shaka, *J. Am. Chem. Soc.*, 1995, **117**, 4199.
171. K. Stott, J. Keeler, Q. N. Van and A. J. Shaka, *J. Magn. Reson.*, 1997, **125**, 302.
172. S. H. Smallcombe, S. L. Patt and P. A. Keifer, *J. Magn. Reson. A*, 1995, **117**, 295.
173. C. Bauer, R. Freeman, T. Frenkiel, J. Keeler and A. J. Shaka, *J. Magn. Reson.*, 1984, **58**, 442.
174. R. J. Ogg, P. B. Kingsley and J. S. Taylor, *J. Magn. Reson. B*, 1994, **104**, 1.
175. C. Dalvit, S. Y. Ko and J. M. Böhlen, *J. Magn. Reson. B*, 1996, **110**, 124.
176. T. Parella, P. Adell, F. Sanchez-Ferrando and A. Virgili, *Magn. Reson Chem.*, 1998, **36**, 245.
177. T. Parella, F. Sánchez-Ferrando and A. Virgili, *J. Magn. Reson.*, 1998, **135**, 50.
178. C. Dalvit, P. E. Wright and M. Rance, *J. Magn. Reson.*, 1987, **71**, 539.
179. A. A. Bothner-By, R. L. Stephens, J.-M. Lee, C. D. Warren and R. W. Jeanloz, *J. Am. Chem. Soc.*, 1984, **106**, 811.
180. A. Bax and D. G. Davis, *J. Magn. Reson.*, 1985, **63**, 207.

181. J. Jeener, B. H. Meier, P. Bachmann and R. R. Ernst, *J. Chem. Phys.*, 1979, **71**, 4546.
182. L. R. Brown, *J. Magn. Reson.*, 1984, **57**, 513.
183. R. V. Hosur, *Prog. NMR Spectrosc.*, 1990, **22**, 1.
184. A. Bax and R. Freeman, *J. Magn. Reson.*, 1981, **44**, 542.
185. C. Dalvit, *J. Magn. Reson. A*, 1995, **113**, 120.
186. C. Dalvit and U. Hommel, *J. Biomol. NMR*, 1995, **5**, 306.
187. N. Birlirakis, R. Cerdan and E. Guittet, *J. Biomol. NMR*, 1996, **8**, 487.
188. C. Dalvit, G. Shapiro, J. M. Böhlen and T. Parella, *Magn. Reson. Chem.*, 1998, **36**, in press.
189. P. Stilbs, *Prog. NMR Spectrosc.*, 1987, **19**, 1.
190. K. F. Morris and C. S. Johnson Jr, *J. Am. Chem. Soc.*, 1992, **114**, 3139.
191. K. F. Morris and C. S. Johnson Jr, *J. Am. Chem. Soc.*, 1993, **115**, 4291.
192. K. F. Morris, P. Stilbs and C. S. Johnson Jr, *Anal. Chem.*, 1994, **66**, 211.
193. H. Barjat, G. A. Morris, S. Smart, A. G. Swanson and S. C. R. Williams, *J. Magn. Reson. B*, 1995, **108**, 170.
194. P. Stilbs, K. Paulsen and P. C. Griffiths, *J. Phys. Chem.*, 1996, **100**, 8180.
195. N. Birlirakis and G. Guittet, *J. Am. Chem. Soc.*, 1996, **118**, 13083.
196. C. Dalvit and J. M. Böhlen, *NMR Biomed.*, 1997, **10**, 285.
197. E. O. Stejskal and J. E. Tanner, *J. Chem. Phys.*, 1965, **42**, 288.
198. W. S. Price and P. W. Kuchel, *J. Magn. Reson.*, 1991, **94**, 133.
199. M. A. Korpela, *Prog. NMR Spectrosc.*, 1995, **27**, 475.
200. J. K. Nicholson, P. J. D. Foxall, M. Spraul, R. D. Farrant and J. C. Lindon, *Anal. Chem.*, 1995, **67**, 793.
201. J. E. Tanner, *J. Chem. Phys.*, 1970, **52**, 2523.
202. M. Liu, J. K. Nicholson and J. C. Lindon, *Anal. Chem.*, 1996, **68**, 3370.
203. M. Lin and M. J. Shapiro, *J. Org. Chem.*, 1996, **61**, 7617.
204. A. Jerschow and N. Müller, *J. Magn. Reson. A*, 1996, **123**, 222.
205. M. Liu, J. K. Nicholson, J. A. Parkinson and J. C. Lindon, *Anal. Chem.*, 1997, **69**, 1504.
206. M. Lin, M. J. Shapiro and J. R. Wareing, *J. Am. Chem. Soc.*, 1997, **119**, 5249.
207. E. K. Gozansky and D. G. Gorenstein, *J. Magn. Reson. B*, 1996, **111**, 94.
208. J. F. Martin, L. S. Selwyn, R. R. Vold and R. L. Vold, *J. Chem. Phys.*, 1982, **76**, 2632.
209. D. Zax and A. Pines, *J. Chem. Phys.*, 1983, **78**, 6333.
210. L. E. Kay and J. H. Prestegard, *J. Magn. Reson.*, 1986, **67**, 103.
211. H. Kogler, O. W. Sørensen, G. Bodenhausen and R. R. Ernst, *J. Magn. Reson.*, 1983, **55**, 157.
212. E. Wörgötter, G. Wagner and K. Wüthrich, *J. Am. Chem. Soc.*, 1986, **108**, 6162.
213. S. W. Fesik, R. T. Gampe and T. W. Rockway, *J. Magn. Reson.*, 1987, **74**, 366.
214. R. H. Griffey and A. G. Redfield, *Q. Rev. Biophys.*, 1987, **19**, 51.
215. G. Otting and K. Wüthrich, *J. Magn. Reson.*, 1989, **85**, 586.
216. G. Otting and K. Wüthrich, *Q. Rev. Biophys.*, 1990, **23**, 39.
217. G. Wider, C. Weber, R. Traber, H. Widmer and K. Wüthrich, *J. Am. Chem. Soc.*, 1990, **112**, 9015.
218. S. W. Fesik, R. T. Gampe, Jr, H. L. Eaton, G. Gemmecker, E. T. Olejniczak, P. Neri, T. F. Holzman, D. A. Egan, R. Edalji, R. Simmer, R. Helfrich, J. Hochlowski and M. Jackson, *Biochemistry*, 1991, **30**, 6574.
219. M. Ikura and A. Bax, *J. Am. Chem. Soc.*, 1992, **114**, 2433.
220. G. Gemmecker, E. T. Olejniczak and S. W. Fesik, *J. Magn. Reson.*, 1992, **96**, 199.
221. A. M. Petros, M. Kawai, J. R. Luly and S. W. Fesik, *FEBS Lett.*, 1992, **308**, 309.
222. P. J. M. Folkers, R. H. A. Folmer, R. N. H. Konings and C. W. Hilbers, *J. Am. Chem. Soc.*, 1993, **115**, 3798.
223. J. Lee, J. Fejzo and G. Wagner, *J. Magn. Reson. B*, 1993, **102**, 322.
224. W. Lee, M. J. Revington, C. Arrowsmith and L. E. Kay, *FEBS Lett.*, 1994, **350**, 87.
225. A. Bax, S. Grzesiek, A. M. Gronenborn and G. M. Clore, *J. Magn. Reson. A*, 1994, **106**, 269.

226. R. H. A. Folmer, C. W. Hilbers, R. N. H. Konings and K. Hallenga, *J. Biomol. NMR*, 1995, **5**, 427.
227. K. Ogura, H. Terasawa and F. Inagaki, *J. Biomol. NMR*, 1996, **8**, 492.
228. C. Zwahlen, P. Legault, S. J. F. Vincent, J. Greenblatt, R. Konrat and L. E. Kay, *J. Am. Chem. Soc.*, 1997, **119**, 6711.
229. C. Dalvit, P. Ramage and U. Hommel, *J. Magn. Reson.*, 1998, **131**, 148.
230. F. J. M. Van De Ven, C. A. G. Haasnoot and C. W. Hilbers, *J. Magn. Reson.*, 1985, **61**, 181.
231. P. Berthault and B. Perly, *J. Magn. Reson.*, 1989, **81**, 631.
232. M. P. Williamson, N. J. Murray and J. P. Waltho, *J. Magn. Reson.*, 1992, **100**, 593.
233. S. Macura, N. G. Kumar and L. R. Brown, *J. Magn. Reson.*, 1984, **60**, 99.
234. L. Müller and A. Pardi, *J. Am. Chem. Soc.*, 1985, **107**, 3484.
235. C. Dalvit, *J. Magn. Reson. B*, 1996, **110**, 225.
236. C. Dalvit, *J. Magn. Reson. B*, 1996, **112**, 186.
237. H. Oschkinat, C. Griesinger, P. J. Kraulis, O. W. Sørensen, R. R. Ernst, A. M. Gronenborn and G. M. Clore, *Nature*, 1988, **332**, 374.
238. G. W. Vuister, R. Boelens and R. Kaptein, *J. Magn. Reson.*, 1988, **80**, 176.
239. C. Griesinger, O. W. Sørensen and R. R. Ernst, *J. Magn. Reson.*, 1989, **84**, 14.
240. I. Pelczer, K. D. Bishop, G. C. Levy and P. N. Borer, *J. Magn. Reson.*, 1991, **91**, 604.
241. H. Geen and R. Freeman, *J. Magn. Reson.*, 1991, **93**, 93.
242. L. Emsley, in Methods in Enzymology (ed. N. J. Oppenheimer and T. L. James), Vol. 239, p. 207, Academic Press, San Diego, 1994.
243. C. Dalvit and U. Hommel, *J. Magn. Reson. B*, 1995, **109**, 334.
244. C. Dalvit, *J. Magn. Reson. B*, 1996, **112**, 282.
245. C. Redfield and C. M. Dobson, *Biochemistry*, 1988, **27**, 122.
246. R. Dunkel, C. L. Mayne, R. J. Pugmire and D. M. Grant, *Anal. Chem.*, 1992, **64**, 3133.
247. R. Dunkel, C. L. Mayne, M. P. Foster, C. M. Ireland, D. Li, N. L. Owen, R. J. Pugmire and D. M. Grant, *Anal. Chem.*, 1992, **64**, 3150.
248. A. Demarco and K. Wüthrich, *J. Magn. Reson.*, 1976, **24**, 201.
249. T.-L. Hwang and A. J. Shaka, *J. Am. Chem. Soc.*, 1992, **114**, 3157.
250. T.-L. Hwang and A. J. Shaka, *J. Magn. Reson. B*, 1993, **102**, 155.
251. R. Wagner and S. Berger, *J. Magn. Reson. A*, 1996, **123**, 119.
252. T. Parella, F. Sanchez-Ferrando and A. Virgili, *J. Magn. Reson.*, 1997, **125**, 145.
253. D. I. Hoult and R. E. Richards, *Proc. R. Soc. London, Ser. A*, 1975, **344**, 311.

This Page Intentionally Left Blank

Index

Note: Figures and Tables are indicated [in this index] by *italic page numbers*

ISBN 0-12-505337-1